SPIN-POLARIZED POSITRON ANNIHILATION SPECTROSCOPY

JOSEF ANDREAS WEBER

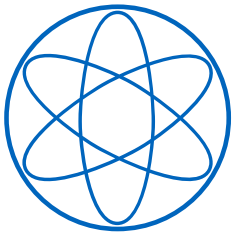

Investigation of Complex Metallic Systems

Doktor der Naturwissenschaften (Dr. rer. nat.)

Physik Department
Technische Universität München

TECHNISCHE UNIVERSITÄT MÜNCHEN
LEHRSTUHL E21

SPIN-POLARIZED POSITRON ANNIHILATION SPECTROSCOPY
INVESTIGATION OF COMPLEX METALLIC SYSTEMS

JOSEF ANDREAS WEBER

Vollständiger Abdruck der von der Fakultät für Physik der Technischen Universität München zur Erlangung des akademischen Grades eines

Doktors der Naturwissenschaften (Dr. rer. nat.)

genehmigten Dissertation.

Vorsitzender:	Prof. Dr. Norbert Kaiser
Prüfer der Dissertation:	1. Priv.-Doz. Dr. Christoph P. Hugenschmidt
	2. Prof. Dr. Rudolf Gross
	3. Prof. Dr. Claudia Felser (nur schriftliche Beurteilung)

Die Dissertation wurde am 21.09.2016 bei der Technischen Universität München eingereicht und durch die Fakultät für Physik am 03.02.2017 angenommen.

ABSTRACT

This thesis focuses on the investigation of the electronic structure and the Fermi surface (FS) of copper, iron, vanadium and Cu_2MnAl. To this end the data acquisition for the new angular correlation of electron positron annihilation radiation (ACAR) spectrometer at the Technische Universität München was designed and new approaches for data evaluation were developed including a novel algorithm to reconstruct 3D electron-positron momentum densities from projections. Using the new toolkit the elemental systems copper, iron and vanadium were investigated and compared to previously reported experimental and theoretical data. Additionally, an extensive study on the Heusler compound Cu_2MnAl with spin-polarized ACAR and magnetic Compton scattering (MCS) was conducted. Spin-polarized ACAR in particular made it possible to measure for the first time the spin dependent FS of this system and to determine the individual contribution of each sheet to the total magnetization. Via the comparison with MCS measurements in combination with suitable ab initio calculations it is now possible to attribute the magnetic momentum density to specific electronic states. This information substantially contributes to the deeper understanding of the technical highly relevant material class of Heusler alloys.

ZUSAMMENFASSUNG

Diese Arbeit widmet sich der Untersuchung der elektronischen Struktur und der Fermi-Fläche von Kupfer, Eisen, Vanadium und Cu_2MnAl. Zu diesem Zweck wurde für das neue Spektrometer zur Messung der Winkelkorrelation der Annihilationsstrahlung von Elektronen-Positronen-Paaren (ACAR) an der Technische Universität München die Datenaufnahme entworfen und Methoden zur Datenverarbeitung inklusive eines neuartigen Algorithmus zur Rekonstruktion von dreidimensionalen Elektron-Positron-Impulsdichten aus ihren Projektionen entwickelt. Mittels dieser Techniken wurden die elementaren Systeme Kupfer, Eisen und Vanadium untersucht und in den Kontext bisheriger theoretischer und experimenteller Ergebnisse aus der Literatur gestellt. Darüber hinaus wurde das Heusler-System Cu_2MnAl mithilfe von spinpolarisiertem ACAR und magnetischer Comptonstreuung (MCS) ausführlich erforscht. Insbesondere spinpolarisiertes ACAR erlaubte erstmals spinaufgelöst die Fermifläche dieses Metalls zu bestimmen und daraus den individuellen Beitrag jeder Subfläche zur Gesamtmagnetisierung zu extrahieren. Ein Vergleich der Spektren und der MCS Messungen mit geeigneten Ab-initio-Rechnungen erlaubt es nun die magnetische Impulsdichte spezifischen elektronischen Zuständen zuzuordnen. Diese Information trägt wesentlich zum grundlegenden Verständnis der technisch hoch relevanten Heusler Legierungen bei.

CONTENTS

The Fermi surface is the stage on which the "drama of the life of the electron" is played out. And in the same way in which the life of mountain people is essentially different from people living in the valleys, the propeties of electrons in lead, which has an exceedingly complicated Fermi surface [...], do not resemble the properties of sodium, whose Fermi surface is a sphere much smoother than a billiard ball.

—Kaganov and Lifshits [1979]

1 INTRODUCTION

The figurative quote of Kaganov and Lifshits already gives an idea how important the knowledge about the Fermi surface (FS) is to understand the properties of a solid. Although theory has made great progress in modeling electronic systems, there are still materials with properties beyond the possibilities of theoretical modeling like e. g., the spin density wave in chromium. Especially if one wants to design new materials with desired features or functionalities, an in-depth understanding of electronic correlations is necessary. However, there is only a limited number of techniques to probe the FS each exhibiting strengths and weaknesses. The most commonly used techniques today comprise e. g., angle-resolved photoemission spectroscopy (ARPES) and characterization via the de Haas-van Alphen (dHvA) effect. Even though ARPES can not only measure the FS but the whole band structure it is limited to the surface of a material while dHvA can probe the bulk properties but requires cryogenic temperatures and high magnetic fields.

An alternative technique which is being used to investigate the electronic structure is the measurement of the angular correlation of electron positron annihilation radiation (ACAR). It enables the analysis of the electronic structure in the bulk *or* the surface at any desired temperature and independent of a magnetic field. With 2D-ACAR a projection of the electron-positron momentum density $\rho^{2\gamma}$ is measured. There are two different approaches to process the acquired data: i) Data can be quantitatively compared to band structure calculations in order to find meaningful input parameters for the theory. ii) The fully three-dimensional $\rho^{2\gamma}$ can be reconstructed by measuring several projections and the FS can then be identified via discontinuities in the reconstruction. Either way, ACAR can provide valuable information about the electronic structure of a material.

In order to fully utilize the possibilities of ACAR spectroscopy, a careful data treatment is essential. Since positron sources have a limited activity and detectors with sufficient high angular resolution only detect a very small fraction of the annihilating positrons (usually less than 10^{-6}), it typically takes a long time - up to a few weeks - to record a single 2D-ACAR projection. Hence, for the subsequent analysis of the data it is crucial to not introduce artifacts by unnecessary interpolation and to preserve the information about the statistical accuracy. This

requires both a specifically adapted data acquisition and carefully programmed data processing algorithms.

In this thesis, a new 2D-ACAR spectrometer at the Technische Universität München (TUM) was co-developed with the particular goal to improve the data acquisition and to establish novel data processing algorithms. To this end, an algorithm for the reconstruction of $\rho^{2\gamma}$ from projections was established. Using these tools, an investigation on the elementary metals copper, iron and vanadium was conducted. Furthermore, the electronic structure of the Heusler system Cu_2MnAl was studied in detail.

The following chapter explains the basic principles of ACAR spectroscopy and the theory of electrons in solids. In the second part of this work, the spectrometer and the data acquisition is introduced. Subsequently, the reconstruction algorithm is presented after introducing the principles of reconstructing densities from its projections. Finally in the third part, the measurements and the results on the aforementioned systems will be addressed and discussed.

Part I

SOLID STATE PHYSICS WITH POSITRONS

2

POSITRON SOURCES

We live in a universe that is predominantly filled with matter. Consequently, if antimatter is required for experiments, some efforts have to be made. Since positrons are lightweight particles they can be created much easier than other antiparticles that are also used for scientific experiments like antimyons (μ^+) or antiprotons. But even for positrons, there are only two methods currently available for experimental use: radioactive β decay and pair production. Both methods will be discussed in detail in the sections below.

2.1 RADIONUCLIDES AS POSITRON SOURCES

Radioactive β^+ decay can be a very efficient way to create positrons on a laboratory scale. Experimental setups utilizing β^+ nuclides are very compact compared to the much more complex positron sources in research centers (see section 2.2). Nuclides with a neutron deficiency in relation to the number of neutrons of a stable isotope are likely to gain energy by converting a proton into a neutron. This is either possible by electron capture or by emission of a positron. The reaction schema for such a β^+ decay is given by the equation:

$$ {}^{A}_{Z}X \rightarrow {}^{A}_{Z-1}Y + e^+ + \nu_e \tag{1} $$

A nuclide X is converted into the isobar Y with a decremented charge number by emitting a positron e^+ and an electron neutrino ν_e. Since this reaction is a three-body process, the energy of the emitted positron is distributed up to an end point energy E_{max}. Fermi [1934] could derive an analytical expression for the intensity of the β spectrum as a function of the kinetic energy $N(E)$ under the assumption that the neutrino has no mass. For a positron it can be written as

$$ N(E)\,dE \propto C\,F_+(Z,E)\,pT\,(E_{max}-E)^2\,dE \tag{2} $$

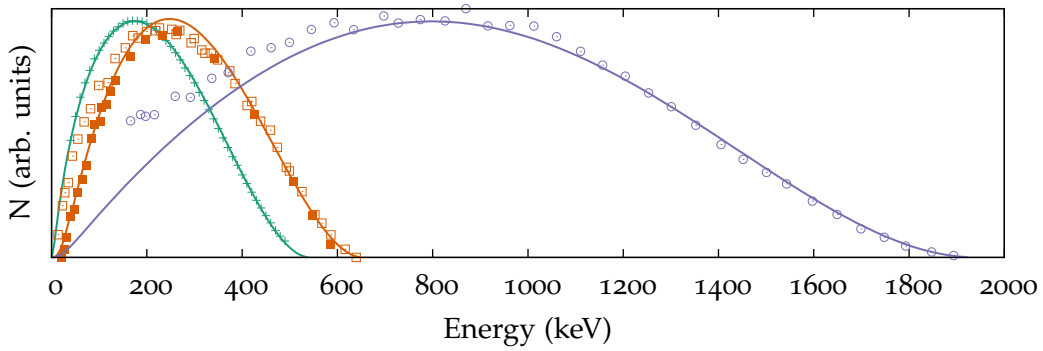

Figure 1: Theoretical β^+ spectra of ^{22}Na and ^{64}Cu and the main emission channel of ^{68}Ga together with the measurements of Wenninger, Stiewe, and Leutz [1968] (+), Cook and Langer [1948] (⊡), Wu and Albert [1949] (■), and Crasemann, Rehfuss, and Easterday [1956] (⊙)

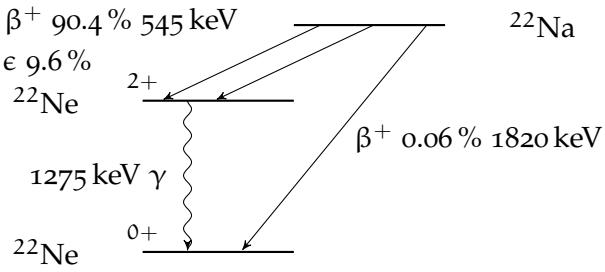

Figure 2: Decay schema of ^{22}Na [Firestone, 2005]

with the positron rest mass m_e, the total energy of the positron $T = E + m_e c^2$ and the positron momentum $p = \frac{1}{c}\sqrt{T^2 - (m_e c^2)^2}$. The factor C takes the transition probability into account and is equal to 1 for allowed transitions. This holds for all technically relevant positron emitters. Finally $F_+(Z, E)$ denotes the so-called Fermi function for positrons which takes the repulsion of the core into account (see appendix A.1 for the full expression). In figure 1 the analytical β spectra for ^{22}Na, ^{64}Cu and ^{68}Ge are depicted, together with published measurements.

Positrons created by β^+ decay carry a longitudinal net polarization P that is given by the ratio of their velocity v to the speed of light c,

$$P = \frac{v}{c} = \sqrt{1 - \frac{E_0}{T}}, \tag{3}$$

with the rest energy E_0 and the total energy T of the emitted positron. The polarization is canonically defined as

$$P = \frac{N^{\uparrow} - N^{\downarrow}}{N^{\uparrow} + N^{\downarrow}}. \tag{4}$$

Here $N^{\uparrow/\downarrow}$ denotes the fraction of positrons with the net polarization parallel/antiparallel to the direction of emittance.

From the many β^+ emitters, there are only some that are used as a positron source in experiments. A selection out of this technical relevant emitters is introduced in the next paragraphs, i. e. ^{22}Na, ^{64}Cu and ^{68}Ga. A comprehensive compilation of the main properties of these emitters is given in table 1.

^{22}Na

Nowadays, the most common positron emitter used in the lab is ^{22}Na, since it has many advantages compared to other positron emitting nuclides. Most important for the experimentalist is the long half life of 2.6 a. Another reason for its frequent use can be explained by means of the decay schema in figure 2: i) the β efficiency is high compared to the electron capture ϵ decay channel and ii) every positron emission of the main deexcitation channel is immediately followed by the emission of a 1275 keV γ quantum. The latter can be used as a starting signal in positron lifetime spectroscopy (PLS) and thus greatly facilitates the experimental effort needed for this technique.

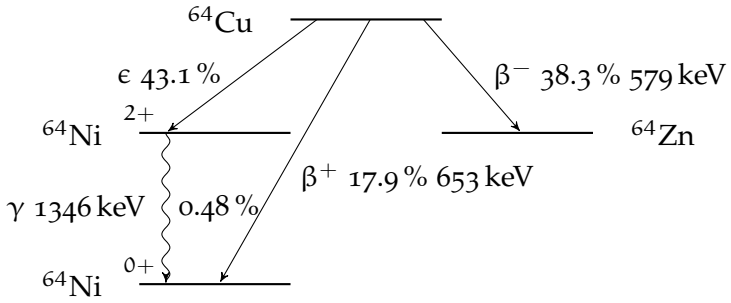

Figure 3: Decay schema of ^{64}Cu [B. Singh, 2007]

^{22}Na is mainly produced in South Africa by bombarding a magnesium target with deuterons according to the reaction $^{24}\mathrm{Mg}\,(\mathrm{d},\alpha)\,^{22}\mathrm{Na}$ [Brits and von S. Toerien, 1988]. It is commercially available as an open solution or sealed in a standardized source capsule.

^{64}Cu

The positron emitter ^{64}Cu is mostly of historical relevance for ACAR spectroscopy. Pioneering research has been done using ^{64}Cu as a source and as a sample (see e. g., Beringer and Montgomery [1942] and Fujiwara and Sueoka [1966]). If a nuclear reactor is at hand ^{64}Cu can simply be created by neutron activation, according to the reaction $^{63}\mathrm{Cu}\,(\mathrm{n},\gamma)\,^{64}\mathrm{Cu}$. Although its branching ratio is low (see figure 3), the high cross section (4.5 b) and the short half life allows the fabrication of highly intense positron sources. This, however, can be also a disadvantage for long term experiments.

An interesting positron source based on ^{64}Cu was build at the research reactor Brookhaven by Lynn et al. [1987]. A copper target was activated at the reactor, subsequently placed in a vacuum chamber and evaporated onto a tungsten surface. Another ^{64}Cu based reactor source was planned and tested in Delft. However, the idea had been abandoned as the pair production of positrons turned out to be more efficient [van Veen et al., 1997].

^{68}Ga

Although ^{68}Ga is a positron emitter, it is misleading to talk about ^{68}Ga sources: Because of the short half life of ^{68}Ga of 68 min it is produced inside the source as the daughter nucleus of ^{68}Ge by electron capture (see the decay schema of the so-called generator system in figure 4). Therefore, the overall half life of ^{68}Ga sources is governed by the longer half life of ^{68}Ge of 275 d. The most interesting feature of ^{68}Ga is the high positron polarization of 90 %, which is a result of the high endpoint energy of 1.9 MeV. This high polarization is extremely convenient for experiments with magnetic materials. Regardless of these benefits, there are only few recent published measurements utilizing ^{68}Ge.

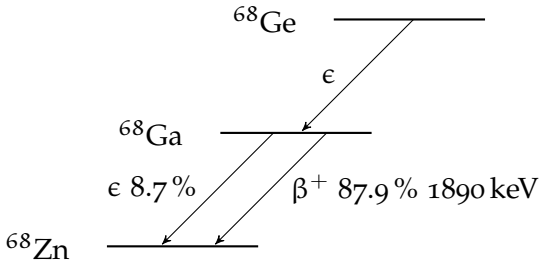

Figure 4: Main decay schema of ^{68}Ge [Burrows, 2002]

NUCLIDE	$T_{1/2}$	E_{max} (keV)	$\bar{E}$ (keV)	$\bar{P}$ (%)
^{22}Na	2.6 a	545	215	67
^{64}Cu	12.7 h	653	282	73
^{68}Ge/^{68}Ga	275 d	1890	856	90

Table 1: Half life $T_{1/2}$, endpoint energy E_{max}, mean Energy $\bar{E}$ and mean polarization of Various nuclear positron sources. Values for half life and endpoint energy are taken from [Burrows, 2002; Firestone, 2005; B. Singh, 2007]; mean energy and mean polarization are calculated taking into account the analytical spectra.

2.2 POSITRON SOURCES AT LARGE-SCALE RESEARCH CENTERS

Research centers with positron beams are in most cases either nuclear reactors or electron accelerators. But there are exceptions like the planned positron beam at the ELI-NP in Măgurele near Bucharest. Although the predominant mechanism for positron creation in these facilities is pair production, there are some appreciable though only historical relevant concepts for reactor based positron beams that do not use pair production.

Two of these concepts have already been mentioned in the previous section and are based on the activation of copper. Another concept was developed by A. P. Mills [2014]: He proposed to use a closed cycle of krypton, which would be activated in a reactor and subsequently frozen onto a surface. However, there has never been an attempt to build such a positron source.

The most relevant mechanism to create positrons is pair production in the field of an atomic core. Pair production can also occur in the field of an electron, but the cross section for this so-called triplet production is much lower. The mechanism for pair production is well known ever since the first days of positron physics: If energy, momentum and angular momentum are conserved, a photon can create an electron-positron-pair in vacuum. The conservation of energy implies that the photon has an energy of at least $2\,m_e c^2 = 1022\,\text{keV}$. From this threshold the cross section increases approximately as a function of energy with $\sigma_{\text{pair}} \propto \log E_\gamma$ for energies below 10 MeV.

As the dispersion relation of photons is linear, but the dispersion relation for electrons and positrons is quadratic, it is not possible to conserve momentum and energy with the three particles alone (see figure 5). Therefore, pairs can only be created in the vicinity of atomic nuclei. The cross section for pair production

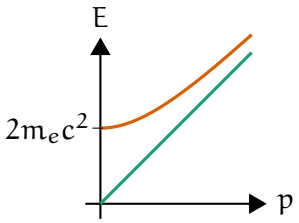

Figure 5: Dispersion relation of a γ quantum and a free positron/electron created by pair production. Since the curves do not cross there has to be an additional particle involved to take the extra momentum.

increases with the atomic number by $\sigma_{pair} \propto Z^2$ [Bethe and Maximon, 1954; Davies, Bethe, and Maximon, 1954]. Thus materials used for the conversion of γ quanta to positrons are always high Z materials like tungsten or platinum.

Finally, also the angular momentum has to be conserved. This can be achieved if the spin of both electron and positron are parallel. Hence, if a polarized γ source is employed, the created positrons will also carry a polarization.

A different mechanism though closely related is the so-called trident process. For electrons with energies above 10 MeV it is directly possible to create an electron positron pair in a converter. However, for most sources this process is of secondary importance.

Reactor-Based Positron Sources

For this kind of positron sources there exist two conceptual different approaches to create γ radiation dependent on the type of reactor. For reactors with a high γ flux, the radiation can be directly used for pair production [Schut et al., 2004]. If the neutron flux is high enough, it can be more efficient to create γ quanta by an intermediate conversion. At the high intense positron source NEPOMUC at the TUM this is done via the reaction $^{113}Cd(n,\gamma)^{114}Cd$ [Hugenschmidt et al., 2014, 2002]. The same concept has been realized at the PULSTAR reactor in the United States of America [Hawari et al., 2009] and is in preparation at the McMaster nuclear reactor in Canada [Mascher, 2015] and the OPAL facility in Australia [Mendis, Bennett, and Schulz, 2013].

Positron Sources at Accelerators

The most common way to create high energetic γ radiation at electron accelerators is by Bremsstrahlung. Therefore, the electrons are directed towards a target where their kinetic energy is converted into bremsstrahlung. An example for the application of this technique is the positron beam EPOS at the linear electron accelerator ELBE near Dresden [Krause-Rehberg et al., 2006] or in Tsukuba in Japan [Akahane et al., 1990]. A totaly different physical effect is employed at the ELI-NP in Măgurele near Bucharest. This facility intends to create high energetic γ rays by the inverse Compton effect.

Laser based Positron Sources

If high intense laser light interacts with matter it is also possible that positrons are produced. They are created directly in a target, if the energy density is high enough like for the PW laser at the Lawrence Livermore National Laboratory [Cowan et al., 1999]. A different mechanism of positron production was recently reported by Sarri et al. [2013]. They used fs laser pulses to fully ionize a gas and accelerate the electrons to relativistic energies. These electrons hit a conversion target and create electron positron pairs either by Bremsstrahlung or by the trident process. Sarri et al. could show that the positrons keep a time structure of the order of fs and possess relativistic energies of around 100 MeV. Even though both experiments yield interesting results there has not yet been the attempt to use the created positrons for experiments.

3

POSITRONS IN VACUUM AND CONDENSED MATTER

3.1 POSITRONS AND POSITRONIUM IN VACUUM

The positron is the anti-particle of the electron as predicted by Dirac [Dirac, 1931]. All the fundamental properties of the positron are equal to the properties of the electron except for the signs of the charge and all charge related quantities like the magnetic moment. Electron-positron pairs can be created and annihilated if all conservation laws are fulfilled. However, to ensure the latter, additional particles have to be present like photons to carry energy or atomic nuclei to conserve momentum.

When a positron and an electron meet in vacuum, they can form a hydrogen-like bound state, so-called positronium. The name was proposed by Ruark [1945], although he was not the first to come up with the idea of a bound electron-positron particle. In a much earlier but unnoticed work, Mohorovičić [1934] proposed the name 'Electrum' and correctly derived the binding energy of this state which is in good approximation half of the binding energy of the hydrogen atom, i. e. $0.5\,R_\infty \approx 6.8\,\mathrm{eV}$.

Four different ground states of positronium can be distinguished. One singlet or para-positronium (p-Ps) state with spin $s = 0$ and magnetic quantum number $m = 0$ and three triplet or ortho-positronium (o-Ps) states with spin $s = 1$ and a magnetic quantum number of $m = -1, 0$ or 1. In the basis of the spin orientations of electron and positron these four states $|s, m\rangle$ can be written as

$$|\Psi_1\rangle = |0,0\rangle \quad = \frac{1}{\sqrt{2}}\left(|\uparrow\downarrow\rangle - |\downarrow\uparrow\rangle\right), \tag{5}$$

$$|\Psi_2\rangle = |1,-1\rangle = |\uparrow\uparrow\rangle, \tag{6}$$

$$|\Psi_3\rangle = |1,0\rangle \quad = \frac{1}{\sqrt{2}}\left(|\uparrow\downarrow\rangle + |\downarrow\uparrow\rangle\right), \tag{7}$$

$$|\Psi_4\rangle = |1,1\rangle \quad = |\downarrow\downarrow\rangle. \tag{8}$$

The first arrow indicates the spin orientation of the positron.

Without a preferred spin-polarization of the positrons and the electrons, each state is equally probable to be formed. Consequently, the probability that an o-Ps is formed, is three times as likely, than that p-Ps is formed. Both o-Ps and p-Ps are not stable and the electron positron pair will annihilate. Wheeler [1946] already theoretically determined the lifetime of the p-Ps state to be 124 ps, which is quite close to value of 125 ps resulting from more precise calculations. The two γ quanta of the p-Ps decay are each emitted with an energy of 511 keV and with antiparallel spin orientation in antiparallel directions, conserving energy, momentum and angular momentum of the p-Ps state. Only if an odd number of γ quanta are emitted it is possible to conserve these quantities in the o-Ps decay. Since this process needs

an additional vertex in the Feynman diagram, its lifetime is significantly longer, i. e. 142 ns (see e. g., Karshenboim [2005]).

In a magnetic field $\mathbf{B} = \begin{pmatrix} 0 \\ 0 \\ B_z \end{pmatrix}$, the ground state energy of the states with $|m| = 1$ is altered while the $m = 0$ states begin to mix. In case the positron polarization is in $\uparrow$-direction, the formation rates F for the triplet $|m| = 1$ states can be derived from equation (6) and (8):

$$F_2 = \frac{1}{4}(1 + P) \tag{9}$$

$$F_4 = \frac{1}{4}(1 - P) \tag{10}$$

By quantum mechanical perturbation calculations it can be shown that the time independent parts of the modified states are given by [Bisi et al., 1962]:

$$\widehat{|\Psi_1\rangle} = \frac{1}{\sqrt{(1+y^2)}}\left(y\,|\Psi_3\rangle + |\Psi_1\rangle\right) \tag{11}$$

$$\widehat{|\Psi_3\rangle} = \frac{1}{\sqrt{(1+y^2)}}\left(|\Psi_3\rangle - y\,|\Psi_1\rangle\right) \tag{12}$$

In these equations, $y = \left(\sqrt{1+x^2} - 1\right)/x$ with $x = 4\mu_B B_z/\hbar\omega_0$, the Bohr magneton μ_B and the ground-state hyper fine splitting $\hbar\omega_0$. For a physical interpretation, one has to evaluate the modified states:

$$\widehat{\langle\Psi_1|\Psi_1\rangle} = \frac{1}{1+y^2}\left(y^2\,\langle\Psi_3|\Psi_3\rangle + \langle\Psi_1|\Psi_1\rangle\right) \tag{13}$$

$$\widehat{\langle\Psi_3|\Psi_3\rangle} = \frac{1}{1+y^2}\left(y^2\,\langle\Psi_1|\Psi_1\rangle + \langle\Psi_3|\Psi_3\rangle\right) \tag{14}$$

Therefore, the perturbed singlet state contains the $y^2/(1+y^2)$ fraction of the o-Ps state Ψ_3. The according holds for the modified o-Ps state Ψ_3. This affects various physical quantities like the annihilation rate and the relative annihilation intensity. The modified singlet annihilation rate $\widehat{\lambda_s}$ for example can now be given as a linear combination of the unperturbed singlet annihilation rate λ_s and the unperturbed triplet annihilation rate λ_t:

$$\widehat{\lambda_s} = \frac{\lambda_s + y^2\lambda_t}{1+y^2} \tag{15}$$

Note that y and thus B_z appears only squared in equation (14). Therefore, all quantities, like the lifetime and the annihilation intensity of these states, do not depend on the *direction* of the magnetic field, but on its absolute value. This changes if a positron source with a polarization P is used.

In order to derive the formation rates for the mixed states, equation (5) and (7) can be substituted in equations (11) and (12):

$$\widehat{|\Psi_1\rangle} = \frac{1}{\sqrt{2\,(1+y^2)}}\left[(1+y)\,|\uparrow\downarrow\rangle - (1-y)\,|\downarrow\uparrow\rangle\right] \tag{16}$$

$$\widehat{|\Psi_3\rangle} = \frac{1}{\sqrt{2\,(1+y^2)}}\left[(1-y)\,|\uparrow\downarrow\rangle + (1+y)\,|\downarrow\uparrow\rangle\right] \tag{17}$$

From the previous calculation, the formation rates for the perturbed states can be given by

$$\begin{aligned}\widehat{F_1} &= \frac{1}{8\,(1+y^2)}\left[(1+y)^2\,(1+P)+(1-y)^2\,(1-P)\right]\\ &= \frac{1}{4}\left(1-\frac{2Py}{1+y^2}\right)\end{aligned} \tag{18}$$

and

$$\begin{aligned}\widehat{F_3} &= \frac{1}{8\,(1+y^2)}\left[(1-y)^2\,(1+P)+(1+y)^2\,(1-P)\right]\\ &= \frac{1}{4}\left(1+\frac{2Py}{1+y^2}\right).\end{aligned} \tag{19}$$

For a nonzero positron polarization, the formation rates are sensitive to the direction of the magnetic field because they depend on y. Therefore, if the annihilation intensity is measured as a function of the magnetic field, a characteristic dependence is obtained which can be used to determine the degree of polarization of the positron source [Ceeh, 2015; Nagai et al., 2000; Page and Heinberg, 1957]. Furthermore, from magnetic field dependent positron annihilation lifetime experiments, the hyperfine splitting of positronium can be determined, which is an important quantity to put theoretical calculations to a test [Bisi et al., 1962; Schleuder, 2015].

3.2 POSITRONS IN CONDENSED MATTER

In order to implant a positron into a solid, it has to have some kinetic energy. For positrons originating from the β^+ decay, the intrinsic energy distribution of the source can be used (see figure 1). But in case of a moderated positron beam, the positrons have to be accelerated in an electric field, usually reaching energies from approximately 1 keV to 50 keV.

Before a positron will face its final fate - annihilation - there are several processes it can undergo in a solid. An overview of the different processes is presented in figure 6. Only the processes relevant for this work are explained in more detail in the following paragraphs.

3.2.1 *Positron Implantation*

Prior to implantation, there is the chance that the positron will be reflected at the potential barrier of the surface. This behavior is analogous to the basic quantum mechanical problem of reflection and transmission of a particle at a potential barrier. Hence, a material with high Z and a high kinetic energy of the incident positron will increase the chance that the positron is reflected (see e. g., [Mäkinen et al., 1992]). In reflection high energy positron diffraction and low energy positron diffraction, the reflection of positrons is employed to investigate the surface (see e. g., [Fukaya et al., 2008]). Compared to the more common low energy electron diffraction and reflection high energy electron diffraction, the respective positron techniques are more element specific and easier to handle theoretically, yielding complementary information about the surface structure.

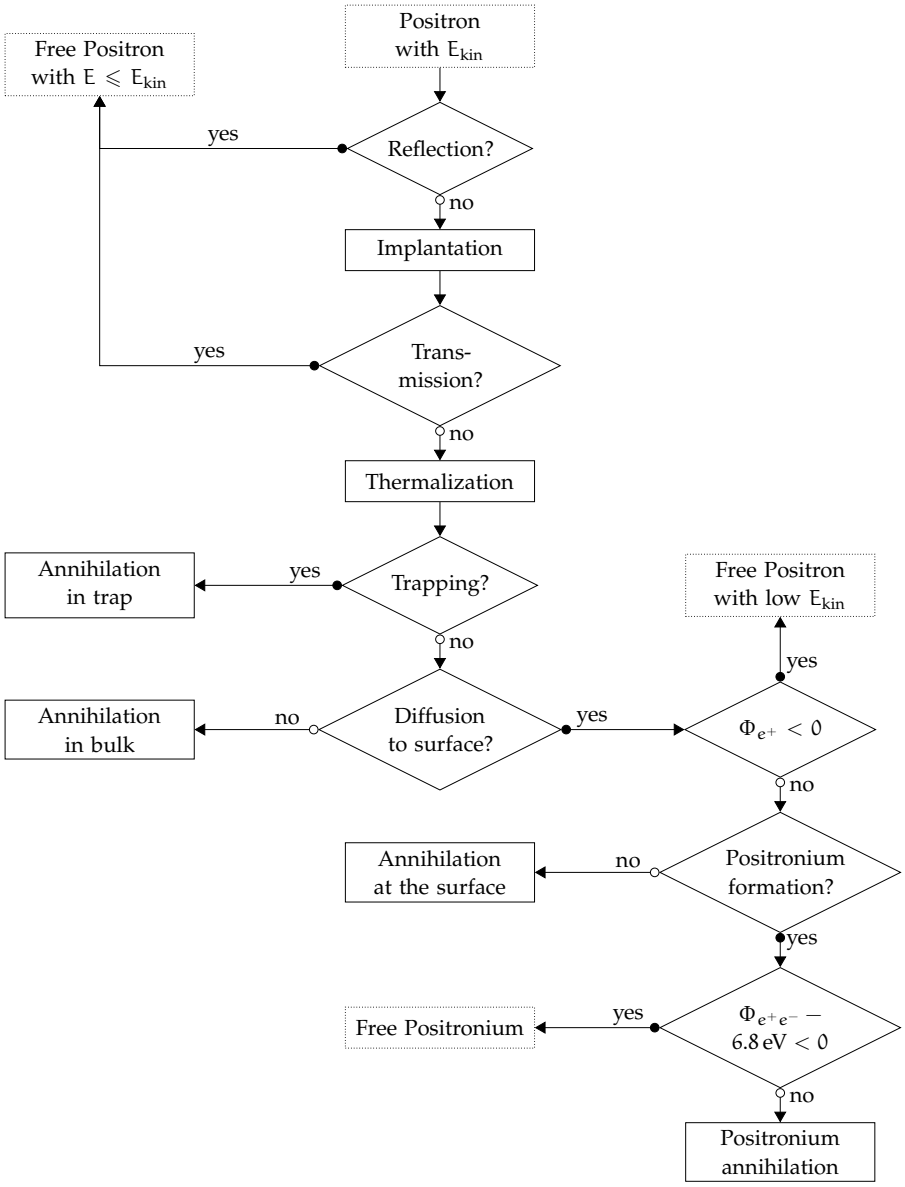

Figure 6: Different interactions of positrons in matter. Positrons which are accelerated towards a sample can get reflected at the surface or, if the sample is thin enough, get transmitted, leading to free positrons with high kinetic energy. But if they are implanted into the solid and do not annihilate in the bulk or in a trap, there is the chance that they diffuse back to the surface. If the work function for positrons Φ_{e^+} is negative, the positrons will leave the solid with a sharp energy distribution (a process called moderation). Otherwise, the positron may annihilate at the surface or form positronium, which can either decay at the surface or is emitted into vacuum.

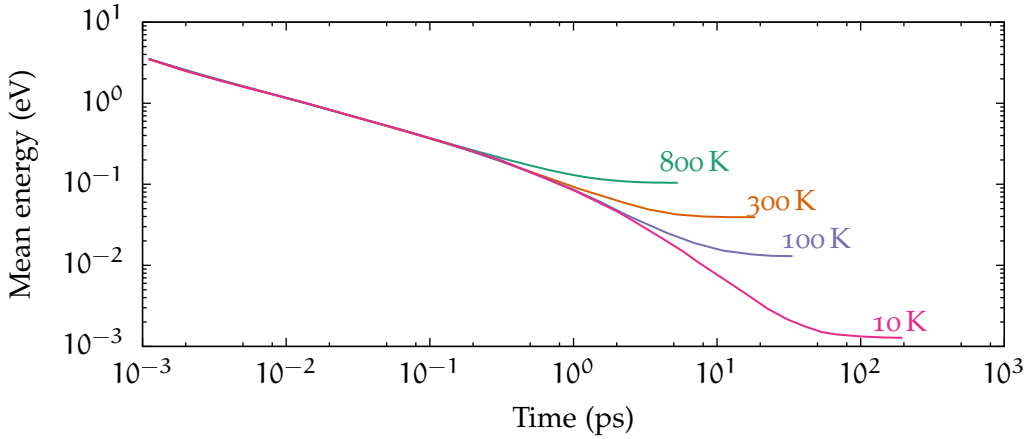

Figure 7: Mean energy of positrons slowing down in Al after implantation as a function of time. Data taken from K. O. Jensen and Walker [1990].

When the surface barrier is overcome, the implanted positrons will rapidly loose kinetic energy and thermalize quickly. The energy loss mechanism is dependent on the positron energy as well as on the material class. Energy loss by Bremsstrahlung is dominant in the MeV range. Yet its cross section for positrons is much smaller compared to electrons because of the repulsion of the positrons by the core. At lower energies the positrons will mainly slow down due to electron scattering and core and valence electron excitation. In metals, plasmon excitation is the main loss mechanism for positrons with energies in the range of the Fermi energy. The last 10th of an eV are finally lost by phonon scattering. Since plasmon excitations are not possible in insulators, complete thermalization is mainly due to phonon scattering and takes considerably longer.

Thermalization at room temperature takes approximately 10 ps, which is much faster than complete thermalization in the low temperature regime (see figure 7). However, positrons in a cold solid loose energy more rapidly. For a temperature of e. g., 10 K the remaining kinetic energy of the positron prior to annihilation will be approximately 1 meV. As the thermal motion affects the experimental resolution in ACAR measurements, it is beneficial for this technique to cool the sample in order to increase the resolution. The momentum sensitivity of ACAR was actually used to proof that the positrons will thermalize even at low temperatures before annihilation [Kubica and Stewart, 1975].

For mono-energetic positrons the implantation depth profile follows a so-called Makhov distribution:

$$I(z) = \frac{m z^{m-1}}{z_0^m} e^{-(z/z_0)^m} \tag{20}$$

This distribution was originally derived for electrons [Makhov, 1961a,b,c] but can be adapted for positrons as well. Makhov determined the shape parameter $m \approx 1.9$ by Monte Carlo calculations. The corrected implantation depth z_0 is connected to the mean implantation depth $\bar{z}$ via the Γ-function:

$$z_0 = \frac{\bar{z}}{\Gamma((1/m)+1)} \tag{21}$$

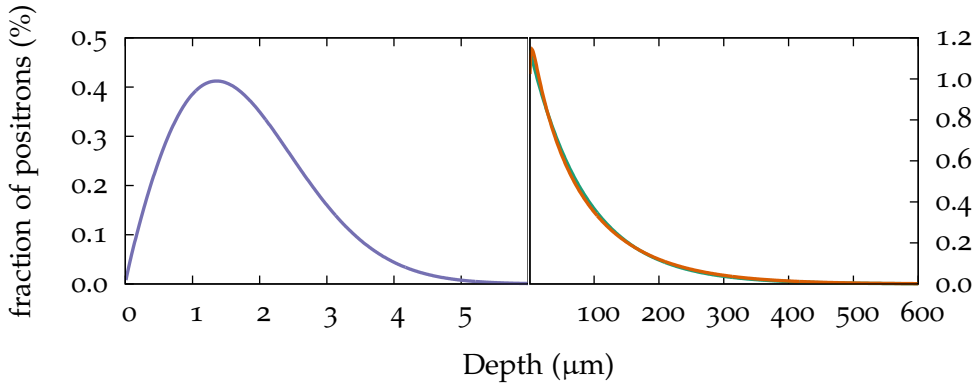

Figure 8: Calculated implantation profiles of positrons into aluminum; left: depth distribution of a mono-energetic beam with 20 keV; right: implantation profile of positrons from a ^{22}Na source. ■: according to the model of Dryzek and Singleton [2006]; ■: Makhov profile weighted with the ^{22}Na β spectrum.

with the mean implantation depth $\bar{z}$:

$$\bar{z} = AE^n. \tag{22}$$

The factor $A \approx 400/\rho \frac{\text{Å}}{\text{keV}^n}$ with the material density ρ and the exponent $n \approx 1.6$ were determined empirically [Allen P. Mills and Wilson, 1982; Vehanen et al., 1987]. Although the Makhov distribution is frequently employed to calculate implantation profiles there also exist further, more complex distribution functions (see e. g., Baker et al. [1991]). Since computational power has increased considerably in the last decades, implantation profiles are nowadays often simulated by Monte Carlo methods for particular problems, especially for layered systems [Ghosh, 1995].

As mentioned in section 2.1, positrons from radioactive sources are not mono-energetic but rather possess a broad energy spectrum (see figure 1). Thus their implantation profile is not Makhov like but exponential as found by transmission studies (see e. g., H. E. Hansen, Linderoth, and Petersen [1982]). From their experiments Dryzek and Singleton [2006] obtained a universal dependence between end point energy E_{max} of a β^+-source and the linear absorption coefficient α:

$$\frac{\alpha}{\rho}\left[\frac{\text{cm}^2}{\text{g}}\right] = \frac{12.6\, Z^{0.17}}{E_{max}^{1.28}}, \tag{23}$$

with the density ρ and the atomic number Z of the target.

A typical Makhov profile for the implantation of 20 keV positrons into aluminum is shown in figure 8 (■). If the energy distribution of ^{22}Na is taken into account the implantation profile calculated in the Makhov approximation differs drastically from the mono-energetic profile (■ in figure 8). Although the Makhov parameter used for this calculation are actually not valid for the energy range of a β-source, the final distribution resembles very closely the empirically derived exponential implantation profile by Dryzek and Singleton.

A notable difference between the implantation profile of a positron beam and a radioactive positron emitter is the much higher mean implantation depth of the radioactive source profile. Hugenschmidt et al. [2015] used this behavior to

separate the contribution from positrons annihilating at the surface from positrons annihilating in the bulk by measuring either with a radioactive source or a positron beam.

3.2.2 *Positron Diffusion*

Thermalized positrons in solids have to be described quantum mechanically since their wave function will emerge into a delocalized Bloch state. However, their motion can also be described by classical diffusion. In absence of an electric field the differential equation for the time dependent positron density $\rho_p(\mathbf{x}, t)$ reads:

$$\frac{\partial \rho_p(\mathbf{x}, t)}{\partial t} = \left(D_p \triangle - \lambda(\mathbf{x})\right) \rho_p(\mathbf{x}, t) \tag{24}$$

Compared to the common diffusion equation, this equation has the additional term $\lambda(\mathbf{x})$ which takes the loss of positrons due to annihilation into account. It comprises the annihilation rate in the bulk λ_{bulk} and the spatially varying trapping rate $\kappa(\mathbf{x})$ which is characteristic for the defect trapping:

$$\lambda(\mathbf{x}) = \lambda_{bulk} + \kappa(\mathbf{x}) \tag{25}$$

Following the Nernst-Einstein relation, the positron diffusion coefficient can be expressed as

$$D_p = \frac{\mu_p(T)}{e} k_B T \tag{26}$$

with the positron mobility $\mu_p(T)$ and the elementary charge e. A measure for the distance the positron will travel before annihilation is the positron diffusion length

$$L_p = \sqrt{D_p \tau} = \sqrt{\frac{D_p}{\lambda}} \tag{27}$$

(see e. g., [Hautojärvi and Corbel, 1995]). Typical diffusion length in defect free metals are in the order of 100 nm [B. Bergersen et al., 1974].

During diffusion the positrons can get localized at trapping centers. Positrons are especially attracted by negatively charged ions or lattice defects (e. g., vacancies or grain boundaries). Especially vacancies act as efficient trapping centers due to the missing repulsion of the atomic core. In metals, they are the main cause for positron trapping. Since the positron is in a delocalized state prior to annihilation, it samples a large volume and is thus a sensitive probe for vacancies. For example at a defect concentration of 1×10^{-6} per atom about 10 % of the positrons get trapped [Hautojärvi and Corbel, 1995].

Positrons in Insulators

Most of the processes mentioned in the previous sections are also valid for insulators. However, the most important difference is the formation of positronium in some insulators. Positronium can exist in a delocalized Bloch state in crystalline solids like α-quartz, or it can get localized in voids or cavities like in polymers and

porous solids. In metals, positronium formation is prohibited due to the shielding of the positron by conduction electrons.

Similar to the vacuum, positronium in a solid exhibits either ortho or para configuration. However, the lifetime of the o-Ps is significantly shortened in matter by the exchange of the bound electron with another electron with antiparallel spin configuration. This so-called 'pick-off process' results in a much higher annihilation rate of o-Ps compared to vacuum.

If an o-Ps gets confined in a void, the overlap of the positronium wave function with the electrons at the inner wall of the void increases with decreasing void size. Since the probability for a pick-off increases with the electron density, the o-Ps lifetime increases if the positronium is trapped in a larger void. Using the semi-classical Tau-Eldrup model [Eldrup, Lightbody, and Sherwood, 1981; Tao, 1972] the void size can be analyzed quantitatively by means of PLS.

3.3 POSITRON LIFETIME SPECTROSCOPY

Positron lifetime spectroscopy (PLS) is the most established positron technique to investigate condensed matter. Since the positron lifetime in a solid is inversely proportional to the electron density ρ_e, the positron lifetime yields information about the electronic environment of the annihilation site of the positron. It can be shown (see e. g., [West, 1973]) that the annihilation probability λ for a free positron and a stationary electron is given by

$$\lambda = \pi r_0^2 c \rho_e \propto \rho_e, \tag{28}$$

with the classical electron radius

$$r_0 = \frac{e^2}{4\pi\epsilon_0 m_e c^2}. \tag{29}$$

Within a solid the positron interacts with the n electrons and the annihilation rate has to be expressed using the wave function $\Psi^{ep}(\mathbf{r}_{pe_1}, ..., \mathbf{r}_{pe_n})$ of the system with the relative coordinates of all electrons and the positron $\mathbf{r}_{pe_j}$:

$$\lambda = \pi r_0^2 c \sum_{\mathbf{r}_{pe_j}=0} |\Psi^{ep}(\mathbf{r}_{pe_1}, ..., \mathbf{r}_{pe_n})|^2 \tag{30}$$

However, even with modern computational methods it is not possible to calculate the wave function of such a large system. Nevertheless, the positron annihilation rate can be calculated reliably (neglecting the 3γ decay) by splitting the positron and electron wave function using the unperturbed electronic wave functions $\Psi_j^e(\mathbf{x})$ of the system:

$$\begin{aligned} \lambda &\approx \pi r_0^2 c \sum_{j=\text{occ.}} \int d\mathbf{x}\ |\Psi^p(\mathbf{x})|^2 \left|\Psi_j^e(\mathbf{x})\right|^2 \gamma_j(\mathbf{x}) \\ &= \pi r_0^2 c \int d\mathbf{x}\, \rho_p(\mathbf{x})\, \rho_e(\mathbf{x})\, \gamma(\rho_e(\mathbf{x})) \end{aligned} \tag{31}$$

This equation is the overlap integral of the positron density ρ_p with the electron density ρ_e modified by the so-called enhancement factor γ. The enhancement

factor takes into account the correlation between electron and positron and can be calculated using approximations with various complexity (see e. g., [Boroński and Nieminen, 1986; Jarlborg and A. K. Singh, 1987]).

Due to the missing positively charged core in a lattice vacancy, the electron density is strongly decreased. Thus, positrons that get trapped there have a significantly increased lifetime. The lifetime in an aluminum vacancy, e. g., increases to approximately 240 ps compared to the bulk lifetime of 160 ps (see the compilation of bulk and vacancy lifetimes of Robles, Ogando, and Plazaola [2007]). This fact, together with the high sensitivity for defects, makes positrons ideally suited for defect spectroscopy.

As the prompt γ quanta in the ^{22}Na decay schema can be used as a starting signal, most lifetime setups rely on this isotope. Other possibilities to get a starting signal are, e. g., the use of a positron beam with time structure or the transmission of a positron through a thin scintillator. Nevertheless, the experimental requirements for these methods are much higher.

A PLS spectra is often a combination of various lifetime components. For example in porous materials there is a short p-Ps lifetime and a distribution of many longer o-Ps lifetimes corresponding to the distribution of pores in the sample. In a metal with defects, the lifetime spectrum consists of the sum of defect lifetimes and a reduced bulk lifetime. This reduction of the bulk lifetime is a consequence of the removal of positrons from the bulk by trapping in defects as can be derived by a calculation (see e. g., [Hautojärvi and Corbel, 1995]). Mathematically a lifetime spectrum $I(t)$ can be expressed as

$$I(t) = \int R(t-\tau) \left(\sum_i A_i \lambda_i e^{-\lambda_i t} \right) d\tau + B(t), \tag{32}$$

where λ_i denotes the different annihilation rates, $R(t)$ the experimental resolution function and $B(t)$ the background in the spectrum. While the resolution $R(t)$ of a spectrometer is typically around 250 ps, there are some experimental setups with significantly better resolution ranging from 160 ps to 140 ps [Bečvář et al., 2000; Vries and Kelling, 1987].

3.4 DOPPLER BROADENING SPECTROSCOPY OF THE ELECTRON-POSITRON ANNIHILATION LINE

Although both, Doppler broadening of the electron positron annihilation radiation (DBAR) and ACAR probe the electron momentum density, they have very different applications and experimental setups. To describe both effects in a physically correct way, a relativistic calculation is required. However, the commonly used approximation can already be derived by a semi-classical approach.

Once a positron annihilates the two antiparallel emitted γ quanta will conserve energy momentum and angular momentum of the initial particles. In order to fulfill the requirement of energy conservation, the sum energy of the quanta γ_1 and γ_2 has to be equal to the energy equivalent of the mass of positron and electron

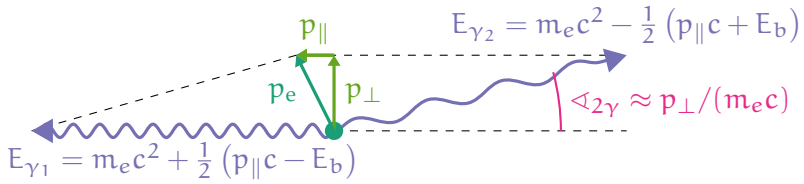

Figure 9: Conservation of energy and momentum in the electron positron annihilation.

minus the electron and positron binding energies E_b (neglecting the kinetic energy of the particles):

$$E_{\gamma_1} + E_{\gamma_2} = 2\, m_e c^2 - E_b \tag{33}$$

Additionally the momentum conservation implies that

$$\frac{E_{\gamma_1}}{c} - \frac{E_{\gamma_2}}{c} = p_\parallel, \tag{34}$$

if the longitudinal momentum of the electron positron pair is $p_\parallel$. Hence, the energy of the emitted γ quanta can be calculated by

$$E_{\gamma_{1/2}} = m_e c^2 + \frac{1}{2}\left(\pm p_\parallel c - E_b\right). \tag{35}$$

The plus sign (minus sign) refers to γ_1 (γ_2) (see figure 9).

Equation (35) shows that the Doppler shift conserves the longitudinal part of the initial electron momentum (neglecting the thermal momentum of the positron). The transversal part $p_\perp$ can only be conserved if both γ quanta are not emitted exactly antiparallel but have an angular deviation from 180°. From figure 9 it can be seen that the angular deviation $\sphericalangle_{2\gamma}$ is given by the ratio of electron momentum and photon momentum:

$$\sphericalangle_{2\gamma} \approx \tan \frac{p_\perp}{m_e c} \approx \frac{p_\perp}{m_e c} \tag{36}$$

The small angle approximation is valid since the measured angles are well below 50 mrad.

The measurand in an ACAR and DBAR experiment - like in any quantum mechanical measurement - is a probability density which as often referred to as $\rho^{2\gamma}(\mathbf{p})$ or the two photon momentum denisty (TPMD). The result of a 2D-ACAR experiment M^{2D} is a 2D-projection of $\rho^{2\gamma}$:

$$M^{2D}(\mathbf{p}_{xy}) \propto \int dp_z\, \rho^{2\gamma}(\mathbf{p}) \tag{37}$$

Likewise, the result of a 1D-ACAR or a DBAR measurement M^{1D} yields a 1D-projection of $\rho^{2\gamma}(\mathbf{p})$:

$$M^{1D}(p_x) \propto \int dp_y \int dp_z\, \rho^{2\gamma}(\mathbf{p}) \tag{38}$$

The TPMD can be calculated in a very similar manner as the positron annihilation rate except that the wave function has to be Fourier transformed:

$$\rho^{2\gamma}(\mathbf{p}) \propto \left| \int d\mathbf{x}\, e^{-i\mathbf{k}\mathbf{x}}\, \psi^{ep}(\mathbf{x}) \right|^2 \tag{39}$$

Notably, the formal similarity of equation (31) and (39) is not incidental. The annihilation rate can also be obtained by integrating over the TPMD:

$$\lambda = \int \mathrm{d}\mathbf{p}\ \rho^{2\gamma}(\mathbf{p}) \tag{40}$$

However, neither during a DBAR nor during an ACAR experiment, the normalization of $\rho^{2\gamma}$ is conserved. Hence, the annihilation rate cannot be extracted from one of these experiments.

In positron science DBAR is an important tool to study the electronic environment of an annihilation site. For this analysis there are two different measurement modalities possible. The coincident Doppler broadening (CDB) spectroscopy uses two energy sensitive detectors to measure *both* annihilation quanta in coincidence while in a standard DBAR experiment only *one* of the annihilation quanta is measured. Since only one detector is needed for DBAR, the experimental setup is much simpler. Additionally, the counting rate is significantly higher, which is especially important if a weak positron source is used.

The unique feature of CDB is the possibility to measure the high momentum part of a spectra with very low background. Since this high momentum part originates predominantly from the annihilation with core electrons, it is not influenced by chemical bonding. Hence, the high momentum part can be used to characterize the element specific environment of the positron annihilation site [Asoka-Kumar et al., 1996; Reiner et al., 2015].

Since the result of a DBAR experiment is a projection of the two dimensional CDB spectrum, the informational content of a DBAR spectrum is much smaller. As a consequence, in a CDB measurement the Compton, small angle scattering and pileup background can be separated (to some extent) from the actual signal. The same is usually not possible for the DBAR spectrum. Because of the high background in DBAR a direct comparison between experiment and ab initio calculation is not feasible. Instead, data are often analyzed by using a zero dimensional line shape parameter, the so-called S-parameter. It is defined as the quotient of the counts in a central region divided by the total number of counts in the photopeak. Since the core annihilation probability for a positron trapped in a defect is significantly reduced, the S-parameter for a material with defects is higher than the S-parameter of the same material without defects. Furthermore the S-parameter allows to distinguish between annihilation in the bulk and on the surface. Hence, using the S-parameter, the positrons diffusion length and thus the defect concentration can be extracted from depth profiling measurement using a positron beam [Hugenschmidt et al., 2015].

4

INVESTIGATION OF THE ELECTRONIC STRUCTURE WITH ACAR

4.1 HISTORY OF ACAR SPECTROSCOPY

In the light of the recent experimental discovery of the Higgs Boson at the Large Hardron Collider at CERN [Aad et al., 2012; Chatrchyan et al., 2012] the number of verified particles in the standard model has again grown by one. In 1929, the situation seemed much simpler. At that time the standard model contained two particles that were thought to be fundamental: The electron and the proton. One year earlier, Paul Dirac had introduced a new quantum mechanical equation [Dirac, 1928] which is fully Lorentz invariant and explains the 'angular momentum' - the spin - of the electron quite naturally.

Once it was realized that the solutions of Dirac's equation with negative energy are physical meaningful, these solutions were associated with the proton [Weyl, 1929]. However, this assumption led to contradictions which Dirac tried to clear by proposing that 'all the states of negative energy are occupied except perhaps a few' [Dirac, 1930]. These holes are positively charged and, so he thought, can be identified as protons. In his opinion, the remaining problems in the theory, e. g., the difference in mass of proton and electron, could be solved by further refinement.

J. R. Oppenheimer refused to believe this explanation and objected that the transition probability, i. e. the probability for the annihilation of a stationary electron and a stationary proton, would be 'absurdly large' [Oppenheimer, 1930]. In consequence, Dirac's model had to be revised. He gave up the idea of the holes being the protons and predicted a 'new kind of particle unknown to experimental physics' which he called 'anti-electron' [Dirac, 1931].

The experimental proof for the anti-electron followed soon: In 1932, only one year after Dirac's prediction, Anderson published evidence for a lightweight positively charged particle [C. D. Anderson, 1932]. Anderson investigated cosmic rays using a Wilson cloud chamber with a magnetic field of 1.5 T. From his experiment he could give an upper limit for the positive charge ('less than twice that of the (...) electron') and for its mass ('less than twenty times that of the (...) electron mass'). He concluded that the charge of this 'positron' is probably equal to that of the electron [C. D. Anderson, 1933]. However, Anderson did not yet connect the positron to the prediction of Dirac.

After Anderson's discovery it became obvious that positrons can not only be found in cosmic rays, but are also created by high energetic γ rays hitting a massive target [C. D. Anderson and Neddermeyer, 1933; Curie and Joliot, 1933; Meitner and Philipp, 1933]. From those experiments it was soon concluded that the positron is the positive electron of Dirac's theory [Blackett, 1933; Blackett and Occhialini, 1933].

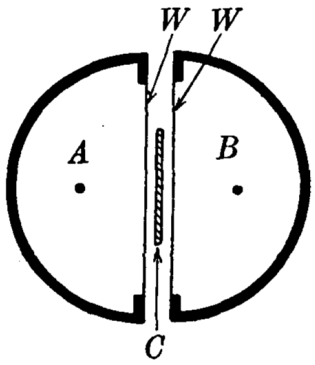

Figure 10: Cross section of the first angular correlation experiment. Between the Geiger-Müller tubes (A and B) with 0.1 mm thin copper foil W is a positron source C. By a so-called Rossi circuit, coincident events are discerned. (Drawing from [Klemperer, 1934])

In recent years, a controversy arose about who discovered the positron first, Anderson or the Chinese physicist Chao. In a nutshell: Both Anderson and Chao were working in the late twenties and early thirties in the laboratory of Prof. Millikan at Caltech. Chao investigated the absorption of 2.6 MeV γ rays in a variety of materials. At that time it was believed that the absorption in this energy range could be described by the Klein-Nishina-Formula. However, Chao measured a substantial larger absorption in high Z materials [Chao, 1930a,b]. Today we know that the larger absorption is due to electron-positron pair production. Nevertheless, Chao could not explain the excess absorption correctly but interpreted the results in a different way. Years later, Anderson wrote about his collaboration with Chao and about an experiment Anderson himself had planned to do which could have led to discovery of the positron much earlier but had not been conducted [C. D. Anderson, 1985]. There is no further proof that Chao had any influence on Anderson. In consideration of these facts Chao cannot be given any credit for the discovery of the positron.

After the unveiling of pair production, the mechanism of positron annihilation was still unknown. Several reactions were discussed:

- Similar to pair production, positrons could annihilate with an electron by emitting *one* γ quantum with an energy of $2m_ec^2$. The momentum for this process is conserved by a near nucleus [Fermi and Uhlenbeck, 1933].
- The annihilation occurs with an electron close to a second electron. A γ quantum of $\frac{4}{3}m_ec^2$ is emitted, while the second electron gets an energy of $\frac{2}{3}m_ec^2$ [Perrin, 1933].
- The positron will annihilate with an electron sending out *two* γ quanta with an energy of m_ec^2 each [Klemperer, 1934].

To test his hypothesis Klemperer conducted the first ACAR experiment [Klemperer, 1934]. Although the angular resolution of his setup had been approximately π (see drawing in figure 10) he concluded that the two γ quanta were emitted in coincidence and antiparallel neglecting the momentum of the initial particles.

Continuing the work of Klemperer, several experiments were carried out, each with increasingly better resolution: Alichanian, Alichanow, and Arzimovitch

[1936] reached a resolution of 30°. An improvement compared to this setup was achieved in the experiment by Beringer and Montgomery [1942] reaching a resolution better than 4°. They could set the limits for the deviation of collinearity to 15 arc minutes and suggested that the reason for this deviation is either scattering of the annihilation radiation or the momentum of the initial particles.

In the late 1940ies the focus began to shift from the fundamental physics of the annihilation process to the information about the solid that is carried by the annihilation radiation. It was then, when the first experiments probing solids with positrons were performed. The first Doppler broadening of the electron positron annihilation radiation (DBAR) experiment was implemented with a crystal spectrometer [Dumond, Lind, and Watson, 1949]. For a comprehensive explanation of DBAR spectroscopy see section 3.4. Compared to the DBAR experiments nowadays the effort was huge and the spectrometer filled a whole room. With an experimental resolution of 5.7 keV full width at half maximum (FWHM) a Doppler broadening of 4.8 keV FWHM was evaluated. From this result Dumond, Lind, and Watson [1949] inferred two things: The theoretical prediction that positrons thermalize before annihilation [Heitler, 1944] is correct and that positrons will annihilate rather with conduction electrons than with electrons in deeper shells due to the strong repulsion by the core.

Shortly after this experiment, the first ACAR experiment probing the electronic structure of a solid [DeBenedetti et al., 1950] was conducted. For their setup DeBenedetti et al. used the so-called 'long slit' geometry, i. e. a pair of detectors with an active area much narrower in one dimension than in the other [see figure 11 a) for a sketch of a similar setup]. Compared to the approach of DuMond et al. they improved the resolution by a factor of two to approximately 6.7 mrad confirming the results of their predecessors.

For the physics community in Munich, the contribution of Maier-Leibnitz to the field of positron physics is of particular interest. Although his setup had a rather poor angular resolution (approximately 100 mrad) he was able to discern between different samples. He applied the same method DBAR spectra are nowadays evaluated [Maier-Leibnitz, 1951], comparing a central region of the spectra to the total amount of counts. Regardless of this pioneering work, Meier-Leibnitz concentrated his efforts on other aspects of physics.

In the following decades a multitude of experiments were conducted on the basis of the first years of ACAR spectroscopy. Only a selected set of experiments will be discussed here:

One study that has to be highlighted is presented in the publication of Green and Stewart [1955]. They measured the angular correlation of the radiation from annihilating positrons in several light metals (Al, Be, Ca, K, Li, Na and Mg) and were able to correlate the FWHM of their measured spectra with an intrinsic property of their samples, i. e. the Fermi energy. At about the same time, Lang, De Benedetti, and Smoluchowski [1955] could prove that electrons in metals exhibit a Fermi gas behavior.

Another breakthrough for ACAR spectroscopy started with the theoretical prediction of parity violation of the weak interaction [T. D. Lee and Yang, 1956]. Inspired by this new theory Jackson, Treiman, and Wyld [1957] published a simple

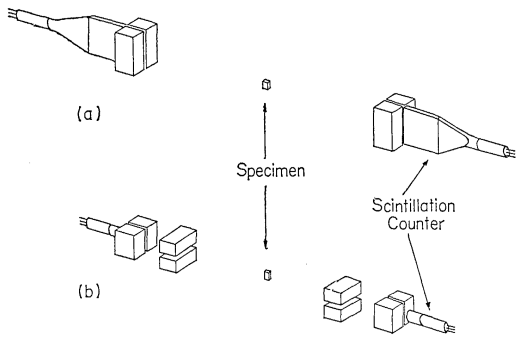

Figure 11: Sketch of two typical 1D-ACAR experimental setups with long slit geometry (a) and point slit geometry (b). Picture taken from Fujiwara and Sueoka [1966].

formula for the longitudinal spin-polarization P of positrons and electrons from β-decay: $P = \frac{v}{c}$, with c beeing the velocity of light and v the velocity of the emitted β-particle. Shortly thereafter two proofs for the polarization of positrons from β^+-decay were published. For the experimental verification Page and Heinberg [1957] used the quenching of para-positronium in Argon while Hanna and Preston [1957] used two measurements with antiparallel magnetized iron. Both groups utilized a 1D-ACAR technique for their measurements.

An advance in the experimental ACAR setup was the so-called point slit geometry [see (b) in figure 11] introduced by Colombino, Fiscella, and Trossi [1963]. It allows to avoid the double integration during the measurement and hence yields more direct information about the TPMD. Thus, a point slit setup is not a 1D-ACAR setup, but rather a very inefficient (in terms of much lower detection efficiency) kind of 2D-ACAR experiment. For this reason the long slit geometry has been used very rarely. Nevertheless, some remarkably high precision measurements with this technique have been published (see e. g., Fujiwara and Sueoka [1966]).

The development of a mathematical solution for the computer tomography problem by Cormack [1963, 1964] inspired Mijnarends [1967] to develop a method to invert the integrations in 1D-ACAR spectroscopy and to obtain the three-dimensional TPMD from several measurements. Although his procedure showed problems with convergence, he was able to reconstruct the electron momentum density of copper [Mijnarends, 1969] and, more notably, the subtracted and summed momentum density of the two spin channels of iron [Mijnarends, 1973b].

The first real 2D-ACAR data were published by Berko, Haghgooie, and Mader [1977]. The results were recorded with a mulitcounter setup Berko and Mader [1975] had developed, intended to overcome the drawbacks of the point slit geometry. A more elegant setup was developed at the same time by Manuel et al. [1978]. They set up two proportional chambers, which are much lighter and easier to maintain than the 32 individual detectors with the massive lead shielding of the Berko setup. A third early 2D-ACAR spectrometer used Anger-type cameres as position sensitive radiation detectors [West, Mayers, and Walters, 1981]. Due to the progresses in medical imaging Anger-type cameras became commercially available at that time and were henceforward widely used for ACAR spectroscopy.

Using the previously developed 2D-ACAR technique, a notable theoretical prediction in solid state physics could be validated: The existence of half-metals. In the early 1980s calculations done by de Groot et al. [1983] on the half-Heusler system NiMnSb exhibited a phenomena called half-metallicity, i. e. a band gap is present at the Fermi level in the minority spin channel but at least one band crosses the Fermi level in the majority spin channel. This band structure causes a 100% polarization of the conduction electrons. The first ones to verify these predictions were Hanssen and Mijnarends [1986] and Hanssen et al. [1990] who applied sophisticated analysis to their spin-polarized 2D-ACAR data.

Nowadays, ACAR spectroscopy is an established tool to investigate complex electronic systems. It is able to complement other techniques to study the electronic structure of metals like the investigation of quantum oscillations, angle-resolved photoemission spectroscopy (ARPES) or Compton scattering. For a comprehensive review of the systems examined with 2D-ACAR spectroscopy, see Ceeh [2015].

4.2 THEORY OF THE ELECTRONIC STRUCTURE OF SOLIDS

The basis for any nonrelativistic quantum mechanical problem like the theory of the electronic structure in a solid is its description by the Schrödinger equation. Although it is possible to write down the Hamiltonian for a solid, it is impossible to solve Schrödinger equation for a many body problem of this size. Therefore, in the beginning of first principle calculations of solids some simplifications were made, that allowed to solve the problem numerically:

- The motion of the atomic nuclei is not included in the calculation. Their position is assumed to be fix. (Born-Oppenheimer approximation)
- Any time dependence is ignored and only the static Schrödinger equation is solved.
- Instead of the real nuclear $\frac{1}{r}$ potential with a pole at $\mathbf{r} = 0$ an effective nuclear potential V_{eff} is used.
- The electronic interaction is not treated directly but is also encoded into the effective potential V_{eff}.

Using these approximations, the many body problem can be split up into $k = 1...n$ equations of single particles:

$$\mathcal{H}\Psi_k(\mathbf{x}) = E_k\Psi_k(\mathbf{x}) \tag{41}$$

with the Hamiltonian

$$\mathcal{H} = \left(-\frac{\hbar^2\nabla^2}{2m_e} + V_{\text{eff}}(\mathbf{x})\right) \tag{42}$$

The most important feature of V_{eff} is that its symmetry and periodicity is the same as that of the crystal lattice. By definition, free electrons move in a potential with complete translational symmetry, i. e. a constant potential. Therefore, their wave functions are plane waves $\Phi(x) = A\exp(ikx)$, with a well defined momentum eigenvalue as the Fourier transform (FT) of $\Phi(x)$ gives a Dirac delta function:

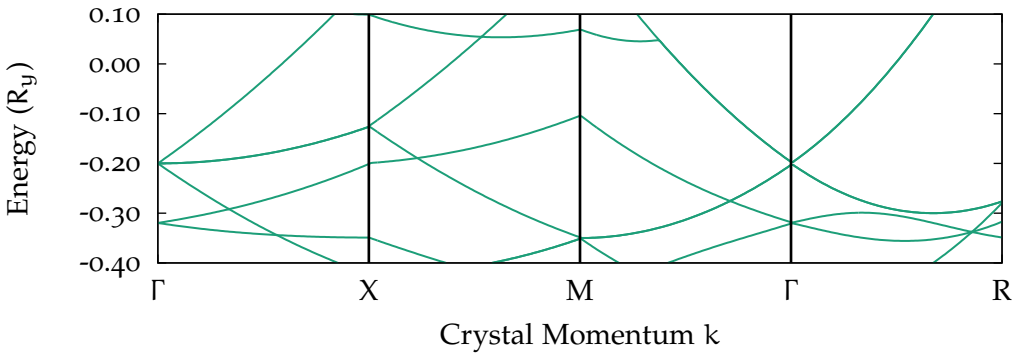

Figure 12: Band structure of a hypothetical simple cubic metal calculated with the pseudopotential method.

$\mathcal{F}(\Phi(x)) \propto \delta(p-k)$. Since V_{eff} breaks the translational symmetry, the electrons cannot be in eigenstates of the momentum operator. However, because of the discrete translational symmetry of the crystal an electronic state is not a continuous distribution of momentum eigenstates, but the sum of momentum states separated by a reciprocal lattice vector $\mathbf{G}$:

$$\mathcal{F}(\Psi_{\mathbf{k}}(\mathbf{x}))(\mathbf{p}) = \sum_{\mathbf{G}} C_{\mathbf{G}}(\mathbf{k})\delta(\mathbf{p}-(\mathbf{G}+\mathbf{k})) \tag{43}$$

Thus, $\Psi_{\mathbf{k}}(\mathbf{x})$ can be written as the Fourier series:

$$\Psi_k(\mathbf{x}) = e^{ikx}\sum_{\mathbf{G}} C_{\mathbf{G}}(\mathbf{k})e^{-i\mathbf{G}x}. \tag{44}$$

This state is called a 'Bloch wave'.

To solve equation (41) it is most convenient to write it in momentum space, which gives a system of linear equations:

$$\left(\frac{\hbar^2\mathbf{k}^2}{2m_e} - E_k\right) C_{\mathbf{G}=0}(\mathbf{k}) + \sum_{\mathbf{G}'} U_{\mathbf{G}'}C_{\mathbf{G}'}(\mathbf{k}) = 0, \tag{45}$$

with the Fourier coefficients $U_{\mathbf{G}}$ of the effective potential $V_{\text{eff}} = \sum_{\mathbf{G}} U_{\mathbf{G}} \exp(i\mathbf{G}x)$. In figure 12 a solution to equation (45) for a hypothetical simple cubic metal is shown. In contrast to an isolated atom with discrete energy eigenvalues, there are now continuous energy bands, i. e. equation (45) yields different solutions for different points in reciprocal space. The band structure defines all of the solid's electronic properties. At $T = 0$ the electrons occupy the states with the lowest energy. Since electrons are Fermions, not more than two electrons are able to occupy the same state. Hence, all electronic states are filled up to a maximum energy, the so-called Fermi energy E_F. The border between occupied and unoccupied states in k-space is represented by the Fermi surface (FS). It is an outline of the band structure at E_F and thus is a fingerprint of the whole electronic structure.

The challenge of the pseudo potential method is, to find an effective potential which gives physically meaningful results. For this reason and to overcome the

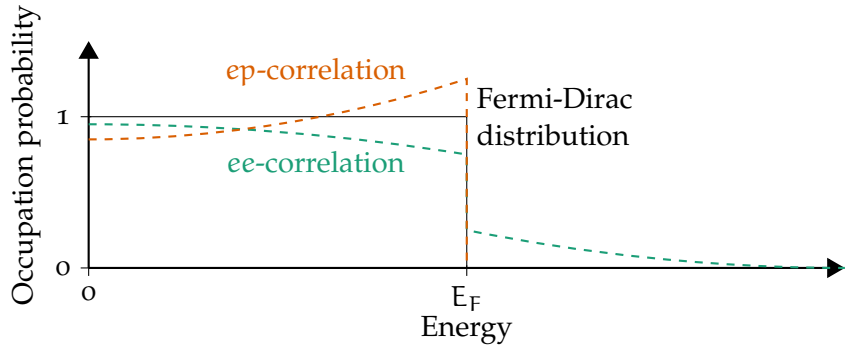

Figure 13: Effect of the electron-electron correlation (■) and the electron-positron correlation (■) on the occupation probability of the electronic states at $T = 0\,K$. Both effects lead to deviations from the Fermi-Dirac distribution.

aforementioned approximations several other theoretical approaches were developed, the most common ones being the density functional theory (DFT) [Hohenberg and Kohn, 1964; Kohn, 1999; Kohn and Sham, 1965] and the dynamical mean-field theory (DMFT) [Georges et al., 1996; Kotliar and Vollhardt, 2004; Metzner and Vollhardt, 1989].

The DFT provides a schema to calculate the electron density $\rho_e(\mathbf{x})$. All other electronic properties are then expressed as a function of $\rho_e(\mathbf{x})$. The interaction between electrons [i. e. the electronic potential $V_{ele}(\mathbf{x})$] is not treated explicitly, but modeled as an interaction with the electron density:

$$V_{ele}(\mathbf{x}) = \int \frac{e^2 \rho_e(\mathbf{x})}{|\mathbf{x} - \tilde{\mathbf{x}}|} \, d\tilde{\mathbf{x}} \,. \tag{46}$$

Therefore, $\rho_e(\mathbf{x})$ is explicitly needed to calculate itself. Nevertheless, a solution can be found by guessing an initial electron density and then iteratively solving the Kohn-Sham equation, to get a new $\rho_e(\mathbf{x})$. An additional exchange correlation potential can be included to model the interaction between individual electrons.

An improvement to the DFT is the DMFT as it includes the electronic correlation explicitly, which can be quite important for correlated materials [Ceeh et al., 2016b]. Furthermore, in DMFT it is possible to calculate the electronic structure at finite temperatures. Hence, the energy bands do have finite width due to scattering. Even at $T = 0\,K$, the occupation density changes as indicated in figure 13. [1]

Similar to the electron-electron (ee) correlations, the presence of a positron can also change the electronic states by electron-positron (ep) correlation. In the expansion of the electron-positron single particle wave-functions, the electronic states at the Fermi energy get a higher occupation density compared to the unperturbed Fermi-Dirac distribution (see figure 13). For this reason, the ep-correlation effect is canonically called 'enhancement'.

Usually enhancement effects are quantified by analytical or quantum Monte Carlo calculations for particular model systems. The results are then parametrized

1 Even the DMFT schema can only approximate the actual many body wave function of a real electronic system. As such a many body wave function goes beyond the possibilities of human understanding, in the following it will be represented by a sum of single particle wave functions.

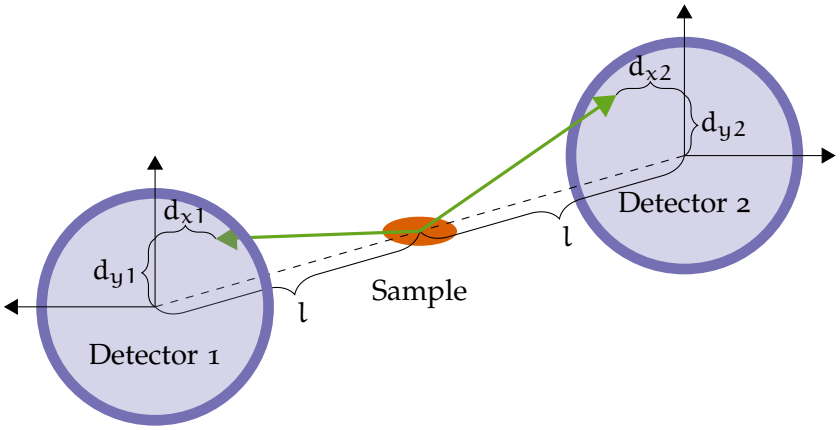

Figure 14: Sketch of a 2D-ACAR setup. Two position sensitive detectors are positioned congruently in the xy-plane at a distance of l from the sample.

either as a function of momentum [Kahana, 1963], energy [Mijnarends and Singru, 1979] or the electron density (which is very useful for DFT calculations) [Boroński and Nieminen, 1986; Jarlborg and A. K. Singh, 1987]. The cited papers represent only the classical enhancement models. Many further approaches to the enhancement problem exist, but up to now it was not possible to treat the ep-correlations in the DMFT schema similar to the ee-correlation.

4.3 THEORY OF ACAR SPECTROSCOPY

While both ACAR and DBAR probe the electron momentum density of a solid, they differ in terms of their experimental resolution, which is a consequence of the nature of both techniques: The resolution for DBAR is restricted by the physical limit to resolve the energy of high energy photons. In contrast, to resolve an angle in an ACAR experiment is (if enough space is available) possible with any desired accuracy. However, a higher accuracy requires a larger detector sample distance which results in a lower counting rate (for details see chapter 8.1). As a rule of thumb the resolution of an ACAR setup is four times better than the one of a DBAR experiment. Another great advantage of ACAR is the use of two-dimensional position sensitive detectors. Thus, one measurement yields a higher informational content, namely a 2D-projections of $\rho^{2\gamma}$, as compared to the 1D projection of a DBAR experiment.

The sketch in figure 14 shows a schematic drawing of a 2D-ACAR setup: An annihilation event in the sample creates two photons that are observed by parallel, position sensitive detectors standing face to face at a distance l from the sample. Using the detected positions, the angular deviation and hence the momentum in the xy-plane of the annihilating electron (neglecting the momentum of the positron) can be determined according to equation (36):

$$p_x \approx \theta_x m_e c \approx \frac{d_{x2} - d_{x1}}{l} m_e c \tag{47}$$

$$p_y \approx \theta_y m_e c \approx \frac{d_{y2} + d_{y1}}{l} m_e c \tag{48}$$

The geometry of one measured event is defined by three distinct spots: The position of the annihilation event $\vec{A}$ and the positions where both γ quanta hit one of the detectors $\vec{D}_{1/2}$. Each of these three vectors has three components, which are affected by measurement uncertainties. The influence of particular uncertainties on the overall resolution can be obtained by an error analysis (see appendix A.3). Kruseman [1999] performed a detailed study of the influence of the respective errors. Not surprisingly, the biggest influence on the total resolution is a consequence of the detectors' position resolution σ_D and the spot size on the sample σ_S. If both detectors are aligned carefully, then all other uncertainties σ_{R_i} (such as positron implantation depth, crystal thickness and the perpendicular extend of the positron spot size on the sample) are insignificant due to the large sample detector distance. In particular, at the Munich 2D-ACAR spectrometer all σ_{R_i} are smaller than 0.02 mrad.

The total experimental angular resolution $\sigma_{x/y}$ in x- and y-direction is given by the root sum square of all measurement uncertainties:

$$\sigma_x = \frac{1}{L}\sqrt{\sigma_{D_1}^2 + \sigma_{D_2}^2 + \sum_i \sigma_{R_i}^2} \approx \frac{1}{L}\sqrt{2}\sigma_D \tag{49}$$

$$\sigma_y = \frac{1}{L}\sqrt{\sigma_{D_1}^2 + \sigma_{D_2}^2 + (2\sigma_S)^2 + \sum_i \sigma_{R_i}^2} \approx \frac{1}{L}\sqrt{2\sigma_D^2 + 4\sigma_S^2}, \tag{50}$$

where L denotes the sample detector distance. The spot size influences only one component of the resolution, as the implantation depth is in the order of 100 µm and thus negligible. Note that the spot size affects σ_y by a factor of 2 while the detector resolution has a weighting of only $\sqrt{2}$.

4.3.1 *The Free Electron Gas*

The first systems probed with ACAR were simple polycrystalline metals [Green and Stewart, 1955]. In most of these systems the charge carriers can be considered a free electron gas, i. e. there is just one conduction band with an approximately quadratic dispersion. At $T = 0\,K$, all states in the conduction band are filled up to the Fermi energy E_F. The corresponding momentum of electrons with the Fermi energy is called Fermi momentum:

$$p_F = \sqrt{2m_e E_F} \tag{51}$$

Since the dispersion relation is isotropic, the Fermi momentum is identical for every direction in momentum space. Therefore, the FS, the three-dimensional border between occupied and unoccupied states in reciprocal space, is nearly spherical. The 2D-projection of this sphere, which is measured in a 2D-ACAR experiment, can be calculated using the Fermi momentum p_F:

$$C^{2D}(p_x, p_y) \propto \sqrt{p_F^2 - p_x^2 - p_y^2} \tag{52}$$

For a 1D-ACAR experiment the projection can also be derived considering the infinitesimal volume element caused by a cut of a plane through the sphere at a distance p_x:

$$C^{1D}(p_x) \propto \pi\,[r(p_x)]^2 = \pi\,\left(p_F^2 - p_x^2\right) \tag{53}$$

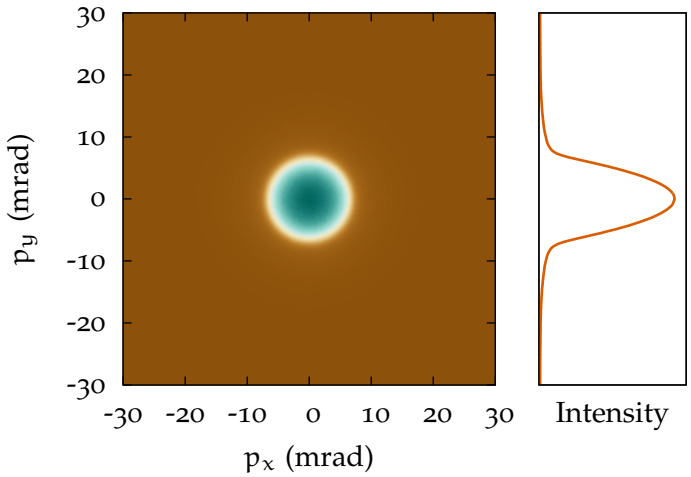

Figure 15: 2D-ACAR measurement of polycrystalline aluminum (*left*) and the according 1D-projection (*right*).

The projection of the Fermi sphere is only one part of a spectrum. Since the positron has also a certain probability to annihilate with a core electron, the measured spectrum will additionally contain a broad spherical background.

In figure 15 the 2D-ACAR spectrum of polycrystalline aluminum is depicted. As expected, the spectrum is isotropic and the most intensity is within a circular region around the center. The projection of this spectrum shows a clear parabolic dependence and hence the Fermi momentum can directly be read off from the intersection of the parabola with the background in the plot.

4.3.2 *ACAR Spectroscopy on Single Crystals*

More complex and interesting than investigating a free electron gas are, however, nonisotropic materials. In a single crystalline solid the momentum is not a well defined quantity due to the discrete translational symmetry. The wave function of an electron in the band j with crystal momentum $\mathbf{k}$ is rather the Fourier series with the periodicity of the reciprocal lattice vectors $\mathbf{G}$:

$$\Psi^e_{j,\mathbf{k}}(\mathbf{x}) = \sum_{\mathbf{G}} A_{\mathbf{G}}(j,\mathbf{k}) e^{-i\mathbf{x}\mathbf{G}} \tag{54}$$

The coefficient $A_{\mathbf{G}}(\mathbf{k})$ is proportional to the probability to measure the momentum $\mathbf{G}+\mathbf{k}$.

Also the positron wave function can be expanded as a Fourier series, but since there is only one positron in the solid, the indices j and $\mathbf{k}$ can be omitted:

$$\Psi^p(\mathbf{x}) = \sum_{\mathbf{G}} B_{\mathbf{G}} e^{-i\mathbf{x}\mathbf{G}} \tag{55}$$

With positron annihilation not just the momentum of one electron, but the momenta of the many-electron system interacting with the positron is measured (see equation (39)). Nowadays ab initio methods are not able to calculate the wave

function of the whole system. However, the many-particle wave function can be approximated by the unperturbed wave functions of the electrons $\Psi^e_{j,\mathbf{k}}$ and the positron Ψ^p.

$$\rho^{2\gamma}(\mathbf{p}) \propto \sum_j \sum_{\mathbf{k}=\text{occ.}} \left| \int d\mathbf{x}\, e^{-i\mathbf{p}\mathbf{x}}\, \Psi^p(\mathbf{x})\, \Psi^e_{j,\mathbf{k}}(\mathbf{x}) \sqrt{\gamma_{j,\mathbf{k}}} \right|^2 \tag{56}$$

The enhancement factor is the same as in equation (31). For ACAR spectroscopy it is relevant that the enhancement factor is larger for states at the Fermi energy.

4.3.3 *From momentum space to crystal momentum space - the Lock-Crisp-West Theorem*

The interpretation of equation (56) is complex as the left side is in momentum space while the right side is given in real space. Assuming the independent particle model (IPM), i. e. $\gamma_{j,\mathbf{k}} = 1$, and using the definitions (54) and (55), equation (56) transforms to

$$\rho^{2\gamma}(\mathbf{p}) \propto \sum_j \sum_{\mathbf{k}=\text{occ.}} \sum_{\mathbf{G}} |C_{\mathbf{G}}(j,\mathbf{k})|^2\, \delta(\mathbf{p} - (\mathbf{G}+\mathbf{k})). \tag{57}$$

Here it was utilized that the FT of the wave function product $\Psi^p(\mathbf{x})\Psi^e_{j,\mathbf{k}}(\mathbf{x})$ is a convolution of the single particle wave functions in momentum space:

$$C_{\mathbf{G}}(j,\mathbf{k}) = \sum_{\mathbf{K}} B_{\mathbf{G}-\mathbf{K}} A_{\mathbf{K}}(j,\mathbf{k}) \tag{58}$$

In equation (57), the Fourier coefficients of one electronic state are distributed over the whole momentum space by the δ function. For completely filled bands $\rho^{2\gamma}$ is a continuous density which decreases for high momenta. In case a band crosses the Fermi level, there will be a sharp break in $\rho^{2\gamma}$ at the Fermi momentum $\mathbf{k}_F$. Again, this break is distributed over reciprocal space. In principle, the Fermi momentum can be identified by the very existence of such a break. In practice, however, the analysis can be cumbersome since the breaks are superimposed on the density of the filled bands. Additionally the density of the crossing band is enveloped by a decreasing density throughout reciprocal space (see figure 16).

As the Fermi breaks are periodic in reciprocal space it is sometimes useful to transform $\rho^{2\gamma}(\mathbf{p})$ from momentum space into the periodic crystal momentum space by summing over all reciprocal lattice vectors $\mathbf{H}$:

$$\rho^{\dagger 2\gamma}(\mathbf{k}) = \sum_{\mathbf{H}} \rho^{2\gamma}(\mathbf{H}+\mathbf{k}) \tag{59}$$

$$\propto \sum_j \sum_{\mathbf{H}} |C_{\mathbf{H}}(j,\mathbf{k})|^2 \Theta_j(\mathbf{k}_F - \mathbf{k}) \tag{60}$$

with a modified Heaviside step function yielding the value of 1 for all states i in all bands j with $|\mathbf{k}| \leqslant |\mathbf{k}_F|$.

$$\Theta_j(\mathbf{k}_F - \mathbf{k}) = \begin{cases} 1 & \text{if band } j \text{ is below the Fermi level} \\ 1 & \text{if band } j \text{ crosses the Fermi level and } |k| \leqslant |k_F| \\ 0 & \text{in any other case} \end{cases} \tag{61}$$

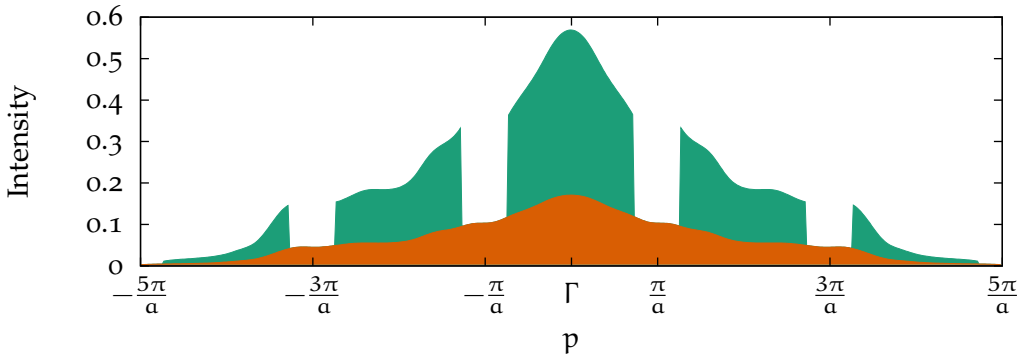

Figure 16: Example of a momentum density of two bands in the extended zone schema. The completely filled band gives a continuous background (■). The discontinuities are caused by the second band crossing the Fermi energy (■).

The quantity $u_j(\mathbf{k}) = \sum_{\mathbf{H}} |C_{\mathbf{H}}(j,\mathbf{k})|^2$ represents the overlap of the positron and the electron wave function and is directly proportional to the annihilation probability of the positron and the $\mathbf{k}$-th electron in the j-th band. Assuming that $u_j(\mathbf{k}) = u_j$, i. e. the annihilation probability in the same band does not vary with $\mathbf{k}$, equation (60) can be simplified further:

$$\rho^{\dagger 2\gamma}(\mathbf{k}) = C_1 + C_2\Theta(\mathbf{k}_F - \mathbf{k}) \tag{62}$$

with two arbitrary constants C_1 and C_2. Hence, the FS can easily be extracted from $\rho^{\dagger 2\gamma}(\mathbf{k})$ as it is constant everywhere except at the Fermi momentum.

The folding of $\rho^{2\gamma}$ into the first Brillouin zone (BZ) was at introduced by Lock, Crisp, and West [1973]. They applied the Lock-Crisp-West (LCW) theorem to projections of $\rho^{2\gamma}$, i. e. real ACAR measurements. However, identifying the FS even from a LCW folded projection of $\rho^{2\gamma}$ is not straight forward. Nevertheless, the LCW facilitates sometimes the interpretation and the comparison between theoretical and experimental data [Ceeh et al., 2016b].

Although the LCW theorem can be helpful, there is no guarantee that the two assumptions used to derive equation (62) are valid in general. Lock, Crisp, and West [1973] themselves showed that the $\mathbf{k}$ dependence of the annihilation probability can be significant. Several further authors testing the LCW folding came to similar results [Kaiser, West, and N. Shiotani, 1986; Rabou and Mijnarends, 1984; A. K. Singh and Singru, 1984]. Additionally, neglecting electron-positron correlations by using the IPM can lead to misguiding results for some systems. However, very often the electron-positron correlation enhances the density of states at the Fermi edge (see e. g., [Kahana, 1963; Kontrym-Sznajd and Sormann, 2014a,b; West, 1995]). Hence, the investigation of the FS can even be facilitated in some cases, but in other cases it can also be obscured [Rusz and Biasini, 2007].

To demonstrate the consequences of the above equations an example of a real 2D-ACAR measurement is given in figure 17. In figure 17 a) the pure ACAR measurement on a copper single crystal with the detector axis parallel to the [100] crystal axis is shown. Clearly, the momentum components $C_{\mathbf{G}}(j,\mathbf{k})$ are the largest for $\mathbf{G} = 0$ as the most intensity is located in the first BZ. The shape of the intensity is nearly spherical for two reasons: i) All the 3d electrons in copper are filled and

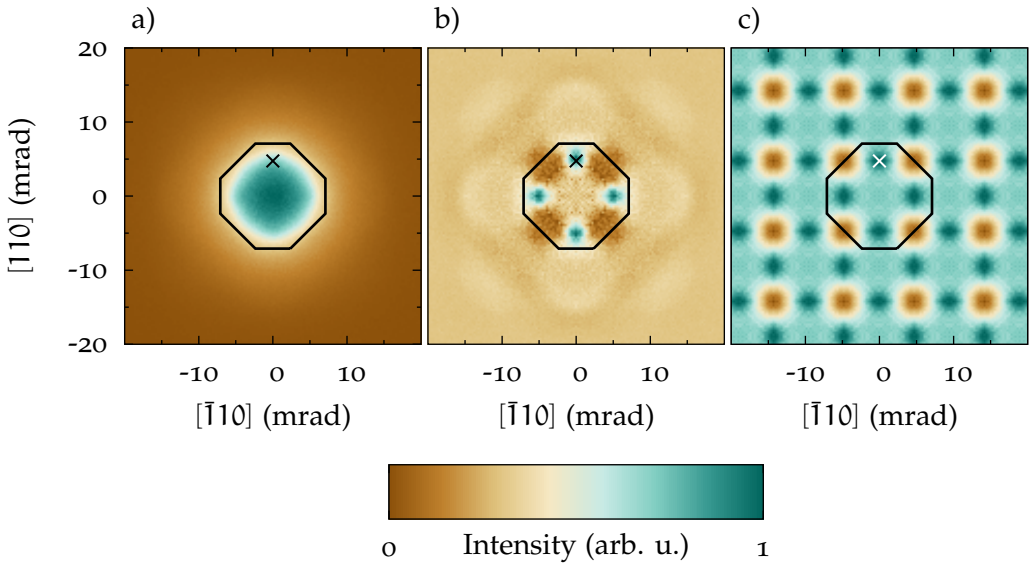

Figure 17: 2D-ACAR measurement of copper, [100]-projection, with the contours of the first BZ. a) Basic 2D-ACAR measurement, i. e. projection of $\rho^{2\gamma}(\mathbf{p})$ in the extended zone schema. b) Anisotropic part of a). c) LCW-backfolding of measurement a), i. e. projection of $\rho^{2\gamma}(\mathbf{k})$ in the repeated zone schema.

the conduction band is formed by one 4s electron which is very little influenced by the d electrons. Therefore, the FS of copper is nearly spherical. ii) Due to the projection, the nonspherical features are evened out. Nevertheless, there is a small deviation from sphericity visible (marked by an x and at all equivalent points). In figure 17 b) the anisotropy of measurement a) is shown. It has been calculated by subtracting the radial mean of the measurement from itself. Here contributions from the second and the third BZ can be identified, although the features in the first BZ are the most dominant. Applying the LCW theorem transfers the measured data into the periodical zone schema creating picture c). The LCW folded density resembles the anisotropy except that it exhibits translational symmetry under displacement by a reciprocal lattice vector. The highest intensity is visible, where the projections of the nearly spherical copper momentum densities overlap and form a lens shaped feature. At the same spot lies the projection of the L-point of the BZ, where the necks of the FS are located.

4.3.4 *Effects of Finite Temperature*

In the sections above it has been implicitly assumed that the temperature is $T = 0\,K$. Higher temperatures give rise to effects caused by the thermal excitation of both the electrons and the positron.

For an electronic system with finite temperature, the occupancy of the states $N(E)$ is given by the Fermi-Dirac statistics:

$$N(E) = \frac{1}{e^{(E-E_F)/(k_B T)} + 1} \tag{63}$$

As a consequence, the border between occupied and unoccupied states is smeared out and the FS is not a well defined property anymore. However, e. g., for a system of free electrons at room temperature, the Fermi-Dirac statistics will just lead to a blurring of the Fermi momentum with a FWHM of 0.14 mrad which is one order of magnitude smaller than the typical experimental resolution.

In comparison to the electron related effects, the positron effects have a more severe influence on the measurement. For a typical positron source, the positron density in the solid is very low. Even if 1×10^9 positrons per second are implanted the mean amount of positrons in the solid is to a good approximation only one. Therefore, the momentum components of the three orthogonal directions of the positron momentum $\mathbf{p} = \begin{pmatrix} p_x \\ p_y \\ p_z \end{pmatrix}$ follow a normal distribution:

$$f(p_x, p_y, p_z) = (2\pi m_e^* k_B T)^{-3/2} e^{-\frac{p_x^2+p_y^2+p_z^2}{2m_e^* k_B T}} \tag{64}$$

The thermal smearing causes a broadening of the resolution by $\sigma = \sqrt{m_e^* k_B T}$. Due to band structure effects, electron-positron correlations and positron-phonon interactions, the ratio of the effective mass m_e^* to the rest mass of the positron can take values from 1 to 2 [Birger Bergersen and Pajanne, 1969; Mikeska, 1967]. Hence, the additional broadening of the resolution at room temperature has typically an FWHM of

$$2\sqrt{2\ln 2}\,\sqrt{m_e^* k_B T} \approx 0.5\,\text{mrad to } 0.7\,\text{mrad}. \tag{65}$$

That means, the experimental resolution can be significantly increased if the sample is cooled to cryogenic temperatures. At the Munich spectrometer, the sample is usually cooled to 10 K which reduces the thermal smearing to less than 0.15 mrad (FWHM).

4.3.5 *Spin-Polarized Positron Spectroscopy on Solids*

In the classical Stoner picture for magnetism in metals, the energy of an electronic state in a ferromagnetic solid depends not only on the band-index j and the crystal momentum $\mathbf{k}$, but also on the spin of the electron. An electron in the state $(j, \mathbf{k}, \uparrow)$ will therefore have a higher energy than an electron in the state $(j, \mathbf{k}, \downarrow)$. As the Fermi energy in both spin channels has to be equal, the $\downarrow$-spin channel (or majority spin channel) is populated by more electrons than the $\uparrow$-spin channel (or minority spin channel). This imbalance of the different number of $\uparrow$-spin and $\downarrow$-spin electrons gives rise to a spontaneous magnetization.

Although the stoner model can explain some observations in ferromagnets, it is not able to properly describe other aspects even in simple metals, like the temperature dependence of the spontaneous magnetization in Fe. In reality, the magnetic interactions are far more complex which gives rise to a variety of magnetic phenomena. Very promising for spintronics applications are e. g., half metals [de Groot et al., 1983; Kübler, William, and Sommers, 1983] which have a 100 % spin-polarization of the conduction electrons (at 0 K) due to a band gap in the minority spin channel. Another example with possible application in computer memory technology are spin structures with a nontrivial topology, so-called Skyrmions,

which were first discovered in the itinerant helimagnet MnSi [Mühlbauer et al., 2009].

An easy way to investigate magnetic properties are transport measurements. However, transport measurements are a just macroscopic observables and thus not suited for in-depth studies of the electronic structure. For this purpose more sophisticated techniques like spin-polarized neutron experiments, spin-polarized ARPES, magnetic Compton scattering or spin-polarized positron measurements are needed.

Spin-polarized ACAR has been applied in prominent investigations [Berko and Zuckerman, 1964; Ceeh et al., 2016a; Genoud et al., 1991; Hanssen and Mijnarends, 1986; Hanssen et al., 1990; Mijnarends, 1973b; Mijnarends and Hambro, 1964]. The prerequisite for spin-polarized positron studies is a positron beam with a certain spin-polarization P [see equation (4)]. To simplify some of the following equations it is useful to define the fraction of polarized positrons

$$F = \frac{N^{\uparrow}}{N^{\uparrow} + N^{\downarrow}} = \frac{1}{2}(P + 1) \tag{66}$$

and the 2D projection of the majority/minority spin channel of the TPMD

$$M_{\mathrm{maj/min}}(p_y, p_z) = \int \rho^{2\gamma}_{\mathrm{maj/min}}(\mathbf{p})\, dp_x\,. \tag{67}$$

In an ACAR experiment one cannot measure $M_{\mathrm{maj/min}}(p_y, p_z)$ directly, but a quantity which is *proportional* to it. Only the annihilation rates give absolute information about the magnitude of $\rho^{2\gamma}_{\mathrm{maj/min}}(\mathbf{p})$. The polarized positron annihilation rate $\lambda_{\uparrow\downarrow}$ of a fully spin-polarized ferromagnetic sample with the spins in the majority spin channel pointing 'up' while the positron spin points 'down' is given by

$$\lambda_{\uparrow\downarrow} = \underbrace{\lambda_{\mathrm{maj}}}_{2\gamma\text{ annihilation}} + \underbrace{\frac{\lambda_t}{\lambda_s}\left(2\lambda_{\mathrm{min}} + \lambda_{\mathrm{maj}}\right)}_{3\gamma\text{ annihilation}}. \tag{68}$$

Vice versa, the annihilation rate $\lambda_{\downarrow\downarrow}$ if the spins in the majority spin channel and the positron spins are pointing 'down' is given by

$$\lambda_{\downarrow\downarrow} = \lambda_{\mathrm{min}} + \frac{\lambda_t}{\lambda_s}\left(2\lambda_{\mathrm{maj}} + \lambda_{\mathrm{min}}\right), \tag{69}$$

with the single/triplet annihilation rate $\lambda_{s/t}$ (see chapter 3.1) and the annihilation rate with the majority/minority spin channel:

$$\lambda_{\mathrm{maj/min}} = \lambda_s \int M_{\mathrm{maj/min}}(p_y, p_z)\, dp_y\, dp_z\,. \tag{70}$$

$\lambda_{\uparrow\downarrow/\downarrow\downarrow}$ can be directly measured with a spin-polarized PLS experiment. Since such an experiment is very difficult to conduct, Berko and Mills, A. P. [1971] came up with a different approach. By measuring the 3γ annihilation rate they were able to approximate $\lambda_{\uparrow\downarrow/\downarrow\downarrow}$.

Therefore, a 2D-ACAR experiment on a fully spin-polarized ferromagnetic sample with the spins in the majority spin channel pointing 'up', while the main emission direction of the positrons pointing 'down' is proportional to

$$M^{\uparrow}(p_y, p_z) \propto P \frac{M_{maj}(p_y, p_z)}{\lambda_{\uparrow\downarrow}} + (1 - P) \frac{M_{min}(p_y, p_z)}{\lambda_{\downarrow\downarrow}} . \tag{71}$$

When the external magnetic field is reversed, the spins majority spin channel will point 'down' and a 2D-ACAR measurement yields

$$M^{\downarrow}(p_y, p_z) \propto (1 - P) \frac{M_{maj}(p_y, p_z)}{\lambda_{\uparrow\downarrow}} + P \frac{M_{min}(p_y, p_z)}{\lambda_{\downarrow\downarrow}} . \tag{72}$$

If the polarization P is known and two 2D-ACAR measurements with antiparallel magnetization direction are performed, the normalized projections of the minority and majority spin channel $\frac{M_{maj/min}}{\lambda_{\uparrow\downarrow/\downarrow\downarrow}}$ can be separated.

As the ratio $\frac{\lambda_t}{\lambda_s} \approx \frac{1}{1115}$ is very small, the 3γ annihilation is usually neglected and $\lambda_{\uparrow\downarrow/\downarrow\downarrow} \approx \lambda_{maj/min}$. For the sake of simplicity, this approximation will be used in the following.

4.4 COMPLEMENTARY METHODS

The textbook example for the experimental determination of the electronic structure, particularly of the FS, is either ARPES or the measurement of quantum oscillations, specifically the de Haas-van Alphen (dHvA) effect. However, there are a lot more methods that can be used to determine the electronic structure e. g., ACAR and the closely related Compton scattering. Moreover, it is possible to extract information about the FS via Raman scattering [LeBlanc, Carbotte, and Nicol, 2010] and even by neutron scattering [Moss, 1969].

In the following, the two most common methods, ARPES and dHvA measurements, are introduced and compared to 2D-ACAR. As Compton scattering was used during this thesis, it is also explained briefly.

Quantum Oscillations in the Magnetization - the de Haas-van Alphen Effect

Classically, free electrons move in a magnetic field H on helical orbits with an angular frequency of $\omega_c = \frac{eB}{m_e}$. In a quantum mechanical description, only orbits with an energy of

$$E_n(k_z) = \frac{\hbar^2}{2m_e} k_z^2 + \left(n + \frac{1}{2}\right) \hbar\omega_c \quad \text{with} \quad n \in \mathbb{N}_0 \tag{73}$$

are allowed. In the context of a free electron gas this would imply that the electronic states condense on so-called Landau cylinders in k-space. Many of the properties of a solid depend on the density of states at the Fermi level. Therefore, if a Landau level crosses the border of the FS and the magnetic field is increased, the electrons are distributed between the other cylinders. This causes a change in the density of states at the Fermi level and a change in the macroscopic properties.

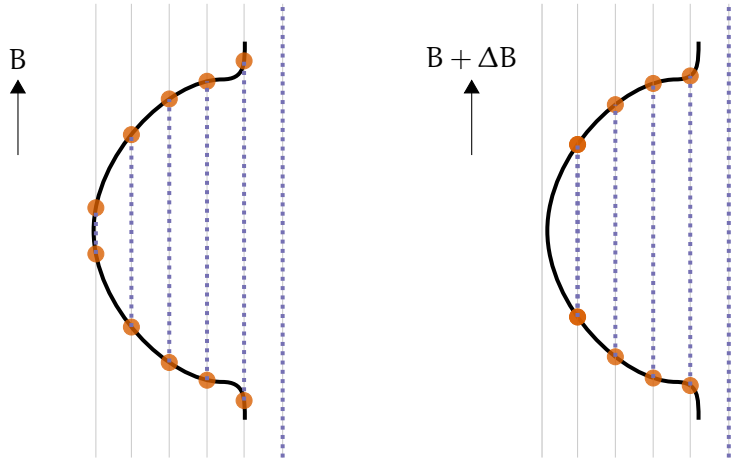

Figure 18: Sketch of a solid in a magnetic field. *Left:* The electrons condense on Landau levels parallel to the magnetic field. The colors indicate the filled states inside the FS and the states on the FS. *Right:* Increasing the magnetic field increases the distance between the Landau levels. The number of states at the Fermi level changes most drastically if a Landau level crosses an extremal border of the FS.

The change is most drastic if one Landau cylinder leaves (or enters) the FS entirely. As can be seen from figure 18, this will only happen at an extremal cross section of the FS.

Onsager deduced a relation for the area enclosed by a Landau level in dependence of the magnetic field [Onsager, 1952]. With this relation it is possible to show that the period with which the Landau level cross the extremal FS borders is given by

$$\Delta\left(\frac{1}{B}\right) = \frac{2\pi e}{\hbar A_{ext}}. \tag{74}$$

Therefore, the oscillation are periodically in $\frac{1}{B}$ and the period is inversely proportional to extremal cross section areas A_{ext} perpendicular to $\mathbf{B}$.

Quantum oscillations can be detected in many properties of the solid like the thermal transport, the ultrasound attenuation [Pippard, 1957a] or in the magnetization and susceptibility. The latter phenomenon, giving rise to the dHvA effect, is mainly used today to map out the FS. For this purpose, the extremal cross-sectional areas of the FS are measured for different field orientations relative to the crystallographic alignment and then compared to theoretical models.

The accuracy of dHvA measurements is very high and exceeds those of all other measurement methods. However, from dHvA data alone often no complete picture of the FS can be created since the measurement gives no information *where* in the BZ the extremal cross section is located. Furthermore, the dHvA effect is limited to cryogenic temperatures as, for the Landau levels to be formed, the scattering length of an electron has to be larger than at least one cyclotron orbit. A long scattering length also requires the sample to be free from any kind of lattice defect, since they can act as scattering centers. In addition, high magnetic fields are needed and thus in case of magnetic field induced phase transitions only the FS of the high field phase can be investigated.

Photoemission Spectroscopy

Owing to the rapid development of synchrotron X-ray sources, especially because of the increase in brightness, photoemission spectroscopy has become one of the most common techniques to study the electronic structure of solids. The fundamental principle of photoelectron spectroscopy is the photo electric effect: If electrons absorb the energy of a photon they will be excited from the occupied states in the solid to the continuous states in vacuum. The law of energy conservation requires that the photon energy $\hbar\omega$ equals the binding energy of the electron E_b plus the kinetic energy E_{kin} and the electron work function Φ:

$$\hbar\omega = E_b + E_{kin} + \Phi \tag{75}$$

As stated by Fermi's golden rule, the transition probability (if the energy is conserved) is proportional to the initial and the final density of states. Thus, using a monochromatic light source, the electronic density of states can be determined by analyzing the energy of the emitted electrons.

If not only the energy of the photoelectrons is detected but additionally the angle of emission, the momentum $p_{\parallel}$ parallel to the sample surface of the initial state can be measured. This method is called angle-resolved photoemission spectroscopy (ARPES). As the electron has to overcome the work function Φ, i. e. a potential barrier at the surface, the momentum $p_{\perp}$ of the initial state perpendicular to the surface is not conserved. However, if a quadratic dispersion relation is assumed, $p_{\perp}$ can be calculated:

$$p_{\perp} = \sqrt{2\, m_e \left(E_{kin} \cos^2(\phi) + V_0\right)} \tag{76}$$

The so-called inner potential $V_0 = \Phi + E_0$ is the difference between the vacuum level and energy at the bottom of the valence band E_0. Although systems with interesting electronic properties show by no means a quadratic dispersion, equation (76) is even used for complex systems [Damascelli, 2004]. A second possibility to get $p_{\perp}$ is to reconstruct it from different projections similar to the reconstruction of $\rho^{2\gamma}(\mathbf{p})$ from 2D-ACAR spectra [Ibach and Lüth, 2009].

ARPES requires the photoelectrons to leave the solid without loosing energy. Since the scattering length of electrons is very low, ARPES can only analyze the topmost atomic layers. It is known that the electronic structure at the surface can differ significantly from the bulk properties. Thus, ARPES results reflect only one aspect of the electronic structure. Even then, the surface has to be and stay extremely clean for an experiment. The latter can be ensured by ultra high vacuum (UHV) conditions, but to prepare a clean and even surface, the sample has to be prepared in UHV, which restricts the number of possible samples. A recent development to overcome the limitation to the surface is hard X-ray ARPES [Gray et al., 2011]. However, the background of scattered electrons can be challenging.

In principle, ARPES measurement can be done at any temperature, although the momentum resolutions gets worse with increasing temperature due to creation and annihilation of phonons during the photo emission process. ARPES can only be done if the sample is magnetic field free. Nevertheless, the magnetic structure can be investigated by spin-resolved photoemission spectroscopy.

Compton Scattering

At first glance, Compton scattering and ACAR spectroscopy both probe the same, the electron momentum density $\rho(\mathbf{p})$ of a solid. However, a closer look reveals that both techniques are indeed different: For instance, there is no weighting of the positron wave function in Compton scattering, but with Compton scattering only 1D projections of $\rho(\mathbf{p})$ can be measured.

Compton scattering is an elastic scattering process of a high energy photon with an electron. In the usual approximation, it is assumed that the electron is at rest. Then, the energie of the scattered photon $E_2(\theta)$ in dependence of the scattering angle θ is given by

$$E_2(\theta) = \frac{E_1}{1 + \frac{E_2}{m_e c^2}(1 - \cos\theta)} \tag{77}$$

This approximation is not useful if the momentum density of the electrons shall be investigated. Using the laws of energy and momentum conservation, a dependence between the energy $E_{1/2}$ of the incident and the outgoing photon $\gamma_{1/2}$ with wavevector $\mathbf{k}_{1/2}$ and the scattered electron's momentum $\mathbf{p}$ can be derived:

$$E_2 - E_1 = \frac{\hbar^2 (\mathbf{k}_1 - \mathbf{k}_2)^2}{2m_e} + \frac{\hbar (\mathbf{k}_1 - \mathbf{k}_2)\,\mathbf{p}}{m_e} \tag{78}$$

The vector product $(\mathbf{k}_1 - \mathbf{k}_2)\,\mathbf{p}$ yields a projection of the electron momentum onto the scattering vector. As only one component of the 3D electron momentum vector can be accessed, a Compton measurement C corresponds to a plane projection of the electron momentum density $\rho(\mathbf{p})$:

$$C(p_z) = \int\int \rho(\mathbf{p})\, dp_x\, dp_y \tag{79}$$

Analogously, a magnetic Compton profile C_{mag} is defined as a projection of the difference between majority and minority electron momentum density:

$$C_{mag}(p_z) = \int\int \rho_{maj}(\mathbf{p}) - \rho_{min}(\mathbf{p})\, dp_x\, dp_z \tag{80}$$

Compared to a 2D-ACAR measurement [equation (39)], a Compton measurement is easier conceptually. There is neither a weighting of the electronic states nor are the electronic states perturbed.

Since the cross sections for the spin and the charge scattering are not equal and depend e. g., on the degree of polarization of the beam, the magnetic Compton scattering (MCS) signal is extracted by a difference measurement with antiparallel sample magnetization:

$$\begin{aligned} C_{mag} &= C^{\uparrow} - C^{\downarrow} && (81)\\ &= \left(\sigma_{spin} C_{mag} + \sigma_{charge} C\right) - \left(-\sigma_{spin} C_{mag} + \sigma_{charge} C\right) && (82) \end{aligned}$$

The subscripts 'charge' and 'spin' correspond to the charge related part and the spin dependent part of the scattering cross section σ. Although the normalization of C_{mag} profile is lost, the relation $\sigma_{mag}/\sigma_{charge}$ and hence the magnetic moment

of the sample can be determined by calibration with a ferromagnetic reference (in most cases Ni). The interaction time of a high energy photon and an electron is very short compared to the time the electron needs to orbit around the core. Therefore, MCS cannot access the orbital part of the magnetization.

Due to the similarity of ACAR and Compton scattering, both techniques have nearly the same advantages and experimental limitations. In Compton scattering it is possible to measure the electronic structure dependent on the temperature and even dependent on the magnetic field. In contrast to positron measurements, the result is not influenced by the defect concentration in the sample as long as the defects do not distort the electronic structure. However, in Compton scattering 1D projections of $\rho(\mathbf{p})$ are measured, and therefore a single measurement contains considerably less information. Although relatively high resolution can be achieved (Billington et al. [2015] reported a resolution of $0.107\,\mathrm{a.u.} \approx 0.77\,\mathrm{mrad}$), if a crystal spectrometer is used to analyze the scatter radiation, the resolution of MCS is worse. Due to restrictions in the measurement geometry in MCS a germanium detector has to be used which has an energy resolution of about 1.5 keV for 200 keV γ radiation [Maskery, 2013]. Compton scattering requires high intensity γ radiation. Therefore, experiments cannot be done in a laboratory but are only feasible at synchrotron facilities. Only a few synchrotrons in the world are equipped with a Compton scattering beamline. For more details about Compton scattering see M. Cooper et al. [2004].

Part II

EXPERIMENTAL SETUP AND PROCEDURES

5 DESIGN DETAILS OF THE MUNICH ACAR SPECTROMETER

An ACAR spectrometer basically consists of a positron source and a sample stage located in between two position sensitive γ ray detectors. In case of a radioactive source, a high magnetic field is usually applied to focus the positrons onto the sample (see e. g., [Ceeh et al., 2013; Hasegawa et al., 1995; Kruseman, 1999; West, Mayers, and Walters, 1981]). If a slow positron beam is used, the focusing field can be much weaker and no large electromagnet is needed. However, at the moment there is worldwide only one functional ACAR spectrometer with connection to a positron beam [Kruseman, 1999] while a second one is in the planing phase [Ceeh et al., 2014].

In this chapter a comprehensive overview of the mechanical and physical part of the ACAR spectrometer at the TUM shall be given. For a more detailed description the reader is referred to the PhD thesis of Hubert Ceeh [Ceeh, 2015].

The Munich 2D-ACAR spectrometer is depicted in the true-to-the-scale sketch in figure 19 a). Positrons are emitted by ^{22}Na inside a standard source capsule and focused onto the sample by a normal conducting magnet. The sample is mounted on the cold finger of a cryostat which can be precisely rotated by means of a rotary flange without having to break vacuum. The annihilation events in the sample create γ quanta which leave the setup through bores in the lead shielding and are detected by two position sensitive Anger cameras. The analog position signals of every detector are centrally digitized and stored on a computer's hard drive for later usage. Unlike to any other ACAR setup, the detectors and the sample are approximately 2 m above ground level to improve the usage of the available space in the experimental hall.

5.1 SOURCE SAMPLE STAGE

Considerable effort has been made to design the source and sample stage of the spectrometer. The main goal was to focus as many positrons as possible onto the smallest possible area on the sample. The latter is important since the spot size influences the resolution of the measurement (see section 4.3). At the same time the annihilation radiation of positrons annihilating in the source capsule or somewhere else in the sample chamber has to be shielded. Additionally, it is desirable to set the sample temperature for two reasons: i) the temperature can also influence the experimental resolution and ii) the spectrometer was planned to investigate temperature dependent changes of the electronic structure. During a 2D-ACAR experiment it is often necessary to change the projection direction, which had to be considered in the design.

As shown in figure 19, a stage was designed by Hubert Ceeh to fulfill the requirements for such 2D-ACAR experiments. The ^{22}Na which was bought from iThemba LABS in South Africa is sealed in a standard source capsule [Krause-

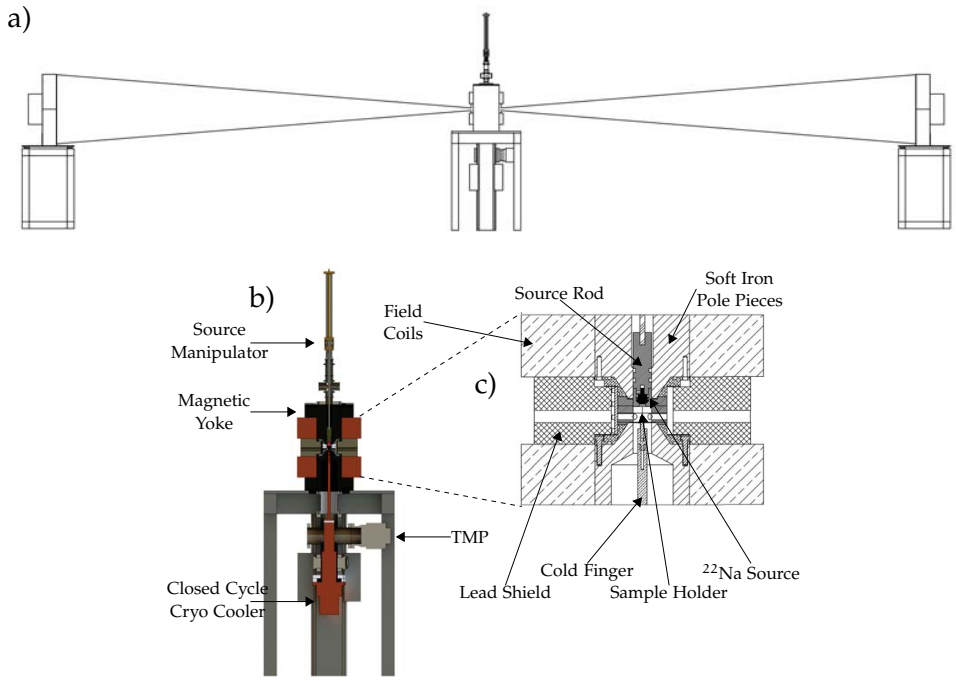

Figure 19: a) Schematic of the Munich ACAR spectrometer. In between the two Anger-type cameras the source sample stage is mounted with electromagnet and cryostat. The lines represents the field of view of both detectors. b) Sectional view of the source and sample stage. c) Magnification of the sample environment with the cryo cooler at the bottom and the source rod at top. (Figures taken from [Ceeh et al., 2013])

Rehberg et al., 2015]. The capsule itself is embedded in a rod out of W_8Cu_2 which serves as a first radiation shield. In order to change the vertical position of the source it is connected to a motor driven manipulator. Thus, the source can be moved into a lead shield to minimize the radiation dose for the researchers during a sample change.

Opposite the source, the sample holder is located. Two types of sample holder were constructed either for temperatures in the range of 10 K to 300 K or for temperatures in the range of 300 K to 650 K. The low temperature sample holder's center piece is the closed cycle cryostat *Sumitomo RDK-415D*, which can reach temperatures down to 4.7 K in the second stage. A cold finger made of copper is fixed at the top of the second stage and ensures thermal contact with the sample. By heat introduction the sample will not reach 4.7 K, but can be cooled to approximately 10 K. Higher temperatures until approximately 300 K can be attained with a resistive heater that is connected to a PID-controller. As temperatures above 300 K may damage the cryostat a second sample holder consisting of a heater and a copper rod was built. The combination of both devices allows to cover a wide temperature range from 10 K to 650 K. For the measurement, one of the sample holder arrangements is fixed onto a differentially pumped, rotary flange with a position resolution of 0.1°. Thereby, the projection direction can easily be changed without breaking vacuum or stopping the cryostat pump.

The positron source as well as the sample are mounted between the poles of a commercially available water cooled electromagnet. The pole pieces were designed

to create a homogeneous magnetic field since strong field gradients can lead to magnetic deflection of positrons. The magnetic field focuses the isotropically emitted positrons onto a spot on the sample with Gaussian profile and a FWHM of ca. (3.8 ± 0.4) mm at 1 T. If correctly mounted, the distance from the sample to the positron source is 20 mm, which is a compromise between positron transport efficiency and reduction of background radiation. Compared to other 2D-ACAR setups, sample and source are accessed via radial bores in the magnet [see figure 19 b)]. It is this improvement which makes the in-situ rotary axis possible in the first place.

By a scroll pump and an additional turbomolecular pump the sample environment can be evacuated to 1×10^{-8} mbar. Compared to ambient pressure the vacuum reduces the absorption of positrons during flight and suppresses thermal flux from the walls of the sample chamber to the sample.

5.2 POSITION SENSITIVE DETECTORS

The principle of Anger cameras is very simple as it is one of the oldest position sensitive detector systems [Anger, 1958]. Anger Cameras convert γ rays by means of a large scale scintillator crystal into light which is detected by a photo multiplier tube (PMT) matrix. Analog electronic circuits evaluate the photo multiplier response and reconstruct the position of the absorbed γ quantum by nonlinear amplification and by determining the center of mass.

The Munich 2D-ACAR setup is equipped with two Anger cameras designed and built by the company *Scintronix* presumably between 1987 and 1990. Both detectors were bought from the positron group of Stephen Dugdale and Ashraf Alam at the University of Bristol. Using a 10.5 mm thick NaI:Tl scintillator crystal, the photopeak efficiency for 511 keV is around 7 % [Ceeh et al., 2013]. The scintillation light is detected by a matrix of 61 PMTs, which are arranged in a hexagonal pattern. Every PMT has a diameter of 63.5 mm and is surrounded by six other multiplier with a spacing of 7 mm. Although the crystal is larger, the detector's field of view is restricted by a ring-shaped lead collimator to a diameter of 16.5″ (419.1 mm). This lead ring accounts for most of the weight of the detector. The distance between sample and each detector is 8837 mm. Therefore, each detector covers a solid angle of $\Omega = 1.77 \times 10^{-3}$. During the construction of the experimental setup, special care was taken that the detectors are well aligned. In particular, the sample and the center of both detectors are collinear and both detectors are parallel to the front side of the sample chamber.

Since NaI crystals are very fragile and can be destroyed by rapid temperature changes each detector is encased in two separate layers of isolation. The outer layer is a styrofoam box which can be removed if necessary, while the inner layer, a transparent plastic housing, is mounted on the detector platform. Solely the back board can be opened to inspect the detector's electronic circuits. To guarantee a constant temperature inside the boxes, the temperature of the detectors and in the experimental hall are continuously monitored.

6 DATA ACQUISITION

When the detectors were received from Bristol, the data processing was mainly based on analog circuits. A major part of this electronic could meanwhile be replaced by modern digital components. In the following chapter, the original analog electronic based data acquisition (DAQ) process is outlined. Many important consideration to this topic are already covered by [Ceeh, 2015]. Furthermore, the reasons for the replacement, the details and the performance of the new DAQ, and the benefits of the new acquisition are presented.

6.1 ANALOG DATA PROCESSING

If a 511 keV γ quantum excites a photoelectron in the NaI crystal, this electron will create a nearly Gaussian shaped light intensity distribution, which is detected by the PMT matrix. The detectors's analog electronic tries to reconstruct the center of mass of the light distribution although it only has information about a fraction of captured light (the PMTs signals) at a finite number of sites (places of the PMTs). For this purpose, the exponentially decaying PMT signals are converted into Gaussian like pulses by pulse shaping amplifiers directly on the PMT base. These amplifiers have to be tested and if necessary adjusted manually in intervals of approximately one or two years to guaranty a homogeneous camera response. For details on the procedure see [Ceeh, 2015]. Before the center of mass can be obtained, every signal is nonlinearly amplified. This is the most crucial step of the process.

Two orthogonal coordinates x and y are needed to define the center of mass. For the calculation of x and y, the PMT matrix is grouped into columns and rows, respectively. The summed up signals of each row and column are weighted by a resistor network and summed up again. This already yields an unnormalized center of mass for the x- and the y-direction. An unweighted energy signal z is generated by adding up all the PMT responses. All of these processes take place on the so-called mixer and mother interface (MIAMI) board.

On the subsequent CANARD board a logic analyzer detects pileups and selects signals within an energy window of $\pm 35\,keV$ around the 511 keV photopeak for further processing. The signals are then shaped by stretching the peak value of the signal to create a plateau. Finally, the x- and y-signals are divided by the z signal to normalize them before they enter a line driver circuit.

The rest of the DAQ does not happen on the camera but is handled by nuclear electronics. At first the bipolar signals are converted to unipolar ones, then the signals are multiplexed and in the end digitized by an analog to digital converter (ADC). The data are then histogramed and stored on a PC.

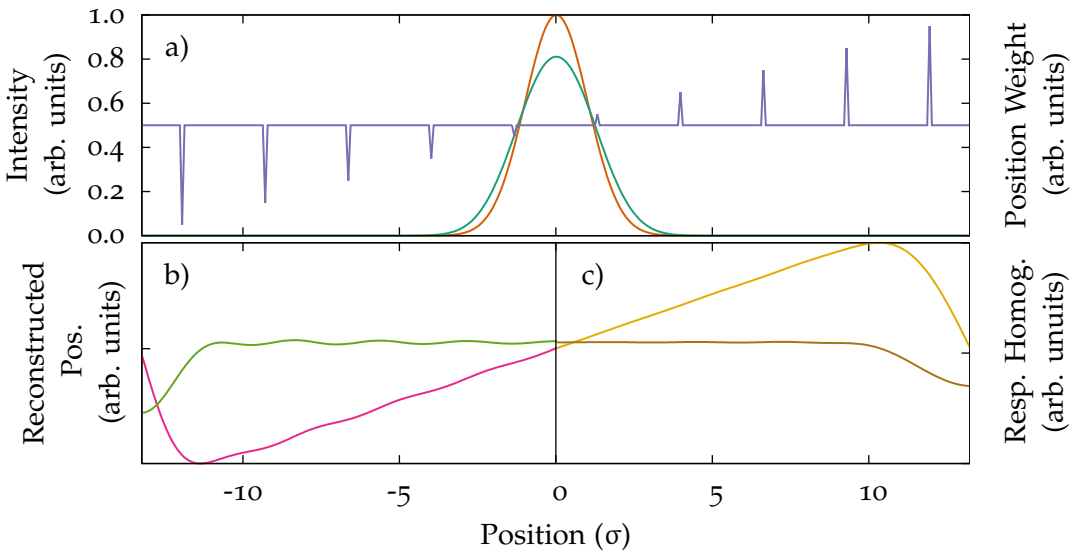

Figure 20: a) ■: $L(x)$; Light distribution in the crystal. ■: $I(x)$; Light intensity captured by one PMT. ■: $G(x)$; PMT centers weighted with the position.
b) ■: $R(x) = (I * G)(x)$; Reconstructed γ absorption position of the camera without correction. ■: $\mathcal{F}^{-1}(\mathrm{Re}\{\mathcal{F}(I)\,\mathcal{F}(G)\})$; Camera homogeneity without correction.
c) ■: $R(x) = (\sqrt{I} * G)(x)$ Reconstructed γ absorption position of the camera with correction. ■: $\mathcal{F}^{-1}\left(\mathrm{Re}\left\{\mathcal{F}(\sqrt{I(x)})\,\mathcal{F}(G(x))\right\}\right)$; Camera homogeneity with correction.

Identifying the Center of Gravity

An Anger camera determines the spot of a γ-quantum-induced photoelectric event in a scintillator by means of the distribution of light in the crystal. In the cameras of the Munich spectrometer this is done by calculating the center of mass of the PMT responses. However, a few issues have to be considered for such a calculation: It is known from simulations that the PMT width is equal to the standard deviation of the light distribution $L(x)$ [Ceeh, 2015]. The fraction of light $I(x)$ which is captured by the PMT is dependent on the distance of the center of the light pulse. $I(x)$ is given by the convolution of the PMT shape $M(x)$ with the light distribution $L(x)$:

$$I(x) = (L * M)(x) = \int_{-\infty}^{\infty} d\tau\, L(\tau) M(x - \tau) \tag{83}$$

$L(x)$ (orange) and $I(x)$ (green) are plotted in fig. 20 a). Notably, $I(x)$ is nearly Gaussian shaped. The Anger cameras's electronic captures $I(x)$ only at discrete sites, i. e. at the positions of the PMT. Hence, the reconstructed position of the camera $R(x)$ as a function of the initial photo event's position is a convolution of $I(x)$ with a weighted PMT lattice function $G(x)$ [violet curve in fig. 20 a)].

$$R(x) = (I * G)(x) = (L * M * G)(x) \tag{84}$$

The weighting of the lattice function $G(x)$ accounts for the resistor network on the camera. In figure 20 b), $R(x)$ is drawn in magenta. It has two different nonlinear features: i) At the boundaries, the nonlinearity is caused by the finite number of multipliers. For these reasons the detectors are furnished with a lead ring, which basically cuts away the nonlinear edges. ii) Throughout the response, there is an

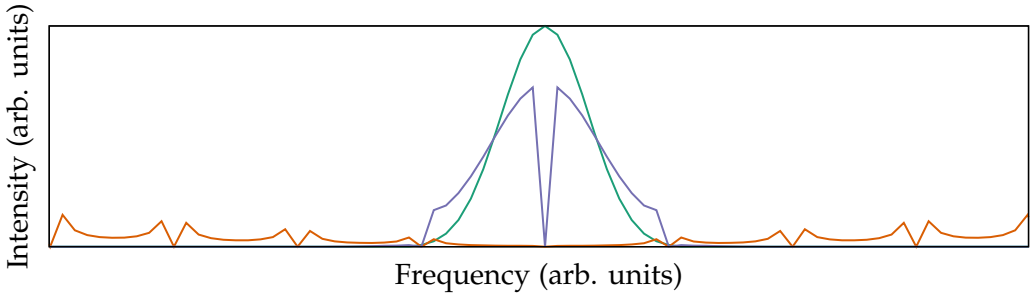

Figure 21: ■: $\mathrm{Re}(\mathcal{F}(I))$, real part of the FT of multiplier response $I(x)$. ■: $\mathrm{Re}\{\mathcal{F}(G)\}$, real part of the FT of the PMT lattice $G(x)$. ■: $\mathrm{Re}\{\mathcal{F}(G)\,\mathcal{F}(I)\}$, real part of the product of the FT of the lattice $G(x)$ and the multiplier response $I(x)$.

oscillating behavior. This introduces systematical errors to the measurements and deteriorates the position resolution of the detector.

The Anger camera can compensate this oscillation with the nonlinear amplification of the multiplier signals. In order to understand the working principle of the nonlinear amplification one has to consider the Fourier space, since a convolution in real space is equivalent to a multiplication in the frequency domain. In this consideration only the real part in Fourier space is treated explicitly, which is responsible for the symmetric contribution in real space. The distribution obtained by the back transformation of the real part of multiplication in Fourier space, i. e. $\mathcal{F}^{-1}(\mathrm{Re}\{\mathcal{F}(L)\,\mathcal{F}(M)\,\mathcal{F}(G)\})$, is shown in figure 20 b) (green). It is proportional to the homogeneity of the camera response.

In figure 21 the three functions $\mathrm{Re}\{\mathcal{F}(I)\}$, $\mathrm{Re}\{\mathcal{F}(G)\}$ and $\mathrm{Re}\{\mathcal{F}(I * G)\}$ are depicted. In accordance with the FT rules, the Gaussion shaped $I(x)$ is transformed into a Gaussian while the lattice function $G(x)$ is represented by a periodic function. The width of the product $\mathrm{Re}\{\mathcal{F}(I * G)\}$ is dominated by the width of $\mathcal{F}(I)$. Therefore, if $\mathcal{F}(I)$ gets narrower, so does $\mathrm{Re}\{\mathcal{F}(I * G)\}(\omega)$. Hence, $\mathcal{F}^{-1}(\mathrm{Re}\{\mathcal{F}(I * G)\})(x)$ has less high frequency components and thereby the oscillation of $R(x)$ is damped.

One way to reduce the width of $\mathcal{F}(I)(\omega)$ is to broaden $I(x)$ for example by taking the square root $\sqrt{I(x)}$. The effect of such a correction is shown in figure 20 c) (yellow). Not only this particular correction is able to linearize the camera response, but any correction function, which can narrow $\mathcal{F}(I)(\omega)$. In the Munich spectrometer, the Anger camera's electronic approximates the root function by two piecewise defined linear functions.

The above considerations show that a reasonably accurate position reconstruction by forming the center of mass is possible with a correction that is locally applied. *Locally* in this context means that every PMT signal is independently corrected. This is important to keep the complexity of the analog data processing on a reasonable level. However, this locality comes with caveats: i) Although the response in figure 20 looks fairly linear, the real detector response still has oscillations probably due to the energy resolution in the scintillator crystal [Leitner, Ceeh, and Weber, 2012]. ii) The linearity is exchanged for statistical accuracy as PMTs with less counts are weighted over proportional. For a detailed analysis on the statistical matter see e. g., [Ceeh, 2015].

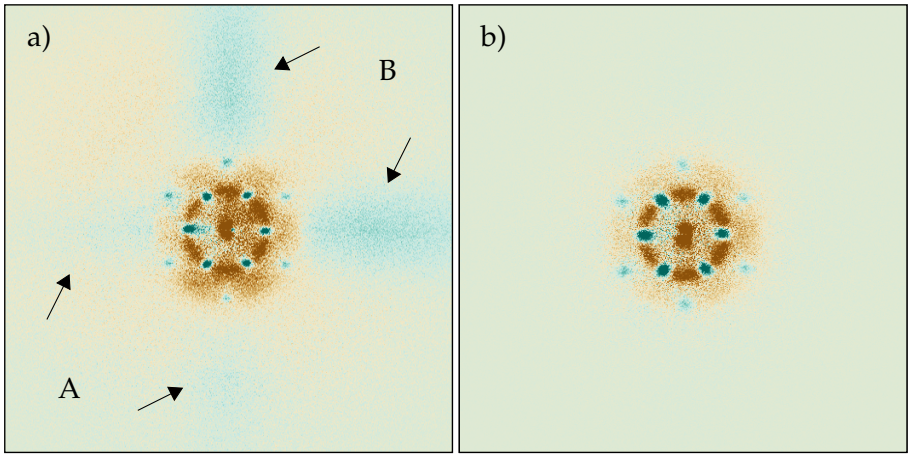

Figure 22: Comparison between initial and improved DAQ on the basis of the anisotropy of a 2D-ACAR spectrum of delocalized positronium in single crystalline α-quartz. a) initial DAQ, the arrows point to artifacts in the spectra. These are caused either by underestimation (A) or overestimation (B) of one coordinate. b) improved DAQ, no artifacts are present.

6.2 PROBLEMS OF THE ORIGINAL DATA ACQUISITION

Shortly after the Anger cameras were received from Bristol, one of them malfunctioned. An integrated circuit (IC) module on the CANARD had stopped working leading to a short circuit that destroyed several other electronic components. A large amount of money and time had to be spend on repairs, especially to replace the damaged ICs. Furthermore, ICs on the PC to ADC interface board were broken and had to be exchanged. Even after the repair some problems with the CANARD board, probably due to a slacking joint somewhere on the board, remained.

Much more serious than the technical problems with the hardware are the artifacts that were induced to the measurement by the original DAQ. To illustrate this problem the anisotropic part of the 2D-ACAR spectrum of delocalized α-quartz, recorded with the original hardware is depicted in figure 22 a). The arrows in the picture highlight features, which are introduced if three of the four digitized coordinates are recorded correctly while one coordinate is wrong. Similar artifacts were reported for the ACAR setup at the Delft University of Technology by Kruseman [1999]. He attributed them to a malfunctioning in the interplay of detector and multiplexer. The reason for the artifacts in the presented spectrum seem to be similar. However, in contrast to Kruseman, the artifacts here also have a small intensity of underestimated coordinates [see (A) in figure 22 a)], which suggests that the mechanism is slightly different.

6.3 IMPROVED DATA ACQUISITION

All those issues lead to the decision to update the DAQ system. The primary idea was to replace the ADC, multiplexer and the analog interface and as much analog data processing on the camera as possible. For this purpose a DAQ system consisting of the 8-channel ADC *SIS3302* and the PC interface *SIS3153* including a VME crate was bought from *Struck Innovative Systeme* for 10500 €.

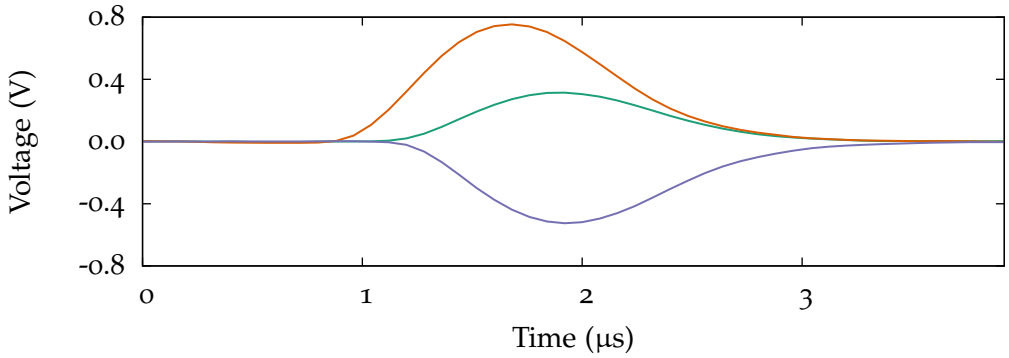

Figure 23: Typical signals from the MIAMI board. ■: Energy signal; ■: x-position signal; ■: y-position signals.

Every channel of the *SIS3302* has a bandwidth of 50 MHz and can record signals with 100 MS s^{-1} and 16-bit resolution. However, the effective resolution is just above 13-bit due to noise and nonlinearities. The maximum input range of this system is 10 V. Further characteristics can be found in the datatsheet of the ADC IC *AD9446*, which is built into every channel. The ADC samples all the time, writing the data points into a ring buffer. When the channel is triggered, the data are copied from the ring buffer into the module's memory and stored until it is read out by the PC. Every channel of the *SIS3302* can trigger itself and/or the neighboring channels if a threshold value for the internal generated trapezoidal filter is reached. The software interface to access the DAQ system is based on the work by Löwe [2016]. A few adjustments were made to the original software to adapt it to the special requirements of the 2D-ACAR spectrometer.

Using this new hardware it was possible to digitize the camera signal directly after the MIAMI board, rendering the whole CANARD board unnecessary. However, the signal outputs of the MIAMI board are neither impedance matched to the ADC's input, nor are they fused in any way. To protect these outputs, impedance matched line driver boards were designed based on the video driver IC *HA5033*. The detailed circuit designed can be found in appendix A.2.

Three signals per camera are connected to the *SIS3302*: The two unipolar x- and y-signal (with either negative or positive polarity) and the unipolar positive energy signal. The energy signal is used to trigger both position signals, which are connected to the neighboring channels. Therefore, the trigger can be used as a rough energy filter, reducing the digitized data volume considerably. Nevertheless, the *SIS3153* USB interface had to be replaced by the *SIS1100* fiber optics interface to be able to transmit the high data volume to the PC. Since the whole signals, consisting of three times 300 16-bit data points per event, are transfered to the PC, the transmission rate can easily exceed 30 MB s^{-1}.

Exemplary, digitized position and energy signals are shown in figure 23. Typically the position signals extend from ca. −1 V to 1 V while the energy signal stays between 0 V to 1 V. The signals can be approximated by a Gaussian curve except for the lower part of the falling edge, which decays more gradually.

In order to extract the position and energy information from the signals, the original DAQ performed a pulse hight analysis. The hight of the curve was recorded

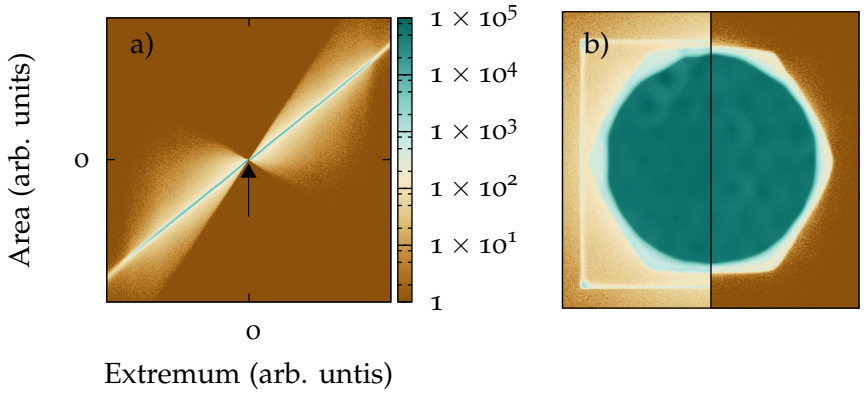

Figure 24: a) Histogram of the signal area against the peak maximum. Colors are scaled logarithmically. The minimum value in the color scale is set to 1.
b) Comparison between the image of a homogeneously irradiated detector without pileup rejection (left) and with pileup rejection (right). Colors are scaled logarithmically.

by stretching the maximum and digitizing this value with a considerably slower ADC. Although the resolution of the present ADC is sufficient for a pulse hight analysis, taking an extremal value is statistically ill defined. Much better defined is the area A under the peak, which can be calculated very easily by summing over the digitized signal S and subtracting the baseline:

$$A = \sum_{i=1}^{300} \left(S_i - \frac{1}{50} \sum_{j=1}^{50} S_j \right) = \sum_{i=1}^{300} S_i - \frac{30}{5} \sum_{i=1}^{50} S_i$$

To ensure that the area under the peak and the peak hight are linearly correlated, a histogram of the area vs. pulse hight for all the signals was created. An example of such a histogram for one position signal is depicted in figure 24 a).

It is apparent that most signals have a linear relation between peak height and curve area as the utter most intensity in 24 a) is located on a straight line. The deviations from linearity can be derived from a logical analysis:

One irregularity, indicated by the arrow in the middle of the plot, is caused by the bipolarity of the signals. At this marked point, the extremum is taken from the 0 V baseline of the signal. Since there is always some kind of noise, e. g., from the ADC's intrinsic noise level, the extremum can never be zero and therefore the histogram is spread.

The second irregularity are the halos of points surrounding the primary line. These halos are noticeable bordered by two invisible, perpendicular lines that meet at the zero crossing. The reason for this are pileups, i. e. two (or more) events that are detected in such temporal proximity that they are both at least partially digitized by 300 samples (3 µs). If both pulses have a positive pulse hight, the extremum will only be taken from the highest pulse while the area is combined from both pulses. Therefore, the area is over-proportionally greater than the extremum. If one pulse has a positive and the other a negative pulse hight, the area has an under-proportionally lower value than the extremum.

The correlation between area and peak hight can be used to detect and sort out pileup events: If straight boundaries are set parallel to the linear relation of

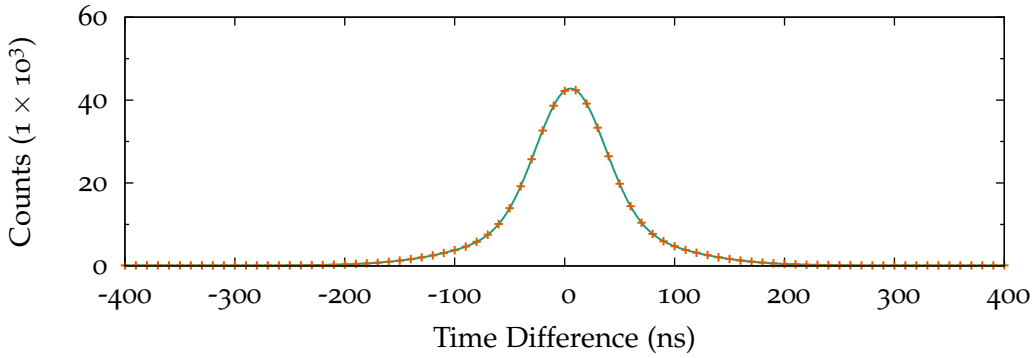

Figure 25: Time difference distribution between two events. The peak represents the coincident events. ■: Experimental data; ■: Theoretical fit with the sum of two Gaussians.

extremum vs. peak area, pileups can be efficiently suppressed. A comparison of a homogeneously irradiated detector with and without pileup rejection is shown in figure 24 b). A large fraction of the pileups is forming a rectangular shape around the detector image, but pileups are also distributed throughout the entire image. The picture changes remarkably if the discussed pileup rejection is applied since the artifacts vanish and the signal to noise ratio is increased. Therefore, this pileup rejection can be used to improve the quality of the data.

For ACAR spectroscopy it is crucial to detect coincident events, i. e. events which occurred at the same time in both detectors. Traditionally this is achieved by the analysis of the signals with a nuclear electronic analog coincident unit. In the present DAQ every digitized signal is assigned with a timestamp, i. e. a 64-bit number which increases with every cycle of the ADC's clock. Therefore, coincident events can easily be found after digitalization by a list search algorithm.

In figure 25 the time difference between random events in detector 1 and 2 is shown. The peak in the center corresponds to the coincident events. Its width indicates the time resolution of the spectrometer. It can be fitted by the sum of two Gaussian curves with $\mathrm{FWHM}_1 = 72\,\mathrm{ns}$ and 59% and with $\mathrm{FWHM}_2 = 180\,\mathrm{ns}$ and 41%. The time interval of acceptance is set by software to 300 ns, which comprises 98% of the coincident events. A longer acceptance time could increase the fraction of coincident counts captured, but at the expense of a higher background by capturing false-positive noncoincident events.

The recorded data are written to the hard disc in three separate binary encoded files: Two files for the single events of every detector and one file for the coincident events. The data format of the files is shown in table 2 and 3. Usually, 10^8 events are collected in a single detector file as well as in the coincident file.

The DAQ was implemented based on the client server principle: While the acquisition server does all the continuous work like collecting the data and storing them on the disc, the client can request data and control the server. The data server was coded in C++ allowing fast and highly efficient arithmetic operations, while the client was coded using python and is therefore more flexible.

The described DAQ has various advantages over the original one. The most important features are: i) elimination of artifacts, ii) the possibility to record the single counts of each detector and the coincident counts simultaneously and iii) saving

timestamp	x-coordinate	y-coordinate	energy
int64	uint32	uint32	uint32

Table 2: Data format of the single events detector files.

Detector 1			Detector2		
x-co.	y-co.	energy	x-co.	y-co.	energy
uint32	uint32	uint32	uint32	uint32	uint32

Table 3: Data format of the coincident events file.

of the data in binary lists. In figure 22 b), the anisotropy of a quartz spectrum recorded with the improved DAQ is shown. No artifacts are visible in this picture, especially compared to figure 22 a).

The storage of the data in binary lists enables a much more reliable data treatment. It begins with the correction of the spatial distortions and ends with the possibility to shift the spectra by any desired amount without interpolation. The latter is important to preserve the statistical nature of the data. Details on this subject can be found in the following chapter 7.

An additional advantage is provided for the annual adjustment of the PMT gains since no changes in the setup have to be made. After all the position compensation and all but one PMT are switched off, the DAQ can directly display the energy spectrum of the inspected PMT. As the recorded data are accessible through the python console, different PMT can be compared efficiently.

Furthermore, when measuring an ACAR spectrum it is now possible to measure the momentum sampling function (MSF) simultaneously (see chapter 7). It can be calculated from the single detector pictures by convolution. A simultaneous recording, in contrast to the previous sequential recording, of single and coincident events saves a lot of valuable measurement time.

7 DATA TREATMENT

An amateur in physics might think that the most challenging part for an experimental physicist is to conduct an experiment and then the results will simply pop out. However, this is not always the case. An experimental physicist knows that collecting data is just the beginning and the data analysis can take as much or even more time than the experiment itself. At first, it is of utter most importance to know what exactly has been measured since often the collected data do not solely represent the pure physical quantity one is looking for. The data may be superimposed by artifacts, distorted, broadened by resolution and decorated with statistical noise. Furthermore, it is vital to handle the data with great care in order to avoid the introduction of artifacts during data processing which may lead to misinterpretation.

7.1 CORRECTING NONLINEARITIES

As mentioned in section 6.1, the nonlinear response of the Anger camera cannot be corrected entirely by means of analog electronics. It was already noted by West, 1995 (see also [West, Mayers, and Walters, 1981]) that systematic errors in the camera response can decrease the resolution approximately by a factor of 1.4. In order to eliminate the nonlinearities, a distortion map was generated. To this end a collimator with a hexagonal hole pattern was placed in front of the uniformly illuminated camera. In figure 26 these holes can be seen as bright spots on the camera. Obviously they do not reflect the regular pattern of the collimator as it is not possible to connect more than two points with one straight line. By fitting the spots with a lattice of Gaussians one obtains the variations from linearity at every location on the camera. Using this information it is possible to correct the position of a γ event on the camera. With this correction the position resolution of the camera was increased by a factor of 1.7 [Leitner, Ceeh, and Weber, 2012].

In practice this correction is only possible since the position of every event is saved in a binary list. Before correction, energy boundaries around the photopeak are applied and only the events within the energy window are processed. If desired, the spectra can be shifted and scaled afterwards to avoid interpolation, since this would destroy the statistical nature of the data. It is often useful to scale the data in such a way that a reciprocal lattice vector corresponds to an integer number of pixels in the spectrum.

7.2 THE MOMENTUM SAMPLING FUNCTION

The momentum sampling function (MSF) is an important correction of the experimental data taking into account the inhomogeneous detection efficiency in momentum space of the experimental setup. To demonstrate the origin of the MSF

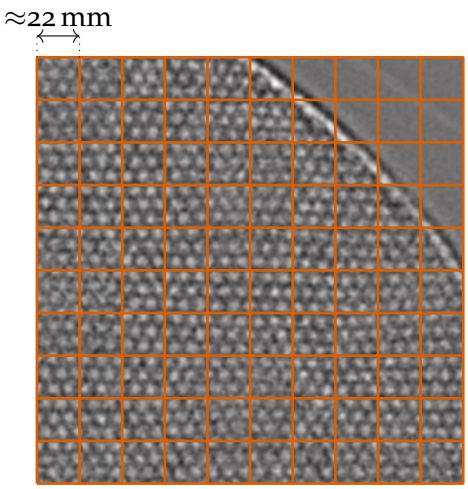

Figure 26: Uniformly illuminated camera behind a collimator with holes in a periodic hexagonal lattice [Leitner, Ceeh, and Weber, 2012]. The bright spots are the projection of the collimator holes. The orange grid is a guide to the eye which visualizes the distortions of the detector.

a one dimensional example will be given in the following: The sketch in figure 27 shows two one-dimensional position sensitive detectors with different detection efficiencies $\epsilon_1(\theta)$ and $\epsilon_2(\theta)$. For this detector arrangement, the possibilities and therefore the probability to detect certain angles varies heavily. There are for example much more possibilities to detect γ quanta that are emitted antiparallel from the source than under an angle of 70°. Moreover, due to the inhomogeneous detection efficiency the probability to detect a γ quanta pair under −70° is higher than to detect a pair under 70°. The dependence between detection probability and angle is called the momentum sampling function. It can be seen that the MSF in one dimension $P(\theta)$ is given by the convolution of $\epsilon_1(\theta)$ and $\epsilon_2(\theta)$:

$$P(\theta) = \int \epsilon_1(\phi)\epsilon_2(\theta - \phi)d\phi. \tag{85}$$

In this equation the small angle approximation was used, which is valid for every ACAR experiment. For the detectors of figure 27 a) the MSF is shown in 27 b). The sharp peak at 0° is universal for equidistant detectors of the same size. The MSF of a 2D-detector ensemble is calculated analogous by the 2D convolution of both detector efficiencies $\epsilon_{1/2}(\theta_x, \theta_y)$. It shall be noted that in the 2D case one coordinate usually has to be inverted, since both detectors have no mirror symmetry.

In practice, the detector efficiency is measured during the actual ACAR measurement by histogramming only a single detector. This has the advantage that not only the detection efficiency of the detector itself is taken into account, but also shadowing effects by the sample can be corrected. To obtain the ACAR spectrum $S(p_1, p_2)$, the coincident measurement $COI(p_1, p_2)$ has to be divided by the momentum sampling function $MSF(p_1, p_2)$:

$$S(p_1, p_2) = COI(p_1, p_2)/MSF(p_1, p_2)$$

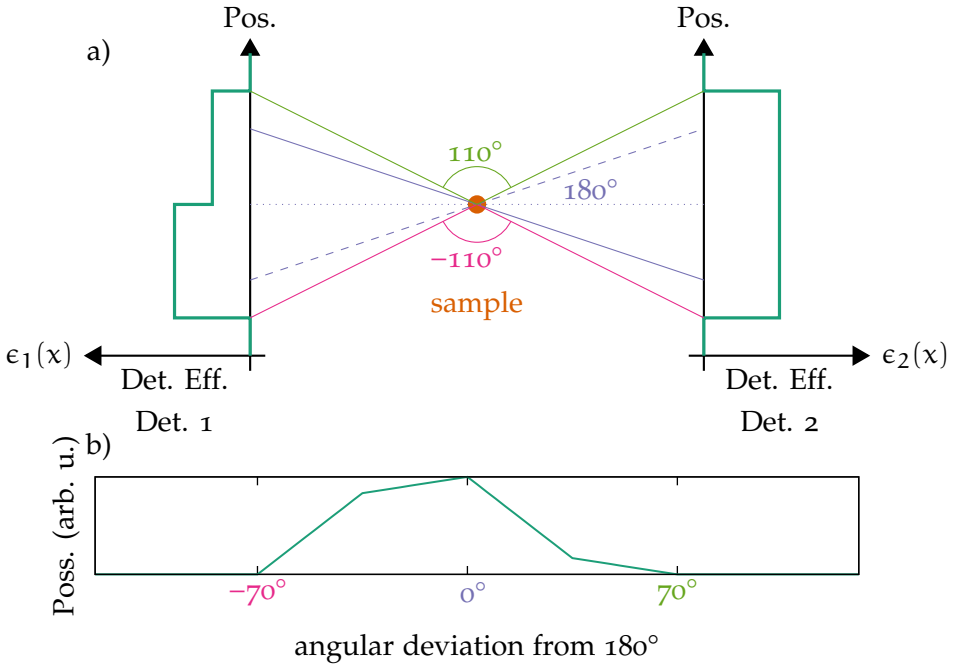

Figure 27: a) Ensemble of two linear position sensitive detectors with varying detection efficiency. Exemplary annihilation events at three different angles are sketched. b) Possibilities to measure an event at a certain angle. This is equivalent to the angular sensitivity of this hypothetical setup.

7.3 FINDING THE CENTER OF THE SPECTRUM

Finding the center of the measured spectra is important since the measurement itself yields no origin just relative angles. Three methods to address this issue are introduced in the following section.

Center by Symmetry

Kruseman [1999] proposed to find the center (c_1, c_2) by minimizing

$$(c_1, c_2) = \underset{\tilde{c}_1, \tilde{c}_2}{\arg\min} \sum_{p_1, p_2} \frac{\left(S(p_1, p_2) - \tilde{S}(p_1 + \tilde{c}_1, p_2 + \tilde{c}_2)\right)^2}{S(p_1, p_2)}. \tag{86}$$

$\tilde{S}$ is the by 180° rotated spectrum. This algorithm has been analyzed in the present thesis, but it was not found to be advantageous regarding exactness and speed.

Center by Convolution

To overcome the drawbacks of the method above a different algorithm had been developed: Since $\rho^{2\gamma}$ is symmetric, the convolution of $\rho^{2\gamma}$ with itself has its maximum at the center of $\rho^{2\gamma}$. This still holds for the projection $P(p_1)$ of $\rho^{2\gamma}$ along p_2,

but to calculate $P * P$ takes much less time. Therefore, the coordinates of the center $c_{1/2}$ are obtained by:

$$c_{1/2} = \arg\max_{p_{1/2}} \sum_{\tau} P(\tau)P(p_{1/2} - \tau) \tag{87}$$

Although this approach is much faster and less complex, it has the drawback that the accuracy is limited by the pixel width of the data as the convolution is discrete. Nevertheless, this method is very useful to get a starting point for the next procedure which is more exact but slower.

Center by Anisotropy

The third algorithm that is introduced has proven to be very reliable. It uses the fact that the anisotropy, when calculated with the wrong center, shows a strong dipolar artifact. Therefore, if no artifact exists the correct center has been found. Again, the identification of the center (c_1, c_2) boils down to a minimization problem:

$$(c_1, c_2) = \arg\min_{\tilde{c}_1, \tilde{c}_2} \sum_{p_1, p_2} \left(ANI(S(p_1, p_2), (\tilde{c}_1, \tilde{c}_2))\right)^2 \tag{88}$$

In this case, the anisotropy function $ANI(S, c)$ takes as an additional argument the assumed center.

Even though this approach is slow it is very precise and therefore the method of choice to determine the center. The speed can be increased if the result of the convolution method is taken as a starting point for the minimization.

7.4 THE RADIAL ANISOTROPY

The radial anisotropy is the most important feature of 2D-ACAR data. It is needed for the methods discussed above but also has some value in itself as it indicates the quality of recorded data and allows a quick estimation of the FS. The latter has been demonstrated in figure 17, where the outline of the FS and its overlap between the first BZ and the higher order BZs is clearly visible in the anisotropy.

Moreover, conclusions about the sample quality can be made if no distinct anisotropy is visible. In this case the sample is either not single crystalline or it has a large amount of defects. The first scenario leads to an averaging of $\rho^{2\gamma}$ by all directions in space which results in an isotropic measurement and to a canceling of the radial anisotropy. In the second scenario most of the positrons annihilate localized at a defect site. A localized positron wave function in real space yields a broad positron momentum distribution in reciprocal space. Hence, the momentum density $\rho^{2\gamma}(\mathbf{p})$, which is proportional to the convolution of the electron and the positron wave function in reciprocal space (see equation (56)), will also get smeared out and the anisotropic part will get strongly suppressed. For a more comprehensive explanation see Prasad et al. [1989].

In this thesis, a fast algorithm to calculate the radial anisotropy was developed. At first the radial isotropy is determined by averaging the data on rings around

the center. With this information, the isotropic distribution is calculated and subtracted from the data which yields the anisotropy.

7.5 DETERMINING THE GAUGE BETWEEN PIXELS AND ANGLE

The quantity that shall be measured with a 2D-ACAR setup is the angular deviation of two γ photons but the quantity which is actually measured is the discretized hight of electronic signals, sorted into an array of pixels. Hence, the pixel binning in angular units has to be determined. Only this gauge gives a physical meaning to the acquired data. Therefore, it is most important to verify the gauge carefully. In this section, four different possibilities are introduced and exemplified by a measured vanadium spectrum.

Lattice Method

The distortion correction discussed in section 7.1 also provides a straight forward method to calculate the gauge. For the correction, a regular hexagonal pattern of holes with a pitch of 9 mm was mapped onto the detector. The correction was designed in such a way that the holes in the image of the lattice on a 2048×2048 matrix have a pitch of 30 pixels. The lattice itself was not placed directly, but for technical reasons with a distance of 100 mm in front of the crystal. From these numbers, a gauge of

$$\frac{9\,\mathrm{mm}}{8735\,\mathrm{mm}\,30\,\mathrm{px}} = 3.434 \times 10^{-5}\,\frac{\mathrm{rad}}{\mathrm{px}}$$

is determined. For the more common binning of 512×512 it corresponds to $1.374 \times 10^{-4}\,\mathrm{rad\,px^{-1}}$.

Using the Lead Collimator

For this method, the distance reference is the ring shaped lead collimator which yields a circular detector image [see figure 24 b)]. From both detector pictures, the diameter of the ring and the detector sample distance the gauge can be calculated. Here, the diameter of the circular image was determined by fitting a circular shape which was convoluted by a Gaussian point spread function. So, not only the gauge but also information about the resolution can be obtained.

The fit to the 512×512 binned pictures yields a radius of 173.7 px and 173.4 px for detector D_1 and detector D_2, respectively. From these numbers a gauge of $1.365 \times 10^{-4}\,\mathrm{rad\,px^{-1}}$ and $1.367 \times 10^{-4}\,\mathrm{rad\,px^{-1}}$, for detector D_1 and detector D_2, can be calculated. The second result of the fit is the detector resolution of $\mathrm{FWHM}_{D1} = 0.79\,\mathrm{mrad}$ and $\mathrm{FWHM}_{D2} = 0.89\,\mathrm{mrad}$.

A source of systematic errors in this method originates from the geometry of the lead ring. Since the γ quanta are not emitted fully parallel with respect to the collimator ring, the picture of the ring is enlarged and the edges are blurred. Furthermore it will also lead to an overestimation of the detector resolution.

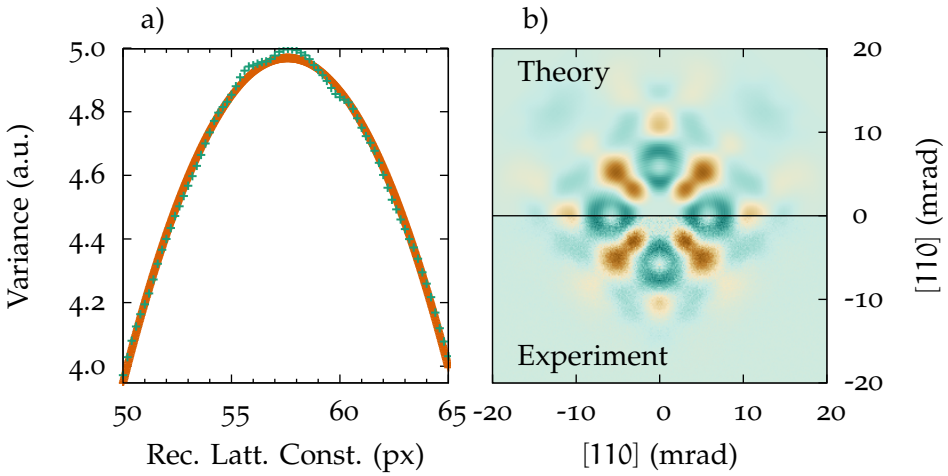

Figure 28: Examples for finding the gauge of a spectrum. a) Using the LCW method and b) by comparison with the theoretical data.

Comparing to Theoretical Calculation

A third possibility to get the gauge of a spectra is to compare experimental with theoretical data. Since the gauge of the theoretical data is known, the experimental gauge can be fixed. For a comparison of theory and experiment, the radial anisotropy turned out to be most suitable as the influence of deeper lying bands is minimized.

In this example, a statistical weighted least squares fit of theoretical and experimental data of vanadium is used. The free parameter of the fit are the experimental resolution in x- and y-direction, the gauge, a multiplicative and an additive constant. Theory can be brought into very good agreement with the experiment [see figure 28 b)]. From the fit, resolutions of $\sigma_x = 1.12\,\mathrm{mrad}$ and $\sigma_y = 1.45\,\mathrm{mrad}$ are obtained. Furthermore the fitting yields a gauge of $1.364 \times 10^{-4}\,\mathrm{rad\,px^{-1}}$. The difference in resolution corresponds to a positron spot size of 4 mm, in good agreement with the measurements of Ceeh, who obtained a diameter of $(3.8 \pm 0.5)\,\mathrm{mm}$ (after the geometrical correction by $\sqrt{2}$) with a Guillotine setup [Ceeh, 2015].

LCW Method

The main aim of the LCW theorem is to emphasize the Fermi break in a measurement. That means, the dynamic range of a LCW folded spectra is enhanced because occupied states add up constructively. However, if the LCW folding is done with the wrong reciprocal lattice constant, occupied states may overlap with unoccupied states and hence the dynamic range is reduced. Doing the LCW folding for various reciprocal lattice constants, the correct lattice constant can therefore be identified by a maximum in the dynamic range of the folded data. Instead of the dynamic range, it is generally more useful to evaluate the data by means of the variance as it is statistically much better defined than a single maximum or minimum value.

	Gauge $(1 \times 10^{-3}\ \frac{\text{mrad}}{\text{px}})$	σ_x (mrad)	σ_y (mrad)
Lattice	137.38 ± 0.16		
Collimator	136.8 ± 0.7	1.19	
Theory Comp.	136.4	1.12	1.45
LCW	138.6 ± 1.2		

Table 4: Main results of the four methods to determine the gauge pixel-to-angle of the spectrometer.

Again, experimental vanadium data are used to demonstrate this method. In figure 28 a), the variance of the LCW normalized to the LCW's mean is plotted as a function of the lattice constant. Since the curve is a bit noisy, the maximum of the curve at a lattice constant of 57.59 px was determined by a parabolic fit. Using the real space lattice constant of vanadium of 3.027×10^{-10} m [Pan, 1966; Podberezskaya, 2012] a gauge of 1.386×10^{-4} rad px^{-1} was calculated. Notably, the gauge can be determined without any knowledge about the experimental setup using no prior knowledge except for the lattice constant and the crystal symmetry.

Discussion and Conclusion

The main results of the four methods are summarized in table 4. If possible, an estimate of the error is given. The agreement between the different methods is very good and the deviation smaller than 1 %.

The most exact gauge is certainly the one obtained by the lattice method, as the pitch of the lattice in the distortion correction was *defined* to be 30 px. Furthermore, deviations from the 9 mm pitch of in the real lattice could not be detected and are thus smaller than 10 µm. The largest uncertainty in this method originates from the distance measurement between sample and lattice, which is smaller than 10 mm.

The collimator method, in contrast, possesses various sources of errors. The most striking uncertainties are the distances sample - detector as well as diameter and uniformity of the ring. The influence of the incomplete attenuation at the edges of the collimator is a bit more complex to take into account.

In the theory comparison, the precision of the result is not a matter of measurement uncertainties. Here, the result depends heavily on the quality of the theoretical calculation. Even the best state-of-the-art calculations are not able to reproduce an experimental spectrum entirely. Hence, the theoretical data gives rise to a systematic error, which cannot be quantified further.

Uncertainties in the LCW-method originate from the experimental lattice constant and from finding the right maximum of the variance. As can be seen in figure 28, the variance curve has artifacts, probably caused by interpolation and the statistical nature of the data.

For the further analysis of the experimental data, the gauge determined with the lattice method is used as it results in the smallest uncertainty.

8

COMPARISON OF γ DETECTOR TECHNOLOGIES SUITED FOR ACAR SPECTROSCOPY

8.1 GENERAL CONSIDERATIONS

Every physical observation is affected by different kinds of systematical errors and measurement uncertainties. As it is the case for every experiment, also in ACAR spectroscopy both, errors and uncertainties, are desired to be as low as possible. For ACAR, systematic errors arise mainly due to misalignment of the setup. These contributions, however, are very small compared to the measurement uncertainties and are not subject to the further analysis here. The dominating measurement uncertainties in ACAR spectroscopy are the angular resolution of the setup and the statistical accuracy of the data. The following paragraphs will present an overview of the relation between detector system and uncertainties in an ACAR measurement and conclude with requirements of detectors for ACAR spectroscopy.

8.1.1 *Figure of Merit for ACAR Spectroscopy*

In an ACAR experiment, the most important uncertainties to consider are the angular resolution σ_Φ and the statistical uncertainty ΔU. As mentioned in section 4.3, the angular resolution is determined by the detector's position resolution σ_D and by the size of the positron spot on the sample. The latter will be omitted in these considerations since it is independent of the detector system.

The angular resolution of the detectors D_1 and D_2 is given by $\sigma_{\Phi_{1/2}} = \frac{\sigma_{D_{1/2}}}{L}$, with the detector sample distance L (see appendix A.3). Assuming that the whole setup consists of two identical detectors which are symmetrically positioned, the total angular resolution is

$$\sigma_\Phi = \sqrt{(\sigma_{\Phi_1})^2 + (\sigma_{\Phi_2})^2} = \sqrt{2}\frac{\sigma_D}{L} \tag{89}$$

Another factor representing the accuracy of a measurement is the statistical uncertainty $\Delta U_{i,j}$ of a data point i, j in a 2D-ACAR measurement M with the number of counts $M_{i,j} = N$. This statistical uncertainty is given by the Poisson statistics

$$\Delta U_{i,j} \approx \frac{\sqrt{N}}{N} = \frac{1}{\sqrt{N}} \tag{90}$$

and is thus only dependent on the number of counts.

For a given number of positrons annihilating in the sample, the probability for detector D_1 to detect a γ quantum is dependent on the detection efficiency ν for 511 keV γ quanta and the solid angle Ω. The latter is given by the quotient $\Omega = \frac{A}{L^2}$,

with A representing the active area of the detector. The probability for the detector D_2 to detect a coincident event is

$$p(D_2|D_1) = \frac{\nu_2}{n} \int_{-\infty}^{\infty} d\theta_x \, d\theta_y \left[\rho^{2\gamma}(\theta_x, \theta_y) * \epsilon_1(\theta_x, \theta_y)\right] \epsilon_2(\theta_x, \theta_y) \tag{91}$$

with the normalization

$$n = \int_{-\infty}^{\infty} d\theta_x \, d\theta_y \, \rho^{2\gamma}(\theta, \phi) \int_{-\infty}^{\infty} d\theta_x \, d\theta_y \, \epsilon_1(\theta_x, \theta_y) \int_{-\infty}^{\infty} d\theta_x \, d\theta_y \, \epsilon_2(\theta_x, \theta_y),$$

the 2γ momentum density $\rho^{2\gamma}(\theta, \phi)$ and the relative detector efficiency $\epsilon(\theta_x, \theta_y)$ in angular dimensions as seen by the γ quanta (see section 7.2). From equation (91) it can be seen that $p(D_2|D_1)$ is limited by the detector with the smaller solid angle. Using this information and assuming that the setup is symmetrical the relation stating the total probability to detect an annihilation event in coincidence can be represented by:

$$p_{\text{total}} \propto \nu^2 \frac{A}{L^2} \tag{92}$$

Thus, for a fix amount of positrons annihilating in the sample, the number of detected counts N is proportional to p_{total} and

$$\Delta U \propto \frac{L}{\nu\sqrt{A}}. \tag{93}$$

Considering equations (93) and (89) it is apparent that by changing the sample detector distance statistical accuracy can be improved at the expense of resolution. Even after a measurement resolution can be easily converted to statistical accuracy by summation over neighboring pixels for example like this: $M_{i,j}^{\text{new}} = M_{2i,2j} + M_{2i+1,j} + M_{2i,2j+1} + M_{2i+1,2j+1}$. In contrast, enhancing the resolution by lowering the statistical accuracy is never possible.

With this in mind it is possible to introduce a figure of merit Q for the quality of the measurement proportional to the inverse product of σ_Φ and ΔU:

$$Q = \frac{\nu\sqrt{A}}{\sigma_D} \propto \frac{1}{\Delta U \sigma_\Phi} \tag{94}$$

All the variables in equation (94) are merely detector dependent and thus Q is appropriate to compare different detector types with respect to their suitability for ACAR.

8.1.2 *Universal Requirements*

Although the figure of merit Q is suitable to compare different types of detectors it does not take into account three universal requirements for ACAR spectroscopy, i. e. the energy and the timing resolution, and the field of view.

To determine coincident events, timing resolution is indispensable. The better the timing resolution, the smaller the probability for an accidental coincidence which would create background. Additionally, the energy resolution will reduce

the background as it removes Compton scattered γ quanta (e. g., from lead shielding) or background radiation. However, these conditions are a sine qua non for ACAR spectroscopy and all the introduced detectors fulfill them sufficiently.

The field of view is not an essential limitation for the use of a detector although a minimum angular range of approximately 30 mrad is required for a typical ACAR spectrum (see e. g., figure 28). This means, for a certain detector size there is a maximum distance to the sample so that a full momentum range can be recorded. However, by using an array of detectors or by recording partial spectra that are afterwards put together, this limitation can be overcome [Inoue et al., 2002; Kanazawa et al., 1987]. Detailed considerations about both, timing resolution and field of view, are also reviewed by West [1995].

8.2 DETECTOR TECHNOLOGIES

Position sensitive detectors for the use of γ spectroscopy can be classified into three distinct categories, i. e. scintillation detectors, gas detectors, and semiconductor detectors. Each of the six different position sensitive detector types which will be introduced in the following section fall into one of these categories. Some of them like Anger cameras and high density avalanche chambers (HIDAC) detectors are well known, commercially available and widely used for ACAR spectroscopy. Others are the results of recent developments in detector technology and just prototypical models are available. The aim of this comparison is to outline which detectors are best suited for ACAR spectroscopy and which developments could be interesting in the future.

8.2.1 *Anger Cameras*

Anger cameras are the most common detectors for 2D-ACAR spectroscopy. They consist of a photomultiplier matrix which is optically coupled to a large scintillator crystal [Anger, 1958]. When a γ quantum hits the scintillator, the center of mass is identified electronically. In most Anger cameras the center of mass is determined by analogue electronics leading to a typical position resolution of $\mathrm{FWHM} > 4\,\mathrm{mm}$. This resolution is sufficient for the key application of Anger cameras, that is medical diagnostics. However, for 2D-ACAR an even better position resolution is desirable. Therefore, a distortion correction was developed in our group which enhanced the resolution for the Munich spectrometer to 3.5 mm [Leitner, Ceeh, and Weber, 2012]. The Anger cameras could be further improved if the multiplier signals are digitized at an earlier stage of the signal processing. This would allow a more sophisticated data treatment and make the nonlinear amplifier obsolete.

Since the different Anger cameras show only slight variations in the specific characteristics, the detectors of the Munich spectrometer are used as a general example: The camera's scintillator is a 10.5 mm thick NaI:Tl crystal with a detection efficiency of approximately 7 %. Using a lead collimator the active area is reduced to a radius of 209.6 mm. This yields a figure of merit of $Q = 7.4$.

The lead collimator has actually gone obsolete due to digital data processing and distortion correction. If the collimator is removed, the active area of the detector and thus Q could be increased. This will be done at the next revision of the spectrometer.

Both Anger cameras were bought from the Bristol positron group for 25 k€. The market price for used Anger cameras is a bit higher but ranges in the same magnitude. The increase in resolution (see section 7.1) was only possible with state-of-the-art digital electronics. This new DAQ system raised the cost by 10 k€.

8.2.2 *HIDAC Detectors*

The origin of high density avalanche chambers (HIDAC) detectors are gas filled multi wire chambers (MWC). Although MWCs provide a good spacial resolution, they have a very low detection efficiency for high energy γ radiation. By placing a converter out of a high density material into the MWC Jeavons, Charpak, and Stubbs [1975] were able to increase the detection efficiency by a factor of 6 up to 4 % for 511 keV photons. This new type of detector was then called high density proportional chamber (HDPC). In most cases, the converter is made up of a stack of alternating layers of lead and an isolating material. A pattern of holes is drilled into the converter such that electrons created by Compton scattering or photo effect can leave the converter and be accelerated by high voltage towards the wires of the chamber. The wires are arranged orthogonal to get positional information for two independent directions. In contrast to HDPCs, HIDACs yield only very limited energy information due to the avalanche regime caused by a higher accelerating voltage between converter and wires. However, the higher voltage increases the time resolution.

A first 2D-ACAR spectrometer with this technology has been setup in Genève in the early 1980ies [Bisson, Descouts, and Dupanloup, 1982]. The spectrometer's unique characteristics was the excellent angular resolution of 0.24 mrad and 0.30 mrad (FWHM) in x- and y-direction, respectively, which is a direct consequence of the good position resolution of 1 mm. Recently a new spectrometer has been set up setup with two HIDACs in Bristol [Dugdale et al., 2013]. It was reported that the active area is 290 mm × 280 mm with a detection efficiency of 12.5 % and a position resolution of 0.96 mm leading to a $Q = 35.6$. The total costs for the spectrometer were in the order of 300 k€.

8.2.3 *GEM Detectors*

Gas electron multiplier (GEM) detectors are closely related to the HIDAC detectors as they are a relatively new development of gas detectors [Sauli, 1997]. In contrast to wires, GEM detectors use 50 µm thin Kapton foils coated with conductive copper layer of 5 µm thickness. These GEM foils are perforated by a pattern of holes with a diameter of 70 µm and a pitch of 140 µm. The large electric field inside these holes causes the electrons to be accelerated resulting in the creation of secondary electrons. The ratio of primary to secondary electrons is typically in the range of 10^2 to 10^3. Using a stack of three foils it can even be increased to 10^4. At present,

GEM technology is actively developed at CERN for the use in particle detectors. For comprehensive information about GEM detectors see e. g., [Sauli, 2011].

Although the detection efficiency of GEM detectors for γ ray is very low, some attempts were made to use them in medical imaging [da Luz et al., 2014]. For high energetic γ rays the detection efficiency is even worse, although some techniques were reported to resolve this issue. E. g., Koike et al. were able to reach efficiencies of ca. 0.7 % (for 141 keV radiation) by coating the first GEM foil with a thin layer of gold [Koike et al., 2011]. Rutzinger in contrast used a stack of lead and fiber glass with a hexagonal pattern of holes which lead to a total detection efficiency of 1.56 % [Rutzinger, 2012]. In this study, the position resolution was only 7.8 mm due to prototypical character of the read-out. If used for X-ray imaging, GEMs were reported to exhibit a position resolution of 100 µm [Sauli, 2001]. However, da Luz et al. [2014] just reported a resolution of 1.67 mm for low energetic γ rays of 14 keV. It is reasonable to assume that this resolution can be increased by a suitable algorithm for position reconstruction. Theoretically, a similar resolution as HIDAC detectors can be achieved, due to the analogous working principle.

The active area of the commercially available GEM foils is either $1 \times 10^4\,\mathrm{mm}^2$ or $9 \times 10^4\,\mathrm{mm}^2$. The necessary electronic readout and ADCs to operate a GEM detector can be obtained like the GEM foils from CERN. The total cost to buy the mandatory parts for a pair of detectors are approximately 30 k€. Here, the costs for the assembly are not included. Since only prototypes of GEM detectors for 511 keV γ radiation exist, no definitive number for the quality factor can be given. Taking the reported values into account, the figure of merit extends from 15.6 to 0.42. A realistic assessment for 511 keV γ radiation, assuming a position resolution of 1 mm and a detection efficiency of 1 %, yields $Q = 1.0$. Of course, Q can be enhanced by using larger foils and by stacking several detectors. Nevertheless, the ratio quality per price will stay the same (see table 5).

8.2.4 *Position-Sensitive Photomultiplier Tubes*

For scintigraphy, especially when small animals or distinct body parts like the breast are examined, compact detectors can be very handy. In this sort of applications position sensitive photo multiplier tubes (PSPMTs) based detectors rather than Anger cameras are used. Instead of conventional dynodes, PSPMT usually have dynode meshes, which linearly map the primary photoelectron onto the anode. The anode itself is segmented by wires, which are read out individually. By processing these signals, the position of the primary event can be determined (see e. g., Qi et al. [2007]).

PSPMT are generally not much larger in diameter than 10 cm. In combination with PSPMT often segmented scintillator crystals are used. However, this segmentation has some disadvantages: The layers of glue that keep the segments together reduce the detection efficiency. These layers normally have a width of 0.25 mm (see e. g., [M. B. Williams et al., 2000; Wojcik et al., 1998]). Therefore, the detection efficiency for a scintillator using segments with a feed length of 1.4 mm is by 28 % lower than for an unsegmented scintillator. Another disadvantage is the systematic error introduced by the segmentation. Although the light distribution is

approximately ten times narrower in a segmented crystal, the position resolution is only slightly better than the position resolution of an Anger Camera with an unsegmented crystal. For example Ceeh [2015] reported a position resolution of 2 mm (FWHM) with a segmentation length of 1.4 mm. This agrees well with the results of M. B. Williams et al. [2000], who reached a spacial resolution of 2.6 mm with a segmentation length of 2 mm and 140 keV γ radiation of ^{99}Tc.

The quality factor for this detector type is calculated using the data of Ceeh et al. [2016a]: In this study the PSPMT R3292 from Hamamatsu was investigated. It possesses an active area of $7.9 \times 10^3\,\mathrm{mm}^2$, which was covered by a segmented CsI scintillator consisting of 1.4 mm × 1.4 mm × 5 mm cuboids. This resulted in a position resolution of 2 mm (FWHM) and a photopeak efficiency of approximately 3.5 %, which yields a quality factor of $Q = 1.5$. One photomultiplier and the necessary electronic for digitalization are commercially available at a price of 60 k€.

8.2.5 *Micro-Channel Plate Detector with Pixalated Scintillator and Backgammon Read-out*

Although micro-channel plates (MCPs) have a long history (see e. g., Wiza [1979]), in combination with scintillators they are not nearly as common as PMTs. A MCP is essentially a particle detector that multiplies secondary electrons which are created by a primary particle. MCPs are therefore predominantly used for electron and ion detection. However, if they are equipped with a photo cathode, they also can be used similar to a PSPMT.

Currently, a MCP based position resolving detector system using pixalated scintillators and a so-called backgammon read-out [Allemand and Thomas, 1976] is developed at the Universität der Bundeswehr by Ackermann et al. [2016]. The aim of this project is to establish a position sensitive detector with high time resolution in order to conduct positron age momentum correlation measurements. The system comprises a MCP provided by Photek Image Intensifier with a diameter of 40 mm, a commercially available pixaleted $CeBr_3$ scintillator and a backgammon read-out which was manufactured at the Universität der Bundeswehr. The $CeBr_3$ crystal consists of 2.5 mm × 2.5 mm × 8 mm cuboids which are assembled in a rectangular pattern with a pitch of 3.3 mm. This yields a photopeak efficiency of 9 % at maximum and an active area of $721\,\mathrm{mm}^2$. The position resolution is merely limited by the pixel size. Therefore, the figure of merit for this type of setup is $Q = 1$. Since some of the system's components are not commercially available, just an estimated price for one detector of 100 k€ can be given [Ackermann, 2015]. This price includes the whole detector as well as the DAQ. For more details about the setup the reader is referred to Ackermann et al. [2016].

8.2.6 *Pixelated Germanium Detectors*

In the 1970ies, first experiments to build pixelated germanium detectors (PGDs) were conducted [Riepe et al., 1979]. Today, PGDs are not experimental anymore but are commercially available. By using two PGDs it is possible to resolve both the angular correlation of a pair of γ quanta and the Doppler shift of the radiation.

Hence, $\rho^{2\gamma}$ can be measured directly and does not have to be reconstructed from projections.

A setup with two identical PGDs by Ortec is currently developed within a collaboration of the TUM and the Universität der Bundeswehr by Löwe et al. [2013]. The principal item of these detectors is a high purity germanium crystal of the dimension 48 mm × 48 mm × 20 mm. It is connected with one electrode at the back side and 36 separate electrodes on the front side. The latter are deposited onto the crystal in an 6 × 6 rectangular grid. Every single one of this pixel is connected to a conventional RC amplifier. The amplified signals are separately digitized by ADCs and further processed by a PC.

In the current configuration, only events where the total photon energy is deposited in a single pixel can be processed. The photopeak efficiency of a γ quantum hitting the center of a pixel was determined in a simulation to be 7.2 %. This means that 7.2 % is the upper limit for the total efficiency since the probability for the full energy being deposited in a single pixel decreases if the γ ray does not hit the center.

By digitizing the influence charge at neighboring pixels, a subpixel resolution of 0.95 mm can be reached. However, this reduces the active are to $1.0 \times 10^3\,\mathrm{mm}^2$ as the outermost pixel cannot be used to detect primary events.

The mean energy resolution for the pixel is 1.5 keV at 511 keV according to the manufacturer's specifications. Therefore, the energy resolution for the coincident setup should be better by a factor of $\sqrt{2}$ at best, i. e. 1 keV or 4.1 mrad. The best choice for the detector sample distance is when the longitudinal and the transversal momentum are equal. This is achieved when each detector is approximately 39 cm away from the sample. At such small distances, higher order errors also play a significant role (see appendix A.3). For more details about the characteristics of the detectors see Löwe [2016], Löwe et al. [2013], and Reiner [2015]

For the use as a 2D-ACAR spectrometer, the figure of merit is $Q = 2.4$. Since the figure of merit was constructed to check a detector's suitability for ACAR, it takes only the detector's position resolution into account and ignores the high energy resolution. The price for the two detectors including the necessary electronics is approximately 530 k€, which makes it the most expansive detector system in this comparison.

8.3 CONCLUSION

Obviously, some of the introduced detector types have not been developed for 2D-ACAR spectroscopy. PGDs e. g., have an energy resolution which allows them to perform direct measurements of the fully 3D TPMD directly while the MCP detector was particularly developed to possess a very good timing resolution. The figure of merit ignores these important quantities taking into account only the position resolution. However, the aim of this comparison is specifically to identify the most suited detectors for 2D-ACAR spectroscopy and to determine how a certain detector type has to be improved in order to compete with already existing position sensitive detectors.

Detector Type	A (mm²)	ν	σ_D (mm)	Q	Price (k€)	$\frac{Q}{Price}$ ($\frac{1}{k€}$)
Anger Camera	138×10^3	0.07	3.5	7.4	35	0.21
HIDAC Detector	81×10^3	0.13	1.0	35.6	300	0.1
GEM Detector	10×10^3	0.01	1.0	1.0	30	0.03
PSPMT	7.9×10^3	0.035	2.0	1.6	120	0.015
MCP	721	0.09	2.5	1.0	200	0.005
PGD	1.0×10^3	0.072	0.95	2.4	530	0.005

Table 5: Characteristic parameters of different types of detectors: active area A, detection efficiency at 511 keV ν, position resolution σ_D, figure of merit Q and estimated price for a pair of detectors. The last column gives the quality per price, which is a good basis for deciding which detectors to buy.

From a quick comparison of the figure of merit Q in table 5 the most suitable detector for 2D-ACAR is apparently the HIDAC type. This type of detector has by far the highest detection efficiency and a very good position resolution of 1 mm. A similar position resolution is listed for the GEM detectors. Although no GEM detector for 511 keV has been reported yet having a resolution as low as 1 mm, it nevertheless seems reasonable since both detector types have a very similar working principle. The higher detection efficiency of the HIDAC spectrometer in Bristol could only be reached by stacking several modules. Of course this approach won't influence the quality per price. In the end, to compete with HIDAC detectors, GEM modules do not only have to reach a resolution of 1 mm but they also have to get cheaper by a factor of 3.

The most cost efficient detector type are the Anger cameras. They are manufactured for medical applications by e. g., Siemens Healthcare or GE Healthcare and sold for large sums of money. However, used Anger cameras can be acquired from second hand retailer to moderate prices. E. g., an identical pair of Anger cameras costs around 50 k€. This is of course twice as expensive as the initial purchase from the Bristol group and lowers the cost efficiency. Nevertheless, Anger cameras stay the most cost efficient detectors by nearly a factor of two. A further advantage which can not be simplified to a figure of merit is the long term stability. As ACAR measurements take quite long, usual timescales are in the order of weeks, it is necessary that the detector characteristics stay constant for this duration. While Anger cameras guarantee stability for weeks and months, gas detectors require constant supervision and care to ensure a stable operation. In particular HIDAC detectors are also prone to wire breaks.

Although the PSPMTs have a similar cost efficiency as the GEM detectors, they have not the same potential to improve neither in terms of performance nor in terms of price, because: i) PSPMTs are a niche product, thus PMT producing companies will not invest vast money in enhancing the technology. Furthermore the low production quantity keeps the prices high. ii) PSPMTs are only developed by a few specialized companies and not by public research facilities. However, the prices for electronic read-outs have declined in the recent years. As half of the price

for a PSPMT setup is caused by the electronics, the cost efficiency may increase up to a factor of approximately two at maximum.

In terms of figure of merit, both the MCP based detector and the PGD perform quite well. Still, in terms of quality per price both types are two orders of magnitude worse than Anger cameras. For this reason it would be a waste of money to use these detectors for 2D-ACAR spectroscopy alone. In the future, technical developments making these detectors competitive are thinkable. However, the technological lead of other detectors makes it rather unlikely that this will happen in the near future.

This comparison of the detector technologies leads to the conclusion that nowadays the most ideal detectors in terms of cost efficiency and in terms of stability are Anger cameras. Since Anger cameras still possess the potential for improvements, especially with respect to position resolution, it is reasonable to concentrate the efforts on this type of detector. In particular, since already a working 2D-ACAR setup based on Anger cameras exists in Munich, an improvement of the cameras would automatically lead to a scientific gain.

Part III

RECONSTRUCTION OF 3D DENSITIES FROM PROJECTIONS

9

OVERVIEW OF METHODS FOR THE RECONSTRUCTION OF 3D DENSITIES FROM PROJECTIONS

The development of computerized tomography (CT) resulted in an enormous progress for numerous fields such as archeology, engineering, biology, but especially medical diagnostics. As a consequence, in 1979, the Nobel Prize in 'Physiology or Medicine' was awarded to the two men who were essential for the developing of CT technology. One of them, Godfrey Hounsfield, worked on the first commercially CT scanner as an electrical engineer at EMI [Hounsfield, 1973]. Hounsfield shared the Nobel Prize together with the physicist Allan Cormack who introduced a mathematical algorithm to reconstruct 3D densities from its projections [Cormack, 1963, 1964].

Although it was awarded with the Nobel Price, Cormack's answer to the tomography problem was neither the first solution nor the last. In the following chapter an overview of reconstruction methods for CT shall be given, albeit CT and the reconstruction from projections of the TPMD are quite distinct problems: By definition CT is the reconstruction of two dimensional slices from projections onto lines while the reconstruction of TPMDs from planes of projections is in first instance a fully three-dimensional problem. However, the latter can be simplified to a reconstruction of independent slices if one accepts to neglect information obtained from the measurement. This is exactly the way conventional approaches treat 2D-ACAR data.

9.1 THE RADON TRANSFORM

In 1917, Radon published his work about a special integral transformation which is usually called the basis for CT [Radon, 1917]. The so-called Radon transform $\mathfrak{R}(f)(p,\phi) = F(p,\phi)$ of a function $f(x,y)$ is defined as:

$$F(p,\phi) = \int_{-\infty}^{\infty} f(p\cos\phi - s\sin\phi, p\sin\phi + s\cos\phi)\, ds \tag{95}$$

An example of the Radon transformation for a specific angle ϕ is depicted in figure 29.

In X-ray CT a single measurement $M_\alpha(p)$ using a X-ray source with intensity I_0 in parallel beam geometry at a projection angle α can be expressed as an integration over the attenuation coefficient $\mu(x,y)$ of the sample:

$$M_\alpha(p) = I_0 \exp\left\{-\int_{-\infty}^{\infty} ds\ \mu(p\cos\alpha - s\sin\alpha, p\sin\alpha + s\cos\alpha)\right\} \tag{96}$$

Therefore, the whole set of measurements $M(p,\alpha)$ for different projection angles α is given by the Radon transformation of $\mu(x,y)$:

$$M(p,\alpha) = I_0 e^{-\mathfrak{R}(\mu)(p,\alpha)} \tag{97}$$

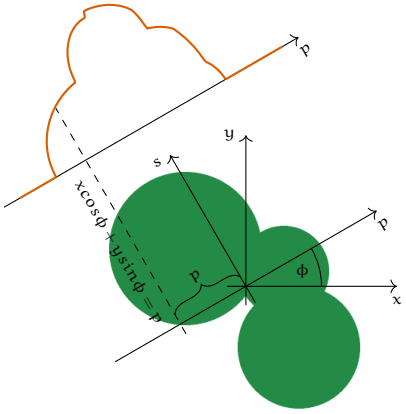

Figure 29: Example of a projection of the green density at an angle α: The orange curve represents the projection which is obtained by integration along the rotated coordinate axis s.

While the Radon transformation in general is a continuous transformation, a CT scan in contrast can sample only a finite number of projection angles. This discretization inevitably leads to a loss of information about the original density. In medical imaging, however, this effect is insignificant compared to the actual resolution of the X-ray detector.

Radon himself already developed an analytical method to invert the integral transformation. His solution utilizes the mean of the tangential lines of a circle around the center $P = (x, y)$ with radius q in f space:

$$\bar{F}_P(q) = \frac{1}{2\pi} \int_0^{2\pi} d\phi \; F(x\cos\phi + y\sin\phi + q, \phi) \tag{98}$$

He was able to show that the original function $f(P)$ can be recovered by calculating

$$f(P) = \frac{1}{\pi} \lim_{\epsilon \to 0} \left(\frac{\bar{F}_P(\epsilon)}{\epsilon} - \int_\epsilon^\infty \frac{\bar{F}_P(q)}{q^2} dq \right) \tag{99}$$

This elegant solution is however useless for real applications as the inevitable experimental noise will introduce severe artifacts. The first one who came up with a practicable solution to the problem of image reconstruction was Cormack [1963, 1964]. Unaware of Radon's work, Cormack developed a stable method to recover a 2D density from a discrete set of projections. His initial intention was to measure the absorption coefficient of the human body for a better dose quantification in radiological therapy [Cormack, 1995]. Although Cormack's work remained relatively unnoticed for a while, several other scientists began, independent of Cormack, to develop methods for reconstructing an image from projections either for medical purpose or for different fields like electron microscopy [Crowther, De Rosier, and Klug, 1970].

The breakthrough of CT came with the development of the first commercial CT scanner by Hounsfield at EMI [Hounsfield, 1973]. Hounsfield made CT available for the broad public for the first time . Since then many methods for image reconstructions have been developed and were continuously improved. In the following, the four most important algorithms to retrieve an image from its projections are introduced.

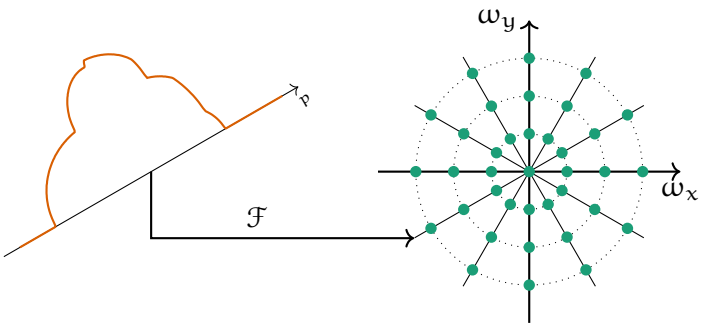

Figure 30: Example of the Fourier slice theorem: The measured projections correspond to slices in Fourier space (thin lines). Due to the radial nature of the data, the spacing between the data points (green dots) gets larger at higher frequencies.

9.2 FOURIER SLICE THEOREM

The Fourier slice theorem connects the Radon and the Fourier transform (FT). Furthermore, it can be employed to derive an algorithm to calculate a reconstruction from projections. This algorithm, often referred to as the method of direct Fourier transformation (DT), was initially used for electron microscopy to resolve the three-dimensional structure of the T4 bacteriophage's tail [Crowther, De Rosier, and Klug, 1970; De Rosier and Klug, 1968]. It can be deduced by considering the FT of a 3D density $\rho(x, y, z)$:

$$\tilde{\rho}(\omega_x, \omega_y, \omega_z) = \int\int\int \rho(x, y, z)\, e^{-i2\pi(\omega_x x + \omega_y y + \omega_z z)}\, dx\, dy\, dz \tag{100}$$

A 2D slice through the density in Fourier space for $\omega_z = 0$, can be written as

$$\tilde{\rho}(\omega_x, \omega_y, \omega_z = 0) = \int\int \left[\int \rho(x, y, z)\, dz\right] e^{-i2\pi(\omega_x x + \omega_y y)}\, dx\, dy\,. \tag{101}$$

The inner integral, $\int \rho(x, y, z)\ dz$, is a projection of $\rho(x, y, z)$ onto the z-plane and therefore equation (101) demonstrates that the FT of a projection and a plane in Fourier space are equal. Using a coordinate transformation it can be shown that this relation still holds for any projection of $\rho(x, y, z)$ (for a proof see e. g., Kak and Slaney [1988]). That means, if *all* projections of ρ are known, $\tilde{\rho}$ can be recovered and by the inverse FT of $\tilde{\rho}$, so can ρ. De facto, a finite number of projections is sufficient to get $\rho(x, y, z)$ with reasonable resolution.

Like the method of Radon, the DT is analytically exact. However, some numerical problems arise: In order to calculate $\tilde{\rho}$, a conversion from radial to Cartesian coordinates is necessary, which requires interpolation in Fourier space. This can easily introduce artifacts especially at high frequencies where the measured data gets more sparse. Partially as an effect of this interpolation, the DT is rather sensitive to experimental noise.

An advantage of the DT in the context of the recovery of the TPMD is that the crystal symmetries can be included very easily. Additionally, it is computationally not very demanding. This may be the reason why the Fourier slice theorem has been frequently used to reconstruct 2D-ACAR data [Kondo et al., 1992; Kubota et al., 1991; Suzuki et al., 1989].

9.3 FILTERED BACK-PROJECTION

The filtered back-projection (FBP) is closely related to the DT method and was introduced shortly afterwards in 1971 [Ramachandran and Lakshminarayanan, 1971]. The starting point for the derivation of the FBP is the inverse FT of $\rho(x, y)$:

$$\rho(x, y) = \int_{-\infty}^{\infty} \int_{-\infty}^{\infty} \tilde{\rho}(\omega_x, \omega_y)\, e^{i2\pi(\omega_x x + \omega_y y)}\, d\omega_x d\omega_y \tag{102}$$

Using the substitution $\omega_x = p\cos(\phi)$ and $\omega_y = p\sin(\phi)$ equation (102) transforms to

$$\rho(x, y) = \int_0^{2\pi} \int_0^{\infty} \tilde{\rho}(p, \phi)\, p\; e^{i2\pi p(x\cos(\phi) + y\sin(\phi))}\, dp\, d\phi. \tag{103}$$

With help of the relation $\tilde{\rho}(p, \phi + \pi) = \tilde{\rho}(-p, \phi)$, the above equation can be rewritten as

$$\rho(x, y) = \int_0^{\pi} \int_{-\infty}^{\infty} \tilde{\rho}(p, \phi)\, |p|\; e^{i2\pi p(x\cos(\phi) + y\sin(\phi))}\, dp\, d\phi. \tag{104}$$

To this formula the Fourier slice theorem can now be applied and $\tilde{\rho}(p, \phi)$ can be replaced by the FT of the measurement $\tilde{M}(p, \phi)$. In order to get a more instructive result, the inner and the outer integral are separated. The inner integral yields

$$F(t, \phi) = \int_{-\infty}^{\infty} \tilde{M}(p, \phi)\, |p|\; e^{i2\pi p t}\, dp, \tag{105}$$

and the outer one

$$\rho(x, y) = \int_0^{\pi} F(x\cos(\phi) + y\sin(\phi), \phi)\, d\phi. \tag{106}$$

These two equations inspired the name 'filtered back projection': Equation (105) weights $\tilde{M}$ with $|p|$ and transforms it back into real space, which is equivalent to a Fourier filter. The back projection part is done by equation (106). For a fixed ϕ and without the integration, all points (x, y) on a straight line which fulfill the condition $r = x\cos(\phi) + y\sin(\phi)$ will have the same value. In other words, $F(t, \phi)$ is smeared out on the reconstruction - i. e. projected back - along the direction of projection.

Equation (105) is a multiplication in Fourier space, which is equivalent to a convolution in real space. Thus, once the FT of $|x|$ is computed no further FT is needed during the reconstruction. For this reason, the FBP was originally called 'convolution method' by Ramachandran and Lakshminarayanan. However, due to fast FT algorithms it is nowadays often more efficient to calculate a convolution as a multiplication in the Fourier domain. Even then the FBP has the advantage that interpolation in Fourier space, which usually introduces severe artifacts, is avoided.

The FBP is not able to take into account the statistical nature of measured data. Especially the filtering with $|p|$ leads to an amplification of high frequency noise. In order to suppress this noise, several different kind of filter algorithms have been developed (see e. g., Shepp and Logan [1974]).

For a long time, the FBP was the method of choice for medical CT [Kak and Slaney, 1988] as it is very fast and stable if the data quality, in terms of statistics, is

high. Since high statistics in the data is accompanied by a high radiation dose for the patient, the FBP has nowadays been replaced by more flexible reconstruction methods.

In the first days of 2D-ACAR spectroscopy, the FBP has been employed frequently to reconstruct the TPMD (see e. g., Farmer et al. [1979]). Manuel [1982] who measured the FS of V and V_3Si was even able to include the symmetry information of the crystal and performed a full three-dimensional reconstruction (details are given by Jarlborg, Manuel, and Peter [1983]). However, for latter studies, the FBP has been replaced by the Cormack's method (CM) due to its consistent treatment of experimental noise.

9.4 CORMACK'S METHOD

The main idea behind Cormack's method (CM) of reconstructing is to expand the measurement into a set of orthogonal functions with known inversion from Radon space to real space. Cormack started by expanding the measurement $M(p, \alpha)$ under the angle α and the underlying density in polar coordinates $\rho(r, \phi)$ into a Fourier series:

$$\rho(r, \phi) = \sum_{n=-\infty}^{\infty} \rho_n(r) e^{-i\phi n} \tag{107}$$

$$M(p, \alpha) = \sum_{n=-\infty}^{\infty} M_n(p) e^{-i\alpha n} \tag{108}$$

with the expansion coefficients $\rho_n(r)$ and $M_n(p)$ given by

$$\rho_n(r) = \frac{1}{2\pi} \int_0^{2\pi} \rho(r, \phi) e^{-in\phi} \, d\phi \tag{109}$$

$$M_n(p) = \frac{1}{2\pi} \int_0^{2\pi} M(p, \alpha) e^{-in\phi} \, d\alpha \tag{110}$$

With some mathematical effort he was able to show that the expansion coefficients for the density can be calculated using the expansion coefficients for the measurement [Cormack, 1963]:

$$\rho_n(r) = \frac{1}{\pi} \frac{d}{dr} \int_0^r \frac{M_n(p) T_n(r/p)}{\sqrt{r^2 - p^2}} \, dp \tag{111}$$

with the Chebyshev polynomials of the first kind, $T_n(x)$. Although this result is analytically exact it has in practice some disadvantages, especially since it requires numerical integration and differentiation. Cormack was aware of these problems and even found two ways to circumvent them. By expanding the expansion coefficients $\rho_n(r)$ and $M_n(p)$ themselves and using several integral transformations Cormack found two different relations [Cormack, 1964].

First Relation

If the $M_n(p)$ are expanded in

$$M_n(\cos\Psi) = 2\sum_{l=0}^{\infty} a_n^l \sin\left[(n+2l+1)\,\Psi\right] \tag{112}$$

using the substitution $p = \cos\Phi$, the coefficients of $\rho(r,\phi)$ can be calculated by

$$\rho_n(r) = \sum_{l=0}^{\infty} (n+2l+1)\, a_n^l R_n^l(r) \tag{113}$$

using the Zernicke polynomials R_n^l. This result is only valid inside the unit circle. However, since most problems can be mapped to the unit circle, this poses no limitation on the solution.

Second Relation

Here the coefficients are expanded with help of the Hermite polynomials $H_m(p)$:

$$M_n(p) = e^{-p^2} \sum_{l=0}^{\infty} b_n^l H_{n+2l}(p) \tag{114}$$

$$\rho_n(r) = \frac{e^{-r^2}}{\sqrt{\pi}} \sum_{l=0}^{\infty} (-1)^l 2^{n+2l}\, l!\, b_n^l S_n^l(r) \tag{115}$$

For simplicity reasons Cormack defined the polynomials $S_n^l(r)$ with help of the Laguerre polynomials L_{2l}^n:

$$S_n^l(r) = r^n L_{2l}^n(r^2) \tag{116}$$

Compared to equation (111), the reconstruction now becomes more or less an expansion into orthogonal functions. Thus, the statistical accuracy of the data can be taken into account very easily. Furthermore symmetries can also be included by choosing the right n for expansion [Kontrym-Sznajd, 1990]. Due to both of these reasons, CM is frequently employed for the reconstruction of ACAR data.

Since the symmetry plays an important role in the reconstruction of the TPMD, the CM has been slightly modified for this purpose. Instead of a Fourier expansion, often an expansion in lattice harmonics[1] is used to include the crystal symmetry more easily (see e. g., Mijnarends [1967] for 1D-ACAR and Louis M. Pecora [1987] for 2D-ACAR). To this day, many ACAR studies employing the CM method exist (for the most recent see Haynes et al. [2012]). However, it is not possible to incorporate the *full* crystalline symmetry with this method, as only 2D slices are reconstructed. Moreover, the CM is only stable for a relatively small basis, which means that sharp edges will become smoothed inevitably. Hence, it is not suited very well to detect the sharp discontinuities of the Fermi breaks.

1 Orthogonal functions with the symmetry group of the crystal lattice.

9.5 THE ALGEBRAIC RECONSTRUCTION TECHNIQUES

All the reconstruction methods mentioned above have one thing in common: they are analytically exact if i) the statistics is infinitely good ii) the resolution is homogeneous iii) the discretization of the measurement is infinitesimal small and iv) an infinite number of projections is measured. In an ACAR measurement none of these requirements are fulfilled exactly. The measurements M_p^α are taken at a finite number of crystal orientations α and for a finite number of pixels p. Hence M_p^α is not continuous in p and α in contrast to the derivation by Cormack (compare equation (108)). The statistical accuracy is limited by the duration of the measurement and the resolution of the spectrometer is not homogeneous due to the positron spot size on the sample. Similarly, a reconstructed density is also discretized in pixels, $\rho(x,y) = \rho_{x,y}$ or voxels, $\rho(x,y,z) = \rho_{x,y,z}$. In the following, only one index will be used for ρ as 2D data or 3D data can be rearranged in a one dimensional way.

Instead of using integrals to describe the measurements, it is now more convenient to formulate the projection of a density ρ_i as an algebraic equation with a linear projection operator $\mathbf{R}$:

$$M_p^\alpha = \sum_i R_{pi}^\alpha \rho_i \Leftrightarrow \mathbf{M}^\alpha = \mathbf{R}^\alpha \boldsymbol{\rho} \tag{117}$$

This approach was introduced as algebraic reconstruction technique (ART) by Gordon, Bender, and Herman [1970]. The basic principle soon grew into a multitude of techniques to handle reconstruction problems using the common concept of inverting equation (117) by means of linear algebra (see Herman and Lent [1976] for an early review). Although this could be done by matrix inversion, most of the methods employ an iterative approach because of the high dimensionality of the problem.

ART based algorithms have not been used in medical imaging for a long time, since they require more memory and computation time than e. g., the FBP. Until the mid 1990s, this was an important argument for using the FBP, but as computational power increased, this advantage became irrelevant.

The ART has the great advantage that it is very flexible. Not only the statistical error of the data can be taken into account during the reconstruction, but also systematic errors such as background or distortions can be included. Moreover, prior knowledge about the object can also be used to increase the quality of a reconstruction (see e. g., Schrapp [2015]).

Using the ART, the quality of the reconstruction is always getting better the more information is used. In contrast, adding a projection with very low statistics can worsen the result of a reconstruction if done with DT, FBP or CM. In medical imaging, this can be crucial if the patient has metallic implants which absorb much more radiation than bone or soft tissue and thus parts of the projection have a very low statistical accuracy.

Based on the aforementioned reasons, the ART was chosen in this thesis for the reconstruction of the TPMD from ACAR measurements. Thereby, it was possible to include the full 3D symmetry of the problem, which greatly increased the quality

of the reconstruction. For the details of the implementation see the following chapter.

10 NOVEL ALGORITHM FOR THE 3D RECONSTRUCTION OF $\rho^{2\gamma}$ FROM ACAR DATA

Although ARTs have very rarely been used in connection with ACAR spectroscopy (see e. g., Pylak, Kontrym-Sznajd, and Dobrzyński [2011] and Weber et al. [2015, 2013, 2014]) there are several important reasons to apply them. ARTs can not only take into account the statistical accuracy of the measured data, but also the crystal symmetry, the experimental resolution and the detection efficiency in momentum space of the experimental setup. Almost any prior knowledge can be included to increase the quality of a reconstruction.

In the following sections, a novel ART algorithm for the reconstruction of 2D-ACAR data is presented. At first, the theoretical concept of the algorithm is introduced, then details about the numerical implementation are given and finally different regularization functionals are compared on theoretical ACAR data.

10.1 MATHEMATICAL PRINCIPLES

As for any ART, the starting point for the reconstruction is a projection operator $\mathbf{R}^{\alpha}$ which projects a three-dimensional density $\boldsymbol{\rho}$ along the direction in space α onto a plane. In the present approach $\mathbf{R}^{\alpha}$ takes into account the full crystal symmetry of the problem. This increases the complexity as $\mathbf{R}^{\alpha}$ projects from the three-dimensional irreducible wedge of $\boldsymbol{\rho}^{2\gamma}$ onto a plane. Conventional CT algorithms, however, only need to consider projections from planes to lines.

One of the difficulties of this approach is the anisotropy of the resolution function of the spectrometer. The resolution function has a Gaussian shape, however the standard deviation is different for x- and y-direction, $\sigma_x > \sigma_y$, due to the positron spot size on the sample (see appendix A.3). The anisotropic resolution lowers the symmetry of the measurement and causes contradictions during a reconstruction procedure if a higher crystal symmetry is assumed. One way to solve this issue is to adjust σ_y by convolving the measurement in y-direction by a Gaussian with width of $\sigma = \sqrt{\sigma_x^2 - \sigma_y^2}$ [Falub, 2002]. The drawback of such a strategy is a loss of valuable experimental resolution.

Another strategy is to deconvolve the measurement prior to reconstruction [Fretwell et al., 1995]. In such a way σ_x and σ_y can be matched. However, it is never possible to reverse the effects of the experimental resolution entirely. Therefore, one may end up again with an unsymmetrical picture after deconvolution. Moreover the statistical nature of the data is not conserved during this process. This is particularly undesirable since the statistical information is still needed for the reconstruction itself. The method developed here uses none of the above mentioned ideas. Instead it employs the fact that a convolution with the resolution can be expressed by a linear operator $\mathbf{C}$. Due to a simple multiplication the experimental resolution becomes a part of the projection.

For the reconstruction, it is necessary to take into account the detection efficiency in momentum space of the setup. Usually this is done beforehand by dividing the spectra with the MSF. In this case, the statistical information has to be stored separately. Hence, it is much more convenient to encode the detection efficiency into a linear operator $\mathbf{S}$ and combine it with the projection. Finally a scaling constant c can be used to account for the number of counts that were recorded in a spectra.

All introduced refinements can be merged into a single linear operator $\mathbf{T}^\alpha$, which is not a simple projection operator anymore but a representation of the actual measurement:

$$\mathbf{M}^\alpha = \mathbf{T}^\alpha \boldsymbol{\rho} = c\mathbf{S}\mathbf{C}\mathbf{R}^\alpha \boldsymbol{\rho} \tag{118}$$

Although $\mathbf{M}^\alpha$ is fairly easy to compute by means of equation (118), the inverse problem, i. e. the calculation of $\boldsymbol{\rho}$ is not as trivial, especially since the dimensionality of the problem does not allow a direct inversion of $\mathbf{T}$. If the matrix $\mathbf{M}^\alpha$ is of the size $I \times I$ then $\boldsymbol{\rho}$ has a size in the order of $I \times I \times I$. Therefore, the inverse problem is, for a typical amount of measured projections, always under-determined even if the crystal symmetry is taken into account.

If the measurement's uncertainties $\boldsymbol{\sigma}^\alpha$ follow a Gaussian distribution, the reconstruction $\mathbf{x}$ maximizing the likelihood can be found by a least squares approach. Although, the uncertainties follow a Poisson rather than a Gaussian distribution, the least squares method will nevertheless maximize the likelihood as the sample size (i. e. the number of counts in a pixel) is large. The least squares function can be written in the following ways:

$$\chi^2(\mathbf{x}) = \sum_\alpha \sum_i \frac{\left(M_i^\alpha - \sum_j T_{ij}^\alpha x_j\right)^2}{(\sigma_i^\alpha)^2} \tag{119}$$

$$= \sum_\alpha \left(\mathbf{M}^\alpha - \mathbf{T}^\alpha \mathbf{x}\right) \mathbf{W}^\alpha \left(\mathbf{M}^\alpha - \mathbf{T}^\alpha \mathbf{x}\right)^T \tag{120}$$

The weighting matrix $\mathbf{W}$ is zero except for the values of $\frac{1}{\sigma_i^2}$ on its diagonal.

Be N the number of measured data points. If $\mathbf{x}$ is in agreement with the statistical accuracy then

$$\chi^2(\mathbf{x}) \approx N \tag{121}$$

in accordance with the Chi-squared distribution. As the reconstruction problem is under-determined, there are many reconstructions $\mathbf{x}$ which satisfy equation (121). There may be even $\mathbf{x}$ with $\chi^2 << N$ which 'overfit' the data. Therefore, a regularization function $g(\mathbf{x})$ can be chosen as an additional constraint. The function $g(\mathbf{x})$ reflects any prior knowledge about $\boldsymbol{\rho}$ that the reconstruction should fulfill. Using the Lagrange multiplier λ a new function $f(\mathbf{x})$ can be defined:

$$f(\mathbf{x}) = \chi^2(\mathbf{x}) + \lambda g(\mathbf{x}) \tag{122}$$

The correct solution $\hat{\mathbf{x}}$, satisfying equation (121) and the constraints $g(\mathbf{x})$ can be expressed by the following optimization problem.

$$\hat{\mathbf{x}} = \arg\min_{\mathbf{x}} f(\mathbf{x}) = \arg\min_{\mathbf{x}} \left(\chi^2(\mathbf{x}) + \lambda g(\mathbf{x})\right) \tag{123}$$

In this thesis an iterative method is chosen to solve this optimization problem since finding a direct numerical solution is impossible on present PCs because of the large size of $\mathbf{T}$. Another reason is that the iterative procedure allows $g(\mathbf{x})$ to be nonlinear.

The basic idea of the iterative method is to calculate the gradient of $f(\mathbf{x})$ and to search for $\hat{\mathbf{x}}$ in the direction $-\nabla f(\mathbf{x})$. From the equations (119) and (122) it follows

$$\frac{\partial f}{\partial x_k} = \sum_{\alpha} \sum_{i} -2 \frac{\left(M_i^{\alpha} - \sum_j T_{ij}^{\alpha} x_j\right) T_{ik}^{\alpha}}{(\sigma_i^{\alpha})^2} + \lambda \frac{\partial g}{\partial x_k} \tag{124}$$

and

$$\nabla f(\mathbf{x}) = \sum_{\alpha} -2 \left(\mathbf{M}^{\alpha} - \mathbf{T}^{\alpha}\mathbf{x}\right) \mathbf{W} (\mathbf{T}^{\alpha})^{T} + \lambda \nabla g(\mathbf{x}). \tag{125}$$

Hence, the computational effort to calculate ∇f is not much larger than calculating f.

$\hat{\mathbf{x}}$ can now be obtained by the following iterations starting with an initial guess $\mathbf{x}_0$:

$$\mathbf{x}_{n+1} = \mathbf{x}_n - a \nabla f(\mathbf{x}_n) \tag{126}$$

The parameter a has to be determined in every step by a line search.

Instead of searching for $\hat{\mathbf{x}}$ directly in the direction of $-\nabla f$ it is often beneficial for the convergence speed to include the curvature of $f(\mathbf{x})$ into the iterations. However, in this case the Hessian matrix is very large and takes a considerable amount of computer memory. Therefore, the physical inspired model of a ball moving with friction in the potential landscape of ∇f is used. In every iteration step the velocity of the virtual ball $\mathbf{v}$ is calculated based on the time interval Δt and the friction coefficient μ:

$$\mathbf{v}_{n+1} = (\mathbf{v}_n - \nabla f(\mathbf{x}_n))\, e^{-\mu \Delta t} \tag{127}$$

Hence, the next position of the virtual ball can be obtained by

$$\mathbf{x}_{n+1} = \mathbf{x}_n + \mathbf{v}_{n+1} \Delta t. \tag{128}$$

Both Δt and μ are fixed during the calculation. They should be selected to achieve a moderate convergence speed since a too high speed may result in the algorithm not converging at all. However, an approximate guess for Δt and μ is enough as $\hat{\mathbf{x}}$ does not depend on this choice.

The last parameter to be determined is the Lagrange multiplier λ. It can be obtained during the minimization routine by choosing a high value and lowering it until the expected value of χ^2 is reached.

10.2 NUMERICAL IMPLEMENTATION

As computer power increased, so grew the possibilities to do more and more complex calculations. Nowadays, the challenge in programming is to formulate a mathematical problems efficiently in order to exploit the power of the computing machine. However, the most potent programming frameworks in terms of calculation speed are often not the most convenient for a programmer and thus the time

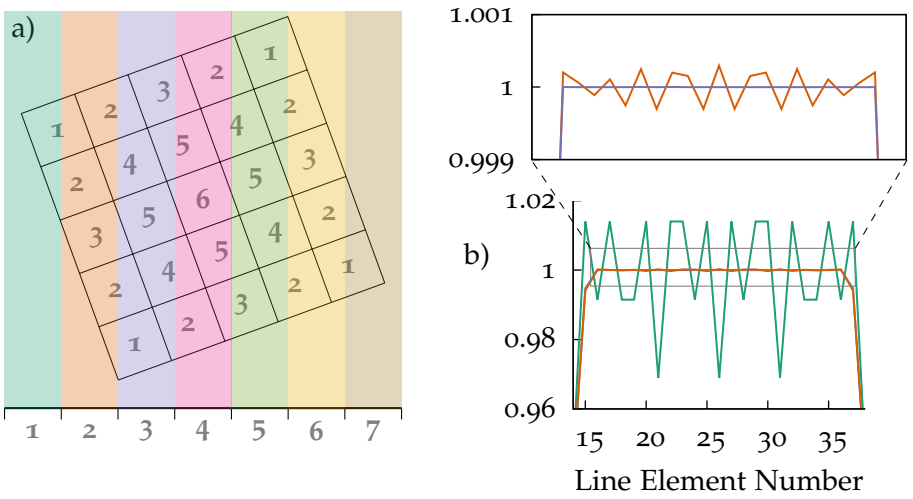

Figure 31: a) Assignment of picture elements to line elements. The numbers indicates which pixel element is mapped to which line element. By the symmetrical numbering, symmetries in $\mathrm{rho}^{2\gamma}$ can be taken into account. b) Comparison between different projection methods illustrated by the projection of a homogeneous square, ■: on the basis of the center, ■: by linear interpolation, ■: by analytical weighting. The enlargement does only show the two latter methods.

gain in calculation speed is compensated by the longer time it takes to write and debug a program. Therefore, in this thesis the programming package `GNU Octave` is used [Eaton et al., 2015] as it is very fast and programs are easy to debug since `Octave` is a script language. Furthermore, it treats every variable as a matrix, which means that the previously introduced algorithm can be realized in an elegant way. Finally it is open software, so everyone can freely use already published scripts.

Basically, there are three options to carry out the operations of equation (118) on a PC: If the operators are implemented as matrices they can either be calculated and loaded into memory before the actual calculations begins or they are created right in time, just when they are needed. The third option is to perform the operations directly without the use of a linear operator. If the machine is equipped with enough main memory the first option is usually the fastest. In this thesis, a mixture of option one and three is used.

The main challenge is to construct the projection operator $\mathbf{R}^{\alpha}$, which stores the assignment of volume elements in $\mathbf{x}$ to picture elements in $\mathbf{M}^{\alpha}$. An example of such an exercise for the 2D case, i. e. the assignment of picture elements to line elements, is illustrated in figure 31 a).

The most simple procedure would be to take the center of each pixel and assign it to the line element with the same x-coordinate. An example of this method [■ in figure 31 b)] demonstrates that it is not very exact and results in severe aliasing artifacts. By splitting the value of a pixel between neighboring line elements weighted by the distance line-element-center to pixel-center, a much better result can be obtained [see ■ curve in figure 31 b)]. Although artifacts are greatly reduced, there are still visible errors as can be seen in the enlargement in figure 31 b). This so-called Moiré effects are caused by the shape of the turned pixel. The color coding in figure 31 a) indicates which fraction of a pixel has to be added to which line element. Clearly, the assignment of pixel fraction to line element is not a lin-

ear function of the center of the pixel but rather a continuous but not differentiable function. It can be given analytically by a sectional definition. This approach was used to generate the violet curve in the enlarged section of figure 31 b). As can be seen, this method greatly improves the quality of the projection.

For a 3D projection, the correct distribution of pixel fractions to line elements is much more difficult than in the 2D case due to the larger degrees of freedom of a cube compared to a square. As defining an analytical function to solve the aliasing problem gets also very complex in 3D, an alternative way has been chosen. Instead of defining a function, a lookup table is created in the following way:

At first a cube with edge length of m voxels and a constant density of $\frac{1}{m^3}$ is defined. It is rotated using linear interpolation and projected onto a plane by summation over one dimension. Afterwards, this projection is convolved with a square with an edge length of m pixels and an areal density of 1. The result is a lookup table to determine the correct weighting factor on the basis of the center position.

In addition to the aliasing difficulty, figure 31 a) also demonstrates how symmetries can be included into the projection tensor $\mathbf{R}$, namely by indexing the pixels respectively voxels in a symmetric way. This will reduce the size of the projection tensor and hence the memory needed to store $\mathbf{R}$. Using 31 a) as an example it can be seen that without symmetries $\mathbf{R}$ would be a matrix of the size 7×25, while with the inscribed four-fold symmetry the size is decreased to 7×6. For a full cubic symmetry the size of $\mathbf{R}$ is reduced by $\frac{1}{48}$ at maximum.

However, even if one takes advantage of a high symmetry, the size of $\mathbf{R}$ is considerable. Without symmetries assuming an edge length of the reconstruction $\mathbf{x}$ of 300, $\mathbf{R}$ would have 300^5 entries and would allocate 19 TB with the `Octave` standard data type. Nevertheless, only a small part of these entries carries real information since one voxel is assigned to a very limited number of pixels and most of the other elements of $\mathbf{R}$ are zeros. For this special kind of problem the concept of sparse matrices has been employed.

Compared to a conventional matrix which allocates a continuous memory block regardless of the value of the elements, a sparse matrix only stores the nonzero elements. This has the disadvantage that inserting new nonzero elements takes more time. However, the memory usage is highly reduced and thereby the storing of projection matrices gets feasible. In order to further decrease the memory usage, matrix elements were rounded such that elements smaller than 10^{-10} were set to zero. The numerical error induced by this rounding is negligible, however the size of matrix decreased by approximately $\frac{1}{4}$ for some projections.

A further benefit of sparse matrices is that less computation time is needed to calculate a product of two matrices or of a matrix and a vector. While in a standard matrix multiplication the element-wise multiplication of every element is evaluated even for the zero elements, the sparse matrix multiplication skips these operations. In order to speed up this process even further, a compiled function was written by means of the `Octave` `C++` interface. This doubled the multiplication speed on the used PC.

As pointed out before, the convolution matrix $\mathbf{C}$ and the projection matrix $\mathbf{R}^\alpha$ can be merged by multiplication. However, the convolution smears out the ele-

ments of $\mathbf{R}^{\alpha}$ raising the number of the nonzero elements. Therefore, a sequential execution of the operators is preferable. Actually, it is of advantage not to implement $\mathbf{C}$ as a matrix at all but rather to execute a fast Fourier transform convolution instead. Since the kernel of the convolution does not change it can be held in memory once it has been Fourier transformed. If $\hat{\mathbf{K}} = \mathcal{F}\{\mathbf{K}\}$ is the FT of the convolution kernel, then the convolution step can be written as

$$\mathbf{C}\left(\mathbf{R}^{\alpha}\mathbf{x}\right) = \mathcal{F}^{-1}\left\{\hat{\mathbf{K}} * \mathcal{F}\{\mathbf{R}^{\alpha}\mathbf{x}\}\right\}, \tag{129}$$

with $*$ denoting an element-wise multiplication. Although the right side of equation (129) might seem more complex it can actually be computed much faster than the left side.

The last two factors in equation (118) are easy to obtain: $\mathbf{S}$ is a diagonal matrix with the elements of the MSF. The MSF is determined from the measured single spectra separately for every projection (see section 7.2). Therefore, in order to take thermal changes and shadowing effects into account $\mathbf{S}$ is dependent on the angle and is actually $\mathbf{S}^{\alpha}$. Finally, c is determined as the number of counts in the measured spectra.

Since $\mathbf{T}^{\alpha}$ is known, the transposed operation, which is needed for equation (125) is given by

$$(\mathbf{T}^{\alpha})^{\mathsf{T}} = (c\mathbf{S}\mathbf{C}\mathbf{R}^{\alpha})^{\mathsf{T}} = c(\mathbf{R}^{\alpha})^{\mathsf{T}}\mathbf{C}^{\mathsf{T}}\mathbf{S}^{\mathsf{T}}. \tag{130}$$

As $\mathbf{C}$ is symmetric and $\mathbf{S}$ is diagonal, the above equation simplifies to

$$(\mathbf{T}^{\alpha})^{\mathsf{T}} = c(\mathbf{R}^{\alpha})^{\mathsf{T}}\mathbf{C}\mathbf{S}. \tag{131}$$

These equations imply that the deviation between measurement and projected reconstruction of equation (125) are again weighted by the momentum sampling function, convolved with the experimental resolution and then smeared out over the reconstruction by $(\mathbf{R}^{\alpha})^{\mathsf{T}}$.

Although using $(\mathbf{R}^{\alpha})^{\mathsf{T}}$ will find the solution of equation (123), it was found that a renormalization of $(\mathbf{R}^{\alpha})^{\mathsf{T}}$ will increase the stability and the convergence speed of the algorithm. As $\mathbf{R}^{\alpha}$ takes several elements of $\mathbf{x}$ and adds them up, each column of $\mathbf{R}^{\alpha}$ is normalized, but not each row. A tensor $\tilde{\mathbf{R}}^{\alpha}$ with normalized rows can be defined by

$$\tilde{R}^{\alpha}_{ij} = \frac{R^{\alpha}_{ij}}{\sum_k R^{\alpha}_{ik}}. \tag{132}$$

Of course, now the columns of $\tilde{\mathbf{R}}^{\alpha}$ are not normalized. This renormalization is favorable because of the finite size of $\mathbf{x}$, as the parallel lines along which $\mathbf{x}$ is projected do not have the same length. In a physical sense the renormalization is equivalent to an optimization with a ball which has different mass in different dimensions.

During optimization it may happen that some values of $\mathbf{x}$ get negative. Obviously, such a result is unphysical. There are two ways to take care of this problem: Either by a suitable regularization which punishes negative values of $\mathbf{x}$ or by setting all negative values to zero or a very small positive number. In this thesis, the second approach was preferred, because it is more strict.

10.3 EFFECT OF REGULARIZATION

Up to now, the regularization functional $g(\mathbf{x})$ of equation (122) has not been explicitly defined, since there are many possible choices, three of which have been investigated in this thesis. These regularizations, namely an entropy functional, a total variation functional and a histogram functional, and their implications together with the consequences for the reconstruction are introduced in this section.

Entropy Regularization

To use an entropy like regularization functional is the classical approach for 'image reconstruction from incomplete and noisy data' [Gull and Daniell, 1978]. This algorithm is often called maximum entropy method (MEM), if the regularization is defined as $h(\mathbf{x}) = -\sum_j x_j \ln(x_j)$ [Shannon, 1948]. As the function $f(\mathbf{x})$ in equation (122) is minimized, the maximum of the entropy is found by minimizing

$$g(\mathbf{x}) = \sum_j x_j \ln(x_j) = -h(\mathbf{x}). \tag{133}$$

Needless to say, both approaches are equivalent.

The MEM has a long history and solid theoretical foundation. In a nutshell, maximizing the entropy $h(\mathbf{x})$ yields a result with the fewest additional information content. Since the reconstruction is under-determined, there are many $\mathbf{x}$ which can be in agreement with the measured data. If all available knowledge about the reconstructed density is incorporated into equation (119), the final result should contain no additional assumptions. This is achieved by the MEM.

For a physicist, the power of this method is impressively demonstrated e. g., by deriving the Maxwell-Boltzmann distribution just using the information that there exists an average energy and the distribution is normalized. Similarly, the Bose-Einstein and the Bose-Dirac distribution can be derived by just a few assumptions (see e. g., [Kapur and Kesavan, 1992]).

Although these considerations are of high theoretical value, for the purpose of regularization a practically oriented analysis is more interesting: The function $g(\mathbf{x})$ has no correlation between the elements x_j. Since $x_j \ln(x_j)$ has its minimum at e^{-1}, this is also the location of the global minimum of $g(x)$. This means, with no additional constrains, a uniform density with every $x_j = \frac{1}{e}$ would maximize the entropy. In case there is a constraint, which states that $\mathbf{x}$ is normalized like

$$\sum_j x_j = N,$$

the density maximizing the entropy is also uniform, but this time $x_j = \frac{1}{N}$. Therefore, it is often said that the entropy regularization results in a flat density. However, this is not the precise way to describe the outcome of the MEM. For instance, if the values of $\mathbf{x}$ follow a Gaussian distributions, either a broad one or a narrow one, the distribution which maximizes the entropy is clearly the narrow distribution. If the elements of $\mathbf{x}$ with the narrow distribution are randomly interchanged, the entropy will stay the same, although $\mathbf{x}$ is not flat in the sense that the difference

between neighboring elements is small. This exemplifies that a flat distribution according to MEM means that the variance of the *histogramed* values of $\mathbf{x}$ is small.

The entropy regularization has previously been used for the reconstruction of $\rho^{2\gamma}$ [Pylak, Kontrym-Sznajd, and Dobrzyński, 2011]. They compared this reconstruction method to the CM and obtained encouraging results. However, in the aforementioned paper, the ART algorithm was quite different to the one presented here and the resolution effects were not accounted for.

Total Variation Regularization

While the MEM assumes that there is no additional information about $\rho^{2\gamma}$ except for the measured projections, more information is actually available: The TPMD should be flat except for the Fermi breaks. In contrast to the MEM, 'flat' can be interpreted in the classical sense, i. e. the value of neighboring voxels of $\mathbf{x}$ should be similar. A possible way to implement this is by the ℓ^2 and the ℓ^1 norm of gradient of $\mathbf{x}$:

$$g(\mathbf{x}) = \sum_{|\nabla \mathbf{x}|_i \leqslant a} (\nabla \mathbf{x})_i^2 + \sum_{|\nabla \mathbf{x}|_i > a} 2a|\nabla|_i - a^2 \tag{134}$$

The section wise definition of $g(\mathbf{x})$ is necessary since a regularization purely based on the ℓ^1 norm would not be differentiable for $\nabla x_j = 0$. Moreover, the total variation functional of equation (134) was constructed in such a way that $\nabla g(x)$ is continuous, which allows the optimization algorithm to find the minimum more easily. The parameter a is chosen to be small compared to the total dynamic range of $\rho^{2\gamma}$. This method is inspired by the total variation method proposed by [Rudin, Osher, and Fatemi, 1992].

Histogram Method

A versatile method of regularization is the histogram method. Prior knowledge about $\rho^{2\gamma}$ is encoded into a histogram $\mathbf{H}$. In principle, a lot of information can be incorporated in the histogram, as it has a large number of degrees of freedom.

The regularization functional is the squared distance between the histogram of $\mathbf{x}$ and $\mathbf{H}$:

$$g(\mathbf{x}) = \sum_i (H_i - (\mathrm{hist}(\mathbf{x}))_i)^2 \tag{135}$$

Instead of calculating a histogram of $\mathbf{x}$ it is computational faster to sort the elements of $\mathbf{x}$ in increasing order. The result of this operation is similar to a histogram with infinite resolution. Moreover, it is easier to calculate the numerical gradient for the sorted histogram.

One difficulty of this method is to find a suitable histogram to describe the existing prior knowledge. In a first test with this regularization method, reconstructions were created from projections of a simulated TPMD. Hence, a histogram of this simulated density could be used.

A related histogram method for regularization in image reconstruction was first proposed by Thurman and Fienup [2007]. In their algorithm they optimized for a

	entropy	total variation	histogram
3 projections	5.3×10^{-7}	1.3×10^{-7}	8.4×10^{-7}
5 projections	4.0×10^{-7}	9.6×10^{-8}	4.6×10^{-7}
17 projections	2.3×10^{-7}	7.3×10^{-8}	3.3×10^{-7}

Table 6: Quadratic difference between original density $\rho^{2\gamma}$ and reconstructed densities $\mathbf{x}$ for various amounts of projections and for different regularization functions. The total number of counts in every set of projections is 275×10^6. For calculating the quadratic differences, the densities were normalized to the original density.

certain residual noise distribution. Hence, the presented approach is quite different, although there are some similarities.

Both the total variation regularization and the histogram method have not been employed in connection with ACAR so far except for this study.

Test of the Introduced Regularizations

To evaluate the effect of regularization on the reconstruction of ACAR data it is most convenient to know the original TPMD from which the projections were created. For this purpose a theoretical three-dimensional $\rho^{2\gamma}$ of copper was calculated (details see [Leitner, 2013; Leitner, Weber, and Ceeh, 2016]). From this density, projections can be created and furthermore the reconstruction can be compared using a simple least squares approach.

$$d^2 = \sum_i \left(\rho_i^{2\gamma} - x_i\right)^2 \tag{136}$$

The regularization was tested for two different scenarios: At first, data were simulated with infinitely good resolution. Therefore, the measurement operator consisted solely of $\mathbf{R}^\alpha$. The second time, the data were also convolved with the experimental resolution. In both cases, three sets of projections with a different number of projections but a constant number of counts in each set were generated (275×10^6 counts without experimental resolution and 500×10^6 with resolution). In every set the projections were calculated by rotating the simulated density around the [110] axis in equidistant steps (22.5°, 15° and 5° respectively). The main symmetry directions at 0°, 54.7° and 90° were avoided, because these provide less information about $\rho^{2\gamma}$ than an arbitrary projection. In a real experiment however, at least one of these directions will be measured additionally, since it provides valuable information about the sample orientation and quality. The overall number of counts was kept constant in order to examine how measurement time is best made use of, by measuring few projections with high statistics or a high number of projections with low statistics.

Regularization for Projection

In figure 32, a cut from [100] to Γ to [110] through the original density is shown with the residual $(\boldsymbol{\rho} - \mathbf{x})$ for each reconstruction from five projections. Obviously,

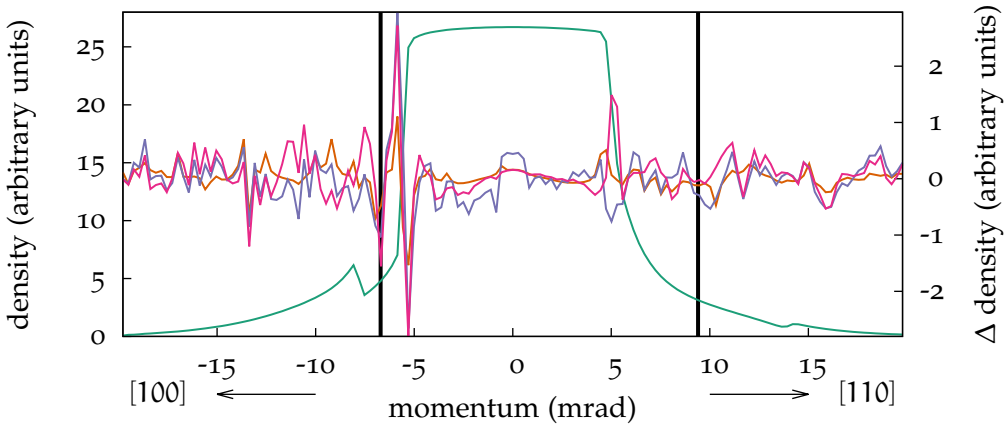

Figure 32: Cut through the original density from [100] to Γ to [110] (■, left axis) and difference between original and reconstruction for different regularization functions: ■ entropy, ■ total variation, ■ histogram (right axis). The vertical lines indicate the first Brillouin zone boundaries.

the difference between original and reconstruction is small. Nevertheless, it is apparent that the total variation regularization yields the reconstruction with the most efficient noise suppression and with the fewest artifacts.

A more quantitative comparison is given in table 6. There, the quadratic deviations from original density $\rho^{2\gamma}$ and reconstructed density $\mathbf{x}$ are listed for different methods of regularization and for different number of projections. With an increasing number of projections d^2 is decreasing for every regularization method. This indicates that the measurement time is used most efficiently if many projections are recorded. But not only the quality of the reconstruction is increasing with the number of projections, the necessary iterations are decreasing. Hence, the problem of reconstruction from many projections is better determined than reconstructing from few, if the total amount of counts is the same.

Table 6 also shows the influence of regularization: Although the entropy regularization has been the only regularization used in connection with the reconstruction from ACAR data, it is not the one which yields the best results. The best result is achieved by the total variation regularization in these examples.

Regularization for Projection and Convolution

The situation changes considerably if the experimental resolution is also taken into account. In table 7 the quadratic difference between the original density and the reconstructions is listed. It is not meaningful to compare the absolute numbers of table 6 and table 7, because of the different starting point of both studies.

The first thing to note is that the best regularization method in this case is the entropy regularization. Also here, the histogram regularization results in the least accurate reconstructions. Generally speaking, the variation in quality between the methods as well as for the different number of projections is small. Again, the quality increases with an increasing number of projections, but especially for the entropy regularization the quality gain is only marginal. The reason for this is that the deconvolution problem is mainly limited by the overall statistics of the data.

	entropy	total variation	histogram
3 projections	3.2×10^{-7}	6.6×10^{-7}	9.1×10^{-7}
5 projections	2.5×10^{-7}	4.9×10^{-7}	5.1×10^{-7}
17 projections	2.3×10^{-7}	3.7×10^{-7}	3.8×10^{-7}

Table 7: Quadratic difference between original density $\rho^{2\gamma}$ and reconstructed densities $\mathbf{x}$ for various amounts of resolution affected projections and for different regularization functions. The total number of counts in every set of projections is 500×10^6. For calculating the quadratic differences, the densities were normalized to the original density.

As the number of counts is kept constant for the simulated measurements, the deconvolution is equally difficult for all sets of projections, even when the reconstruction problem becomes easier with the number of projections. This shows that the quality of the reconstructions is mainly limited by the experimental resolution.

Conclusion

In this comparison, the effect of regularization on the reconstruction from either unblurred or blurred projected data was demonstrated. It could be shown that for the reconstruction of projections which are not affected by resolution, the total variation regularization gives the best results. However, if the experimental point spread function is taken into account, the entropy regularization results in a reconstruction that is closest to the original.

Furthermore, with this investigation the dispute whether or not it is advantageous to collect few projections with much statistics or many projections with low statistics could be resolved. Clearly, the best reconstruction is obtained if many projections are recorded. However, with the current angular resolution of the setup, the quality gain by measuring many projections is negligible, as the deconvolution is a more difficult problem than the actual reconstruction.

Part IV

EXPERIMENTAL RESULTS

11 INVESTIGATION OF ELEMENTARY SYSTEMS

The FS of most elementary system is thought to be explored quite well with a lot of experimental results having been published. For this reason measurements on three elementary metals, i. e. copper, iron and vanadium, have been conducted in order to demonstrate that the previously published results can be confirmed and to benchmark the developed reconstruction technique. Especially the spin-polarized investigation of iron is an important groundwork for the later spin-polarized investigation of the Heusler system Cu_2MnAl.

11.1 TEMPERATURE DEPENDENT MEASUREMENTS ON COPPER

Noble metals usually include all metals with a high degree of robustness against acids or other external influences. In a stricter, physical sense, noble metals comprise only copper, silver and gold. These elements possess eleven additional electrons compared to the foregoing noble gas configuration. The electrons completely fill the d states leaving one electron to fill the outer s state. While the d electrons are tightly bound the s electron exhibits a nearly free-electron-like behavior possessing an almost quadratic dispersion relation. However, compared to the alkali metals which also possess one conduction electron, the conduction electrons in noble metals are significantly influenced by the d electrons and the Fermi surfaces are less spherical than the ones of the alkali metals.

The noble metals were among the first elements where the FS was systematically explored for reasons of their 'metallurgical convenience' [Pippard, 1957b]: On the one hand, the topology of their FS is rather simple due to the single conduction electron. On the other hand, their FS is not entirely spherical and thus complex enough to put theoretical predictions beyond the free electron gas model to a test. Furthermore, copper, silver and gold are much easier to handle experimentally than e. g., lithium, sodium or potassium.

The first study of copper's FS was done by Pippard [1957b] by measuring the anomalous skin effect. His results were immediately confirmed by Moliner [1958] via a tight binding approach. With extensive effort Roaf [1962] was able to reconstruct the FS from the dHvA measurements of Shoenberg [1962] and to compare them to in the mean time published theoretical predictions of Burdick [1961] and Segall [1961].

A first positron study on copper which went beyond detecting free electron like behavior (see e. g., Lang, De Benedetti, and Smoluchowski [1955]) was the 1D-ACAR study (using the point-silt geometry) of Fujiwara and Sueoka [1966] who were able to identify details of the FS. Many more positron studies on copper were conducted in the following years and copper became a standard system to benchmark new spectrometers (see listing 1). The latest and most notable of these studies was the investigation of Kondo et al. [1993] who reconstructed the TPMD

via 19 measured projections with a high experimental resolution of $1.05\,\mathrm{mrad} \times 0.78\,\mathrm{mrad}$ at 26 K.

As can be seen from listing 1, the interest from theoretical and experimental side in bulk copper has declined in the recent years except for the investigation with ARPES. As the copper surface, like the surface of all noble metals, keeps very clean under UHV conditions, ARPES measurements can be performed much easier on these systems. This advantage triggered some impressive measurements of the FS (see e. g., Lindroos et al. [2001] and Winkelmann et al. [2012]).

POSITRON STUDIES: Bearasley et al., 1975; Berko, Cushner, and J. C. Erskine, 1968; Berko, Haghgooie, and Mader, 1977; Fujiwara and Sueoka, 1966; Haghgooie, Mader, and Berko, 1978; Kondo et al., 1993; Matsumoto and Wakoh, 1988; Melngailis, 1970; Mijnarends, 1969, 1973b; Senicki et al., 1972, 1973; Smedskjaer and Legnini, 1990; Wakoh et al., 1979

QUANTUM OSCILLATION STUDIES: Coleridge et al., 1972, 1982; Jan and Templeton, 1967; M. J. G. Lee, 1969; Roaf, 1962; Shoenberg, 1962; Zornberg and F. M. Mueller, 1966

PHOTOEMISSION STUDIES: Baalmann et al., 1986; Becker et al., 1975; Berglund and Spicer, 1964; Bisio et al., 2006, 2009; Con Foo et al., 1996; Courths and Hüfner, 1984; Knapp et al., 1979; Lettington, 1964; Lindroos et al., 2001; McDougall, Balasubramanian, and E. Jensen, 1995; Qu et al., 1995; Roth et al., 2016; Wincott et al., 1986; Winkelmann et al., 2012

COMPTON STUDIES: G. E. W. Bauer and Schneider, 1985; Bearasley et al., 1975; Eisenberger and Reed, 1974; Pattison, N. K. Hansen, and Schneider, 1982; Sakurai et al., 1999

THEORETICAL STUDIES: Bross et al., 1964; Burdick, 1961, 1963; Faulkner, Davis, and Joy, 1967; Fehrenbach and Bross, 1993; Matsumoto and Wakoh, 1988; Moliner, 1958; Segall, 1961; Snow and Waber, 1967

Listing 1: Selection of publications on the electronic structure of copper.

Although the electronic structure of copper is well known, Liviu Chioncel predicted (not published) that the electronic structure of copper is influenced by electronic correlations. These correlations should especially induce a temperature dependent subtle change in the electronic structure, which has already been qualitatively been observed by Knapp et al. [1979] and McDougall, Balasubramanian, and E. Jensen [1995] with ARPES. As ACAR is one of the few methods which is able to probe the electronic structure dependent on the temperature, it is ideally suited to verify these predictions. Moreover, as the FS of copper at low temperatures is rather well known, it can serve as reference for testing the previously introduced reconstruction algorithm on actual measurements.

Sample Preparation and Measurements

The sample was prepared from a large copper single crystal [see figure 34 a)]. Since copper is very ductile it was not possible to prepare a single crystalline surface by mechanical polishing. Therefore, the crystal was electrolytically etched in solution of 90 % distilled water and 10 % of phosphoric acid (85 wt. % in H_2O) applying a voltage of 3 V between the copper sample and another copper cathode. This resulted in a single crystalline surface as could be verified by Laue back reflection and by the strong anisotropic ACAR signal.

Two sets of measurements were done at 10 K and at 300 K. For both temperatures 19 projections were recorded turning the sample in equidistant steps of 5° from the [110] to the [100] direction. In total (i. e. summed over all projections) 180×10^6 counts were collected for the low temperature measurement and 260×10^6 counts for the high temperature measurement. For a comparison with theory, a [100] projection with much higher statistical accuracy (100×10^6 counts) was recorded.

Comparison to Theoretical Calculation

For a first evaluation of the measurements, a theoretical [100] spectra was calculated using the Munich SPR-KKR package [Ebert, Ködderitzsch, and Minár, 2011]. In figure 33 a) a comparison for the anisotropy between the theoretical and the experimental spectra is shown. Qualitatively, most of the experimental features are well reproduced by the theoretical calculation. However, especially in higher order BZs, there is a significant difference between experiment and theory. E. g., in the experiment at (-7 mrad,7 mrad) the outline of the FS can be identified as an above average intensity, while in the theory this feature is not present. Furthermore, the high intensity at the L-point in the experiment is not reflected by the theory.

In the LCW folded densities in figure 33 b) the situation is very similar: Although the overall agreement is good, there are some details slightly different in theory and experiment. Most notably is the intensity at the L-point, which is much higher in the theory. The second difference is the shape of the low intensity around the X-point. In the theory, this pocket is broader in the XW-direction than in the experiment.

Temperature Dependent Reconstruction

Using the newly developed algorithm (see chapter 10) the fully 3D TPMD was reconstructed using the measured projections. The TPMD was backfolded into the first BZ according to the LCW theorem before the FS was then determined by looking for the iso-value which devides the BZ into two parts of equal volume. The result can be seen in figure 34 b). Cuts through the reconstructed densities and the outline of the isosurface are shown in figure 35 a) for the 10 K measurements and in 35 b) for the room temperature (300 K) measurement.

Both reconstructions give a correct topology of copper's well-known FS: They are nearly spherical except for the necks in the [111] directions [see fig. 34 b)]. In figure 35 cuts in the [110] plane through the reconstructed k space density are

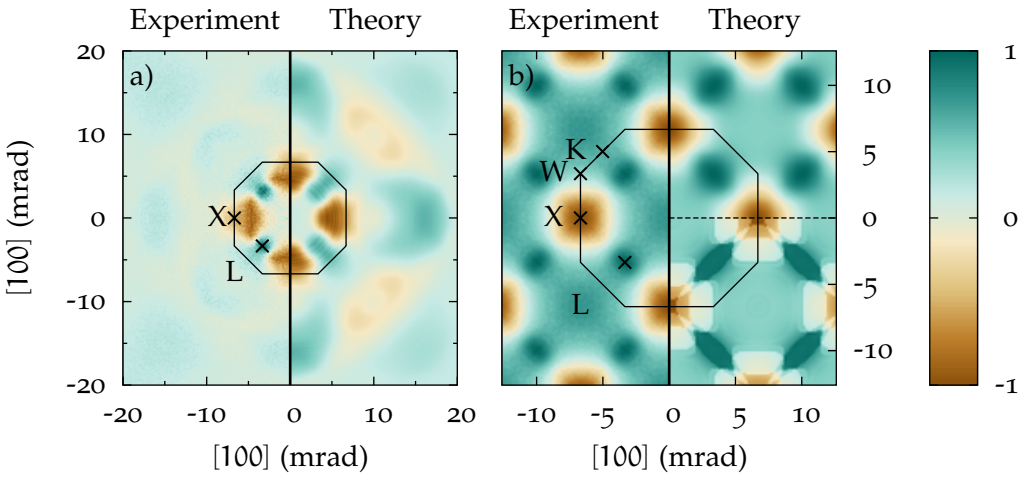

Figure 33: Comparison between experiment and theory of the copper [100] projection at 10 K. The theoretical data were convolved with the experimental resolution. a) Anisotropy b) LCW-folded density. The lower half of the theory was not convolved with the experimental resolution. The colorscale is given in relative units.

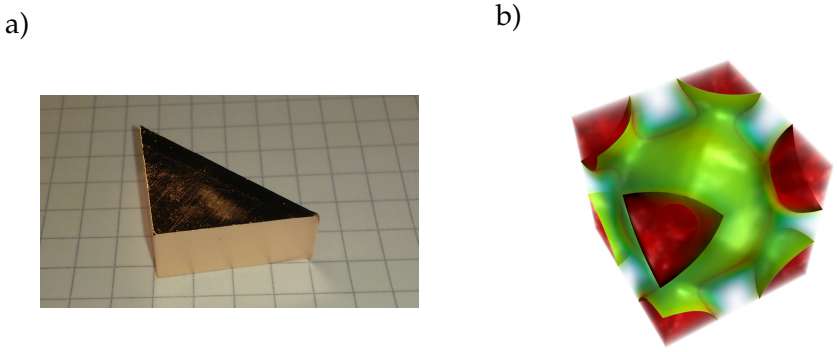

Figure 34: a) Copper sample b) Reconstructed 3D $\rho^{2\gamma}$ of copper in k space. The solid surface corresponds to the isosurface where half of the BZ is filled.

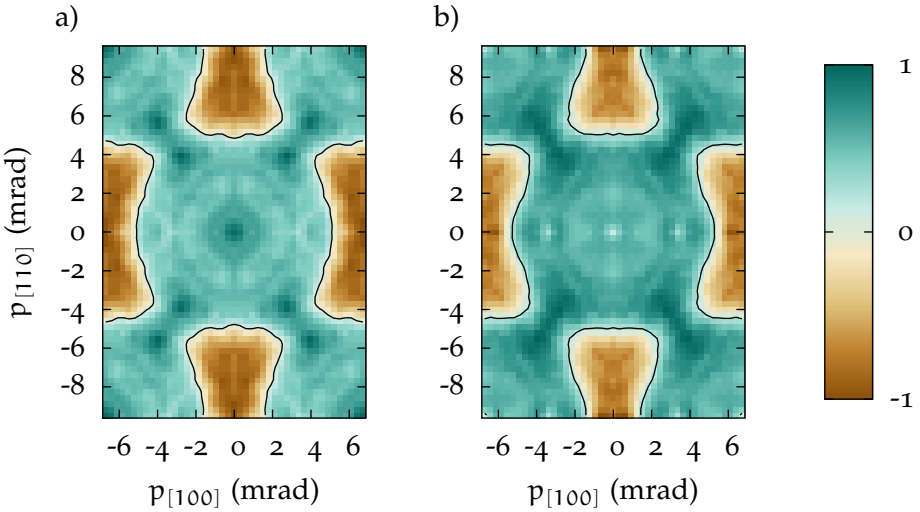

Figure 35: Cut through the reconstructed and LCW folded TPMD a) for 10 K and b) for 300 K. The black contour line represents the isosurface boundary where half of the BZ is occupied.

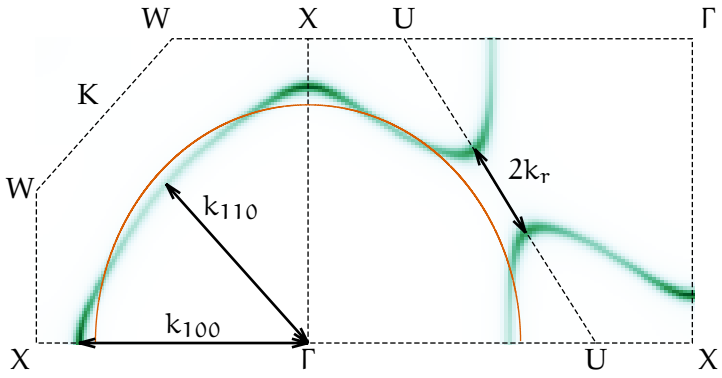

Figure 36: Cut through the Bloch spectral function of copper at the Fermi energy for two planes in k-space. The orange semicircle is a cut through the Fermi sphere according to an assumed free electron gas in copper.

shown. These cuts are along the necks and hence the famous 'dog bone' shape can be seen. The reconstruction based on the low temperature measurements is considerably more noisy than the high temperature reconstruction. This is an effect of the different statistical accuracy of both measurements. As the FS details (e. g., the bulge in [100] direction) are much more pronounced in the high temperature measurement it can be assumed that the 180×10^6 counts were not sufficient to reconstruct the low temperature FS.

A second difference between figures 35 a) and b) is that the low temperature measurement has a high intensity at the Γ point. This feature is even more prominent in the extended zone schema (not shown). A possible explanation is that at 10 K a thin layer of contamination (by water or carbon) forms at the surface and hinders the re-emission of positronium. Because a ^{22}Na positron source is used, only a very small fraction of positrons is able to diffuse to the surface and the amount of formed positronium is expected to be small. This consideration is consistent with the intensity of the observed effect which *is* very small ($< 1\,\%$).

For a quantitative comparison with theoretical calculations Liviu Chioncel calculated the Bloch spectral function at the Fermi energy in the DMFT frame work. The spectral function $A(\mathbf{k}, E)$ gives the probability to find an electron with the energy E and the momentum $\mathbf{k}$. A cut through two main symmetry planes of the spectral function for $E = E_F$ is shown in figure 36. Additionally the outline of the Fermi sphere is sketched for a free electron system with the electron density of copper. Similar to the typical textbook example, in copper the energy of bands close to the BZ boundary is lowered compared to the free electron gas which leads to a bulging of the FS and even the forming of necks. Since the total number of states has to stay constant (the volume enclosed by the FS for a one electronic system is half of the BZ's volume) the FS is dented e. g., in [110] direction like a deformed rubber ball.

Typically, three measures are given to compare experimentally as well as theoretically determined copper FSs, namely the FS's extend in [100] and [110] direction and the radius of the neck (see figure 36). In table 8 these quantities are given for the theoretical calculation in fig. 36, for the high temperature reconstruction and for three additional literature sources: a quantum oscillation experiment [Co-

	Temperature (K)	k_{100}	k_{110}	k_r
Theory (fig. 36)		5.712	5.017	1.135
dHvA[a]	< 4	5.550	4.986	0.989
ARPES[b]	300	5.63	4.97	1.34
2D-ACAR[c]	26	5.406	5.122	1.115
present work (high temp.)	300	5.252	4.932	1.290

Table 8: FS dimensions of copper in mrad extracted from the theoretical calculation in fig. 36, from three literature sources and from the high temperature reconstruction in fig. 35 b).

a Coleridge and Templeton, 1982.
b Con Foo et al., 1996.
c Kondo et al., 1993.

leridge and Templeton, 1982] and a 2D-ACAR reconstruction [Kondo et al., 1993] and for ARPES results [Con Foo et al., 1996]. The low temperature reconstruction was not evaluated due to the insufficient quality.

Quantitatively, all four sources are in good agreement with each other for k_{110} and k_r with a maximum deviation from the mean of 0.16 mrad. Notably, the deviation is nearly one order of magnitude smaller than the resolution of the present measurement. It is very interesting to note that values for k_r in ARPES and this work are in very good agreement. This might be due to the fact that k_r is temperature dependent and both of the measurements were done at room temperature while dHvA and the 2D-ACAR measurement of Kondo et al. [1993] were both performed at low temperatures.

Despite the good agreement of k_{110} and k_r, the deviation of the k_{100} values is much larger. In particular, the theoretical result is larger than all the measured values. As dHvA measurements are usually very exact, the deviation is either caused by a wrong input parameter in the calculation or due to a wrong model with which Coleridge and Templeton [1982] fitted the FS to their data.

Discussion

Surprisingly, although copper is well studied and thought to be simple it exhibits phenomena, which are still not completely understood. Like in previous works, a general agreement between measurements and theory could be confirmed. Furthermore, indications for the temperature dependent change of the electronic structure could be observed. For an unambiguous study of this phenomenon, the low temperature measurements have to be repeated collecting more statistics. Moreover, a better experimental resolution would help to provide evidence for temperature dependent changes.

11.2 SPIN-POLARIZED POSITRON MEASUREMENTS ON IRON

From a cultural perspective iron is a very important material since 1500 B.C. when the first humans mastered the process of iron smelting. A new age of civilization started, the iron age. At this time people were mainly interested in iron due to its hardness and toughness and because they were able to change these properties by alloying or heat treatment. Already during this time another property of iron was discovered: ferromagnetism. Although ferromagnetism is not an exclusive property of iron and can be found in several other materials, it is still named after the element it was first observed in.

The electronic structure of iron has been intensively studied because of its prototypical character for ferromagnetism. An overview of experimental and theoretical studies is given in listing 2. One of the first positron studies was conducted by Hanna and Preston, who could prove that positrons created from β-decay possess a nonzero spin-polarization [Hanna and Preston, 1957, 1958]. Mijnarends was able to reconstruct the fully 3D summed momentum density $\Sigma\rho(\mathbf{p}) = \frac{\rho^{\uparrow}(\mathbf{p})}{\lambda^{\uparrow}} + \frac{\rho^{\downarrow}(\mathbf{p})}{\lambda^{\downarrow}}$ and the difference momentum density $\Delta\rho(\mathbf{p}) = \frac{\rho^{\uparrow}(\mathbf{p})}{\lambda^{\uparrow}} - \frac{\rho^{\downarrow}(\mathbf{p})}{\lambda^{\downarrow}}$ (see section 4.3.5). The same was latter done with Compton scattering by Tanaka et al. [1993]. In 1988, Genoud et al. published an ACAR study with very high angular resolution of 0.3 mrad and 0.5 mrad in p_x and p_y direction , respectively.

Two notable investigations of iron's electronic structure are the dHvA studies of Baraff [1973] and Gold et al. [1971]. With a lot of effort they set up high precision equipment and were able to resolve most of the FS sheets with high accuracy. However, their results do not agree completely with state-of-the-art calculations. With ARPESs it seems to be much more difficult to investigate this metal: The first ARPES study which allowed to draw a similar comprehensive picture of the FS was not published until 30 years later [Schäfer et al., 2005].

In the early years, it was very challenging for theoreticians to include the exchange interaction into band theoretical calculations. Therefore, the first calculated band structure of iron by Wood [1962] was created for the nonmagnetic case. The bands were then rigidly shifted to obtain the experimentally determined magnetic moment. Such a procedure yields of course only a rough estimate of the true band structure. The first calculation which included the exchange splitting was done by Wakoh and Yamashita [1966]. They also included the first 3D images of the FS, which are roughly consistent with later results. Over the following years, theoretically models were constantly refined until a most recent thorough study of the topology of the FS of iron identifying several topological nontrivial points in the BZ [Gosálbez-Martínez, Souza, and Vanderbilt, 2015].

Upon cooling from the melt, pure iron will solidify at 1811 K in the δ phase, changing its crystal structure from bcc to fcc at 1667 K and then back to bcc again at 1185 °C (see e. g., [Funtikov, 2004]). Physically, the transition δ to γ to α iron is interesting because it is suspected to be driven by the loss of magnetic correlations. However, it makes the growth of large single crystalline samples very challenging. Possible approaches to get single crystals are stress annealing or the use of an advantageous temperature gradient in order to favor to growth of grains with a specific direction. A different approach to get single crystals is to add a small

POSITRON STUDIES: Berko et al., 1964, 1965; Genoud et al., 1988; Hanna and Preston, 1957, 1958; Kawasuso et al., 2011, 2012; Mijnarends, 1973a,b; Mijnarends and Hambro, 1964; Šob, 1982; Šob, S. Szuszkiewicz, and M. Szuszkiewicz, 1984; S. Szuszkiewicz, Rozenfeld, and M. Szuszkiewicz, 1979

QUANTUM OSCILLATION STUDIES: J. R. Anderson et al., 1963; Baraff, 1973; Coleman, Lowrey, and Polo, 1981; Gold et al., 1971

PHOTOEMISSION STUDIES: Cui et al., 2007a, 2006, 2010, 2007b; Eastman, Himpsel, and Knapp, 1980; Eastman et al., 1979; Sakisaka et al., 1990; Sakisaka, Rhodin, and D. Mueller, 1985; Sánchez-Barriga et al., 2012; Schäfer et al., 2005; Turner, Donoho, and J. L. Erskine, 1984

COMPTON STUDIES: Benea et al., 2012; Chioncel et al., 2014; M. J. Cooper and Duffy, 2000; Dobrzyński and Żukowski, 1999; Genoud and A. K. Singh, 1989; Y. Kubo and Asano, 1990; Sakai et al., 1991; Sakai and Ôno, 1976; Tanaka et al., 1993; Tokii and Matsumoto, 2006

THEORETICAL STUDIES: Callaway et al., 1977; Chioncel et al., 2014; Genoud and A. K. Singh, 1989; Gosálbez-Martínez, Souza, and Vanderbilt, 2015; Y. Kubo and Asano, 1990; Maglic and F. M. Mueller, 1971; Nautiyal and Sushil Auluck, 1985, 1986; Pou et al., 2002; M. Singh, Wang, and Callaway, 1975; Wakoh and Yamashita, 1966; Wood, 1962

Listing 2: Selection of publications on the electronic structure of iron.

amount of silicon (typically 3 %) to the pure iron. Silicon stabilizes the bcc phase and makes conventional growth techniques feasible. Some of the cited studies in listing 2 used silicon stabilized bcc iron. Certainly, the question remains whether and how strong the silicon influences the electronic structure of pure iron since this has not been investigated so far.

In this thesis, 2D-ACAR measurements on bcc Fe and $Fe_{0.97}Si_{0.03}$ have been conducted. The measurements will be compared to band theoretical calculations and amongst each other.

Sample Characterization and ACAR Measurements

From Peter Böni at TUM two single crystalline rods were obtained: A pure bcc iron crystal and a crystal with 3 at. % of silicon. From both rods, oriented samples were cut and polished in the crystal lab. The pure iron crystal is shown in figure 37 a) and b) while the $Fe_{0.93}Si_{0}.03$ sample is shown in figure 37 c).

To ensure the sample quality, the pure iron crystal was analyzed by means of energy dispersive X-ray spectroscopy (EDX) and X-ray diffraction (XRD). The EDX analysis was not able to detect a significant amount of other elements than iron. In figure 38 the result of the θ-2θ scan is shown. The main peak at 65.08° agrees well with the [200]-reflex and a lattice constant of 286.6 nm [Fang et al., 2012]. The

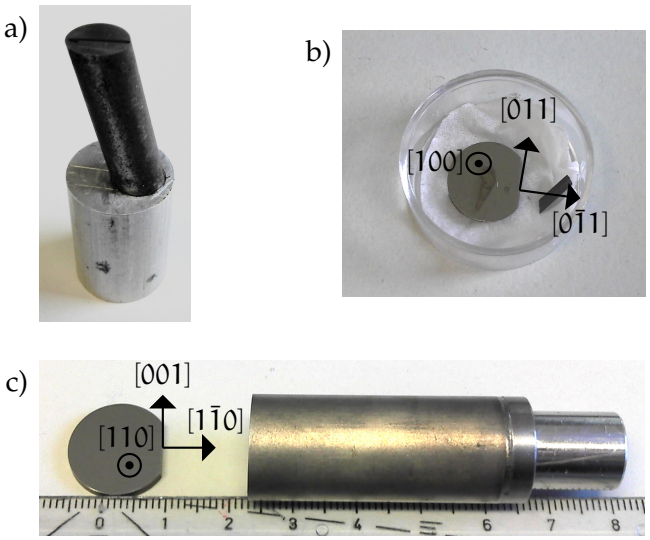

Figure 37: Iron samples: a) Single crystal of bcc iron. b) Polished disc cut from the single crystal with crystallographic directions indicated. c) $Fe_{0.93}Si_{0.03}$ single crystal and prepared disc with crystallographic directions indicated.

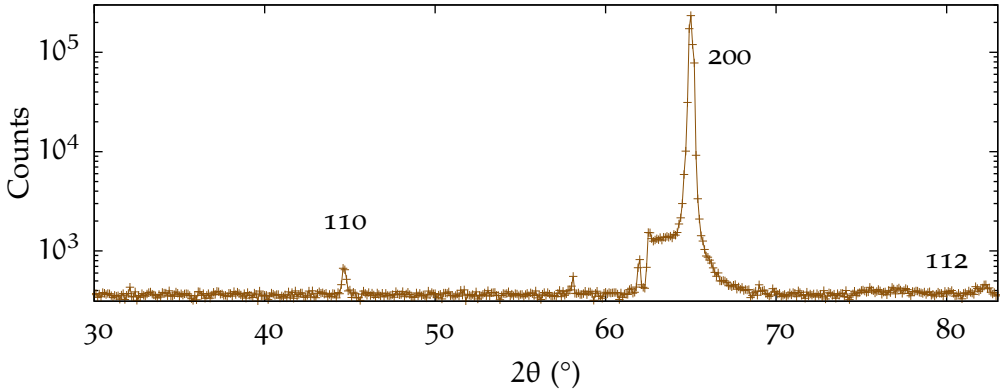

Figure 38: Diffraction pattern of the Fe sample along the [100] direction. The [110] peak is probably caused by iron dust on the sample.

second peak at 44.7° can be identified as the [110] reflex. As the intensity of these peaks is very low, it cannot be caused by differently oriented grains in the sample but rather by remaining iron dust particles on the sample. Hence, XRD confirms the sample to be single crystalline.

On both iron samples, spin-polarized ACAR measurements were conducted at room temperature. In table 9 the measurements and the recorded counts are summarized. For the Fe sample, five projections in equidistant steps including the [100] and [110] directions were measured, while for the $Fe_{0.97}Si_{0.03}$ sample the three main symmetry directions were recorded. Usually, about 150×10^6 counts were collected in each measurement.

Comparison to Theoretical Calculation

In order to evaluate the quality of the measured data, a theoretical [110] projection of iron's TPMD using the Munich SPR-KKR package [Ebert, Ködderitzsch, and

	Field Direction	[100]	11.25°	22.50°	33.75°	[110]	[111]
Fe	antiparallel	149.15	147.20	126.72	175.90	162.27	
	parallel	196.14	163.25	172.03	145.69	143.39	
$Fe_{0.97}Si_{0.03}$	antiparallel	159.74				275.46	150.43
	parallel	122.61				256.04	180.73

Table 9: Number of counts in 1×10^6 for the measured projections. The angles are given for the rotation around [001] relative to [100]. The field direction is given relative to the spin-polarization of the positrons.

Minár, 2011] was created. As this data serves only as a first test, no spin-polarized calculations were performed. The resulting band structure (not shown) agrees qualitatively well with previously published band structures of iron although in the spin-polarized case, there exist a different band structures for majority and minority spin channel, respectively.

Here, only the $Fe_{0.97}Si_{0.03}$ data are compared to theory because of the higher statistical accuracy. To increase the statistical accuracy even further, both measurements with antiparallel magnetization were summed and symmetrized according to the twofold symmetry of the projection. The direct comparison between theory and experiment revealed that the $Fe_{0.97}Si_{0.03}$ sample was misaligned and the recorded spectra had to be turned by 2.7°. Due to the new data acquisition, this could be done before histogramming thus conserving the statistics of the data. In figure 39 the theoretical calculation and the measurements on $Fe_{0.97}Si_{0.03}$ are shown for the raw spectra, the anisotropy and for the LCW folded data. In each case a direct comparison (left column) and the difference (theory − experiment) is depicted. The spectra were scaled in such a way that the squared difference is minimized.

Similar to the vanadium measurement (see figure 44) distinct features from high momentum components can be recognized much more clearly in the theoretical spectrum than in the experimental one, even though the theoretical spectra was convolved with the experimental resolution. The reason for this is probably an overestimation of the contributions from higher order BZs. This is also backed up by the difference of experiment and theory in figure 39 b). The structured features outside the first BZ are all in green which means, they are present in the theory but not in the experiment.

As usual, the anisotropy agrees much better with the theory than the actual raw spectra. The direct comparison in figure 39 c) shows a good qualitative agreement. However, there are several details different in the experiment e. g., the high intensity knob at (−7.5 mrad,±10 mrad) or the high intensity arc at (−15 mrad,0 mrad) does not agree very well with theory. As the isotropic part was already subtracted, the difference of the anisotropies [fig. 39 d)] looks quite different compared to the raw spectra difference in fig. 39 b). Nevertheless, some of the features in 39 b) are also present in d), like the drop shaped high intensity pocket at (0 mrad,±12.5 mrad) or the pillow at (0 mrad,±17 mrad).

The LCW of the measurement in fig. 39 e) agrees very well with the theoretical data. The main differences are the width of the arms between the N and P points

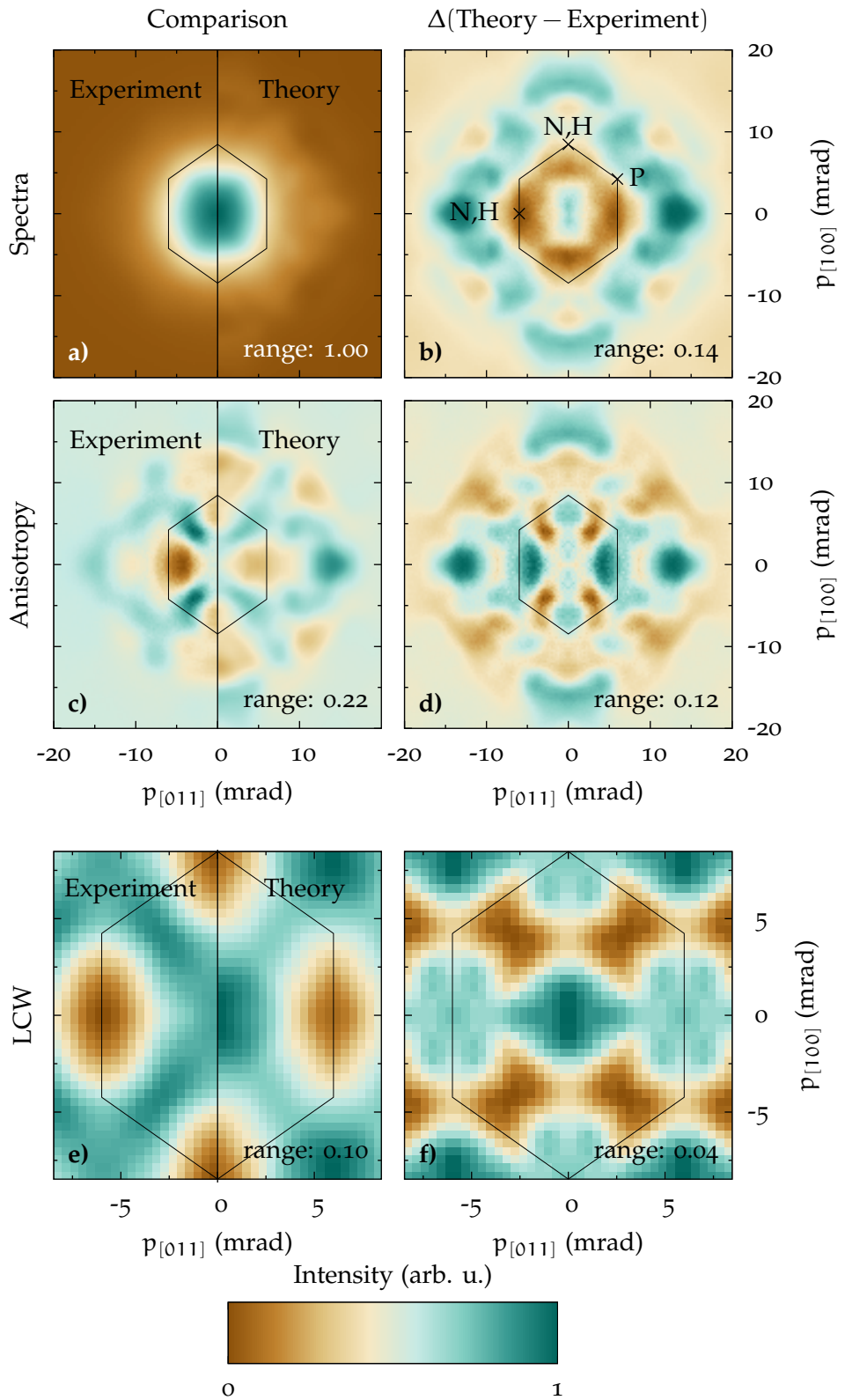

Figure 39: Theoretical and experimental data for the [011] projection of $Fe_{0.97}Si_{0.03}$. The relative dynamic range is given in every plot explicitly. *Left:* Comparison between experimental and theoretical spectra either by the raw data, the anisotropy or by the LCW-folding. *Right:* Difference between theory and experiment Δ(Theory − Experiment) for raw data, anisotropy and LCW-folding. The polygon in the center corresponds to the outline of the first BZ. In b), some of the high symmetry points are marked. For the [011] projection, N and H overlie.

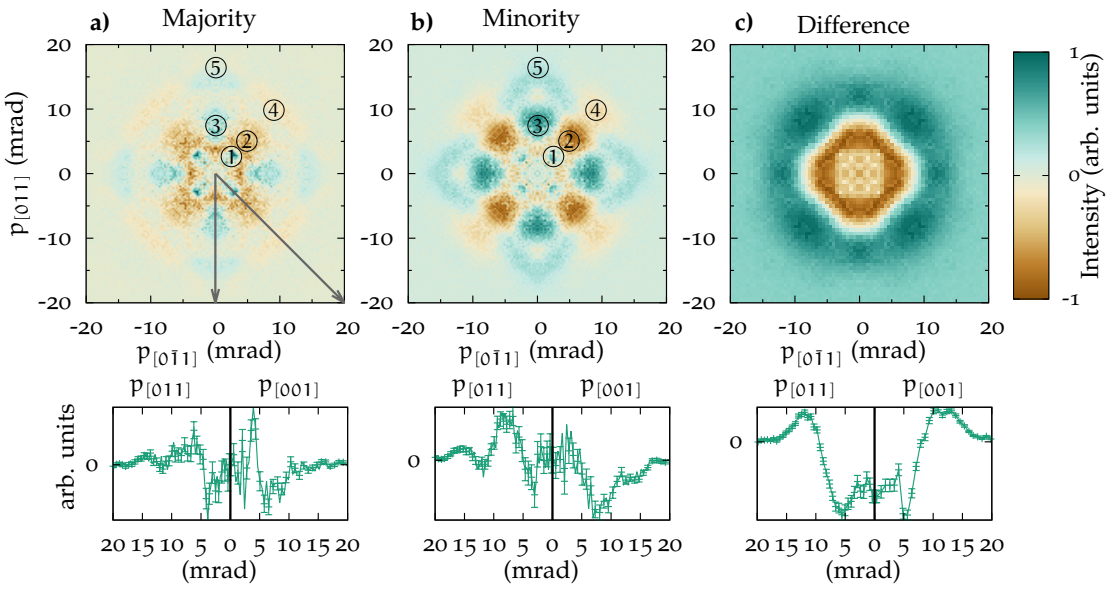

Figure 40: 2D projections along [110] of $Fe_{0.97}Si_{0.03}$ at room temperature. The measured anisotropy of a) majority and the b) minority density are displayed wile in c), the difference between majority and minority $(M_{maj} - M_{min})$ with the total number of counts in each spectrum normalized to one is shown. The lower row depicts cuts through the upper pictures as indicated by the arrows in a) along the [001] and [011] directions.

and depth of the ellipsoidal hole at N,H as can be seen in figure 39 f). Since the LCW mainly reflects whether or not a state in k-space is occupied, the differences here is probably caused by an incorrect Fermi level in the calculation. A more profound calculation, could certainly improve here the agreement between theory and experiment.

Spin-polarized measurements

Since the positron beam in the setup possesses a net polarization of $(31 \pm 4)\,\%$ [Ceeh, 2015] it is possible to probe the electronic structure of iron spin-dependent. Although, a lot of dHvA measurements were made on iron, it is as a matter of principle not possible to identify the majority or the minority character of the detected FS sheets. With ACAR this would be theoretically possible. However, iron has as many as 9 different FS sheets with some of them being smaller than 3 % of the extent of the BZ, which corresponds to about one fifth of the resolution of the spectrometer [Gosálbez-Martínez, Souza, and Vanderbilt, 2015]. Therefore, it is extremely challenging to separate and resolve all the features of the FS without substantial theoretical input.

In order to demonstrate the success of the spin-polarized measurements, the majority, the minority and the difference between both spin channels for $Fe_{0.97}Si_{0.03}$ is shown in fig. 40 for the [100] projection and in fig. 41 for the [110] projection. Especially from the difference measurement [fig. 40 and 41 c)] it can be seen that both spin channels are quite distinct - otherwise the difference would have been homogeneous. Both differences exhibit a transition from high intensity at high

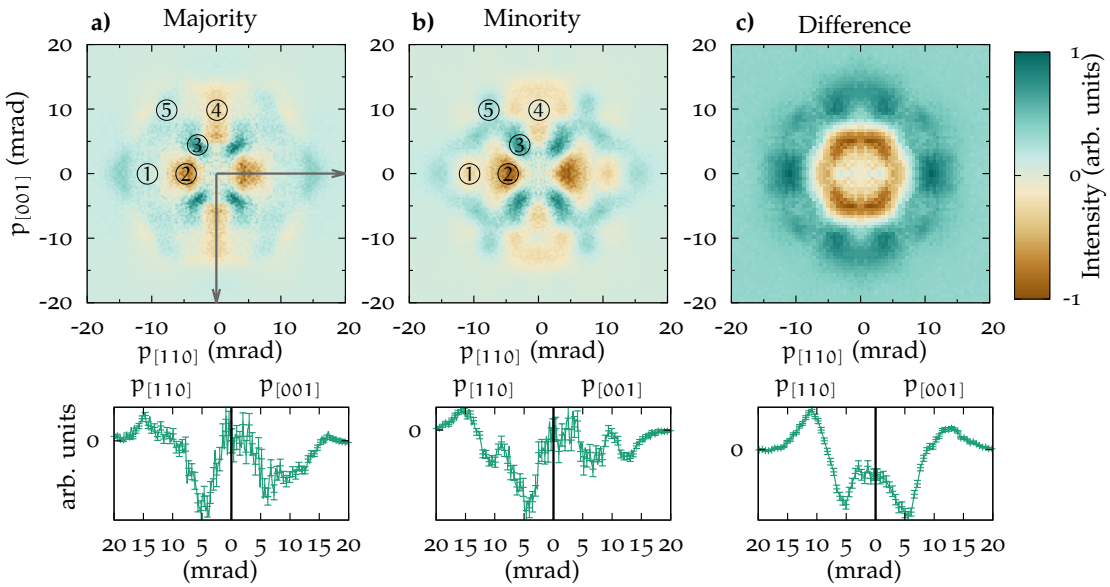

Figure 41: 2D projections along [110] of $Fe_{0.97}Si_{0.03}$ at room temperature. The measured anisotropy of a) majority and the b) minority density are displayed wile in c), the difference between majority and minority $(M_{maj} - M_{min})$ with the total number of counts in each spectrum normalized to one is shown. The lower row depicts cuts through the upper pictures as indicated by the arrows in a) along [001] and [011] directions.

momenta to a low intensity at low momenta. Since the measurements are not physically correctly normalized (see section 4.3.5), but rather normalized to the sum, such a behavior should be universal to spin-polarized ACAR measurements. In a rough approximation, the majority momentum density equals the minority density plus the magnetic excess states. Therefore, the majority density is broader and the difference will yield this inverse Mexican-hat-like dependence.

Due to iron's large saturation field of approximately 2.2 T [Danan, Herr, and Meyer, 1968] the sample cannot be fully magnetized at an external field of 1 T. As the large dimensions of the sample prevent an empirical test of the magnetization it has to be calculated. To estimate the effective magnetization of the sample, the demagnetization factor has to be known. By approximating the geometry and using the dependence given in [Aharoni, 1998], a demagnetization factor of 0.70 can be approximated. Using the data of H. J. Williams [1937] on the field dependent magnetization of $Fe_{0.97}Si_{0.03}$ it can be estimated that the sample reaches just 65 % of the saturation magnetization. Hence, the effective polarization of a measurement is reduced to 20 %.

Using this effective polarization, the majority and minority spin channel were separated. In figure 40 and 41 a) and b) the results are shown for the [100] and [110] projection, respectively. In the [100] projection (figure 40), most of the features are very similar in both spin channels. It is mainly the intensity which changes from majority to minority. The elements ①, ② and ③ are common to the majority and minority spectra. However, ① is the most dominant feature in the majority spin channel, while ② and ③ are much more pronounced in the minority spin channel. In contrast, the items ④ and ⑤ are different in the both spin channels. In the

majority channel ② and ④ are clearly separated by a high intensity region, while in the minority spin channel the two elements are connected. Furthermore, the arrow like feature ⑤ is much wider in the minority channel.

The [110] projection (figure 41) shows more characteristics which are unique to minority or majority spin channel, probably due to the lower symmetry. The most dominant elements are the low intensity wedge ② and the high intensity finger ③. Both have distinct shape in the majority and the minority spin channel, with the finger being much longer in the minority spectrum. Notably, the low intensity pillow ① and the high intensity pillow ④ are even missing in the majority spin channel. Finally, also the tilting of the knob-like feature ⑤ is different to both spin channels.

The many differences of majority and minority spin channel suggest that the analysis of the measurement was successful and that both spin channels could be separated. For an assignment of the various features to characteristics of the Fermi surface of iron, state-of-the-art band structure calculations are indispensable.

Comparison of Fe to $Fe_{0.97}Si_{0.03}$

As mentioned above, for some studies iron crystals with a low amount of silicon, which stabilizes the bcc phase, were used. For example N. Shiotani et al. [1992] argued that the influence of 3 % silicon on the magnetic properties of iron is small and hence the influence on the electronic structure is also expected to be insignificant and limited to structural disorder.

In this thesis the electronic structures of both Fe and $Fe_{0.97}Si_{0.03}$ are compared directly for the first time. To exclude effects of varying sample magnetization only the summed spectra $\Sigma M = M^{\uparrow} + M^{\downarrow}$ are considered. Since both crystals were measured with a different crystallographic axis pointing along the direction of positron emittance, both measurements were convolved with a Gaussian point spread function of 0.86 mrad (FWHM) in order to make the resolution isotropic. Thus, a direct comparison of the datasets is possible.

Figure 43 shows the normalized 1D [011] projection of Fe and $Fe_{0.97}Si_{0.03}$. Already in this plot, the difference between Fe and $Fe_{0.97}Si_{0.03}$ is striking as the TPMD of pure iron is narrower. The anisotropies of both samples [see fig. 42 a)] look qualitatively very similar. However, the anisotropy of iron is much less pronounced than the one of $Fe_{0.97}Si_{0.03}$ although both spectra were equally normalized. That the differences are not limited to a scaling effect as can be seen from the cuts along the [100] and the [011] direction in figure 42 c). Although the cuts are similar, there are a lot of characteristics which are unique to one spectrum. The most dominant feature in the Fe anisotropy is the large low intensity pocket ①. If the silicon would cause significant disorder, one would expect the $Fe_{0.97}Si_{0.03}$ anisotropy to be blurred or to be less pronounced. This is not the case as demonstrated by the difference between both spectra in fig. 42 b). Except for the very dominant high to low intensity transition caused by the different width of the Fe and $Fe_{0.97}Si_{0.03}$ distributions there exist certain features which are common to both datasets and appear in white like the four small capsules at ③. Other features

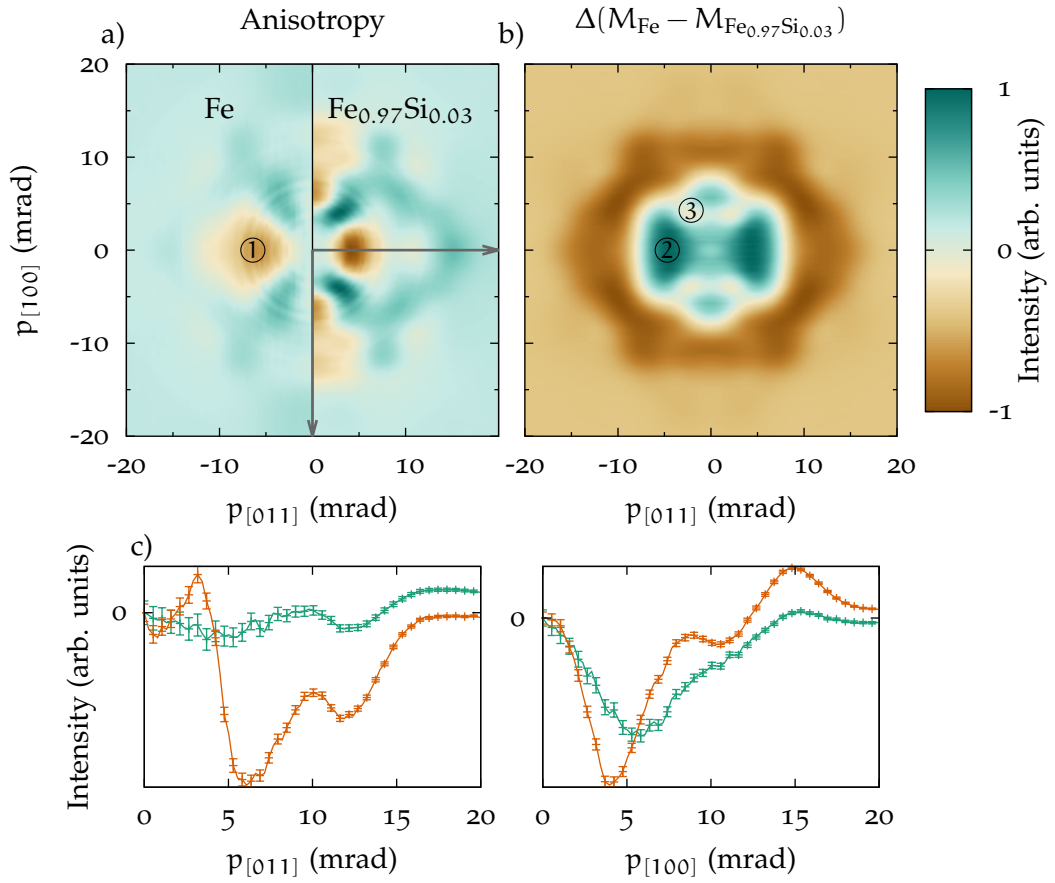

Figure 42: Comparison of the TPMDs of Fe and $Fe_{0.97}Si_{0.03}$. In each graph, the sum of majority and minority spin channel in the [011] projection is shown. a) Anisotropies of the normalized spectra, b) difference $\Delta(M_{Fe} - M_{Fe_{0.97}Si_{0.03}})$, c) cuts through the anisotropy of Fe and $Fe_{0.97}Si_{0.03}$ along the arrows in a).

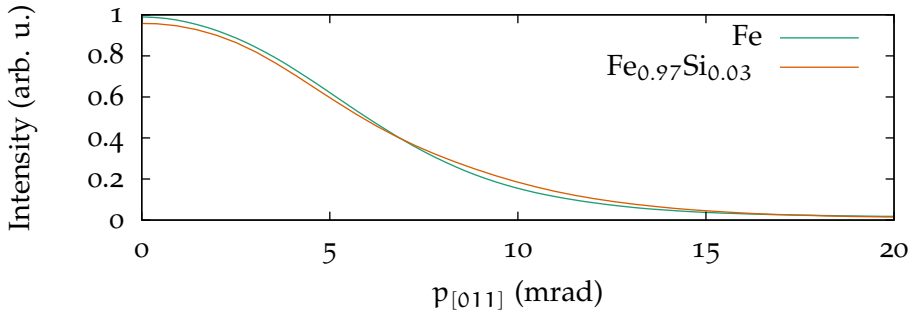

Figure 43: Normalized 1D [011] projection of Fe and $Fe_{0.97}Si_{0.03}$ using the summed majority and minority spin channel.

can be attributed exclusively to one of the two datasets, e. g., the high intensity pockets at ②.

A simple explanation for these observations is that the iron sample has a low but notable defect concentration. This is supported by two facts: i) The Fe distribution is narrower (the S-parameter is higher) which indicates an increased annihilation with valence electrons and therefore annihilation in defects. ii) A weak anisotropic signal also hints at a small defect concentration, because the electron momentum components are blurred by the confined positron wave-function.

For an elemental system, it is rather unusual to have structural defects after crystal growth as the ordering kinetics are very fast. However, due to the difficulties of single crystal growth of iron it seems to be possible that defects were introduced. Another possibility is that the defects were introduced during sample preparation. Hence, they could by removed by etching. The usual removal of defects via heat treatment is not possible in this case because of the structural phase change.

Additional to the defect caused isotropic contribution in the iron spectrum, there are distinct differences in the anisotropies which indicate that either i) the electronic structure in the Fe sample is significantly influenced by the defects, ii) the electronic structure in the $Fe_{0.97}Si_{0.03}$ sample is significantly influenced by the Si or iii) both. To find out which of the above holds an investigation on a defect free sample or the backup from theoretical calculations is necessary.

Discussion

Iron is a system with great relevance which has been heavily investigated in the past. However, the recent publication of Gosálbez-Martínez, Souza, and Vanderbilt [2015] demonstrates that iron still exhibits properties waiting for an experimental verification like the tiny pockets in band 10. Here, two iron compositions, namely pure iron and $Fe_{0.97}Si_{0.03}$, were investigated with 2D-ACAR. It was found, that the general agreement between first ab initio calculations was remarkably good. Furthermore, using the polarization of the positrons the majority and the minority spin channel of electron momentum density could be separated as demonstrated in figure 40 and 41. During the direct comparison of the ACAR spectra of pure iron and $Fe_{0.97}Si_{0.03}$ it was revealed that the spectra differ significantly. However, this is probably not caused by the presence of Si in Fe but by defects which are present in the pure iron sample.

Since the quality of the recorded data is very high it could be possible to address some of the theoretical predicted FS features by Gosálbez-Martínez, Souza, and Vanderbilt [2015]. Considering that most of the prognosticated FS features are small compared to the experimental resolution, they can probably only be found indirectly by a comparison with theoretical spectra. Already the first principle calculations done in this thesis were in very good agreement with the experimental data (see figure 39). With more sophisticated calculations, the agreement between theory and experiment could certainly be improved. Therefore, also quantitative predictions about the FS seem to be possible with the correct theoretical input.

For future studies, especially the spin-polarized information is interesting, as it allows to experimentally distinguish between majority in minority sheets. With

some theoretical effort it should be feasible to compare this data to the spin polarized ARPES results of Schäfer et al. [2005] in order to classify to what extend the transition from the bulk to the surfaces affects the electronic structure and the FS.

11.3 THE ELECTRONIC STRUCTURE OF VANADIUM

Vanadium is one of the first 3d transition metals with an electron configuration of [Ar] $3d^3$ $4s^2$. Compared to Al which has also three conduction electrons, its electronic structure is far more complex and cannot be modeled by the free electron gas. Interestingly, the isoelectronic systems niobium, tantalum and dubnium have a very similar electronic structure [Papaconstantopoulos, 2015]. Thus, understanding the electronic structure of vanadium is relevant for these systems, too.

Vanadium has been intensively studied (see listing 3) mainly with positron annihilation. The reason for this might be that the FS gives a very pronounced signal in the ACAR spectrum. Furthermore, vanadium seems to be difficult to characterize with quantum oscillation and photoemission studies as the cited publications cover just a few aspects of the electronic structure: The quantum oscillation experiments were only able to resolve the N-hole pockets but gave very little information about the jungle-gym surface and no information about the first octahedral hole surface at all. The photo emission studies could solely measure three points of the dispersion relation. Even previous positron studies often did not identify the FS directly (although at least in one case a 3D reconstruction was calculated [L. M. Pecora et al., 1988]), but rather compared their measurements to band theoretical calculations. An exception is the work of Manuel [1982] who reconstructed the different FS sheets.

In this thesis, two approaches are chosen: i) the experimental results are compared to state-of-the-art DMFT calculations ii) the complete FS is extracted from the measurements.

POSITRON STUDIES: Dugdale et al., 1994, 2013; Hughes et al., 2004; Major et al., 2004; Manuel, 1982; Manuel et al., 1983; Matsumoto and Wakoh, 1986; L. M. Pecora et al., 1988; Nobuhiro Shiotani et al., 1975; A. K. Singh et al., 1985; A. K. Singh and Singru, 1984; Wakoh, Yasunori Kubo, and Yamashita, 1975

QUANTUM OSCILLATION STUDIES: Parker et al., 1974; Phillips, 1971

PHOTOEMISSION STUDIES: Perić et al., 1995; Pervan et al., 1996

OTHER EXPERIMENTAL STUDIES: Chen et al., 2005; N. Shiotani et al., 1992; Nobuhiro Shiotani et al., 1993

THEORETICAL STUDIES: Bouarab et al., 1992; Boyer, Papaconstantopoulos, and Klein, 1977; Papaconstantopoulos, J. R. Anderson, and McCaffrey, 1972; A. K. Singh and Jarlborg, 1985; Solanki, Ahuja, and S. Auluck, 1992; Tokii and Wakoh, 2003

Listing 3: Selection of publications on the electronic structure of vanadium.

Sample Preparation and Measurement

A single crystalline vanadium rod with 10 mm length, 6 mm diameter and a purity of 5N was bought from GoodFellow. It was oriented and cut into a disc of approximately 1 mm thickness and its surface polished in the crystal lab. In figure 45 a), the finished sample with crystallographic directions is shown.

Five projections were recorded at room temperature by turning the sample around the [110] axis, collecting in average 35×10^6 counts. The projections comprised the main symmetry directions [001], $[1\bar{1}0]$, and $[1\bar{1}1]$ and the projections 20° and 70° with respect to the [001] direction.

Comparison with Theory

Two 2D-ACAR spectra, namely the [001]-projection, were calculated by Liviu Chioncel from the Universty of Augsburg based on either the LDA or the DMFT schema. Both calculations included the electron-positron correlation by an enhancement model. In this study, ACAR measurements on vanadium ([100] projection) are analyzed qualitatively and quantitatively with LDA/DMFT calculations in several ways: By comparing the spectra directly, by comparing the anisotropies and the LCWs.

In figure 44, the experimental and theoretical data are presented: In the left column a direct comparison between experiment, LDA and DMFT is shown. It can be noted that the agreement between theory and experiment is excellent. The presence of an unusual strong anisotropy is even evident from the raw spectra. Especially at the (H,Γ_2)-point there is substantially less spectral intensity. This can also be observed in the anisotropy, where Γ_1 and Γ_2 are connected by a pronounced diagonal feature. Since the shape of the FS is predicted by theoretical calculations (see e. g., Major et al. [2004]), this low intensity can be attributed to the jungle-gym and the octahedral hole surface, which both extend in this diagonal direction. A second distinct detail is the low intensity bulb at the (N,P)-point. This bulb originates from the ellipsoidal hole pocket at the N point. The described features can also be found after the LCW transform in k-space: The diagonal jungle-gym tubes and the octahedral hole pocket at Γ as well as the N-centered hole pocket. The presented data are in reasonable agreement with previous measurements (see e. g., A. K. Singh et al. [1985] for the LCW and the raw spectra or Dugdale et al. [2013] for the LCW).

In order to identify the differences between the two theories and the measurement more easily, the right column was created showing the quantity

$$\Delta M = a(\text{theory}) - (\text{experiment}) + b. \tag{137}$$

The scaling contstant a and the background b were determined by a least squares fit. It can be noted that the anisotropy and the LCW k-space density are almost identical and hence ΔM is very small. For both quantities it does not matter which sort of calculation - DMFT or LDA - has been used. However, for the raw spectra the differences are significantly larger, especially for the LDA calculation: On the LDA side one can see a large discrepancy in the first BZ which resembles the jungle

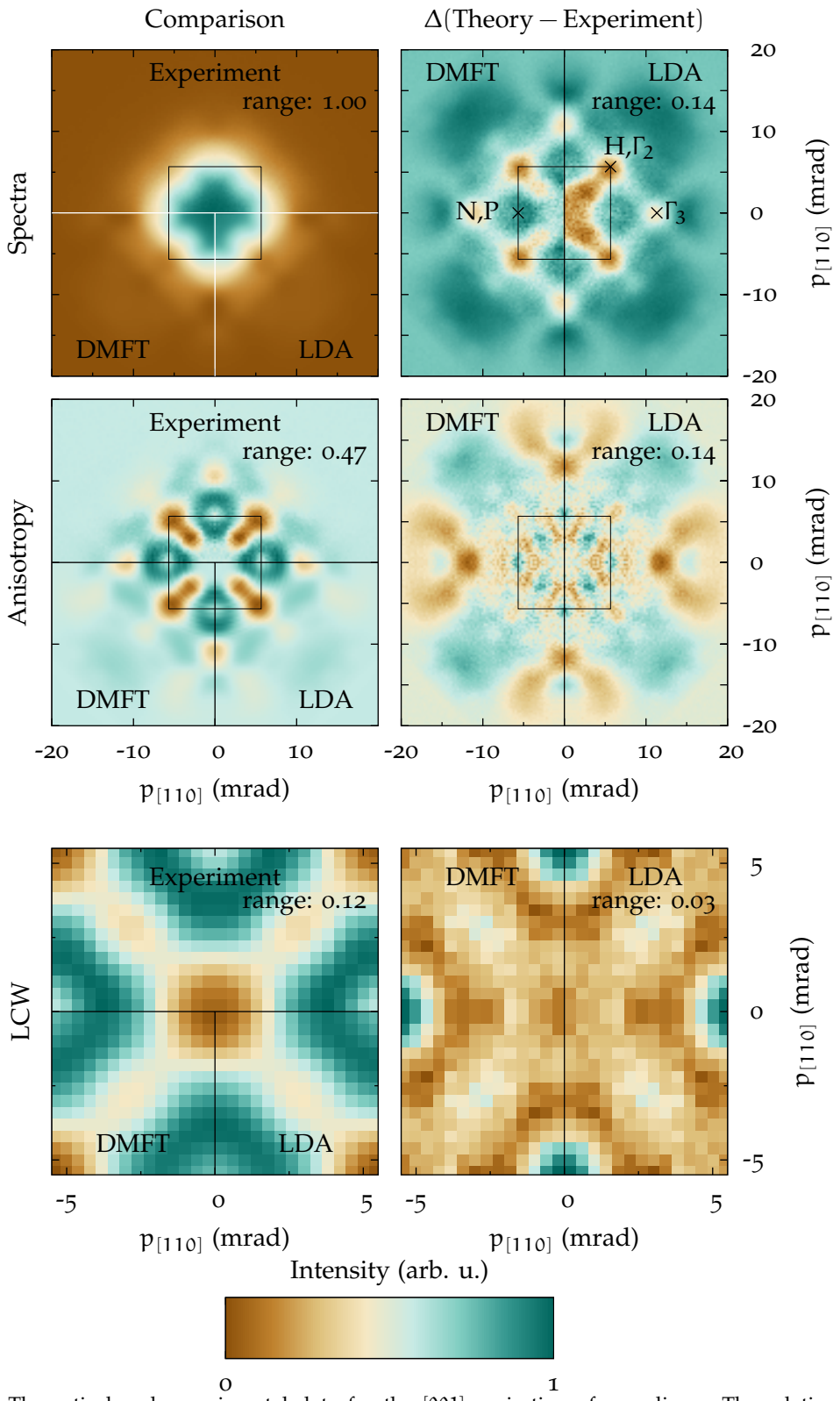

Figure 44: Theoretical and experimental data for the [001] projection of vanadium. The relative dynamic range is given in every plot explicitly. *Left:* Comparison between DMFT and LDA spectra with the experimental ones either by the raw data, the anisotropy or by the LCW-folding. *Right:* Difference between theory and experiment Δ(Theory − Experiment) for raw data, anisotropy and LCW-folding. The square in the center corresponds to the outline of the first BZ. In the upper right figure, some of the high symmetry points are marked. The subscript index corresponds to the second/third neighboring BZ. For the [001] projection, N and P as well as Γ and H overlie.

gym and the octahedral hole surface. The experimental intensity of this feature is much larger than the intensity in the calculation. In the DMFT calculation, there is also some discrepancy especially at the Γ_2 points, but the overall agreement is much better.

To asses the agreement between experiment and theory quantitatively the χ^2 per degree of freedom for LDA and DMFT is given in the following table.

	χ^2(LDA)	χ^2(DMFT)
Raw Spectrum	120.15	102.90
Anisotropy	4.12	4.05
LCW	2.99	3.03

These results verify the previous qualitative estimation: i) For the anisotropy and the LCW, the agreement between experiment for both calculations is very good. In particular, the difference of χ^2 is statistically not significant. ii) The agreement for the raw spectra is less perfect and the DMFT is able describe the data significantly better.

A possible explanation for the large difference in $\rho(\mathbf{p})$ and a small difference in $\rho(\mathbf{k})$ is the weighting of the momentum coefficients. For a specific momentum $\mathbf{p}$ the difference between theory and experiment is given by

$$\Delta M(\mathbf{p}) = \sum_j \left(\left| C_{\mathbf{G},j}(\mathbf{k}) \right|^2 - \left| E_{\mathbf{G},j}(\mathbf{k}) \right|^2 \right) \delta(\mathbf{p} - (\mathbf{k} + \mathbf{G})) \tag{138}$$

with a reciprocal lattice vector $\mathbf{G}$ and the momentum coefficients $C_{\mathbf{G},j}(\mathbf{k})$ and $E_{\mathbf{G},j}(\mathbf{k})$ of the theoretical and experimental electronic state $\Psi_j(\mathbf{k})$. In the LCW however, the difference is given by

$$\Delta M(\mathbf{k}) = \sum_{\mathbf{G}} \sum_j \left(\left| C_{\mathbf{G},j}(\mathbf{k}) \right|^2 - \left| E_{\mathbf{G},j}(\mathbf{k}) \right|^2 \right). \tag{139}$$

Since the coefficients $|C|^2$ and $|E|^2$ are normalized, any $\mathbf{G}$ dependence cannot be seen in the LCW transform. Furthermore, as the $\mathbf{G}$ dependence is very similar for states in the same band j it will also mostly cancel out in the anisotropy. Hence, the $\mathbf{G}$ dependence is most decisive in the comparison with the raw spectra.

The $\mathbf{G}$ dependence in the momentum coefficients is mathematically a consequence of the potential that the electron experiences in the solid. As the exchange correlation potential is treated in the DMFT explicitly, the large difference between the LDA spectra and the experiment is probably an electronic correlation effect.

3D Reconstruction

Despite being studied intensively - both theoretically and experimentally - there is only very limited information about the FS of vanadium. Although Manuel [1982] did a reconstruction of the FS he only gave a very qualitative comparison. Two exceptions with quantifiable results are the dHvA study of Phillips [1971] and the theoretical study of Tokii and Wakoh [2003]. Results of both investigations are shown in figure 45 b).

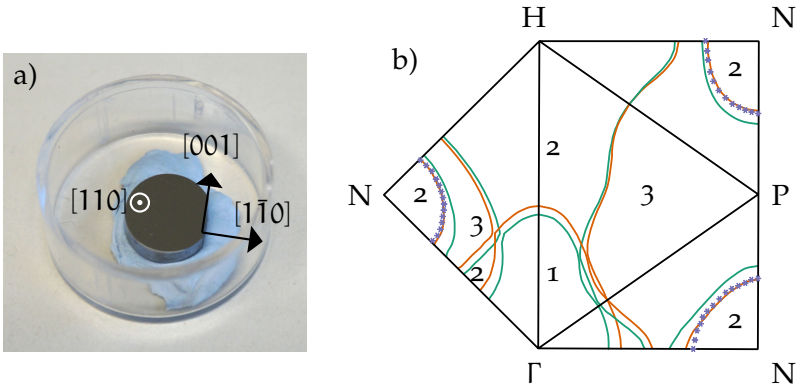

Figure 45: a) Vanadium sample with crystal directions: The [110] direction is in plane; [001] and [1$\bar{1}$0] are out of plane. b) FS outline in various high symmetry planes in the BZ for LDA (green) and LDA+U (orange) calculations by Tokii and Wakoh [2003]. The violet stars correspond to the experimental results on the shape hole pocket by dHvA measurements [Phillips, 1971].

Phillips [1971] was able to resolve the shape of the ellipsoid N-hole pockets and gave the dimensions of the semi-axis NP, NΓ and NH as 0.224, 0.212 and 0.176 in units of the reciprocal lattice constant. Tokii and Wakoh [2003] performed LDA and LDA+U calculations with which they could reproduce the results of Phillips [1971]. As Tokii and Wakoh [2003] gave cuts through the main symmetry directions of the FS [see fig. 45 b)] their result can be compared with the experimentally determined FS.

The reconstruction of the 3D $\rho^{2\gamma}(\mathbf{p})$ was created from the five measured projections as explained in chapter 10 taking into account the full symmetry of the problem and the experimental resolution. Using the LCW procedure for 3D, $\rho^{2\gamma}(\mathbf{p})$ was then folded back into $\mathbf{k}$-space. In order to show the FS an iso-value was chosen according to the experiments of Phillips [1971]. In figure 46 a) the reconstructed FS sheets are shown.

All theoretically predicted features are present in the reconstruction: The N-hole pockets, the jungle-gym and the bulged octahedron. Notably, they do not agree with the sheets shown in the well-known FS Database [*Fermi Surface Database, Vanadium* 14.07.2007]. In particular, there is no connection between the N-hole pockets and the jungle-gym surface between Γ and N. This connection is also not present in the calculations of Tokii and Wakoh [2003] [see fig. 45 b)]. Compared to the measurements of Phillips [1971] the N-hole pocket is a bit shortened in NP direction, while the other semi-axis of the ellipsoid agree very well. In contrast to the reconstruction of Manuel [1982], the N-hole pocket agrees much better with the theoretical prediction. Several details of the Tokii and Wakoh [2003] calculation are reproduced by the reconstruction. The jungle-gym e. g., widens from Γ to H and has a larger diameter in the HN direction than in the HP direction. However, other details are not as accurately reflected. Specifically, the jungle-gym is much narrower in the calculation at the BZ center than it is in the reconstruction which might be attributed to the limited experimental resolution.

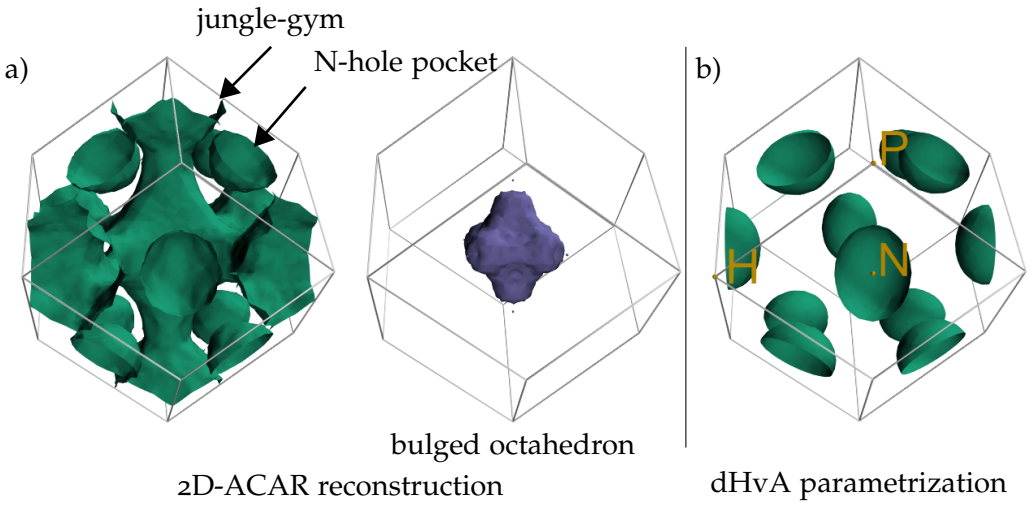

Figure 46: a) Reconstructed Fermi surfaces of vanadium. Both surfaces are hole like, i. e. the occupied states are between the ellipsoidal N-hole pockets and the jungle-gym for the left surface, and outside of the octahedron for the right surface. b) N-hole surface experimentally determined by an ellipsoidal parametrization of dHvA-measurements from Phillips [1971].

Discussion

In this study the electronic structure of vanadium was investigated by comparing 2D-ACAR measurements and band theoretical calculations. It was found that the calculations can reproduce the experimental results. A better quantitative agreement is achieved by the DMFT calculations, however just for the raw spectra, probably due to a more exact correlation potential. Additionally, the FS was extracted from the measurement by a 3D reconstruction. Three FS sheets were found which agree topologically with previous calculations. Moreover, the reconstruction can confirm several details predicted by calculation.

12

SPIN-POLARIZED STUDIES ON THE HEUSLER SYSTEM Cu_2MnAl

The material class of Heusler alloys is known for diverse extraordinary phenomena found in these systems [Graf, Felser, and Parkin, 2011]. One examples of these exceptional properties is half-metallicity, which was predicted in the early 80s by de Groot et al. [1983] and Kübler, William, and Sommers [1983] and was later verified by means of spin-polarized 2D-ACAR spectroscopy [Hanssen and Mijnarends, 1986; Hanssen et al., 1990]. Other examples include the shape memory effect in Ni_2MnGa [Ullakko et al., 1996] and the zero gap semiconductor Fe_2TiSn [Ślebarski et al., 2000]. The most recent and most exotic member of the Heusler family is the material Mn_2CoAl being the precursor of a novel material class, the spin gapless semiconductors [Ouardi et al., 2013].

These examples prove that the relation between elemental composition and electronic properties is very sensitive as shown by several theoretical studies [Kübler, William, and Sommers, 1983; Şaşıoğlu, Sandratskii, and Bruno, 2008]. For this reason, detailed knowledge about the electronic interactions is necessary to verify and to improve the accuracy of theoretical calculations. In particular for the development of novel materials with specific properties, reliable ab initio calculations are essential.

The attempt of the present study is to contribute substantially to the understanding of and to increase the knowledge about Heusler alloys. For this purpose, the Heusler compound Cu_2MnAl was chosen as it is the model system for understanding the electronic correlations in this family of materials. (see e. g., Galanakis and Şaşıoğlu [2012], Krumme et al. [2011], and Şaşıoğlu, Sandratskii, and Bruno [2008]). Moreover it is the first compound Heusler, Starck, and Haupt [1903] discovered and thus already interesting from a historical point of view. Additionally, Cu_2MnAl has practical relevance as it is used as neutron monochromator and polarizer material [Delapalme et al., 1971; Neubauer et al., 2012].

12.1 SAMPLE PREPARATION

Several reports suggested that the single-crystal growth of Cu_2MnAl is challenging as it forms congruently but decomposes peritectoidly into Cu_9Al_4, Cu_3Mn_2Al, and β-Mn below 923 K (see e. g., Robinson, McCormick, and Street [1995] for a comprehensive overview). Nevertheless, Neubauer et al. [2012] succeeded to grow large single crystals by means of optical float zoning. It is presumed that the phase decomposition is suppressed by the slow kinetics due to the advantageous temperature profile during and after growth.

For this experiment, a single crystal of Cu_2MnAl (serial number: OFZ87) with a diameter of 8 mm and a length of 40 mm was grown by Andreas Bauer at E21/TUM. The starting materials were stoichiometric amounts of copper (6N),

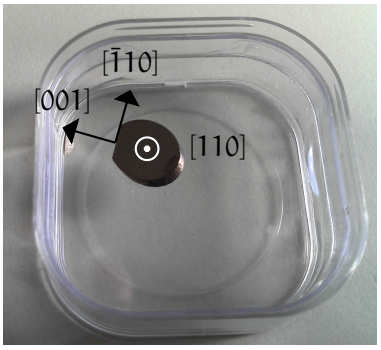

Figure 47: Cu_2MnAl sample OFZ87-3-2 prepared with the crystallographic directions indicated. The diameter is approximately 8 mm and the thickness is 1 mm.

manganese (4N), and aluminum (6N). Prior to the determination of the weight, the manganese flakes were etched and cast to solid rods in order to remove impurities. The precasting and the further preparation of the two polycrystalline feed rods was carried out in an inductively heated all-metal-sealed rod casting furnace that is based on a Hukin-type cold crucible. These two rods were then mounted into the all-metal-sealed image furnace for the actual single crystal growth. Before the start of the growth process the furnaces were pumped and baked out until UHV pressure was reached. During growth, an atmosphere of about 2 bar of 6N argon additionally purified by point-of-use gas purifiers was created in the furnace. The rods were rotated counter clockwise at 6 rpm while the focus of the furnace was constantly moved resulting in a growth speed of 10 mm/h.

By Laue back-reflection the resulting single-crystal ingot was oriented and cut with a wire saw. In figure 47 the sample (hereafter called OFZ87-3-2) with the crystallographic orientations is depicted. The slightly oval disc has a diameter of approximately 8 mm and a thickness of 1 mm. The large surfaces were carefully polished. For the magnetization measurements and wavelength-dispersive X-ray fluorescence spectroscopy (WDX) cuboid samples of $2 \times 2 \times 1\,mm^3$ were cut from of a neighboring part of the same ingot.

12.2 SAMPLE CHARACTERIZATION

Before making general statements about the nature of the electronic interactions in Cu_2MnAl it is important to characterize the sample to have a well defined starting point for the investigation of the electronic structure.

Determination of the Lattice Constant

The lattice constant of the sample is highly important for two reasons: On the one hand it is necessary as an input parameter for the ab initio calculations and on the other hand it is influenced by the order of the sample and can provide a measure for the sample quality.

In order to determine the lattice parameter of the investigated sample, a XRD measurement on the sample OFZ87-3-2 was conducted by Wolfgang Kreuzpaint-

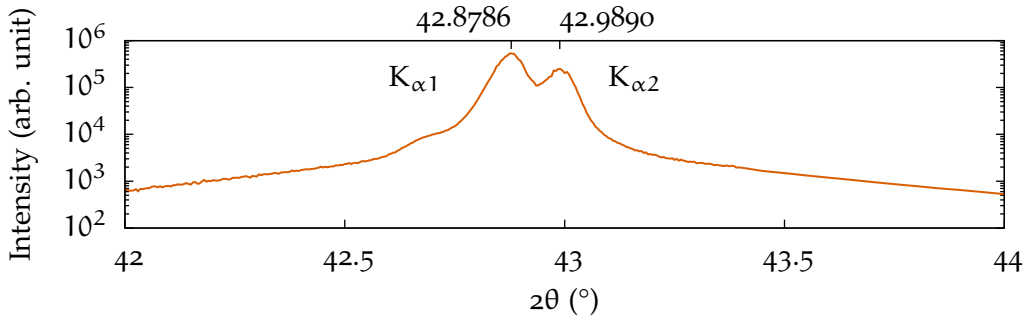

Figure 48: Cutout of the diffractogram of Cu_2MnAl around the [022] peak. The $K_{\alpha 1}$ and $K_{\alpha 2}$ lines can clearly be discerned.

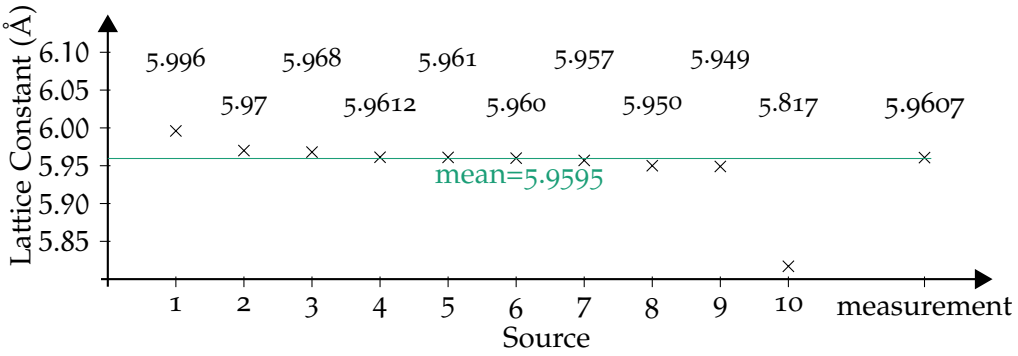

Figure 49: Experimentally determined lattice constants from various sources: 1) Neubauer et al., 2012 2) Robinson, McCormick, and Street, 1995 3) Buschow, van Engen, and Jongebreur, 1983 4) Dubois and Chevereau, 1979 5) Kunzler et al., 1980 6) Dunlap, Stroink, and Dini, 1986 7) Sołtys, 1981 8) Paranjpe and Begum, 1980 9) Oxley, Tebble, and K. C. Williams, 1963 10) Dong et al., 2012. The green line corresponds to the mean value of source 2 to 9.

ner at E21/TUM. This measurement yielded a lattice parameter of (596.07 ± 0.01) pm at room temperature.

In figure 49 the previously in the literature reported lattice constants are listed. Except for the highest and the lowest values, which were probably affected by systematic problems, all the reported lattice constants agree within 1.8 %. However, the accuracy of a typical diffraction measurement is much higher. Hence, this variety already indicates different order in the samples.

In comparison with the literature values, the investigated sample's lattice constant is close to their mean. However, solely from this fact no conclusions about the short range order in the sample can be drawn.

12.2.1 *Analysis of the Composition*

In this investigation WDX was chosen, to measure the composition the Cu_2MnAl sample. Using this technique, very accurate measurements of the sample stoichiometry can be made. At first, X-ray fluorescence transitions will be excited by incident electrons. In contrast to EDX, where the total spectrum of fluorescence is collected, in WDX, only the intensity of narrow parts of the spectra is recorded

	Cu	Mn	Al
%	50.73 ± 0.17	23.97 ± 0.14	25.26 ± 0.21
stoichiometry	2.030 ± 0.007	0.959 ± 0.006	1.011 ± 0.008

Table 10: Result of the WDX analysis. The first row gives the percentage of atoms in the sample while the second row gives the stoichiometrical composition

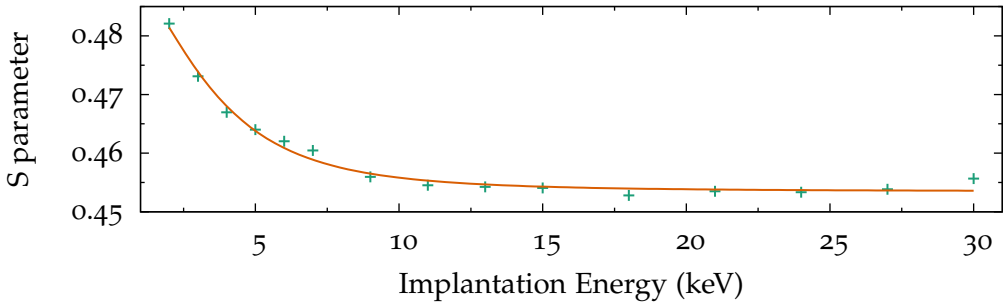

Figure 50: S parameter as a function of the positron implantation energy (green) and fitted dependence using the Monte Carlo software package VEPFIT (orange).

with very high accuracy. By comparing this intensity to the intensity of reference materials with similar but known composition, the exact composition of the sample can be inferred. Obviously, the quality of the result crucially depends on the choice of the reference materials.

The WDX analysis was done by Sebastian Widmann at the University of Augsburg, not on the sample OFZ87-3-2 itself but on a neighboring piece. The result of this analysis is given in table 10. Although the composition is not perfect, it is very close to the nominal 2:1:1 stoichiometry. However, there seems to be a significant Mn deficiency in the sample, which has to be compensated by Cu and Al sitting on Mn sites. This result seems conclusive as manganese has the highest vapor pressure and is thus prone to vanish during crystal growth. The deficit in Mn content could also stem from the thermodynamics of the growth. If manganese is more soluble in the melt than in the solid, the melt zone will have an increased Mn content, while the Mn content in the crystal will vary from the starting point of growth until an equilibrium between molt and solid is reached. This theory could be checked by further WDX measurements.

12.2.2 *Defect analysis*

In order to ensure the sample quality with respect to the vacancy concentration, a detailed DBAR study has been conducted by Markus Reiner on the sample using the high intense positron beam NEPOMUC [Hugenschmidt et al., 2015]. As shown in chapter 3.2.1, by varying the energy of the incident positrons, a variation in the implantation depth can be achieved.

Figure 50 shows the measured S parameter for various implantation depths. By Reiner using the software VEPFIT [van Veen et al., 1991] the positron diffusion length was extracted from this data. Using further reasonable assumptions for the diffusivity and the charge carrier mobility he gained a vacancy concentration in the

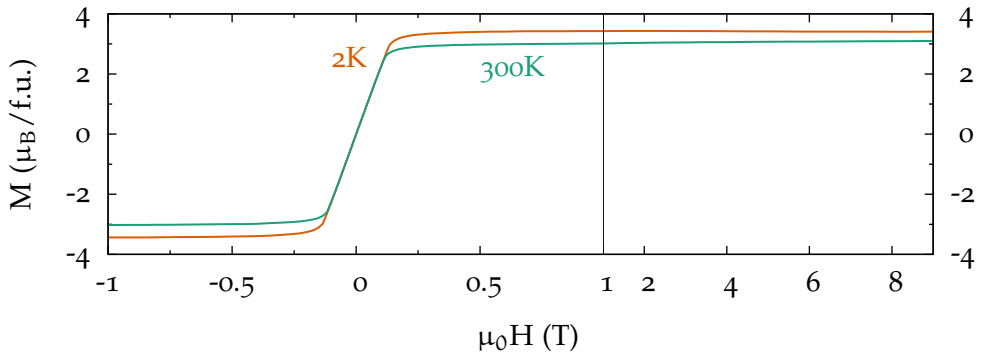

Figure 51: Magnetization measurement by means of the PPMS at 2 K (orange) and 300 K (green). In order to enlarge the most interesting section around 0 T, the x-axis in the left part and the right part are scaled differently.

order of 10^{-5} per atom [Hugenschmidt et al., 2015]. This vacancy concentration is very low and close to the detection limit. Therefore, the sample is particularly suited for ACAR spectroscopy as no defect signature will alter the signal of the electronic states.

12.2.3 *Magnetization Measurements*

The magnetization of the Cu_2MnAl sample was determined in three different ways: By magnetic Compton scattering (see section 4.4), by a vibrating sample magnetometer (VSM) and by a physical properties measurement system (PPMS). While for the first two methods the sample OFZ87-3-2 was used, the PPMS is only able to measure samples with a smaller size and therefore the measurement was conducted on a neighboring piece of the same single crystal.

Measurement with the Physical Property Measurement System

The magnetization measurements on a neighboring sample were done by Andreas Bauer using an of the shelf PPMS by Quantum Design. For the dc magnetization measurements, the device employs a so-called extraction technique, which is based on the same physical principles like a VSM (see bellow). In order to get a quantitative result, the apparatus has to be gauged with a sample of well-known magnetization, in this case a nickel sample. Further details about the PPMS can be found e. g., in A. Bauer [2014] and Wagner [2014].

The result of the magnetization measurement (not taking into account the demagnetization factor) is shown in figure 51. It is evident that no hysteresis is present in the specimen. This indicates a small magnetocrystalline anisotropy on the one hand and a high sample quality on the other hand. The magnetization of the sample saturates well below 1 T at 2 K while at 300 K there is still a very small increase of the magnetization up to 9 T. From this data it is possible to extract a saturation magnetization of 3.4 μ_B (f.u.)$^{-1}$ at 2 K and 3.1 μ_B (f.u.)$^{-1}$ at 300 K.

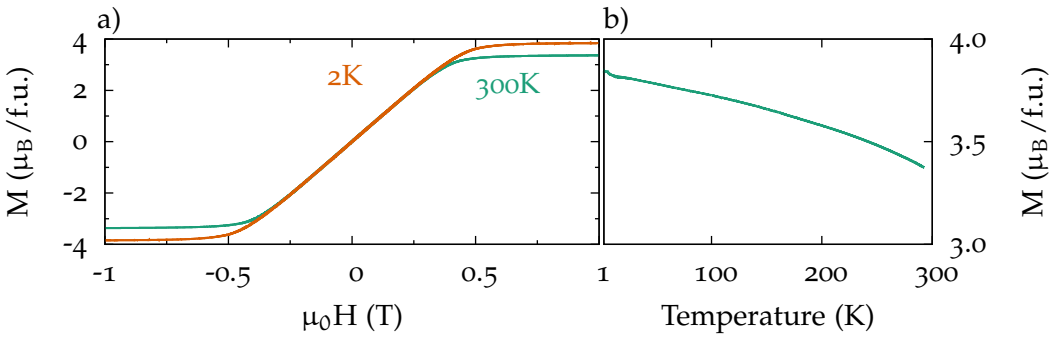

Figure 52: Magnetization measurement on the sample OFZ87-3-2 with the VSM. a) Magnetization vs. external magnetic field at 2 K (orange) and at 300 K (green). b) Temperature dependent magnetization at 1 T.

Measurement with the Vibrating Sample Magnetometer

The working principle of a VSM is based on moving ('vibrating') a ferromagnetic sample in a constant magnetic field past a pair of pickup coils. In these coils a voltage is induced which is proportional to the magnetization of the sample. For a quantitative measurement this apparatus was calibrated with a nickel sample. The crucial difference between the PPMS and the VSM is that the used VSM from Oxford Instruments is able to measure larger samples. Therefore, it was possible to determine the magnetization of the sample OFZ87-3-2 up to 1 T directly.

The results of the VSM measurements in figure 52 a) look quite similar to the PPMS measurements in figure 51. However, the susceptibility, i. e. the slope, around 0 T is much smaller than in the previous measurement. This difference is caused by the influence of the sample geometry to the demagnetization factor. Since the magnetic field inside the VSM was perpendicular to the flat side of the sample, the demagnetization factor was large. Nevertheless, the measurement revealed that the magnetization of the sample is fully saturated at 1 T and 2 K and to the uttermost extend at 1 T and 300 K. The values for the magnetization were 3.4 μ_B (f.u.)$^{-1}$ at 300 K and 3.8 μ_B (f.u.)$^{-1}$ at 2 K.

In addition to the field dependence, also the temperature dependence of the magnetization has been recorded for temperatures between 2 K to 300 K (see figure 52 b)). At 300 K, the drop in magnetization is only marginal. From this fact it can be concluded that the Curie temperature has to be much higher than 300 K. This is in good agreement with previous studies where a Curie temperature of approximately 630 K was found [Endō, Ohoyama, and Kimura, 1964; Oxley, Tebble, and K. C. Williams, 1963; Paranjpe and Begum, 1980].

Magnetization Studied by Magnetic Compton Spectroscopy

Magnetic Compton scattering can determine the spin dependent electron density in a solid. However, it is not possible to extract the magnetization from this information directly, because of the unknown ratio of the magnetic and the charge cross section. Nevertheless, by using a ferromagnetic reference sample the spin dependent contribution to the magnetization can be derived.

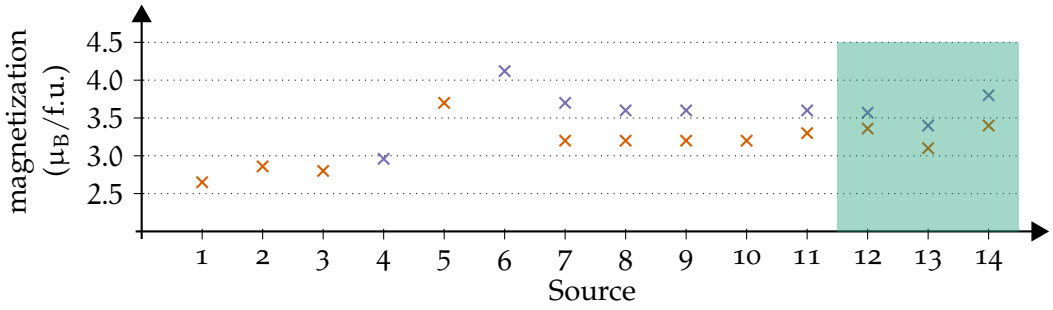

Figure 53: Magnetic moment of Cu_2MnAl from various sources in literature. The orange/blue points correspond to the magnetic moment at 300 K/4 K (if not noted differently). The green highlighted points correspond to the values which were experimentally determined during this thesis. 1) Żukowski et al., 1997 by magnetic Compton 2) Żukowski et al., 1997 by magnetic balance 3) Dunlap, Stroink, and Dini, 1986 4) Hurd, Shiozaki, and McAlister, 1982 5) Paranjpe and Begum, 1980 6) Oxley, Tebble, and K. C. Williams, 1963, extrapolated to 0 K 7) Felcher, Cable, and Wilkinson, 1963, blue value at 77 K 8) Buschow, van Engen, and Jongebreur, 1983 9) Neubauer et al., 2012 10) Robinson, McCormick, and Street, 1995 11) Endō, Ohoyama, and Kimura, 1964 12) magnetic Compton 13) PPMS, and 14) VSM.

As systematic errors are small, the accuracy is limited by the statistical precession of the measurement. Therefore, the magnetization can be determined much more precisely than with a VSM or PPMS. Using this technique in a static magnetic field of 1 T, a magnetization of $(3.57 \pm 0.08)\,\mu_B\,(\text{f.u.})^{-1}$ at 4 K and $(3.36 \pm 0.07)\,\mu_B\,(\text{f.u.})^{-1}$ at 300 K was measured.

Conclusion

As the magnetic moment is an essential property of Cu_2MnAl, many measurements have already been reported. An overview of literature values at 4 K (blue) and 300 K (orange) is given in figure 53. Obviously, the reported measurements are widely scattered. One reason for this is certainly the accuracy of the magnetization measurements. Even the PPMS and the VSM measurement vary significantly although the magnetization was determined on neighboring pieces of the same crystal. Hence, the deviation has to be caused by a systematic error.

Another reason for the different magnetization is the different short range order of the samples. Already Heusler noted that by heat treatment, the magnetization of Cu_2MnAl specimens can be increased [Heusler, Starck, and Haupt, 1903]. This observation was confirmed by several other groups and was attributed to an increase in order (see e. g., Endō, Ohoyama, and Kimura [1964] and Oxley, Tebble, and K. C. Williams [1963]). Especially, the very low magnetic moment in the report of Żukowski et al. [1997] can only be caused by a not fully ordered state, since the magnetic Compton measurement is usually very accurate.

Besides the outliers (source 1 to 6 in figure 53), there is a clear trend visible in sources 7 to 11, which report a magnetic moment of around $3.2\,\mu_B\,(\text{f.u.})^{-1}$ at 4 K and $3.6\,\mu_B\,(\text{f.u.})^{-1}$ at 300 K. In most cases, these studies employ a very careful heat treatment to ensure a fully ordered state. As the magnetization of the sample

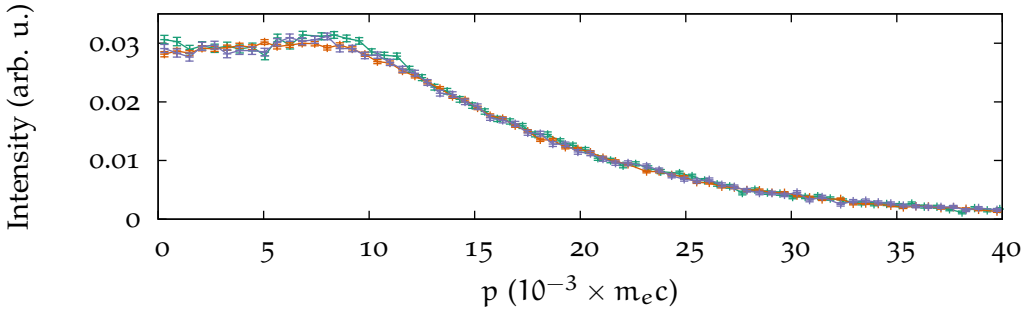

Figure 54: Magnetic Compton profiles of Cu_2MnAl at 300 K. ■) [100] projection; ■) [110]-projection; ■) [111]-projection.

OFZ87-3-2 is very much in agreement with these measurements it is safe to assume that this sample is, despite a slight Mn deficiency, in a well ordered state.

12.2.4 *Magnetic Compton Measurements*

Compton scattering experiments, rely on both high intensity and high energy radiation and are therefore nowadays only done at synchrotron facilities. Hence, it is possible to employ the X-ray polarization in order to do MCS. The investigation of the sample OFZ87-3-2 with Compton scattering was performed in Japan at the Compton beam line of SPRING-8, by the group of John Duffy from Warwick.

In figure 54, the measured magnetic Compton profiles for the main symmetry directions are shown. All three of them are very similar for various reasons: i) The resolution of approximately 3 mrad evens out the details, ii) the 1D projection decreases the particularities and iii) the magnetism is carried by core states, which are typically very symmetric.

12.2.5 *Spin-Polarized 2D-ACAR*

The spin-polarized 2D-ACAR measurements were carried out at the previously reported spectrometer (see chapter 5). Fife different projection were acquired: Two main symmetry projections, namely [100] and [110], and three projections at angles 29.8°, 35.3°, and 59.8° with respect to the [100] direction. For every projections two measurements with antiparallel magnetic field were recorded, collecting typically 1.3×10^9 counts. All measurements took place at room temperature. In figure 55 and 56 the measured [100] and [110] projections are shown and in section 12.4.1 the results are discussed.

12.3 THEORETICAL BAND STRUCTURE CALCULATIONS

The basis for the calculation of an ACAR spectrum is the electronic band structure. Several ab initio software packages exist for the calculation of band structures, approaching the many body problem with various levels of sophistication. In the present investigation two different approaches were used: the ELK code [ELK,

2015] for the calculation of 2D-ACAR spectra and the MIKA Doppler package [Torsti et al., 2006] for the calculation of the TPMD of the Mn 3d orbitals.

The calculation of the 2D-ACAR spectra were done by Stephen Dugdale and David Ernsting from Bristol using the ELK code with the experimentally determined lattice constant of 5.961 Å. ELK is an open source package under the GNU General Public License for electronic structure calculations of solids. It employs density functional theory i. e. it solves the Kohn-Sham equations for electrons using a basis set of linear augmented plane waves. The generalized gradient approximation (GGA) schema [Perdew, Burke, and Ernzerhof, 1996] was employed to model the electronic exchange-correlation. The calculation gave a spin moment of $3.52\,\mu_B\,(\text{f.u.})^{-1}$. To account for the reduced saturation magnetization at room temperature, the magnetic moment was fix to the experimentally determined $3.2\,\mu_B\,(\text{f.u.})^{-1}$. The electron-positron correlations were modeled using the Drummond parametrization of the enhancement factor [Barbiellini and Kuriplach, 2015; Drummond et al., 2011] in the GGA framework for a vanishingly small positron density. Additionally, calculations in the IPM, not including electron positron correlations, were done. For the final projection of $\rho^{2\gamma}(\mathbf{p})$ the tetrahedron interpolation method described by Ernsting et al. [2014] was employed.

The MIKA Doppler package is also a density functional code which has been developed in a joint project at several north European universities. Although it is still frequently applied for the calculation of CDB and DBAR spectra (see e. g., Reiner et al., 2015) the development has been discontinued. In contrast to ELK, MIKA Doppler uses the atomic superposition method in the LDA schema for solving the Kohn-Sham equations. Therefore, especially the low momentum part of calculated spectra shows a significant deviation from experiments as an atomic superposition method is not suited for the calculation of delocalized electronic states. However, the atomic superposition allows the decomposition of the spectra into the atomic states. Hence, the MIKA Doppler package was chosen to calculate the 3d states of Mn, which are said to be the source of the magnetic moment in Cu_2MnAl. The electron-positron correlation was taken into account within the model of Boroński and Nieminen [1986]. Instead of the original source code the slightly modified version by Löwe [2016] was compiled which is able to calculate $\rho^{2\gamma}(\mathbf{p})$ instead of the 1D projection.

12.4 RESULTS AND DISCUSSION

In contrast to the 2D-ACAR and the MCS measurements, the XRD, WDX, magnetization, and DBAR measurements were mainly done to analyze the quality of the sample. Hence, they are a prerequisite to ensure that the sample quality is sufficiently high. These preliminary investigation showed that the sample OFZ87-3-2 properties are in very good agreement with literature values and that the defect concentration is very low. Therefore, an electronic structure investigation by 2D-ACAR is well accepted to give meaningful results.

In the following the main results of the electronic structure investigation are presented. At first the 2D-ACAR measurements are compared to spectra obtained

by band theoretical. In the next section the FS reconstruction will be shown and finally, the lifetime scaled 2D-ACAR spectra are contrasted to MCS data.

12.4.1 *Comparison with Theoretical Calculation*

While theoretical calculations of 2D-ACAR spectra yield minority or majority spin channels, the actual measurement only gives a linear combination of both spin channels (see section 4.3.5). According to equation (71), the true minority or majority spectra can be calculated from the spectra with antiparallel sample magnetization:

$$M_{maj}(p_x, p_y) \propto F\, M^{\uparrow}(p_x, p_y) - (1-F)\, M^{\downarrow}(p_x, p_y) \tag{140}$$

$$M_{min}(p_x, p_y) \propto -(1-F)\, M^{\uparrow}(p_x, p_y) + F\, M^{\downarrow}(p_x, p_y) \tag{141}$$

In figure 55 a) and b) the anisotropy of the obtained majority and minority [100] projections are compared to the anisotropies of the theoretical spectra that were convolved with the experimental resolution. In figure 56, the same data are shown for the [110] projection.

The anisotropic contribution of the spectra is still visible at high moments up to 20 mrad. This indicates a good sample quality and agrees very well with the previous defect analysis. Crystal defects usually lead to a localization of the positron wave function in real space which would hence lead to a broad positron wave function in momentum space. As $\rho^{2\gamma}$ is a convolution of positron and electron wave function [see equation (58)], a localized positron makes the TPMD more blurry and isotropic and erases especially the anisotropic high momentum signals.

In both projections the measured minority and majority spectra show very distinctive features. For example, the majority [100] projection has a high intensity pocket at the equivalent points $(\pm 4\,\mathrm{mrad}, \pm 4\,\mathrm{mrad})$ [see figure 55 a)] while the minority spectra shows low intensity at these points [see figure 55 b)]. These features arise from the different FS topologies of minority and majority spin channel as most of the completely filled bands are common to both spin channels.

Furthermore, the theoretical spectra agree very well with the experimental ones. Remarkably, even the effect of the anisotropic resolution, which weakens the 4-fold symmetry in the [100] projection has a complementary effect for theoretical and experimental data. The most prominent example is the high intensity detail in the minority spin channel [figure 55 b)] at approximately $(\pm 5\,\mathrm{mrad}, 0\,\mathrm{mrad})$, which is slightly broader than at the equivalent points $(0\,\mathrm{mrad}, \pm 5\,\mathrm{mrad})$. These observations prove on the one hand that the agreement between measurement and theory is excellent and on the other hand that the separation of the minority and majority spin channels was successful.

In column c) of figure 55 and 56 the difference

$$\Delta M = \frac{M^{\uparrow}}{\int M^{\uparrow}\,dp} - \frac{M^{\downarrow}}{\int M^{\downarrow}\,dp} \propto \frac{M_{maj}}{\lambda_{maj}} - \frac{M_{min}}{\lambda_{min}} \tag{142}$$

is shown. This quantity is ideally suited to compare theory with experiment as no knowledge about the polarization of the positron beam is necessary. The signal in

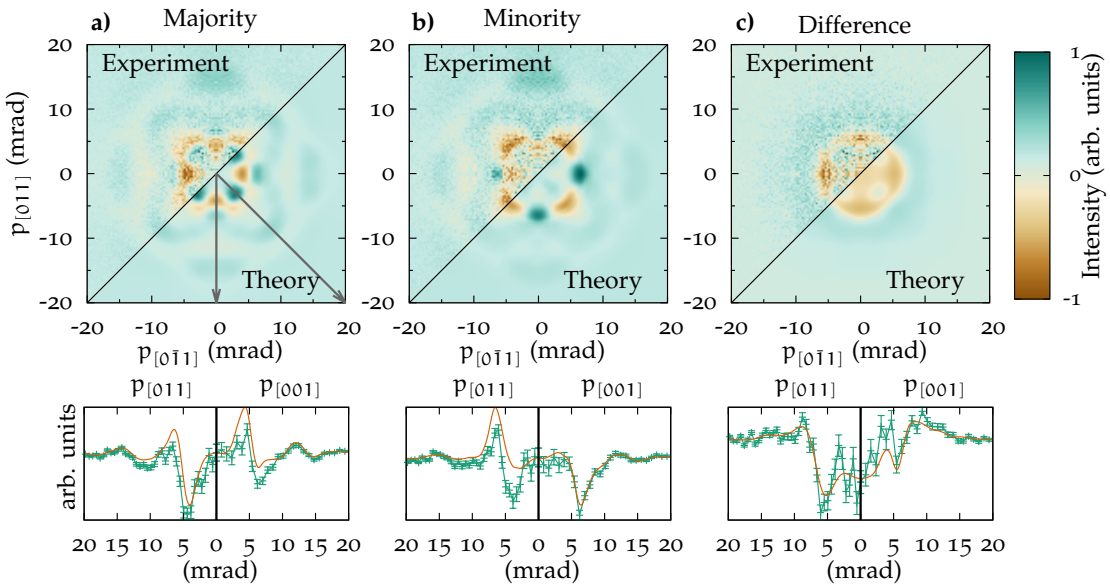

Figure 55: 2D projections along [100] of Cu_2MnAl at room temperature. The measured anisotropy of a) majority and the b) minority density respectively is compared with the theoretical results. The theoretical spectra were convolved with the resolution function of the spectrometer. The column c) depicts the difference between majority and minority density with the total number of counts in each spectrum normalized to one. The lower row shows cuts through the upper pictures as indicated by the arrows in a) along [001] and [011] directions for theory (orange) and experiment (green) [Weber et al., 2015].

these plots is caused primarily by the Mn 3d electrons as they are the main source of the magnetic moment. However, as the annihilation rates $\lambda_{maj/min}$ have not been taken into account, ΔM cannot be related to a meaningful physical quantity, but helps enormously to compare experiment and theory. It can be deduced from both projections that experiment and theory are very much in agreement. Especially the 1D cuts in the lower panels of figures 55 c) and 56 c) display a very good qualitative and quantitative congruency.

For an assessment of the quality of the calculations and for an evaluation of the different enhancement models (i. e. Drummond and IPM), the theoretical spectra were compared to measured data by means of a least squares fit taking into account the statistical accuracy. In order to exclude the influence of the beam polarization, only the difference spectra ΔM and the sum spectra

$$\Sigma M = \frac{M^{\uparrow}}{\int M^{\uparrow}\,dp} + \frac{M^{\downarrow}}{\int M^{\downarrow}\,dp} \propto \frac{M_{maj}}{\lambda_{maj}} + \frac{M_{min}}{\lambda_{min}} \tag{143}$$

for the [100] and the [110] direction were analyzed.

The Drummond enhancement strongly increases the agreement for the ΣM: The reduced χ^2 decreased from 4.4×10^2 to 2.0×10^2 and from 5.3×10^2 to 2.4×10^2 for the [100] and for the [011] projection, respectively. However, the enhancement improves the agreement only marginally for ΔM from 1.176 to 1.173 and from 1.190 to 1.187 for the [100] and for the [011] projection, respectively.

It might seem surprising that the enhancement does not have a big influence on ΔM, while it has a such a huge impact on ΣM. Presumably, the magnitude of

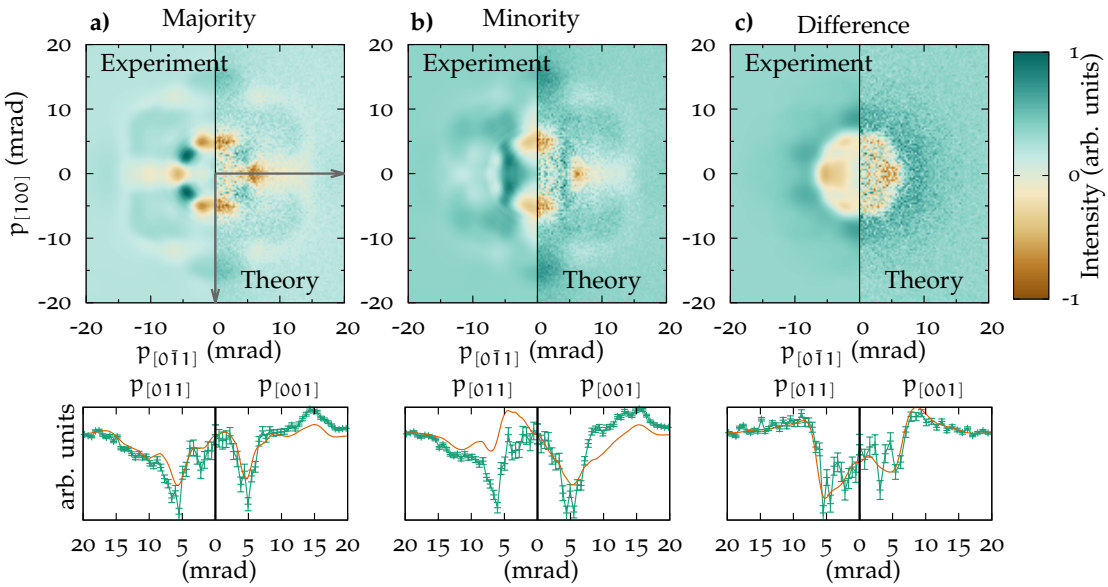

Figure 56: 2D projections along [110] of Cu_2MnAl at room temperature. The measured anisotropy of a) majority and b) minority density respectively is compared with the theoretical results. The theoretical spectra were convolved with the resolution function of the spectrometer. The column c) depicts the difference between majority and minority density with the total number of counts in each spectrum normalized to one. The lower row shows cuts through the upper pictures as indicated by the arrows in a) along [001] and [011] directions for theory (orange) and experiment (green).

the electron-positron correlation is in first instance directly related to the overlap of the positron with the electron wave function. Therefore, enhancement effects are usually larger for delocalized electronic states. As the signal in the difference spectra is mainly caused by the localized Mn 3d electrons, the enhancement does not play such an important role as for ΣM, where all electronic states are included. Unlike the claims of Biasini and Rusz [2006] and Rusz and Biasini [2007], ΔM *is* affected by enhancement although the effect is quite small. Hence, this result affirms the study of Ceeh et al. [2016b] who proved the importance of enhancement for ΔM by spin-polarized measurements on nickel.

12.4.2 *Measurement of the Spin Dependent Fermi Surface*

The extraction of the spin dependent Fermi surface (FS) of Cu_2MnAl can take place in two methodically different ways. The FS can be either taken from the ab initio calculations. As the calculations were verified by the comparison with previous experimental data, also the calculated FS was indirectly validated. From an experimentalist point of view it is however more sound to extract the FS directly from the measurement.

For this purpose, the reconstruction algorithm proposed in chapter 10 has been adapted for the use of spin-polarized data. Instead of first calculating $\frac{M_{maj/min}}{\lambda_{maj/min}}$ and then solving two separate reconstruction problems, it is more consistent to get

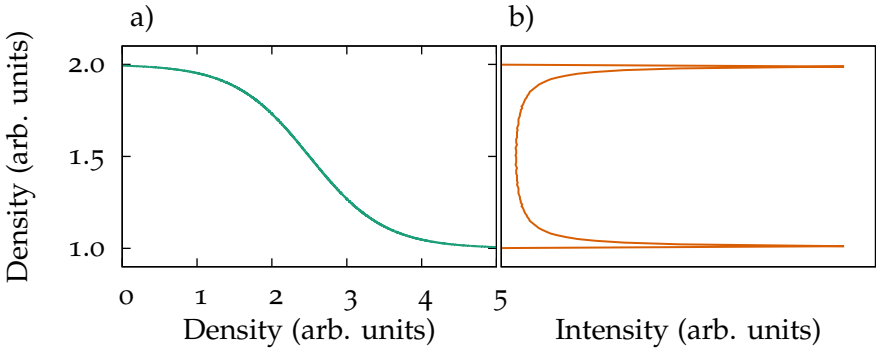

Figure 57: Example of the histogram method. a) Exemplary density $\rho^{2\gamma}(\mathbf{k})$ in the reduced zone schema. It has plateaus and due to the experimental resolution smooth transitions. b) Histogram of the density. The peaks are at the position of the plateaus.

the reconstructions $\mathbf{x}_{maj/min}$ of $\rho^{2\gamma}_{min/min}$ by minimizing the functional $h(\mathbf{x}_{maj}, \mathbf{x}_{min})$. Analogously to equations (119) and (122) $h(\mathbf{x}_{maj}, \mathbf{x}_{min})$ can be defined as

$$\begin{aligned} h(\mathbf{x}_{maj}, \mathbf{x}_{min}) = &\sum_{\alpha,i} \frac{\left(M^{\uparrow}_{\alpha} - T_{\alpha}\left(F\,\mathbf{x}_{maj} + (1-F)\,\mathbf{x}_{min}\right)\right)^2_i}{\sigma^2_{\uparrow,i}} \\ &+ \sum_{\alpha,i} \frac{\left(M^{\downarrow}_{\alpha} - T_{\alpha}\left((1-F)\,\mathbf{x}_{maj} + F\,\mathbf{x}_{min}\right)\right)^2_i}{\sigma^2_{\downarrow,i}} \\ &+ \lambda \left(\sum_j x_{j,maj} \ln\left(x_{j,maj}\right) + \sum_j x_{j,min} \ln\left(x_{j,min}\right) \right) \end{aligned} \tag{144}$$

For the minimization of $h(\mathbf{x}_{maj}, \mathbf{x}_{min})$, the same gradient approach as described in chapter 10 was used. By the 3D LCW, the result of the minimization $\mathbf{x}_{maj/min}$ was back folded into the first BZ to obtain $\rho^{2\gamma}(\mathbf{k})_{maj/min}$.

Identifying the Fermi Surface Breaks

In theory, the FS can be easily identified by looking for discontinuities in $\rho^{2\gamma}(\mathbf{k})$. However, as the reconstruction cannot reverse the experimental resolution, in practice the discontinuities get smeared out and in some cases cannot be identified unambiguously. In simple metals with only one FS sheet, e. g., like in copper, the FS can be identified as the isosurface on $\rho^{2\gamma}(\mathbf{k})$ which divides the volume of the BZ in two parts of equal volume. In more complicated systems, the iso-value to plot the FS was often determined by searching for an extremum in the gradient $\nabla\rho^{2\gamma}(\mathbf{k})$ (see e. g., [Haynes et al., 2012]). However, the extremum can yield different iso-values for different directions in k-space. Therefore, a more global method to determine the iso-value was chosen.

A LCW folded density $\rho^{2\gamma}(\mathbf{k})$, has flat plateaus, where the density is almost constant, and steps which correspond to the FS. In figure 57 a) an exemplary density is shown where the sharps steps are smeared by the experimental resolution. A histogram created from such a density has peaks at the density values of the

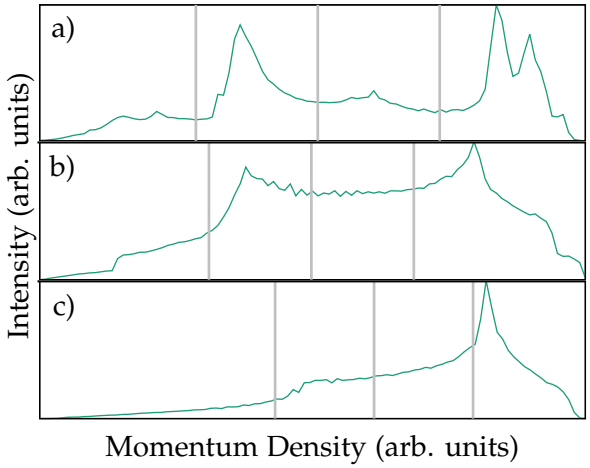

Figure 58: Histograms of LCW folded momentum densities $\rho^{2\gamma}(\mathbf{k})$ of the majority spin channel of Cu_2MnAl a) reconstructed from theoretical data, b) reconstructed from theoretical data folded with the experimental resolution and c) reconstructed from experimental data. The vertical lines are the values where Fermi breaks could be identified.

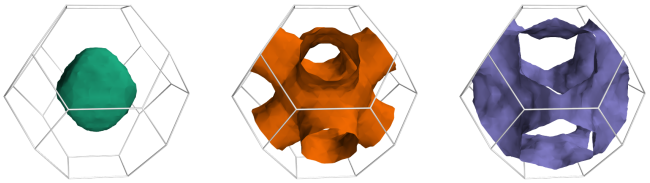

Figure 59: Reconstruction from calculated projections of the majority spin channel of Cu_2MnAl. The histogram of the underlying density is shown in figure 58 a).

plateaus. Thus, the valleys in between the peaks will correspond to the rising edge of a step. A histogram form the density in figure 57 a) is depicted in figure 57 b). The valley between the two peaks corresponds to the inflection point in the density. In figure 58 a) a histogram of a LCW density obtained from a reconstruction using five calculated projections is shown. Since the resolution of the ab initio calculation is effectively determined by the chosen binning, the peaks and the valleys can be easily discerned. The vertical lines in the histogram mark the minimum value in each valley and correspond to the iso-value taken to draw the surfaces in figure 59. These surfaces are almost indistinguishable from the original majority Fermi surfaces of the theory [see figure 60 a)].

If the theoretical projections are convolved with a resolution function and given statistical noise (appropriate to the experimental data), the plateaus in $\rho^{2\gamma}(\mathbf{k})$ become rounded. The effect on the histogram can be seen in figure 58 b), where the clear peaks have been strongly suppressed or have even vanished. Identifying the lower and the upper iso-values is still straightforward, being placed to the left of the two remaining peaks at the point where the gradient starts to change. The middle iso-value is then placed in the center assuming that the steps in $\rho^{2\gamma}(\mathbf{k})$ are of equal height. This is not necessarily true, given that the positron samples different states differently, but in Cu_2MnAl the sheets all have very similar character (as they all belong to d electronic states) and so one might expect the steps to be of similar size. The iso-values chosen in this way are the vertical lines in fig-

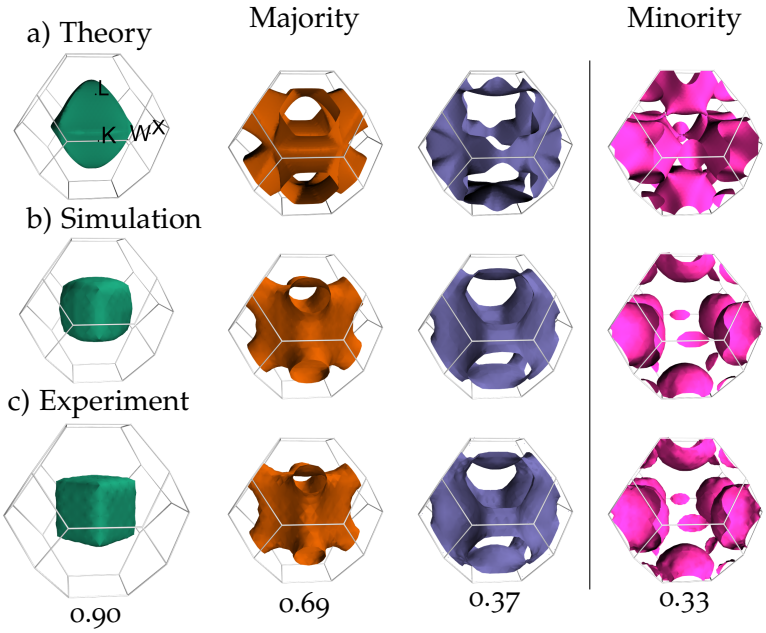

Figure 60: Majority (left) and minority sheets (right) of the FS of Cu_2MnAl. Spin-resolved Fermi sheets are obtained a) from fixed spin moment (3.2 μ_B/f.u.) calculations, b) from isosurfaces of reconstructed simulated data convolved with the experimental resolution function including statistical noise, and c) from the isosurfaces of experimental data. The occupied fraction of the BZ volume of the experimentally determined FS is given below each sheet [Weber et al., 2015].

ure 58 b), which were used to draw the FS sheets of the simulation in figure 60 b). For real experimental data, the histogram looks quite similar, as can be seen in 58 c). Therefore, the isosurface values could be chosen in exactly the same manner as before.

Results of the Reconstruction

Previously, band structure calculations for Cu_2MnAl were performed by Ishida et al. [1981, 1978], who predicted three majority and two minority sheets. The majority sheets are all hole-like and lie centered in the BZ. The two larger ones possess the same topology, i. e. eight necks, one at every L-point, while the smaller one has the shape of an octahedron. The minority sheets consist of one electron-like X-centered pocket and one much smaller ellipsoidal formed hole pocket between Γ and K. The present calculations with an unrestricted spin moment (i. e. 3.51 μ_B (f.u.)$^{-1}$) qualitatively reproduce very well the results of Ishida et al. [1981]. However, in the fixed moment calculation with the experimentally determined 3.2 μ_B (f.u.)$^{-1}$ the small minority hole pockets vanish completely.

In figure 60 the calculated spin-resolved FS sheets from the 3.2 μ_B (f.u.)$^{-1}$ fixed moment calculation are depicted together with the results of the reconstruction. In order to be able to compare experiment with theory, projections were generated using the theoretical data according to the five measured projections. The theoretical projections were additionally convolved with the experimental resolution and decorated with statistical noise. From this data, the reconstruction in figure 60 b) was created.

As expected, the broadening in the projections leads to a smearing of the sharp Fermi-breaks. Hence, the reconstructed Fermi-surface sheets are more smooth and some of the original details are missing while other features get mixed with adjacent sheets. The reconstruction of the experimental data in figure 60 c) are affected in a similar way by the resolution. Notably, the reconstructed Fremi-surface sheets are almost identical. Despite the smearing effects, the topology of the reconstruction matches the original data and even small features like the pockets at the K-point of the minority sheet are reproduced correctly.

The occupied fraction of a spin dependent Fermi-surface sheet directly gives the magnetic moment in $\mu_B\,(\text{f.u.})^{-1}$. Integrating over the occupied states and dividing by the volume of the BZ the magnetization of the individual sheets given in figure 60 c) was obtained. The values add up to a total magnetization of $(1.6 \pm 0.5)\,\mu_B\,(\text{f.u.})^{-1}$. Here, the error was estimated by enlarging and reducing the Fermi-surface by the amount of one voxel.

The $1.6\,\mu_B\,(\text{f.u.})^{-1}$ are much smaller than the results of the previous magnetization measurements (see figure 53). However, a magnetic moment of $3.6\,\mu_B\,(\text{f.u.})^{-1}$ is obtained, if it is assumed that there are two additional completely filled bands existing in the majority spin channel, which is also suggested by the calculation. As the largest majority sheet (violet) and the minority sheet approximately cancel each other, it is feasible to say that 5/9 of the magnetic moment stem from tightly bound states, while 4/9 are caused by the conduction electrons. Although there is a small negative contribution to the magnetization from the minority surface, these electrons cannot be treated like a free electron gas as Żukowski et al. [1997] reported, since the minority surface is not a Γ centered sphere.[1]

Conclusion

By spin-polarized 2D-ACAR measurements on the Heusler system Cu_2MnAl, a novel approach for extracting spin-resolved Fermi surfaces was shown. To this end the algorithm proposed in chapter 10 was modified to work with spin-polarized data. Furthermore a new way to identify the FS iso-value was introduced. Using these mathematical tools, it was possible to extract the Fermi-surface from the data. As predicted by theory, there are unoccupied states in all bands at the Γ-point. The small minority pockets are absent in the reconstruction, as suggested by the fixed spin moment calculations which are appropriate for this room temperature experiment. The experimentally determined FS sheets are shown to be in excellent agreement with the theory.

12.4.3 *Magnetic ACAR and Comparison with Magnetic Compton Scattering*

MCS and spin-polarized 2D-ACAR both probe spin resolved the electron momentum density $\rho(\mathbf{p})$ in a solid. A MCS profile C_{mag} can be extracted readily by two Compton measurements with antiparallel sample magnetization, while in an ACAR measurement additional information about the annihilation rates is needed

1 Żukowski et al. later realized their misinterpretation when they reconstructed 3D momentum densities from their Compton spectra and found no negative density [Dobrzyński and Żukowski, 1999].

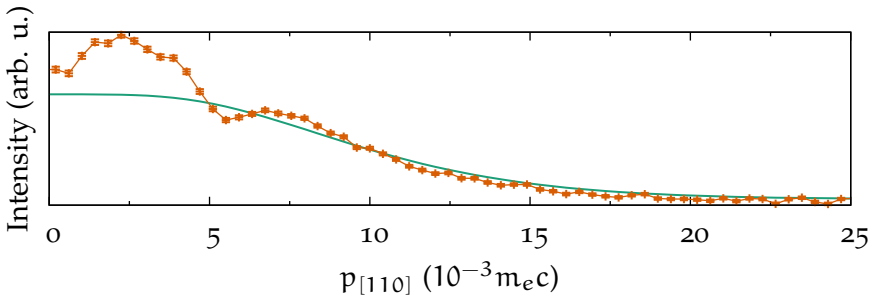

Figure 61: One dimensional projections of electron-positron momentum densities: ■: Calculated M^{Mn} of the Mn 3d electronic states; ■: M^{mag} obtained by a fit to the Mn 3d electron density.

[Berko and Zuckerman, 1964; Hanssen et al., 1990; Mijnarends, 1973b]. Therefore, in the past magnetic ACAR spectra could not be measured. However, with spin-polarized PLS measurements, a magnetic ACAR spectra M_{mag} of Cu_2MnAl could be extracted:

$$M_{mag} = M^{\uparrow} - aM^{\downarrow} \tag{145}$$

with the scaling constant a:

$$a = \frac{\tau_{min} + F\left(\tau_{maj} - \tau_{min}\right)}{\tau_{maj} - F\left(\tau_{maj} - \tau_{min}\right)} \tag{146}$$

Another possibility to obtain M^{mag} is to use additional information about M^{mag}. It is known that the main magnetic moment in Cu_2MnAl is carried by the localized Mn 3d electrons [Brown et al., 1996; Felcher, Cable, and Wilkinson, 1963; Kübler, William, and Sommers, 1983; Rakhecha, Chakravarthy, and Satya Murthy, 1976, 1978]. Therefore, it is plausible that the high momentum part of M^{mag} will resemble an atomic Mn 3d electron momentum density. This idea has already been validated by Żukowski et al. [1997] using Compton scattering.

The Mn 3d electron momentum density M^{Mn} was calculated by means of the MIKA Doppler program package [Torsti et al., 2006]. Using a least squares method, taking into account the statistical accuracy of the 2D-ACAR measurements, M^{mag} was fitted at the high momentum part $p > 7\,mrad$ of M^{Mn}. This means, approximately the first two BZs, where the conduction electrons are most dominant, were excluded from the fitting. All five measured projections were included consistently into the fitting procedure, which yielded a value of 1.0117 for the scaling constant c (No error for c can be given here, since the systematic error is much greater than the statistical accuracy of the fit). The result of the experimentally determined M^{mag} and the Mn 3d density are shown in figure 61. For a better comparability only a 1D projection of the 2D data is shown. It can be seen that both experimental datasets, are for high momenta in reasonable agreement with the theoretical Mn 3d momentum density whereas for low momenta the experimental data exceed the theoretical density.

It has to be noted that the fitting range is chosen arbitrarily. Nearly any value of c can be obtained if an adequate fitting range is chosen, since the theoretical curve does not describe the experiment with sufficient accuracy. Therefore, the fitting result rather gives a boundary between the delocalized and the localized Mn 3d part of the magnetic spectra.

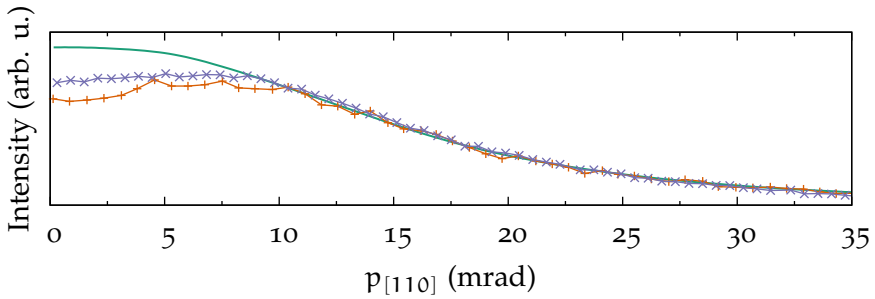

Figure 62: Magnetic Compton [110] profile of Cu_2MnAl. ■:present data; ■: calculated Mn 3d density and ■ measurement, both taken from Żukowski et al. [1997].

Magnetic Compton Measurements

As for the system Cu_2MnAl already MCS measurements by Żukowski et al. [1997] exist, one might expect that these results should agree with the magnetic ACAR measurements. However, a comparison of M^{mag} in figure 61 and the Żukowski data (orange crosses in figure 62) show significant differences especially at low momenta. As the magnetic moment of the sample used by Żukowski et al. was unusual low (see figure 53), the MCS experiment was repeated (see section 12.2.4) using the same sample which was probed with 2D-ACAR. In this way, effects of different order in the samples can be excluded. The present results together with the theory and the data of Żukowsi at al. is shown in figure 62. Although the theory curves in figure 61 and 62 refer to the same Mn 3d electron density, they have a different shape. This originates from the positron wave-function which affects the ACAR data.

In the high momentum region of figure 62 ($p > 10\,mrad$) both experimental data fit very well the theoretical Mn 3d momentum density. In the low momentum region, there is only a small difference between the present Compton measurement and the previously published data. Therefore, a possible disorder in the Żukowski sample did not have a huge influence on the electronic structure and can explain by no means the different between MCS and ACAR.

The theoretical Mn 3d densities agree much better with the MCS profile than with the ACAR profile. It is rather unlikely that this difference is caused by the electron-positron correlation, as state-of-the-art models usually treat the enhancement state dependent and would therefore just shift the weighting between different states. Most likely, the difference is caused by the positron wave function sampling the electronic structure. Two effects are thinkable:

1. The positron is more sensitive to delecoalized electronic states and electrons in outer shells than it is to the core electrons. Therefore, the positron can 'magnify'[2] magnetic valence states that have actually a very low contribution to the magnetic moment.

2. As the positron samples the majority and the minority density differently, it is possible that not all nonmagnetic states cancel each other.

2 Note that this 'magnification' by the positron wave-function is a different effect than the enhancement by electron-positron correlations

However, the latter effect is estimated to be rather small and only significant in strongly correlated systems [Biasini and Rusz, 2006; Ceeh et al., 2016b; Rusz and Biasini, 2007]. Hence, by means of the magnetic ACAR spectra and with the aid of further theoretical calculations it can be possible to pin point the electronic states, which are involved in the generation of the magnetism in Cu_2MnAl.

13

CONCLUSION AND OUTLOOK

During this thesis a new 2D-ACAR spectrometer and in particular the data acquisition has been set up at the TUM. For the analysis of the data new algorithms and data treatment tools were developed amongst them a novel algorithm to reconstruct the TPMD from projections. Using this toolkit the elementary systems copper, iron, and vanadium and the Heusler alloy Cu_2MnAl were investigated.

Spectrometer

The ACAR spectrometer consists of a sample environment where temperatures between 10 K to 650 K in magnetic fields up to 1.2 T can be reached in UHV conditions. Positrons are emitted onto the sample by a ^{22}Na source and focused onto a spot size of 4 mm. The detectors, two Anger-type γ cameras are both positioned collinear to the sample at a distance of 8.84 m each. After implementation of the new data acquisition, the resolution (FWHM) of the spectrometer could be improved to $\sigma_y \approx 1.12\,\mathrm{mrad}$, $\sigma_x \approx 1.45\,\mathrm{mrad}$.

Data Acquisition

The data acquisition of the spectrometer has been completely redesigned, getting rid of more than 2 m² of analog electronics which was very susceptible to breakdowns. Besides the increased reliability, the new data acquisition has additional advantages: i) The data are now free of artifacts (see figure 22). ii) The data are stored in lists which enables distortion correction increasing the angular resolution by a factor of 1.3. iii) The listmode also allows to shift or turn the data without the need for interpolation, since the accuracy of the digitalization is much higher than the bin width of the image. Therefore, the statistical accuracy of the data can now always be conserved.

Comparison of Detector Technologies

Due to the research done in the Munich positron groups, it was possible to do a quantitative comparison of γ detector technologies with respect to their application in ACAR spectroscopy. From the six detectors, HIDACs are by far the detectors with the highest quality ratio Q. However, if one considers the quality per price, Anger cameras perform better than HIDAC detectors by a factor of two and furthermore are more robust in daily usage. The quality per price ratio of all other detectors is at least one magnitude lower.

Novel Reconstruction Algorithm for ACAR Data

One main goal of this thesis was to develop an algorithm for the reconstruction of the fully 3D $\rho^{2\gamma}$ from its projections. The presented algorithm takes into account the *full* symmetry of the BZ, the statistical accuracy and the resolution of the measured data. This is a major improvement to existing reconstruction techniques. No further prior knowledge about $\rho^{2\gamma}$ is necessary resulting in an unbiased reconstruction.

Several regularization functionals were tested in combination with the reconstruction algorithm. It was found that the entropy regularization yields the best results. Furthermore, the open question whether it is favorable to collect many projections with low statistics or few projections with high statistics could be answered: For a high resolution it is clearly better to collect many projections. However, if the resolution gets worse, the advantage of taking many projections gets less critical as the deconvolution problem is mathematically more ill defined than the reconstruction problem.

Results: Copper

On copper, measurements at 10 K and at room temperature (300 K) were carried out. A first comparison with ab initio calculations gave a good qualitative agreement. For both temperatures a reconstruction of the TPMD was created. Although the low temperature reconstruction suffered from the low statistical accuracy of the data, the dimensions of the high temperature FS were in good quantitative agreement with other high temperature literature values, verifying the previously observed temperature dependence of the FS.

Results: Iron

Two different iron samples, $Fe_{0.93}Si_{0.03}$ and a pure iron specimen, were both investigated with spin-polarized 2D-ACAR. Scrutinizing the measurements to theoretical spectra resulted in a good qualitative agreement. For the [100] and the [110] projection, the majority and minority spectra were extracted. A comparison between the spectra of both samples revealed that the pure iron specimen exhibits a considerable vacancy concentration. For a future in depth analysis, solid band structure calculation are necessary. As iron was recently discussed to show non trivial topological points in the BZ [Gosálbez-Martínez, Souza, and Vanderbilt, 2015], such an investigation could be provide new insights of iron's electronic structure.

Results: Vanadium

The measured vanadium data were quantitatively compared to LDA and DMFT spectra calculated by Liviu Chioncel. Thereby, it could be shown that the DMFT calculations fit the experimental data best. The extend of the agreement is good enough that even the experimental resolution could be extracted. However, a comparison between experimental and theoretical anisotropy and LCW folding gives

an equally good agreement of the LDA calculation. Consequently, mainly the enveloping function of the LDA and DMFT data differ. Furthermore, the three Fermi surface sheets of vanadium could be reconstructed. The presented reconstruction agrees better with the theoretical predictions than previous results.

Results: Cu_2MnAl

The Heusler alloy Cu_2MnAl was investigated with spin-polarized 2D-ACAR. From the measurements, projections of the minority and the majority TPMD could be extracted. These spectra were in excellent agreement with band theoretical calculations. Using an adapted reconstruction algorithm for spin-polarized data, the majority and minority sheets of the FS could be extracted. For the first time spin-polarized ACAR data were used to directly extract the FS. Furthermore, integrating over the volume of the individual sheets yielded the magnetic moment contribution to the total magnetization. The sum over the individual moments agrees well with the magnetization of the sample if one assumes that the majority spin channel possesses two additional completely filled bands compared to the minority spin channel. This result is also backed up by calculation.

By means of the MCS measurements and using suitable calculations it is now feasible to assign certain features in the measurement to specific electronic states. This can contribute to the general understanding of magnetism in Heusler systems.

Future Work

The quality of the acquired data could clearly profit from an increase in experimental resolution. This could either be achieved by increasing the detector sample distance or by increasing the position resolution of the detectors. The latter solution is preferable as a larger sample detector distance would decrease the count rate. Especially for a further investigation of iron, a better resolution would be indispensable to detect the predicted features of Gosálbez-Martínez, Souza, and Vanderbilt [2015]. Furthermore, with a better resolution the temperature dependent changes in the FS of copper could be observed with much higher accuracy.

The continuation of the Cu_2MnAl investigation will be very promising as the mapping of electronic states to the spectra could contribute to the understanding of Heusler systems in general.

In this thesis it was shown that the ACAR spectrometer at the TUM is able to investigate the electronic structure of complex materials. With the present setup correlated electron systems, half metals and many materials more can be probed in the bulk, spin dependent and over a wide temperature range. When the setup is moved to the new experimental east hall and connected to the high intense positron source NEPOMUC, also the change of the electronic structure from the surface to the bulk could be observed. This will be particularly interesting for the demanding research on 2D electronic systems and topological insulators.

Part V

APPENDIX

A

ADDITIONAL DETAILS

A.1 FERMI FUNCTION

The Fermi function is a correction to the analytical β-spectrum that takes the influence of the Coulomb potential into account (see section 2.1) and was derived by Fermi [1934]. For positrons it can be written as

$$F_+(Z,E) = \frac{2(1+S)}{\Gamma(1+2S)^2}\left(2p_e\frac{r_d}{\hbar}\right)^{2S-2} e^{\pi\eta}\,|\Gamma(S+i\eta)|^2 \tag{147}$$

with

Z charge of the daughter nucleus

E kinetic energy of the positron

Γ the gamma function

$S = \sqrt{1-(\alpha Z)^2}$

α the fine-structure constant

$\eta = -\alpha\frac{ZT}{pc}$

T the total energy of the positron

p_e the momentum of the positron

c the speed of light

r_d radius of the daughter nucleus

A.2 LINE DRIVER CIRCUIT

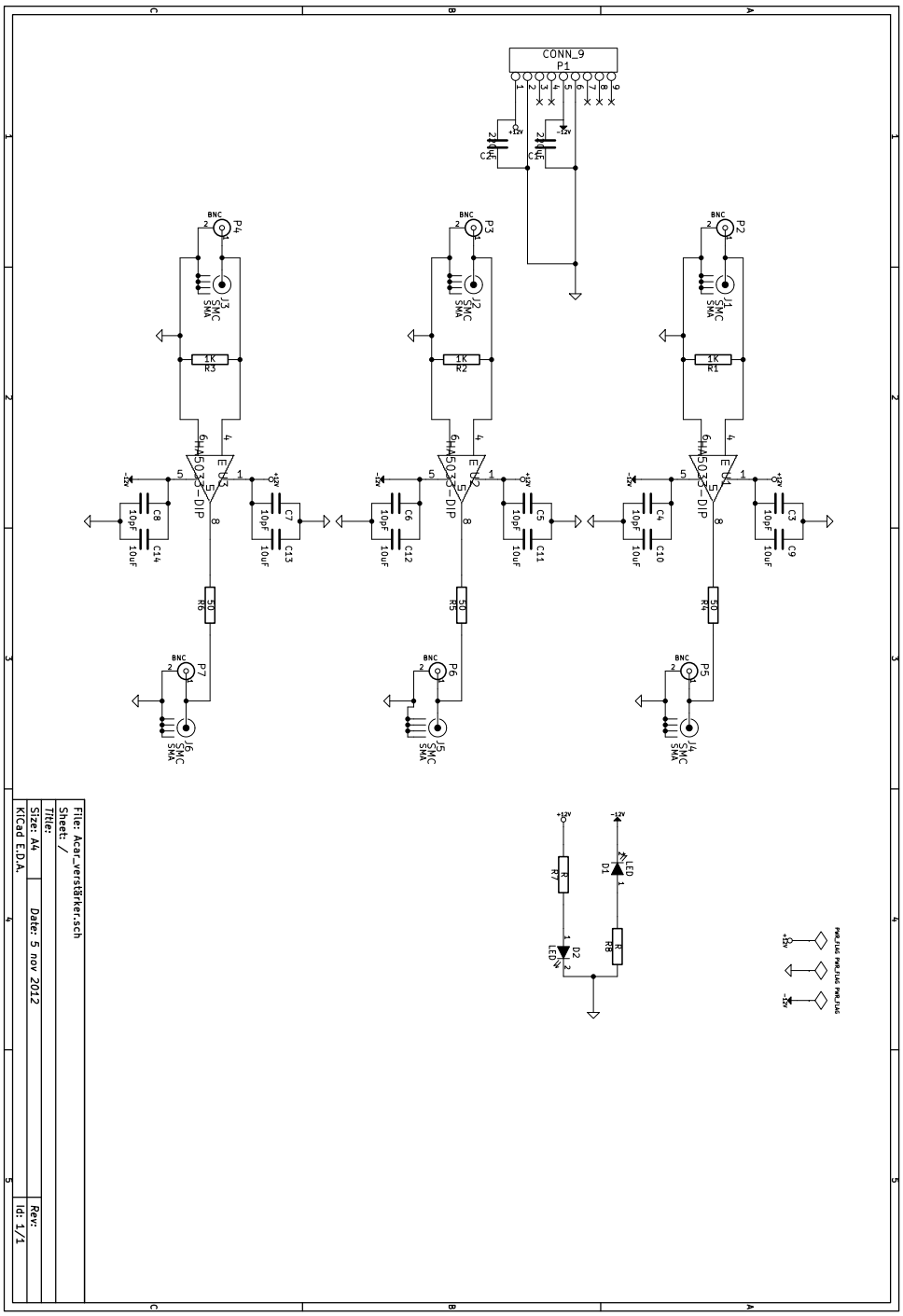

A.3 RESOLUTION OF AN ACAR SPECTROMETER

If we consider an ACAR setup with two position sensitive detectors as sketched in figure 63, the angular deviation from 180° of an annihilation event in x-direction is given by:

$$\Phi_x = \frac{D_{1_x} - A_x}{A_z - D_{1_z}} + \frac{D_{2_x} - A_x}{D_{2_z} - A_z} \tag{148}$$

The angular deviation in y-direction is calculated analogously and thus will be omitted in the further considerations.

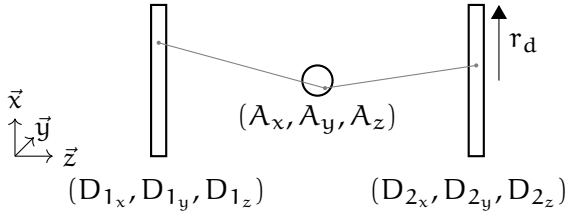

Figure 63: Sketch of an annihilation event at a position $\vec{A}$: The two γ quanta are detected on the positions $\vec{D}_1$ and $\vec{D}_2$.

The influence of the uncertainty of each coordinate to the total error is given by the partial derivatives. For a symmetrical setup with detector sample distance of $L \approx |D_{1_z} - A_z| \approx |D_{2_z} - A_z|$ and circular detectors with a radius of r_d the partial derivatives can be simplified in the following way:

$$\left|\frac{\partial \Phi_x}{\partial D_{1_x}}\right| = \left|\frac{1}{D_{1_z} - A_z}\right| \approx \frac{1}{L} \tag{149}$$

$$\left|\frac{\partial \Phi_x}{\partial D_{2_x}}\right| = \left|\frac{1}{D_{2_z} - A_z}\right| \approx \frac{1}{L} \tag{150}$$

$$\left|\frac{\partial \Phi_x}{\partial A_x}\right| = \left|-\frac{1}{D_{2_z} - A_z} - \frac{1}{A_z - D_{1_z}}\right| \approx \frac{2}{L} \tag{151}$$

$$\left|\frac{\partial \Phi_x}{\partial D_{1_z}}\right| = \left|\frac{D_{1_x} - A_x}{(A_z - D_{1_z})^2}\right| \approx \frac{0.42 r_d}{L^2} \tag{152}$$

$$\left|\frac{\partial \Phi_x}{\partial D_{2_z}}\right| = \left|-\frac{D_{2_x} - A_x}{(D_{2_z} - A_z)^2}\right| \approx \frac{0.42 r_d}{L^2} \tag{153}$$

$$\left|\frac{\partial \Phi_x}{\partial A_z}\right| = \left|-\frac{D_{1_x} - A_x}{(A_z - D_{1_z})^2} + \frac{D_{2_x} - A_x}{(D_{2_z} - A_z)^2}\right| \approx \frac{2 \cdot 0.42 r_d}{L^2} \tag{154}$$

The partial derivatives in equation (152), (153) and (154) are dependent on the position of the γ quantum hitting the sample. As an estimation for $(D_{2_x} - A_x)$ in equation (152) and the corresponding terms in equations (153) and (154), the mean absolute difference has been taken:

$$\overline{|(D_{2_x} - A_x)|} = \frac{1}{\frac{1}{4}\pi r_d^2} \int_0^{r_d} dx\, x \sqrt{r_d^2 - x^2} = \frac{4}{3\pi} r_d \approx 0.42 r_d \tag{155}$$

The contribution of the detector's position resolution σ_D to the angular resolution can now be calculated by means of equations (149) and (150):

$$\left|\frac{\partial\Phi}{\partial D_1}\right|\sigma_D = \left|\frac{\partial\Phi}{\partial D_2}\right|\sigma_D = \frac{\sigma_D}{L} \tag{156}$$

The size of the positron spot on the sample σ_S will influence the angular resolution according to equation (151):

$$\left|\frac{\partial\Phi_x}{\partial A_x}\right|\sigma_S = \frac{2\sigma_S}{L} \tag{157}$$

The errors due to the finite size of the detector's scintillator crystal are given by (152) and (153), while the longitudinal dimension of the positron spot size on the sample is given by equation (154). As for a usual setup, r_d is two magnitudes smaller than L and therefore all three contributions can be neglected. Only the transverse positron spot size on the sample and the position resolution of the detector have a significant influence to the resulting angular resolution of the setup.

B

ACRONYMS

1D-ACAR	one-dimensional angular correlation of electron positron annihilation radiation
2D-ACAR	two-dimensional angular correlation of electron positron annihilation radiation
ACAR	angular correlation of electron positron annihilation radiation
ADC	analog to digital converter
ARPES	angle-resolved photoemission spectroscopy
ART	algebraic reconstruction technique
BZ	Brillouin zone
CANARD	
CDB	coincident Doppler broadening
CM	Cormack's method
CT	computerized tomography
DAQ	data acquisition
DBAR	Doppler broadening of the electron positron annihilation radiation
DFT	density functional theory
dHvA	de Haas-van Alphen
DMFT	dynamical mean-field theory
DT	direct Fourier transformation
EDX	energy dispersive X-ray spectroscopy
FBP	filtered back-projection
FS	Fermi surface
FT	Fourier transform
FWHM	full width at half maximum
GEM	gas electron multiplier
GGA	generalized gradient approximation
HDPC	high density proportional chamber
HIDAC	high density avalanche chambers
IC	integrated circuit
IPM	independent particle model
LCW	Lock-Crisp-West
LDA	local density approximation
MCP	micro-channel plate
MCS	magnetic Compton scattering

MEM	maximum entropy method
MIAMI	mixer and mother interface
MSF	momentum sampling function
MWC	multi wire chambers
o-Ps	ortho-positronium
p-Ps	para-positronium
PC	personal computer
PGD	pixelated germanium detector
PLS	positron lifetime spectroscopy
PMT	photo multiplier tube
PPMS	physical properties measurement system
PSPMT	position sensitive photo multiplier tube
TPMD	two photon momentum denisty
TUM	Technische Universität München
UHV	ultra high vacuum
VSM	vibrating sample magnetometer
WDX	wavelength-dispersive X-ray fluorescence spectroscopy
XRD	X-ray diffraction

C

LIST OF PUBLICATIONS

Weber, Josef Andreas, Andreas Bauer, Peter Böni, Hubert Ceeh, John A. Duffy, Stephen B. Dugdale, David Ernsting, Christian Pfleiderer, Michael Leitner, and Christoph Hugenschmidt (2016a). "Unraveling the magnetic interactions in the localized ferromagnetic Heusler compound Cu_2MnAl." In preparation.

Weber, Josef Andreas, Andreas Bauer, Peter Böni, Hubert Ceeh, Stephen B. Dugdale, David Ernsting, Wolfgang Kreuzpaintner, Michael Leitner, Christian Pfleiderer, and Christoph Hugenschmidt (2015). "Spin-Resolved Fermi Surface of the Localized Ferromagnetic Heusler Compound Cu_2MnAl Measured with Spin-Polarized Positron Annihilation". *Physical Review Letters* 115 (20), 206404.

Weber, Josef Andreas, Peter Böni, Hubert Ceeh, Liviu Chioncel, Michael Leitner, and Christoph Hugenschmidt (2016b). "Electronic Structure Determination of Vanadium by 2D-ACAR." In preparation.

Weber, Josef Andreas, Peter Böni, Hubert Ceeh, Michael Leitner, and Christoph Hugenschmidt (2013). "First 2D-ACAR Measurements on Cu with the new Spectrometer at TUM". *Journal of Physics: Conference Series* 443.1, 012092.

Weber, Josef Andreas, Peter Böni, Hubert Ceeh, Michael Leitner, Pascal Neibecker, and Christoph Hugenschmidt (2016c). "Spin-Polarized Electronic Structure of Iron." In preparation.

Weber, Josef Andreas, Hubert Ceeh, Christoph Hugenschmidt, Michael Leitner, and Peter Böni (2014). "The effect of regularization on the reconstruction of ACAR data". *Journal of Physics: Conference Series* 505.1, 012047.

Weber, Josef Andreas, Hubert Ceeh, Michael Leitner, Michaela Schleuder, and Christoph Hugenschmidt (2016d). "A New Approach to Digital Constant Fraction Timing with Implications on Positron Lifetime Spectroscopy." In preparation.

LIST OF PATENTS

Ceeh, Hubert, Pascal Neibecker, and Josef Andreas Weber (2015a). "Method and Device for Producing a Three-Dimensional Object." EU Patent (Pending) WO2016131757 (A1).

LIST OF CO-AUTHORED PUBLICATIONS

Ceeh, Hubert, Josef Andreas Weber, Peter Böni, Michael Leitner, Diana Benea, Liviu Chioncel, Hubert Ebert, Jan Minár, Dieter Vollhardt, and Christoph Hugenschmidt (2016). "Local electron-electron interaction strength in ferromagnetic nickel determined by spin-polarized positron annihilation". *Scientific Reports* 6, 20898.

Ceeh, Hubert, Josef Andreas Weber, Christoph Hugenschmidt, Michael Leitner, and Peter Böni (2013a). "First measurements with the Munich 2D-ACAR spectrometer on Cr". *Journal of Physics: Conference Series* 443.1, 012094.

— (2014). "Positron beam optics for the 2D-ACAR spectrometer at the NEPOMUC beamline". *Journal of Physics: Conference Series* 505.1, 012041.

Ceeh, Hubert, Josef Andreas Weber, Michael Leitner, Peter Böni, and Christoph Hugenschmidt (2013b). "The source-sample stage of the new two-dimensional angular correlation of annihilation radiation spectrometer at Technische Universität München". *Review of Scientific Instruments* 84.4, 043905.

Hugenschmidt, Christoph, Hubert Ceeh, Thomas Gigl, Florian Lippert, Christian Piochacz, Philip Pikart, Markus Reiner, Josef Andreas Weber, and Samantha Zimnik (2013). "The Upgrade of the Neutron Induced Positron Source NEPOMUC". *Journal of Physics: Conference Series* 443.1, 012079.

Hugenschmidt, Christoph, Hubert Ceeh, Thomas Gigl, Florian Lippert, Christian Piochacz, Markus Reiner, Klaus Schreckenbach, Sebastian Vohburger, Josef Andreas Weber, and Samantha Zimnik (2014). "Positron Beam Characteristics at NEPOMUC Upgrade". *Journal of Physics: Conference Series* 505.1, 012029.

Hugenschmidt, Christoph et al. (2015). "Quality of Heusler single crystals examined by depth-dependent positron annihilation techniques". *Applied Physics A* 119.3, 997.

Leitner, Michael, Hubert Ceeh, and Josef Andreas Weber (2012). "Eliminating spatial distortions in Anger-type gamma cameras". *New Journal of Physics* 14.12, 123014.

Leitner, Michael, Josef Andreas Weber, and Hubert Ceeh (2016). "Fermi surface determination from momentum density projections". *New Journal of Physics* 18.6, 063033.

Sekania, Michael, W. H. Appelt, Hubert Ceeh, Christoph Hugenschmidt, Michael Leitner, Josef Andreas Weber, and Liviu Chioncel (2016a). "Electronic Structure of Palladium in the Presence of Many-Body Effects - Experiment." In preparation.

— (2016b). "Evolution of the Many-Body Effects in the Iso-Electornic Systems Chromium, Molybdenum, Tungsten." In preparation.

BIBLIOGRAPHY

Aad, G. et al. (2012). "Observation of a new particle in the search for the Standard Model Higgs boson with the ATLAS detector at the LHC". *Physics Letters B* 716.1, 1.

Ackermann, Ulrich (2015). Private Communication.

Ackermann, Ulrich, Stephan Eschbaumer, Andreas Bergmaier, Werner Egger, Peter Sperr, Christoph Greubel, Benjamin Löwe, Paul Schotanus, and Günther Dollinger (2016). "Position and time resolution measurements with a microchannel plate image intensifier: A comparison of monolithic and pixelated CeBr3 scintillators". *Nuclear Instruments and Methods in Physics Research Section A: Accelerators, Spectrometers, Detectors and Associated Equipment* 823, 56.

Aharoni, Amikam (1998). "Demagnetizing factors for rectangular ferromagnetic prisms". *Journal of Applied Physics* 83.6, 3432.

Akahane, T., T. Chiba, N. Shiotani, S. Tanigawa, T. Mikado, R. Suzuki, M. Chiwaki, T. Yamazaki, and T. Tomimasu (1990). "Stretching of slow positron pulses generated with an electron linac". *Applied Physics A* 51.2, 146.

Alichanian, A. I., A. I. Alichanow, and L. A. Arzimovitch (1936). "Conservation of Momentum in the Process of Positron Annihilation". *Nature* 137, 703.

Allemand, R. and G. Thomas (1976). "Nouveau détecteur de localisation". *Nuclear Instruments and Methods* 137.1, 141.

Anderson, Carl D. (1932). "The Apparent Existence of Easily Deflectable Positives". *Science* 76.1967, 238.

— (1933). "The Positive Electron". *Physical Review* 43 (6), 491.

— (1985). "Unraveling the Particle Content of the Cosmic Rays." *Early History of Cosmic Ray Studies*. Ed. by Yataro Sekido and Harry Elliot. Vol. 118. Astrophysics and Space Science Library. Springer Netherlands, 117. ISBN: 978-94-010-8899-2.

Anderson, Carl D. and Seth H. Neddermeyer (1933). "Positrons from Gamma-Rays". *Physical Review* 43 (12), 1034.

Anderson, James R. and A. V. Gold (1963). "de Haas-van Alphen Effect and Internal Field in Iron". *Physical Review Letters* 10 (6), 227.

Anger, Hal O. (1958). "Scintillation Camera". *Review of Scientific Instruments* 29.1, 27.

Asoka-Kumar, P., M. Alatalo, V. J. Ghosh, A. C. Kruseman, B. Nielsen, and K. G. Lynn (1996). "Increased Elemental Specificity of Positron Annihilation Spectra". *Physical Review Letters* 77 (10), 2097.

Baalmann, A., W. Braun, E. Dietz, A. Goldmann, J. Wurtenberg, J. Krewer, and R. Feder (1986). "Photoemission along the surface normal of Cu(001): experiment and theory". *Journal of Physics C: Solid State Physics* 19.16, 3039.

Baker, J. A., N. B. Chilton, Kjeld O. Jensen, A. B. Walker, and P. G. Coleman (1991). "Material dependence of positron implantation depths". *Applied Physics Letters* 59.23, 2962.

Baraff, David R. (1973). "de Haas-van Alphen Effect and Fermi Surface of Ferromagnetic Iron". *Physical Review B* 8 (7), 3439.

Barbiellini, Bernardo and Jan Kuriplach (2015). "Proposed Parameter-Free Model for Interpreting the Measured Positron Annihilation Spectra of Materials Using a Generalized Gradient Approximation". *Physical Review Letters* 114 (14), 147401.

Bauer, Andreas (2014). "Investigation of itinerant antiferromagnets and cubic chiral helimagnets". Dissertation. München: Technische Universität München.

Bauer, Gerrit E. W. and Jochen R. Schneider (1985). "Electron correlation effect in the momentum density of copper metal". *Physical Review B* 31 (2), 681.

Bearasley, G., Stephan Berko, J. Mader, and M. Shulman (1975). "Comments on the Lock-Crisp-West theorem with experimental examples". *Applied Physics A* 5 (4), 375.

Becker, H., E. Dietz, U. Gerhardt, and H. Angermüller (1975). "Momentum distribution of photoelectrons emitted from Cu and Ag single crystals, and its polarization dependence". *Physical Review B* 12 (6), 2084.

Bečvář, F., J. Čížek, L. Lešták, I. Novotný, I. Procházka, and F. Šebesta (2000). "A high-resolution BaF_2 positron-lifetime spectrometer and experience with its long-term exploitation". *Nuclear Instruments and Methods in Physics Research Section A: Accelerators, Spectrometers, Detectors and Associated Equipment* 443.2–3, 557.

Benea, D., J. Minár, L. Chioncel, S. Mankovsky, and H. Ebert (2012). "Magnetic Compton profiles of Fe and Ni corrected by dynamical electron correlations". *Physical Review B* 85 (8), 085109.

Bergersen, B., E. Pajanne, P. Kubica, M. J. Stott, and C. H. Hodges (1974). "Positron diffusion in metals". *Solid State Communications* 15.8, 1377.

Bergersen, Birger and Erkki Pajanne (1969). "Positron Effective Mass in an Electron Gas". *Physical Review* 186 (2), 375.

Berglund, C. N. and W. E. Spicer (1964). "Photoemission Studies of Copper and Silver: Experiment". *Physical Review* 136 (4A), A1044.

Beringer, Robert and C. G. Montgomery (1942). "The Angular Distribution of Positron Annihilation Radiation". *Physical Review* 61 (5-6), 222.

Berko, Stephan, S. Cushner, and J. C. Erskine (1968). "Fermi surface and conventional positron annihilation experiments: Copper as a test case". *Physics Letters A* 27.10, 668.

Berko, Stephan, M. Haghgooie, and J. J. Mader (1977). "Momentum density measurements with a new multicounter two-dimensional angular correlation of annihilation radiation apparatus". *Physics Letters A* 63.3, 335.

Berko, Stephan and J. J. Mader (1975). "Momentum density measurements by positron annihilation in metals and alloys; Recent experiments with a multicounter two-dimensional angular correlation apparatus". *Applied physics* 5.4, 287.

Berko, Stephan and Mills, A. P. (1971). "Spin Distribution Studies In Ferromagnetic Metals By Polarized Positron Annihilation Experiments". *Journal de Physique Colloques* 32.C1, 287.

Berko, Stephan and Joel Zuckerman (1964). "Polarized Positron Annihilation in Ferromagnets". *Physical Review Letters* 13 (11), 339.

— (1965). "Eratum: Polarized Positron Annihilation in Ferromagnets". *Physical Review Letters* 14 (3), 89.

Bethe, H. A. and L. C. Maximon (1954). "Theory of Bremsstrahlung and Pair Production. I. Differential Cross Section". *Physical Review* 93 (4), 768.

Biasini, Maurizio and Ján Rusz (2006). "Cancellation of probe effects in measurements of spin-polarized momentum density by electron–positron annihilation". *Journal of Physics: Condensed Matter* 18.22, L289.

Billington, David et al. (2015). "Magnetic frustration, short-range correlations and the role of the paramagnetic Fermi surface of $PdCrO_2$". *Scientific Reports* 5, 12428.

Bisi, A., A. Fiorentini, E. Gatti, and L. Zappa (1962). "Magnetic Quenching of Positronium in Solids and Positron Helicity". *Physical Review* 128 (5), 2195.

Bisio, F., M. Nývlt, J. Franta, H. Petek, and J. Kirschner (2006). "Mechanisms of High-Order Perturbative Photoemission from Cu(001)". *Physical Review Letters* 96 (8), 087601.

Bisio, F., A. Winkelmann, W.-C. Lin, C.-T. Chiang, M. Nývlt, H. Petek, and J. Kirschner (2009). "Band structure effects in surface second harmonic generation: The case of Cu(001)". *Physical Review B* 80 (12), 125432.

Bisson, P. E., P. Descouts, and A. Dupanloup (1982). "A high angular resolution 2-D correlation apparatus for positron annihlation studies". *Helvetica Physica Acta* 55, 100.

Blackett, P. M. S. (1933). "The positive electron". *Nature* 132.3346, 917.

Blackett, P. M. S. and G. P. S. Occhialini (1933). "Some photographs of the tracks of penetrating radiation". *Proceedings of the Royal Society of London. Series A* 139.839, 699.

Boroński, E. and R. M. Nieminen (1986). "Electron-positron density-functional theory". *Physical Review B* 34 (6), 3820.

Bouarab, S., H. Nait-Laziz, C. Demangeat, A. Mokrani, and H. Dreyssé (1992). "Spin-polarized electronic structure of vanadium". *Physical Review B* 46 (2), 889.

Boyer, L. L., Dimitris A. Papaconstantopoulos, and B. M. Klein (1977). "Effect of self-consistency and exchange on the electronic structure of the transition metals, V, Nb, and Ta". *Physical Review B* 15 (8), 3685.

Brits, R. J. N. and F. von S. Toerien (1988). "The separation of ^{22}Na from Mg by cation exchange on a macroporous resin". *International Journal of Radiation Applications and Instrumentation. Part A. Applied Radiation and Isotopes* 39.10, 1045.

Bross, H. and H.-G. Junginger (1964). "Application of the modified augmented plane wave method to copper". *Physics Letters* 8.4, 240.

Brown, D., M. D. Crapper, K. H. Bedwell, L. B. Flannery, M. Petty, and P. A. Skull (1996). "A study of the Cu_2MnAl Heusler alloy using ultraviolet photoemission spectroscopy". *Journal of Physics: Condensed Matter* 8.32, 5941.

Burdick, Glenn A. (1961). "Topology of the Fermi Surface of Copper". *Physical Review Letters* 7 (5), 156.

— (1963). "Energy Band Structure of Copper". *Physical Review* 129 (1), 138.

Burrows, T. W. (2002). "Nuclear Data Sheets for A = 68". *Nuclear Data Sheets* 97.1, 1.

Buschow, K. H. J., P. G. van Engen, and R. Jongebreur (1983). "Magneto-optical properties of metallic ferromagnetic materials". *Journal of Magnetism and Magnetic Materials* 38.1, 1.

Callaway, J. and C. S. Wang (1977). "Energy bands in ferromagnetic iron". *Physical Review B* 16 (5), 2095.

Ceeh, Hubert Andreas (2015). "The new 2D-ACAR spectrometer for sipin-resolved measurements of the electronic structure in correlated systems". Dissertation. München: Technische Universität München.

Ceeh, Hubert Andreas, R. Engels, C. Wesolek, Josef Andreas Weber, and Christoph Hugenschmidt (2016a). "Study of position-sensitive PMTs as gamma cameras for 2D-ACAR". *Materials Science Forum*. to be published.

Ceeh, Hubert Andreas, Josef Andreas Weber, Peter Böni, Michael Leitner, D. Benea, L. Chioncel, H. Ebert, J. Minár, D. Vollhardt, and Christoph Hugenschmidt (2016b). "Local electron-electron interaction strength in ferromagnetic nickel determined by spin-polarized positron annihilation". *Scientific Reports* 6, 20898.

Ceeh, Hubert Andreas, Josef Andreas Weber, Christoph Hugenschmidt, Michael Leitner, and Peter Boni (2014). "Positron beam optics for the 2D-ACAR spectrometer at the NEPOMUC beamline". *Journal of Physics: Conference Series* 505.1, 012041.

Ceeh, Hubert Andreas, Josef Andreas Weber, Michael Leitner, Peter Böni, and Christoph Hugenschmidt (2013). "The source-sample stage of the new two-dimensional angular correlation of annihilation radiation spectrometer at Technische Universität München". *Review of Scientific Instruments* 84.4, 043905.

Chao, C. Y. (1930a). "Scattering of Hard γ-Rays". *Physical Review* 36 (10), 1519.

— (1930b). "The Absorption Coefficient of Hard γ-Rays". *Proceedings of the National Academy of Sciences of the United States of America* 16.6, 431.

Chatrchyan, S. et al. (2012). "Observation of a new boson at a mass of 125 GeV with the CMS experiment at the LHC". *Physics Letters B* 716.1, 30.

Chen, C., M. N. Gale, A. S. Kheifets, M. Vos, and M. R. Went (2005). "Spectral momentum densities of vanadium and vanadium oxide as measured by high energy (e, 2e) spectroscopy". *Journal of Physics: Condensed Matter* 17.48, 7689.

Chioncel, L., D. Benea, H. Ebert, I. Di Marco, and J. Minár (2014). "Momentum space anisotropy of electronic correlations in Fe and Ni: An analysis of magnetic Compton profiles". *Physical Review B* 89 (9), 094425.

Coleman, R. V., W. H. Lowrey, and J. A. Polo (1981). "Magnetotransport and the Fermi surface of iron". *Physical Review B* 23 (6), 2491.

Coleridge, P. T. and I. M. Templeton (1972). "High precision de Haas-van Alphen measurements in the noble metals". *Journal of Physics F: Metal Physics* 2.4, 643.

— (1982). "Fermi-surface radii in copper, silver, and gold". *Physical Review B* 25 (12), 7818.

Colombino, P., B. Fiscella, and L. Trossi (1963). "Point slits versus linear slits in the angular correlation of positron annihilation radiation". *Il Nuovo Cimento* 27.3, 589.

Con Foo, J. A., A. P. J. Stampfl, A. Ziegler, B. Mattern, M. Hollering, R. Denecke, L. Ley, J. D. Riley, and R. C. G. Leckey (1996). "Direct k-space photoemission imaging of the Fermi surface of Cu". *Physical Review B* 53 (15), 9649.

Cook, C. Sharp and Lawrence M. Langer (1948). "The Beta-Spectra of Cu^{64} as a Test of the Fermi Theory". *Physical Review* 73 (6), 601.

Cooper, M. J. and J. A. Duffy (2000). "Spin densities studied in momentum space". *Journal of Physics and Chemistry of Solids* 61.3, 345.

Cooper, Malcolm, Peter Mijnarends, Nobuhiro Shiotani, Nobuhiko Sakai, and Arun Bansil (2004). *X-ray Compton scattering*. Oxford: Oxford University Press.

Cormack, A. M. (1963). "Representation of a Function by Its Line Integrals, with Some Radiological Applications". *Journal of Applied Physics* 34.9, 2722.

— (1964). "Representation of a Function by Its Line Integrals, with Some Radiological Applications. II". *Journal of Applied Physics* 35.10, 2908.

— (1995). "Some early radiotherapy optimization work". *International Journal of Imaging Systems and Technology* 6.1, 2.

Courths, R. and S. Hüfner (1984). "Photoemission experiments on copper". *Physics Reports* 112.2, 53.

Cowan, T. E. et al. (1999). "High energy electrons, nuclear phenomena and heating in petawatt laser-solid experiments". *Laser and Particle Beams* 17 (04), 773.

Crasemann, Bernd, D. E. Rehfuss, and H. T. Easterday (1956). "Disintegration of Ge^{68}". *Physical Review* 102 (5), 1344.

Crowther, R. A., D. J. De Rosier, and A. Klug (1970). "The Reconstruction of a Three-Dimensional Structure from Projections and its Application to Electron Microscopy". *Proceedings of the Royal Society of London A: Mathematical, Physical and Engineering Sciences* 317.1530, 319.

Cui, X. Y., K. Shimada, M. Hoesch, Y. Sakisaka, H. Kato, Y. Aiura, M. Higashiguchi, Y. Miura, H. Namatame, and M. Taniguchi (2007a). "Angle-resolved photoemission spectroscopy study of Fe(1 1 0) single crystal: Many-body interactions between quasi-particles at the Fermi level". *Surface Science* 601.18, 4010.

Cui, X. Y., K. Shimada, Y. Sakisaka, H. Kato, Y. Aiura, M. Higashiguchi, Y. Miura, H. Namatame, and M. Taniguchi (2006). "High-resolution angle-resolved photoemission study of Fe (1 1 0)". *Physica B: Condensed Matter* 383.1, 146.

Cui, X. Y., K. Shimada, Y. Sakisaka, H. Kato, M. Hoesch, T. Oguchi, Y. Aiura, H. Namatame, and M. Taniguchi (2010). "Evaluation of the coupling parameters of many-body interactions in Fe(110)". *Physical Review B* 82 (19), 195132.

Cui, X. Y. et al. (2007b). "High-resolution angle-resolved photoemission spectroscopy of iron: A study of the self-energy". *Journal of Magnetism and Magnetic Materials* 310.2, Part 2, 1617.

Curie, Irène and F. Joliot (1933). "Sur l'origine des électrons positifs". *Comptes Rendus de l'Académie des Sciences* 196, 1581.

Da Luz, H. Natal, J. A. Mir, X. Carvalho, and J. M. F. dos Santos (2014). "X-ray imaging with GEMs using 100 μm thick foils". *Journal of Instrumentation* 9.06, C06007.

Damascelli, Andrea (2004). "Probing the Electronic Structure of Complex Systems by ARPES". *Physica Scripta* 2004.T109, 61.

Danan, H., A. Herr, and A. J. P. Meyer (1968). "New Determinations of the Saturation Magnetization of Nickel and Iron". *Journal of Applied Physics* 39.2, 669.

Davies, Handel, H. A. Bethe, and L. C. Maximon (1954). "Theory of Bremsstrahlung and Pair Production. II. Integral Cross Section for Pair Production". *Physical Review* 93 (4), 788.

De Rosier, D. J. and A. Klug (1968). "Reconstruction of Three Dimensional Structures from Electron Micrographs". *Nature* 217.5124, 130.

De Groot, R. A., F. M. Mueller, P. G. van Engen, and K. H. J. Buschow (1983). "New Class of Materials: Half-Metallic Ferromagnets". *Physical Review Letters* 50 (25), 2024.

DeBenedetti, S., C. E. Cowan, W. R. Konneker, and H. Primakoff (1950). "On the Angular Distribution of Two-Photon Annihilation Radiation". *Physical Review* 77 (2), 205.

Delapalme, A., J. Schweizer, G. Couderchon, and R. Perrier de la Bathie (1971). "Étude de l'alliage de Heusler (Cu_2MnAl) comme monochromateur de neutrons polarisés". *Nuclear Instruments and Methods* 95.3, 589.

Dirac, P. A. M. (1928). "The Quantum Theory of the Electron". *Proceedings of the Royal Society of London. Series A, Containing Papers of a Mathematical and Physical Character* 117.778, 610.

— (1930). "A Theory of Electrons and Protons". *Proceedings of the Royal Society of London. Series A, Containing Papers of a Mathematical and Physical Character* 126.801, 360.

— (1931). "Quantised Singularities in the Electromagnetic Field". *Proceedings of the Royal Society of London. Series A* 133.821, 60.

Dobrzyński, L. and E. Żukowski (1999). "Reconstruction of the uncompensated electron momentum density distribution by the maximum entropy method". *Journal of Physics: Condensed Matter* 11.41, 8049.

Dong, L. M., Z. D. Han, Y. Z. Guan, W. Li, and X. Y. Zhang (2012). "Mechanical properties and work function of $L2_1$ structure $AlCu_2X$ (X=Ti, Mn, Zr, or Hf) intermetallics". *Materials Science and Engineering: A* 545, 13.

Drummond, N. D., P. López Ríos, R. J. Needs, and C. J. Pickard (2011). "Quantum Monte Carlo Study of a Positron in an Electron Gas". *Physical Review Letters* 107 (20), 207402.

Dryzek, Jerzy and Doug Singleton (2006). "Implantation profile and linear absorption coefficients for positrons injected in solids from radioactive sources ^{22}Na and $^{68}Ge/^{68}Ga$". *Nuclear Instruments and Methods in Physics Research Section B: Beam Interactions with Materials and Atoms* 252.2, 197.

Dubois, Bernard and Dominique Chevereau (1979). "Decomposition of the Heusler alloy Cu_2MnAl at 360°C". *Journal of Materials Science* 14.10, 2296.

Dugdale, S. B., M. A. Alam, H. M. Fretwell, M. Biasini, and D. Wilson (1994). "Application of maximum entropy to extract Fermi surface topology from positron annihilation measurement". *Journal of Physics: Condensed Matter* 6.31, L435.

Dugdale, S. B., J. Laverock, C. Utfeld, M. A. Alam, T. D. Haynes, D. Billington, and D. Ernsting (2013). "The Bristol HIDAC 2D-ACAR Spectrometer". *Journal of Physics: Conference Series* 443.1, 012083.

Dumond, J. W. M., D. A. Lind, and B. B. Watson (1949). "Precision Measurement of the Wave-Length and Spectral Profile of the Annihilation Radiation from Cu^{64} with the Two-Meter Focusing Curved Crystal Spectrometer". *Physical Review* 75 (8), 1226.

Dunlap, R. A., G. Stroink, and K. Dini (1986). "Permanent magnetic properties of Cu-Mn-Al alloys". *Journal of Physics F: Metal Physics* 16.8, 1083.

Eastman, D. E., F. J. Himpsel, and J. A. Knapp (1980). "Experimental Exchange-Split Energy-Band Dispersions for Fe, Co, and Ni". *Physical Review Letters* 44 (2), 95.

Eastman, D. E., J. F. Janak, A. R. Williams, R. V. Coleman, and G. Wendin (1979). "Electronic structure of magnetic 3d metals: Ground state, Fermi surface and photoemission properties". *Journal of Applied Physics* 50.B11, 7423.

Eaton, John W., David Bateman, Søren Hauberg, and Rik Wehbring (2015). *GNU Octave version 4.0.0 manual: a high-level interactive language for numerical computations*.

Ebert, H., D. Ködderitzsch, and J. Minár (2011). "Calculating condensed matter properties using the KKR-Green's function method—recent developments and applications". *Reports on Progress in Physics* 74.9, 096501.

Eisenberger, P. and W. A. Reed (1974). "Gamma-ray Compton profiles of copper and nickel". *Physical Review B* 9 (8), 3242.

Eldrup, M., D. Lightbody, and J. N. Sherwood (1981). "The temperature dependence of positron lifetimes in solid pivalic acid". *Chemical Physics* 63.1–2, 51.

ELK (2015). URL: http://elk.sourceforge.net/.

Endō, Keizo, Tetuo Ohoyama, and Ren'iti Kimura (1964). "On the Magnetic Moment of Mn in Aluminum Heusler Alloy". *Journal of the Physical Society of Japan* 19.8, 1494.

Ernsting, D., D. Billington, T. D. Haynes, T. E. Millichamp, J. W. Taylor, J. A. Duffy, S. R. Giblin, J. K. Dewhurst, and S. B. Dugdale (2014). "Calculating electron momentum densities and Compton profiles using the linear tetrahedron method". *Journal of Physics: Condensed Matter* 26.49, 495501.

Falub, Claudiu Valentin (2002). "The Delft intense slow positron beam 2D-ACAR facility for analysis of nanocavities and quantum dots". PhD thesis. Technische Universiteit Delft.

Fang, C. M., M. A. van Huis, B. J. Thijsse, and H. W. Zandbergen (2012). "Stability and crystal structures of iron carbides: A comparison between the semi-empirical modified embedded atom method and quantum-mechanical DFT calculations". *Physical Review B* 85 (5), 054116.

Farmer, W. S., F. Sinclair, Stephan Berko, and G. M. Beardsley (1979). "Studies of the Fermi surface of V_3Si by 2D ACAR measurements". *Solid State Communications* 31.7, 481.

Faulkner, J. S., Harold L. Davis, and H. W. Joy (1967). "Calculation of Constant-Energy Surfaces for Copper by the Korringa-Kohn-Rostoker Method". *Physical Review* 161 (3), 656.

Fehrenbach, G. M. and H. Bross (1993). "Self-consistent spline augmented-plane-wave calculation: Ground-state properties of Cu". *Physical Review B* 48 (24), 17703.

Felcher, G. P., J. W. Cable, and M. K. Wilkinson (1963). "The magnetic moment distribution in Cu_2MnAl". *Journal of Physics and Chemistry of Solids* 24.12, 1663.

Fermi Surface Database, Vanadium (14.07.2007). URL: http://www.phys.ufl.edu/fermisurface/html/Z023.html (visited on 05/17/2016).

Fermi, Enrico (1934). "Versuch einer Theorie der β-Strahlen. I". German. *Zeitschrift für Physik* 88.3-4, 161.

Fermi, Enrico and George E. Uhlenbeck (1933). "On the Recombination of Electrons and Positrons". *Physical Review* 44 (6), 510.

Firestone, R. B. (2005). "Nuclear Data Sheets for". *Nuclear Data Sheets* 106.1, 1.

Fretwell, H. M., S. B. Dugdale, M. A. Alam, M. Biasini, L. Hoffmann, and A. A. Manuel (1995). "Reconstruction of 3D Electron-Positron Momentum Densities from 2D Projections: Role of Maximum-Entropy Deconvolution Prior to Reconstruction". *Europhysics Letters* 32.9, 771.

Fujiwara, Kunio and Osamu Sueoka (1966). "A Precise Measurement of the Angular Correlation of Annihilation Radiation in Copper Single Crystals". *Journal of the Physical Society of Japan* 21, 1947.

Fukaya, Y., M. Hashimoto, A. Kawasuso, and A. Ichimiya (2008). "Surface structure of Si(111)-(8×2)–In determined by reflection high-energy positron diffraction". *Surface Science* 602.14, 2448.

Funtikov, A. I. (2004). "Phase Diagram of Iron." *High-Pressure Shock Compression of Solids VII: Shock Waves and Extreme States of Matter*. Ed. by V. E. Fortov, L. V. Al'tshuler, R. F. Trunin, and A. I. Funtikov. New York, NY: Springer New York, 225. ISBN: 978-1-4757-4048-6.

Galanakis, I. and E. Şaşıoğlu (2012). "Ab-initio calculation of effective exchange interactions, spin waves, and Curie temperature in $L2_1$- and $L1_2$-type local moment ferromagnets". *Journal of Materials Science* 47.21, 7678.

Genoud, P., A. A. Manuel, E. Walker, and M. Peter (1991). "Spin-polarized 2D ACAR in nickel across the Curie temperature". *Journal of Physics: Condensed Matter* 3.23, 4201.

Genoud, P. and A. K. Singh (1989). "Calculation of Compton profiles in ferromagnetic iron using LMTO wavefunctions". *Journal of Physics: Condensed Matter* 1.32, 5363.

Genoud, P., A. K. Singh, A. A. Manuel, T. Jarlborg, E. Walker, M. Peter, and M. Weller (1988). "Electron momentum distribution and spin density of ferromagnetic iron studied by spin-polarised positron annihilation". *Journal of Physics F: Metal Physics* 18.9, 1933.

Georges, Antoine, Gabriel Kotliar, Werner Krauth, and Marcelo J. Rozenberg (1996). "Dynamical mean-field theory of strongly correlated fermion systems and the limit of infinite dimensions". *Reviews of Modern Physics* 68 (1), 13.

Ghosh, V. J. (1995). "Positron implantation profiles in elemental and multilayer systems". *Applied Surface Science* 85, 187.

Gold, A. V., L. Hodges, P. T. Panousis, and D. R. Stone (1971). "De Haas-van Alphen Studies of Ferromagnetic Iron and a Model for its Fermi Surface". *International Journal of Magnetism* 2, 357.

Gordon, Richard, Robert Bender, and Gabor T. Herman (1970). "Algebraic Reconstruction Techniques (ART) for three-dimensional electron microscopy and X-ray photography". *Journal of Theoretical Biology* 29.3, 471.

Gosálbez-Martínez, Daniel, Ivo Souza, and David Vanderbilt (2015). "Chiral degeneracies and Fermi-surface Chern numbers in bcc Fe". *Physical Review B* 92 (8), 085138.

Graf, Tanja, Claudia Felser, and Stuart S. P. Parkin (2011). "Simple rules for the understanding of Heusler compounds". *Progress in Solid State Chemistry* 39.1, 1.

Gray, A. X. et al. (2011). "Probing bulk electronic structure with hard X-ray angle-resolved photoemission". *Nature Materials* 10.10, 759.

Green, R. E. and A. T. Stewart (1955). "Angular Correlation of Photons from Positron Annihilation in Light Metals". *Physical Review* 98 (2), 486.

Gull, S. F. and G. J. Daniell (1978). "Image reconstruction from incomplete and noisy data". *Nature* 272.5655, 686.

Haghgooie, M., J. J. Mader, and Stephan Berko (1978). "Direct observation of the high-momentum components of the conduction band of copper by two-dimensional angular correlation of annihilation radiation". *Physics Letters A* 69.4, 293.

Hanna, S. S. and R. S. Preston (1957). "Positron Polarization Demonstrated by Annihilation in Magnetized Iron". *Physical Review* 106 (6), 1363.

— (1958). "Polarization of Positrons and Annihilation in Ferromagnetic Materials". *Physical Review* 109 (3), 716.

Hansen, H. E., S. Linderoth, and K. Petersen (1982). "Positron implantation profile in nickel". *Applied Physics A* 29.2, 99.

Hanssen, K. E. H. M. and P. E. Mijnarends (1986). "Positron-annihilation study of the half-metallic ferromagnet NiMnSb: Theory". *Physical Review B* 34.8, 5009.

Hanssen, K. E. H. M., P. E. Mijnarends, L. P. L. M. Rabou, and K. H. J. Buschow (1990). "Positron-annihilation study of the half-metallic ferromagnet NiMnSb: Experiment". *Physical Review B* 42.3, 1533.

Hasegawa, Masuyuki, Toshinobu Chiba, Atsuo Kawasuso, Takashi Akahane, Masashi Suezawa, Sadae Yamaguchi, and Koji Sumino (1995). "Positron-Annihilation 2D-Acar Study of Divacancy and Vacancy-Oxygen Pairs in Si". *Materials Science Forum* 196-201, 1481.

Hautojärvi, P. and C. Corbel (1995). "Positron spectroscopy of defects in metals and semiconductors". *Positron spectroscopy of solids*. IOP, 491.

Hawari, Ayman I., David W. Gidley, Jun Xu, Jeremy Moxom, Alfred G. Hathaway, Benjamin Brown, and Richard Vallery (2009). "The Intense Slow Positron Beam Facility at the NC State University PULSTAR Reactor". *AIP Conference Proceedings* 1099.1, 862.

Haynes, T. D., R. J. Watts, J. Laverock, Zs Major, M. A. Alam, J. W. Taylor, J. A. Duffy, and S. B. Dugdale (2012). "Positron annihilation study of the Fermi surface of Ni_2MnGa". *New Journal of Physics* 14.3, 035020.

Heitler, W. (1944). "Quantum Theory of Radiation." London: Oxford University Press, 230.

Herman, Gabor T. and Arnold Lent (1976). "Iterative reconstruction algorithms". *Computers in Biology and Medicine* 6.4, 273.

Heusler, Friedrich, W. Starck, and Erich Franz Adalbert Haupt (1903). "Über magnetische Manganlegierungen". *Verhandlungen der Deutschen Physikalischen Gesellschaft*, 219.

Hohenberg, P. and W. Kohn (1964). "Inhomogeneous Electron Gas". *Physical Review* 136 (3B), B864.

Hounsfield, G. N. (1973). "Computerized transverse axial scanning (tomography): Part 1. Description of system". *The British Journal of Radiology* 46.552, 1016.

Hugenschmidt, Christoph, Hubert Andreas Ceeh, Thomas Gigl, Florian Lippert, C. Piochacz, Markus Reiner, K. Schreckenbach, S. Vohburger, Josef Andreas Weber, and S. Zimnik (2014). "Positron Beam Characteristics at NEPOMUC Upgrade". *Journal of Physics: Conference Series* 505.1, 012029.

Hugenschmidt, Christoph, G. Kögel, R. Repper, K. Schreckenbach, P. Sperr, B. Straßer, and W. Triftshäuser (2002). "Monoenergetic positron beam at the reactor based positron source at FRM-II". *Nuclear Instruments and Methods in Physics Research Section B: Beam Interactions with Materials and Atoms* 192.1–2, 97.

Hugenschmidt, Christoph et al. (2015). "Quality of Heusler single crystals examined by depth-dependent positron annihilation techniques". *Applied Physics A* 119.3, 997.

Hughes, R. J., S. B. Dugdale, Zs. Major, M. A. Alam, T. Jarlborg, E. Bruno, and B. Ginatempo (2004). "Evolution of the Fermi surface and the oscillatory exchange coupling across Cr and Cr-based alloys". *Physical Review B* 69 (17), 174406.

Hurd, C. M., I. Shiozaki, and S. P. McAlister (1982). "Electrical and magnetic properties of Pd_2MnIn, Pd_2MnSn, Cu_2MnAl, and Cu_2NiSn Heusler alloys". *Physical Review B* 26 (2), 701.

Ibach, Harald and Hans Lüth (2009). *Festkörperphysik: Einführung in die Grundlagen*. Berlin: Springer-Verlag.

Inoue, Koji, Haruo Saito, Yasuyuki Nagashima, Toshio Hyodo, Yasuyoshi Nagai, Shinichi Muramatsu, Shota Nagai, and Keisuke Masuda (2002). "A position-sensitive γ-ray detector for positron annihilation 2D-ACAR based on metal package photomultiplier tubes". *Nuclear Instruments and Methods in Physics Research Section A: Accelerators, Spectrometers, Detectors and Associated Equipment* 487.3, 471.

Ishida, Shoji, H. Asato, E. Iwashima, Y. Kubo, and J. Ishida (1981). "Fermi surfaces of Cu_2MnAl, Pd_2MnSn and Ni_2MnSn". *Journal of Physics F: Metal Physics* 11.5, 1035.

Ishida, Shoji, Junji Ishida, Setsuro Asano, and Jiro Yamashita (1978). "Band Calculation of Cu_2MnAl". *Journal of the Physical Society of Japan* 45.4, 1239.

Jackson, J. D., S. B. Treiman, and H. W. Wyld (1957). "Possible Tests of Time Reversal Invariance in Beta Decay". *Physical Review* 106 (3), 517.

Jan, J.-P. and I. M. Templeton (1967). "Precision Measurements of $\langle 111 \rangle$ de Haas-van Alphen Frequencies in Copper, Silver, and Gold". *Physical Review* 161 (3), 556.

Jarlborg, T., A. A. Manuel, and M. Peter (1983). "Experimental and theoretical determination of the Fermi surface of V_3Si". *Physical Review B* 27 (7), 4210.

Jarlborg, T. and A. K. Singh (1987). "Local-density approach for calculation of electron-positron enhancement in transition metals". *Physical Review B* 36 (9), 4660.

Jeavons, A. P., G. Charpak, and R. J. Stubbs (1975). "The high-density multiwire drift chamber". *Nuclear Instruments and Methods* 124.2, 491.

Jensen, Kjeld O. and A. B. Walker (1990). "Positron thermalization and non-thermal trapping in metals". *Journal of Physics: Condensed Matter* 2.49, 9757.

Kaganov, Moisei I. and I. M. Lifshits (1979). "Electron theory of metals and geometry". *Soviet Physics Uspekhi* 22.11, 904.

Kahana, S. (1963). "Positron Annihilation in Metals". *Physical Review* 129.4, 1622.

Kaiser, J. H., R. N. West, and N. Shiotani (1986). "Electronic structure studies with positrons: a new approach to wavefunction effects". *Journal of Physics F: Metal Physics* 16.9, 1307.

Kak, A. C. and M. Slaney (1988). *Principles of Computerized Tomographic Imaging*. New York: IEEE Press.

Kanazawa, Ikuzo, Shoichiro Tanigawa, Ryoichi Suzuki, Yoji Mizuhara, Mizuka Sano, and Hiroo Inokuchi (1987). "Two-dimensional electron momentum distribution in graphite revealed by means of angular correlation of positron annihilation". *Journal of Physics and Chemistry of Solids* 48.8, 701.

Kapur, J. N. and H. K. Kesavan (1992). *Entropy Optimization Principles with Applications*. San Diego, CA: Academic Press. ISBN: 0123976707.

Karshenboim, Savely G. (2005). "Precision physics of simple atoms: QED tests, nuclear structure and fundamental constants". *Physics Reports* 422.1–2, 1.

Kawasuso, Atsuo, Masaki Maekawa, Yuki Fukaya, Atsushi Yabuuchi, and Izumi Mochizuki (2011). "Spin-polarized positron annihilation measurements of polycrystalline Fe, Co, Ni, and Gd based on Doppler broadening of annihilation radiation". *Physical Review B* 83.10, 100406.

— (2012). "Doppler broadening of annihilation radiation measurements on 3d and 4f ferromagnets using polarized positrons". *Physical Review B* 85 (2), 024417.

Klemperer, Otto (1934). "On the annihilation radiation of the positron". *Mathematical Proceedings of the Cambridge Philosophical Society* 30 (03), 347.

Knapp, J. A., F. J. Himpsel, A. R. Williams, and D. E. Eastman (1979). "Temperature dependence of bulk and surface energy bands in copper using angle-resolved photoemission". *Physical Review B* 19 (6), 2844.

Kohn, W. (1999). "Nobel Lecture: Electronic structure of matter-wave functions and density functionals". *Reviews of Modern Physics* 71 (5), 1253.

Kohn, W. and L. J. Sham (1965). "Self-Consistent Equations Including Exchange and Correlation Effects". *Physical Review* 140 (4A), A1133.

Koike, Takahisa, Shoji Uno, Tomohisa Uchida, Michiko Sekimoto, Takeshi Murakami, Koich Miyama, Masayoshi Shoji, Takuya Fujiwara, Eiichi Nakano, and Junsei Chiba (2011). "A new gamma-ray detector with gold-plated gas electron multiplier". *Nuclear Instruments and Methods in Physics Research Section A: Accelerators, Spectrometers, Detectors and Associated Equipment* 648.1, 180.

Kondo, H., T. Kubota, H. Nakashima, Y. Murakami, and S. Tanigawa (1993). "Study on the Three-Dimensional Electron Momentum Density and the Fermi Surface in Cu by Positron Annihilation". *physica status solidi (b)* 177.2, 345.

Kondo, H., T. Kubota, H. Nakashima, and Shoichiro Tanigawa (1992). "Positron Study of Momentum Density and Fermi Surface in Cu". *Materials Science Forum* 105 - 110, 675.

Kontrym-Sznajd, Grażyna (1990). "Three-Dimensional Image Reconstruction with Application in Positron Annihilation". *physica status solidi (a)* 117.1, 227.

Kontrym-Sznajd, Grażyna and Heinrich Sormann (2014a). "Electron-positron momentum densities in crystalline solids". *physica status solidi (b)* 251.1, 140.

— (2014b). "The influence of a positron on electron–positron momentum densities in metallic materials". *Physica Scripta* 89.1, 015808.

Kotliar, Gabriel and Dieter Vollhardt (2004). "Strongly correlated materials: Insights from dynamical mean-field theory". *Physics Today* 57.3, 53.

Krause-Rehberg, R., L. Büttner, F. Börner, and N. van der Walt (2015). URL: http://positron.physik.uni-halle.de/.

Krause-Rehberg, R., S. Sachert, G. Brauer, A. Rogov, and K. Noack (2006). "EPOS - An intense positron beam project at the ELBE radiation source in Rossendorf". *Applied Surface Science* 252.9, 3106.

Krumme, B., H. C. Herper, D. Erb, C. Weis, C. Antoniak, A. Warland, K. Westerholt, P. Entel, and H Wende (2011). "Induced magnetic Cu moments and magnetic ordering in Cu_2MnAl thin films on MgO(0 0 1) observed by XMCD". *Journal of Physics D: Applied Physics* 44.41, 415004.

Kruseman, A. C. (1999). "Two-Dimensional ACAR and Low-Background DBAR Studies on Materials with Defects". PhD thesis. Delft University of Technology.

Kubica, P. and A. T. Stewart (1975). "Thermalization of Positrons and Positronium". *Physical Review Letters* 34 (14), 852.

Kübler, J., A. R. William, and C. B. Sommers (1983). "Formation and coupling of magnetic moments in Heusler alloys". *Physical Review B* 28 (4), 1745.

Kubo, Y. and S. Asano (1990). "Magnetic Compton profiles of iron and nickel". *Physical Review B* 42 (7), 4431.

Kubota, T., H. Kondo, H. Nakashima, Y. Murakami, and S. Tanigawa (1991). "Study on Momentum Density and Fermi Surface in Paramagnetic Cr and W by Positron Annihilation". *physica status solidi (b)* 168.1, 179.

Kunzler, J. V., T. A. Grandi, W. H. Schreiner, P. Pureur, and D. E. Brandão (1980). "Spin-disorder resistivity in the $Cu_2Mn(Al_{1-x}Sn_x)$ Heusler alloys". *Journal of Physics and Chemistry of Solids* 41.10, 1023.

Lang, G., S. De Benedetti, and R. Smoluchowski (1955). "Measurement of Electron Momentum by Positron Annihilation". *Physical Review* 99 (2), 596.

LeBlanc, J. P. F., J. P. Carbotte, and E. J. Nicol (2010). "Signatures of Fermi surface reconstruction in Raman spectra of underdoped cuprates". *Physical Review B* 81 (6), 064504.

Lee, Martin J. G. (1969). "Phase-Shift Analysis of the Fermi Surface of Copper". *Physical Review* 187 (3), 901.

Lee, T. D. and C. N. Yang (1956). "Question of Parity Conservation in Weak Interactions". *Physical Review* 104 (1), 254.

Leitner, Michael (2013). "Electron momentum reconstruction in ACPAR". Diplomarbeit. Universität Wien.

Leitner, Michael, Hubert Andreas Ceeh, and Josef Andreas Weber (2012). "Eliminating spatial distortions in Anger-type gamma cameras". *New Journal of Physics* 14.12, 123014.

Leitner, Michael, Josef Andreas Weber, and Hubert Andreas Ceeh (2016). "Fermi surface determination from momentum density projections". *New Journal of Physics* 18.6, 063033.

Lettington, A. H. (1964). "Band structure of copper from photo-emission experiment". *Physics Letters* 9.2, 98.

Lindroos, M., J. Avila, M. E. Dávila, Y. Huttel, M. C. Asensio, and A. Bansil (2001). "Angle-scanned photoemission spectrum from Cu(1 0 0): theory vs experiment". *Surface Science* 482–485, Part 1, 718.

Lock, D. G., V. H. C. Crisp, and R. N. West (1973). "Positron annihilation and Fermi surface studies: a new approach". *Journal of Physics F: Metal Physics* 3.3, 561.

Löwe, Benjamin (2016). Dissertation. München: Universität der Bundeswehr.

Löwe, Benjamin, Markus Reiner, Werner Egger, Christoph Hugenschmidt, and Günther Dollinger (2013). "A position sensitive germanium detector for the measurement of angular deviation of annihilation radiation". *Journal of Physics: Conference Series* 443.1, 012098.

Lynn, K. G., M. Weber, L. O. Roellig, Jr. Mills A. P., and A. R. Moodenbaugh (1987). "A High Intensity Positron Beam at the Brookhaven Reactor". NATO ASI Series 169. Ed. by J.W. Humberston and E.A.G. Armour, 161.

Maglic, R. and F. M. Mueller (1971). "Wannier Representation of Electron Energy Bands and Iron Fermi Surface". *International Journal of Magnetism* 1, 289.

Maier-Leibnitz, H. (1951). "Impuls bei der Vernichtung langsamer Positronen in verschiedenen festen Stoffen". *Zeitschrift Naturforschung Teil A* 6, 663.

Major, Zs., S. B. Dugdale, R. J. Watts, J. Laverock, J. J. Kelly, D. C. R. Hedley, and M. A. Alam (2004). "Refining Fermi surface topologies from ab initio calculations through momentum density spectroscopies". *Journal of Physics and Chemistry of Solids* 65.12, 2011.

Makhov, AF. (1961a). "The Penetration Of Electrons Into Solids. 1. The Intensity Of An Electron Beam, Transverse Paths Of Electrons". *Soviet Physics-Solid State* 2.9, 1934.

— (1961b). "The Penetration Of Electrons Into Solids. 2. The Distribution Of Electrons In Depth". *Soviet Physics-Solid State* 2.9, 1942.

— (1961c). "The Penetration Of Electrons Into Solids. 3. The Absorption Of The Energy Of An Electron Beam". *Soviet Physics-Solid State* 2.9, 1945.

Mäkinen, J., S. Palko, J. Martikainen, and Hautojarv (1992). "Positron backscattering probabilities from solid surfaces at 2-30 keV". *Journal of Physics: Condensed Matter* 4.36, L503.

Manuel, A. A. (1982). "Construction of the Fermi Surface from Positron-Annihilation Measurements". *Physical Review Letters* 49 (20), 1525.

Manuel, A. A., Ø. Fischer, M. Peter, and A. P. Jeavons (1978). "An application of proportional chambers to the measurement of the electronic properties of solids by positron annihilation". *Nuclear Instruments and Methods* 156.1–2, 67.

Manuel, A. A., R. Sachot, P. Descouts, M. Peter, R. M. Singru, and A. K. Singh (1983). "Study of the electron momentum distribution in vanadium by positron annihilation". *Solid State Communications* 45.9, 799.

Mascher, P. (2015). URL: http://engphys.mcmaster.ca/faculty/dr-peter-mascher/ (visited on 02/13/2015).

Maskery, Ian (2013). "Spin densities in 4f and 3d magnetic systems". Phd Thesis. Coventry: University of Warwick.

Matsumoto, Makoto and Shinya Wakoh (1986). "Two-Dimensional Angular Correlation Distributions of Positron Annihilation Radiation in Vanadium and Chromium". *Journal of the Physical Society of Japan* 55.11, 3948.

— (1988). "Position-electron many-body enhancement effects in copper". *Physica B+C* 149.1, 57.

McDougall, B. A., T. Balasubramanian, and E. Jensen (1995). "Phonon contribution to quasiparticle lifetimes in Cu measured by angle-resolved photoemission". *Physical Review B* 51 (19), 13891.

Meitner, L. and K. Philipp (1933). "Die Anregung positiver Elektronen durch γ-Strahlen von ThC"". German. *Naturwissenschaften* 21.24, 468.

Melngailis, John (1970). "Positron Annihilation in Copper - Comparisons of Different Results". *Physical Review B* 2 (2), 563.

Mendis, Kith, John. W. Bennett, and Jamie Schulz (2013). "The Utilization of Australia's Research Reactor, OPAL".

Metzner, Walter and Dieter Vollhardt (1989). "Correlated Lattice Fermions in d = ∞ Dimensions". *Physical Review Letters* 62 (3), 324.

Mijnarends, P. E. (1967). "Determination of Anisotropic Momentum Distributions in Positron Annihilation". *Physical Review* 160 (3), 512.

— (1969). "Determination of the Fermi Surface of Copper by Positron Annihilation". *Physical Review* 178 (2), 622.

— (1973a). "Positron annihilation in 3d metals: I. Band-structure calculation of momentum densities in copper and ferromagnetic iron". *Physica* 63.2, 235.

— (1973b). "Positron annihilation in 3d metals: II. Investigation of spin and momentum density in magnetized iron with polarized positrons". *Physica* 63.2, 248.

Mijnarends, P. E. and L. Hambro (1964). "Positron annihilation in magnetised single crystals of iron". *Physics Letters* 10.3, 272.

Mijnarends, P. E. and R. M. Singru (1979). "Point-geometry angular correlation curves for Cu: A study of enhancement in positron annihilation". *Physical Review B* 19 (12), 6038.

Mikeska, H. J. (1967). "Phonon effects in the motion of positrons in metals". *Physics Letters A* 24.8, 402.

Mills, A. P. (2014). "Possibilities with pulsed polarized high density slow positrons". *Journal of Physics: Conference Series* 505.1, 012039.

Mills, Allen P. and Robert J. Wilson (1982). "Transmission of 1 - 6-keV positrons through thin metal films". *Physical Review A* 26 (1), 490.

Mohorovičić, St. (1934). "Möglichkeit neuer Elemente und ihre Bedeutung für die Astrophysik". *Astronomische Nachrichten* 253.4, 93.

Moliner, F. Garcia (1958). "On the fermi surface of copper". *Philosophical Magazine* 3.26, 207.

Moss, S. C. (1969). "Imaging the Fermi Surface Through Diffuse Scattering from Concentrated Disordered Alloys". *Physical Review Letters* 22 (21), 1108.

Mühlbauer, S., B. Binz, F. Jonietz, C. Pfleiderer, A. Rosch, A. Neubauer, R. Georgii, and P. Böni (2009). "Skyrmion Lattice in a Chiral Magnet". *Science* 323.5916, 915.

Nagai, Yasuyoshi, Yasuyuki Nagashima, Jaehong Kim, Yoshiko Itoh, and Toshio Hyodo (2000). "Measurement of positron spin polarization by using the Doppler broadening method". *Nuclear Instruments and Methods in Physics Research Section B: Beam Interactions with Materials and Atoms* 171.1-2, 199.

Nautiyal, Tashi and Sushil Auluck (1985). "Electronic structure of ferromagnetic iron: Fermi surface". *Physical Review B* 32 (10), 6424.

— (1986). "Electronic structure of ferromagnetic iron: Band structure and optical properties". *Physical Review B* 34 (4), 2299.

Neubauer, A., F. Jonietz, M. Meven, R. Georgii, G. Brandl, G. Behr, P. Böni, and C. Pfleiderer (2012). "Optical floating zone growth of high-quality Cu_2MnAl single crystals". *Nuclear Instruments and Methods in Physics Research Section A: Accelerators, Spectrometers, Detectors and Associated Equipment* 688, 66.

Onsager, L. (1952). "Interpretation of the de Haas-van Alphen effect". *The London, Edinburgh, and Dublin Philosophical Magazine and Journal of Science* 43.344, 1006.

Oppenheimer, J. R. (1930). "Two Notes On the Probability of Radiative Transitions". *Physical Review* 35 (8), 939.

Ouardi, Siham, Gerhard H. Fecher, Claudia Felser, and Jürgen Kübler (2013). "Realization of Spin Gapless Semiconductors: The Heusler Compound Mn_2CoAl". *Physical Review Letters* 110 (10), 100401.

Oxley, D. P., R. S. Tebble, and K. C. Williams (1963). "Heusler Alloys". *Journal of Applied Physics* 34.4, 1362.

Page, Lorne A. and Milton Heinberg (1957). "Measurement of the Longitudinal Polarization of Positrons Emitted by Sodium-22". *Physical Review* 106.6, 1220.

Pan, VM (1966). "A Phase Equilibrium Diagram for the Vanadium-Gallium System (Diagramma Ravnovesiya Faz Sistemy Vandii-Gallii)". *The Structure of Metallic Alloys*, 55.

Papaconstantopoulos, Dimitris A. (2015). *Handbook of the Band Structure of Elemental Solids: From Z= 1 To Z= 112*. Boston, MA: Springer US.

Papaconstantopoulos, Dimitris A., James R. Anderson, and Joseph W. McCaffrey (1972). "Self-Consistent Energy Bands in Vanadium at Normal and Reduced Lattice Spacings". *Physical Review B* 5 (4), 1214.

Paranjpe, S. K. and R. J. Begum (1980). "Magnetic properties of mixed Cu_2MnAl-Pd_2MnAl heusler alloys". *Journal of Magnetism and Magnetic Materials* 15–18, Part 1, 477.

Parker, Robert D. and Michael H. Halloran (1974). "Experimental study of the Fermi surface of vanadium". *Physical Review B* 9 (10), 4130.

Pattison, P., N. K. Hansen, and Jochen R. Schneider (1982). "Anisotropy in the compton profile of copper". *Zeitschrift für Physik B Condensed Matter* 46.4, 285.

Pecora, L. M., A. C. Ehrlich, A. A. Manuel, A. K. Singh, M. Peter, and R. M. Singru (1988). "Momentum density of vanadium: A reconstruction from two-dimensional positron-annihilation data". *Physical Review B* 37 (12), 6772.

Pecora, Louis M. (1987). "3D Tomographic Reconstruction from 2D Data Using Spherical Harmonics". *Nuclear Science, IEEE Transactions on* 34.2, 642.

Perdew, John P., Kieron Burke, and Matthias Ernzerhof (1996). "Generalized Gradient Approximation Made Simple". *Physical Review Letters* 77 (18), 3865.

Perić, B., T. Valla, M. Milun, and P. Pervan (1995). "On the electronic structure of vanadium: the angular resolved photoelectron spectroscopy of V(100) surface". *Vacuum* 46.8–10, 1181.

Perrin, F. (1933). "Materialisation d'electrons lors du choc de deuxelectrons. Processus divers d'annihilation deselectrons positifs". *Comptes Rendus de l'Academie des Sciences* 197, 1302.

Pervan, P., T. Valla, M. Milun, A. B. Hayden, and D. P. Woodruff (1996). "Photoemission and inverse photoemission spectroscopy of V(100)". *Journal of Physics: Condensed Matter* 8.23, 4195.

Phillips, R. A. (1971). "The De Haas-van Alphen effect in vanadium". *Physics Letters A* 36.5, 361.

Pippard, A. B. (1957a). "A proposal for determining the fermi surface by magneto-acoustic resonance". *Philosophical Magazine* 2.21, 1147.

— (1957b). "An Experimental Determination of the Fermi Surface in Copper". *Philosophical Transactions of the Royal Society of London. Series A, Mathematical and Physical Sciences* 250.979, 325.

Podberezskaya, N. V. (2012). "Heat-resistant metals in Mendeleev's periodic table". *Crystallography Reports* 57.6, 768.

Pou, Pablo, Fernando Flores, José Ortega, Rubén Pérez, and Alfredo Levy Yeyati (2002). "Electron correlation effects and ferromagnetism in iron". *Journal of Physics: Condensed Matter* 14.23, L421.

Prasad, R., R. Benedek, J. E. Robinson, and A. Bansil (1989). "Positron annihilation in vacancies: Korringa-Kohn-Rostoker formulation and application to Cu". *Physical Review B* 40 (13), 8620.

Pylak, M., Grażyna Kontrym-Sznajd, and L. Dobrzyński (2011). "Electron–positron momentum density distribution of Gd from 2D ACAR data via Maximum Entropy and Cormack's methods". *Applied Physics A* 104 (2), 587.

Qi, Y. J., M. J. Zhang, C. L. Zhao, and R. F. Wojcik (2007). "Performance comparison of subtractive resistive readout with conventional resistive readout for a high-resolution compact gamma camera". *Nuclear Science Symposium Conference Record, 2007. NSS '07. IEEE*. Vol. 5, 3725.

Qu, Zhe, Anura Goonewardene, Krishnan Subramanian, Jeevananda Karunamuni, Neeraj Mainkar, Liangang Ye, Roger L. Stockbauer, and Richard L. Kurtz (1995). "Imaging the Fermi surface of Cu using photoelectron spectroscopy". *Surface Science* 324.2, 133.

Rabou, L. P. L. M. and P. E. Mijnarends (1984). "Approximate validity of the Lock-Crisp-West theorem in positron annihilation". *Solid State Communications* 52.11, 933.

Radon, Johann (1917). "Über die Bestimmung von Funktionen durch ihre Integralwerte längs gewisser Mannigfaltigkeiten". *Berichte über die Verhandlungen der Königlich Sächsischen Gesellschaft der Wissenschaften zu Leipzig*. Vol. 69. B. G. Teubner Leipzig, 262.

Rakhecha, V. C., R. Chakravarthy, and N. S. Satya Murthy (1976). "Magnetic moment distribution in Cu_2MnAl". *Proceedings of the conference on neutron scattering*. Gatlinburg.

— (1978). "A polarised neutron study of magnetic moment density in Cu_2MnAl". *Pramana-Journal of Physics* 11.2, 159.

Ramachandran, G. N. and A. V. Lakshminarayanan (1971). "Three-dimensional Reconstruction from Radiographs and Electron Micrographs: Application of Convolutions instead of Fourier Transforms". *Proceedings of the National Academy of Sciences* 68.9, 2236.

Reiner, Markus (2015). "Point defects in MnSi and YBCO studied by Doppler broadening spectroscopy using a positron beam". Dissertation. München: Technische Universität München.

Reiner, Markus, Thomas Gigl, R. Jany, G. Hammerl, and Christoph Hugenschmidt (2015). "Detection and imaging of the oxygen deficiency in single crystalline $YBa_2Cu_3O_{7-\delta}$ thin films using a scanning positron beam". *Applied Physics Letters* 106.11, 111910.

Riepe, G., D. Protic, R. Kurz, W. Triftshaeuser, and Zs. Kajcsos (1979). "A high purity germanium position-sensitive detector for positron annihilation experiments". *Proceedings of the fifth international conference on positron annihilation*. Japan: Japan Inst of Metals, 371.

Roaf, D. J. (1962). "The Fermi Surfaces of Copper, Silver and Gold II. Calculation of the Fermi Surfaces". *Philosophical Transactions of the Royal Society of London. Series A, Mathematical and Physical Sciences* 255.1052, pp.

Robinson, J. S., P. G. McCormick, and R. Street (1995). "Structure and properties of Cu_2MnAl synthesized by mechanical alloying". *Journal of Physics: Condensed Matter* 7.22, 4259.

Robles, J. M. Campillo, E. Ogando, and F. Plazaola (2007). "Positron lifetime calculation for the elements of the periodic table". *Journal of Physics: Condensed Matter* 19.17, 176222.

Roth, F., C. Lupulescu, E. Darlatt, A. Gottwald, and W. Eberhardt (2016). "Angle resolved photoemission from Cu single crystals: Known facts and a few surprises about the photoemission process". *Journal of Electron Spectroscopy and Related Phenomena* 208. Special Issue: Electronic structure and function from state-of-the-art spectroscopy and theory, 2.

Ruark, Arthur E. (1945). "Positronium". *Physical Review* 68 (11-12), 278.

Rudin, Leonid I., Stanley Osher, and Emad Fatemi (1992). "Nonlinear total variation based noise removal algorithms". *Physica D: Nonlinear Phenomena* 60.1–4, 259.

Rusz, Ján and Maurizio Biasini (2007). "Positron wave-function effects in the measurement of the two-dimensional angular correlation of the annihilation radiation of a spin-polarized system". *Physical Review B* 75 (23), 235115.

Rutzinger, Martin (2012). "Design and Charakterisierung eines Gas-Elektronen-Multiplier (GEM) Detektors zum ortsaufgelösten Nachweis von 511 keV Gammastrahlung". Bachelorarbeit. München: Technische Universität München.

Sakai, Nobuhiko, M. Ito, H. Kawata, T. Iwazumi, M. Ando, N. Shiotani, F. Itoh, Y. Sakurai, and S. Nanao (1991). "Application of circularly polarized x-rays to magnetic Compton-scattering experiments". *Nuclear Instruments and Methods in Physics Research Section A: Accelerators, Spectrometers, Detectors and Associated Equipment* 303.3, 488.

Sakai, Nobuhiko and Kazuo Ôno (1976). "Compton Profile Due to Magnetic Electrons in Ferromagnetic Iron Measured with Circularly Polarized γ Rays". *Physical Review Letters* 37 (6), 351.

Sakisaka, Y., T. Maruyama, H. Kato, Y. Aiura, and H. Yanashima (1990). "Angle-resolved photoemission study of relativistic effects in the bulk electronic structure of Fe". *Physical Review B* 41 (17), 11865.

Sakisaka, Y., Thor Rhodin, and D. Mueller (1985). "Angle-resolved photoemission from Fe(110): Determination of $E(\vec{k})$". *Solid State Communications* 53.9, 793.

Sakurai, Y., S. Kaprzyk, A. Bansil, Y. Tanaka, G. Stutz, H. Kawata, and N. Shiotani (1999). "A high-resolution Compton scattering study of Cu: experiment and theory". *Journal of Physics and Chemistry of Solids* 60.7, 905.

Sánchez-Barriga, J. et al. (2012). "Effects of spin-dependent quasiparticle renormalization in Fe, Co, and Ni photoemission spectra:An experimental and theoretical study". *Physical Review B* 85 (20), 205109.

Sarri, G. et al. (2013). "Table-Top Laser-Based Source of Femtosecond, Collimated, Ultrarelativistic Positron Beams". *Physical Review Letters* 110 (25), 255002.

Şaşıoğlu, E., L. M. Sandratskii, and P. Bruno (2008). "Role of conduction electrons in mediating exchange interactions in Mn-based Heusler alloys". *Physical Review B* 77 (6), 064417.

Sauli, Fabio (1997). "GEM: A new concept for electron amplification in gas detectors". *Nuclear Instruments and Methods in Physics Research Section A: Accelerators, Spectrometers, Detectors and Associated Equipment* 386.2–3, 531.

— (2001). "Gas detectors: achievements and trends". *Nuclear Instruments and Methods in Physics Research Section A: Accelerators, Spectrometers, Detectors and Associated Equipment* 461.1–3, 47.

— (2011). *Gaseous radiation detectors: Fundamentals and applications*. Cambridge: Cambridge University Press, 1. ISBN: 978-1-107-04301-5.

Schäfer, J., M. Hoinkis, Eli Rotenberg, P. Blaha, and R. Claessen (2005). "Fermi surface and electron correlation effects of ferromagnetic iron". *Physical Review B* 72 (15), 155115.

Schleuder, Michaela (2015). "Messung der spinabhängigen Lebensdauer von Positronen in Eisen und Untersuchung von magnetischem Quenching von Positronium in Teflon". Bachelorarbeit. München: Technische Universität München.

Schrapp, Michael Johannes (2015). "Multi Modal Data Fusion in Industrial X-ray Computed Tomography". PhD thesis. Technische Universität München. ISBN: 978-3-8440-3541-4.

Schut, H., A. van Veen, J. De Roode, and F. Labohm (2004). "Long term performance of the reactor based positron beam POSH". *Materials Science Forum*. Vol. 445. Trans Tech Publ, 507.

Segall, B. (1961). "Calculated Shape of the Fermi Surface of Copper". *Physical Review Letters* 7 (5), 154.

Senicki, E. M. D., E. H. Becker, A. G. Gould, and B. G. Hogg (1972). "Angular correlation of positron annihilation radiation in copper single crystals". *Physics Letters A* 41.4, 293.

Senicki, E. M. D., E. H. Becker, A. G. Gould, R. N. West, and B. G. Hogg (1973). "Positron annihilation in copper single crystals". *Journal of Physics and Chemistry of Solids* 34.4, 673.

Shannon, C. E. (1948). "A Mathematical Theory of Communication". *Bell System Technical Journal* 27.3, 379.

Shepp, L. A. and B. F. Logan (1974). "The Fourier reconstruction of a head section". *Nuclear Science, IEEE Transactions on* 21.3, 21.

Shiotani, N., Y. Tanaka, M. Ito, Naoya Sakai, Yoji Sakurai, Hiroshi Sakurai, F. Itoh, T. Iwazumi, H. Kawata, and Motohide Ando (1992). "Electron Momentum Distribution in Vanadium". *Materials Science Forum* 105 - 110, 833.

Shiotani, Nobuhiro, Takuya Okada, Tadashi Mizoguchi, and Hisashi Sekizawa (1975). "Angular Distribution of Positron Annihilation Radiation in Vanadium and Niobium–Experiment". *Journal of the Physical Society of Japan* 38.2, 423.

Shiotani, Nobuhiro, Yoshikazu Tanaka, Yoshiharu Sakurai, Nobuhiko Sakai, Masahisa Ito, Fumitake Itoh, Toshiaki Iwazumi, and Hiroshi Kawata (1993). "Compton Scattering Study of Electron Momentum Density in Vanadium". *Journal of the Physical Society of Japan* 62.1, 239.

Shoenberg, D. (1962). "The Fermi Surfaces of Copper, Silver and Gold I. The de Haas-van Alphen Effect". *Philosophical Transactions of the Royal Society of London. Series A, Mathematical and Physical Sciences* 255.1052, 85.

Singh, A. K. and T. Jarlborg (1985). "Calculation of Compton profiles and positron annihilation matrix elements using LMTO wavefunctions". *Journal of Physics F: Metal Physics* 15.3, 727.

Singh, A. K., A. A. Manuel, R. M. Singru, R. Sachot, E. Walker, P. Descouts, and M. Peter (1985). "Electron momentum distribution and Fermi surface of vanadium studied by positron annihilation". *Journal of Physics F: Metal Physics* 15.11, 2375.

Singh, A. K. and R. M. Singru (1984). "Application of the Lock-Crisp-West theorem to vanadium and paramagnetic chromium". *Journal of Physics F: Metal Physics* 14.7, 1751.

Singh, Balraj (2007). "Nuclear Data Sheets for A = 64". *Nuclear Data Sheets* 108.2, 197.

Singh, M., C. S. Wang, and J. Callaway (1975). "Spin-orbit coupling, Fermi surface, and optical conductivity of ferromagnetic iron". *Physical Review B* 11 (1), 287.

Ślebarski, A., M. B. Maple, E. J. Freeman, C. Sirvent, D. Tworuszka, M. Orzechowska, A. Wrona, A. Jezierski, S. Chiuzbaian, and M. Neumann (2000). "Weak ferromagnetism induced by atomic disorder in Fe_2TiSn". *Physical Review B* 62.5, 3296.

Smedskjaer, L. C. and D. G. Legnini (1990). "A study on symmetrization of 2D ACAR positron annihilation data". *Nuclear Instruments and Methods in Physics Research Section A: Accelerators, Spectrometers, Detectors and Associated Equipment* 292.2, 487.

Snow, E. C. and J. T. Waber (1967). "Self-Consistent Energy Bands of Metallic Copper by the Augmented-Plane-Wave Method". *Physical Review* 157 (3), 570.

Šob, M. (1982). "Positron annihilation in iron and B2-ordered alloys FeAl and FeTi". *Journal of Physics F: Metal Physics* 12.3, 571.

Šob, M., S. Szuszkiewicz, and M. Szuszkiewicz (1984). "Polarized Positron Annihilation and Enhancement Effects in Ferromagnetic Iron". *physica status solidi (b)* 123.2, 649.

Solanki, A. K., R. Ahuja, and S. Auluck (1992). "The fermi surface properties of vanadium". *Physica B: Condensed Matter* 179.3, 257.

Sołtys, J. (1981). "X-ray diffraction research of the order–disorder transitions in the ternary heusler alloys B_2MnAl (B = Cu, Ni, Co, Pd, Pt)". *physica status solidi (a)* 66.2, 485.

Suzuki, Ryoichi, Makoto Osawa, Shoichiro Tanigawa, Makoto Matsumoto, and Nobuhiro Shiotani (1989). "Positron Study of Electron Momentum Density and Fermi Surface in Titanium and Zirconium". *Journal of the Physical Society of Japan* 58.9, 3251.

Szuszkiewicz, S., B. Rozenfeld, and M. Szuszkiewicz (1979). "Positron annihilation studies of the electronic structure of B.C.C. Fe". *physica status solidi (b)* 94.1, 273.

Tanaka, Yoshikazu, Nobuhiko Sakai, Yasunori Kubo, and Hiroshi Kawata (1993). "Three-dimensional momentum density of magnetic electrons in ferromagnetic iron". *Physical Review Letters* 70 (10), 1537.

Tao, S. J. (1972). "Positronium Annihilation in Molecular Substances". *The Journal of Chemical Physics* 56.11, 5499.

Thurman, Samuel T. and James R. Fienup (2007). "Noise histogram regularization for iterative image reconstruction algorithms". *Journal of the Optical Society of America A* 24.3, 608.

Tokii, Maki and Makoto Matsumoto (2006). "Magnetic Compton profiles of Fe by effective potentials". *Journal of Physics: Condensed Matter* 18.15, 3639.

Tokii, Maki and Shinya Wakoh (2003). "An Effective Potential of Metallic Vanadium and Chromium". *Journal of the Physical Society of Japan* 72.6, 1476.

Torsti, T. et al. (2006). "Three real-space discretization techniques in electronic structure calculations". *physica status solidi (b)* 243.5, 1016.

Turner, A. M., A. W. Donoho, and J. L. Erskine (1984). "Experimental bulk electronic properties of ferromagnetic iron". *Physical Review B* 29 (6), 2986.

Ullakko, K., J. K. Huang, C. Kantner, R. C. O' Handley, and V. V. Kokorin (1996). "Large magnetic-field-induced strains in Ni_2MnGa single crystals". *Applied Physics Letters* 69.13, 1966.

Van Veen, A., F. Labohm, H. Schut, J. de Roode, T. Heijenga, and P. E. Mijnarends (1997). "Testing of a nuclear-reactor-based positron beam". *Applied Surface Science* 116, 39.

Van Veen, A., H. Schut, J. de Vries, R. A. Hakvoort, and M. R. Ijpma (1991). "Analysis of positron profiling data by means of "VEPFIT"". *AIP Conference Proceedings* 218.1, 171.

Vehanen, A., K. Saarinen, P. Hautojärvi, and H. Huomo (1987). "Profiling multilayer structures with monoenergetic positrons". *Physical Review B* 35 (10), 4606.

Vries, J. De and F. E. T. Kelling (1987). "Fast timing with photomultiplier dynode pulses". *Nuclear Instruments and Methods in Physics Research Section A: Accelerators, Spectrometers, Detectors and Associated Equipment* 262.2–3, 385.

Wagner, Michael (2014). "Suche nach topologisch nichttrivialen Eigenschaften stark korrelierter Materialien". Dissertation. München: Technische Universität München.

Wakoh, Shinya, Stephan Berko, M. Haghgooie, and J. J. Mader (1979). "Two-dimensional angular correlation of positron-annihilation radiation in copper". *Journal of Physics F: Metal Physics* 9.11, L231.

Wakoh, Shinya, Yasunori Kubo, and Jiro Yamashita (1975). "Angular Distribution of Positron Annihilation Radiation in Vanadium and Niobium–Theory". *Journal of the Physical Society of Japan* 38.2, 416.

Wakoh, Shinya and Jiro Yamashita (1966). "Band Structure of Ferromagnetic Iron Self-Consistent Procedure". *Journal of the Physical Society of Japan* 21.9, 1712.

Weber, Josef Andreas, Andreas Bauer, Peter Böni, Hubert Andreas Ceeh, Stephen B. Dugdale, David Ernsting, Wolfgang Kreuzpaintner, Michael Leitner, Christian Pfleiderer, and Christoph Hugenschmidt (2015). "Spin-Resolved Fermi Surface of the Localized Ferromagnetic Heusler Compound Cu_2MnAl Measured with Spin-Polarized Positron Annihilation". *Physical Review Letters* 115 (20), 206404.

Weber, Josef Andreas, Peter Böni, Hubert Andreas Ceeh, Michael Leitner, and Christoph Hugenschmidt (2013). "First 2D-ACAR Measurements on Cu with the new Spectrometer at TUM". *Journal of Physics: Conference Series* 443.1, 012092.

Weber, Josef Andreas, Hubert Andreas Ceeh, Christoph Hugenschmidt, Michael Leitner, and Peter Böni (2014). "The effect of regularization on the reconstruction of ACAR data". *Journal of Physics: Conference Series* 505.1, 012047.

Wenninger, H., J. Stiewe, and H. Leutz (1968). "The 22Na positon spectrum". *Nuclear Physics A* 109.3, 561.

West, R. N. (1973). "Positron studies of condensed matter". *Advances in Physics* 22.3, 263.

— (1995). "Positron studies of the electronic structure of solids." Ed. by A. Dupasquier and A.P. Mills. Proceedings of the International School of Physics "Enrico Fermi". IOS Press. Chap. 2.2, 75.

West, R. N., J. Mayers, and P. A. Walters (1981). "A high-efficiency two-dimensional angular correlation spectrometer for positron studies". *Journal of Physics E: Scientific Instruments* 14.4, 478.

Weyl, Hermann (1929). "Elektron und Gravitation. I". German. *Zeitschrift für Physik* 56.5-6, 330.

Wheeler, John Archibald (1946). "Polyelectrons". *Annals of the New York Academy of Sciences* 48.3, 219.

Williams, H. J. (1937). "Magnetic Properties of Single Crystals of Silicon Iron". *Physical Review* 52 (7), 747.

Williams, Mark B., Allen R. Goode, Victor Galbis-Reig, Stan Majewski, Andrew G. Weisenberger, and Randolph Wojcik (2000). "Performance of a PSPMT based detector for scintimammography". *Physics in Medicine and Biology* 45.3, 781.

Wincott, P. L., N. B. Brookes, D. S. -L. Law, and G. Thornton (1986). "Relativistic effects on the surface electronic structure of Cu(001): Observation of a spin-orbit-gap surface state". *Physical Review B* 33 (6), 4373.

Winkelmann, Aimo, Christian Tusche, A. Akin Ünal, Martin Ellguth, Jürgen Henk, and Jürgen Kirschner (2012). "Analysis of the electronic structure of copper via two-dimensional photoelectron momentum distribution patterns". *New Journal of Physics* 14.4, 043009.

Wiza, Joseph Ladislas (1979). "Microchannel plate detectors". *Nuclear Instruments and Methods* 162.1–3, 587.

Wojcik, R., S. Majewski, B. Kross, D. Steinbach, and A. G. Weisenberger (1998). "High spatial resolution gamma imaging detector based on a 5" diameter R3292 Hamamatsu PSPMT". *Nuclear Science, IEEE Transactions on* 45.3, 487.

Wood, J. H. (1962). "Energy Bands in Iron via the Augmented Plane Wave Method". *Physical Review* 126 (2), 517.

Wu, C. S. and R. D. Albert (1949). "The Beta-Ray Spectra of Cu^{64}". *Physical Review* 75 (2), 315.

Zornberg, E. I. and F. M. Mueller (1966). "Fermi Surface of Copper". *Physical Review* 151 (2), 557.

Żukowski, E. et al. (1997). "Spin-dependent electron momentum densities in Cu_2MnAl studied by Compton scattering". *Journal of Physics: Condensed Matter* 9.49, 10993.

ACKNOWLEDGMENTS

As John Donne said 'No man is an Iland, intire of it selfe;' and neither could I have finished this work without the help of many others. At this point, I'd like to thank all those people who supported me on during my thesis.

Zu aller erst möchte ich mich bei Christoph Hugenschmidt der mich bei der Verwirklichung meines Projekts immer unterstützt hat und mir genug Freiraum lies auch eigene Ideen umzusetzen. Mit seinem Enthusiasmus für das Experimentieren konnte er nicht nur mich sondern die gesamte Positronengruppe anstecken.

Genauso möchte ich mich bei Peter Böni und Christian Pfleiderer für die gute Atmosphäre am Lehrstuhl und die hilfreichen Diskussionen bedanken.

I'd like to thank Stephen Dugdale for his great support and his patience despite the long distance and of course I want to thank him and Ashraf Alam for selling us the Anger cameras.

Furthermore, I am grateful to John Duffy and his group for the magnetic Compton measurements on Cu_2MnAl.

Liviu Chioncel und seiner Gruppe in Augsburg möchte ich für die fruchtbare Zusammenarbeit danken.

Bei allen Mitarbeitern des Physikdepartments insbesondere des Kristalllabors, der feinmechanischen Werkstatt, des Materiallagers, der Elektronikwerkstatt und des Elektroniklagers sowie allen Mitarbeitern am FRMII möchte ich mich für ihre Unterstützung bedanken. Mein großer Dank gilt hier Susanne Mayr, die mir bei meiner Arbeit sehr geholfen hat.

Dem Team des MLL allen voran Ludwig Beck möchte ich für seine unbürokratische Hilfe und die Aufnahme unter sein Dach danken. Ohne ihn wäre diese Arbeit nicht möglich gewesen.

Den Kollegen mit denen ich mein Containerbüro geteilt habe möchte ich für die fruchtbare Atmosphäre, die vielen Ideen und Diskussionen und noch vieles mehr danken. Michael, du hast mich ganz maßgeblich unterstützt. Pascal, deine Zielstrebigkeit hat auch mir sehr geholfen. Vielen Dank. Mit niemandem habe ich während meiner Doktorarbeit so eng zusammen gearbeitet wie mit dir, Hubert. Von und mit dir habe ich sehr viel gelernt und ich möchte mich für deine Hilfsbereitschaft und Geduld bedanken.

Der ganzen NEPOMUC Gruppe möchte ich für die freundliche Aufnahme und ihre Hilfsbereitschaft danken. Allen voran Sebastian Vohburger und Reinhard Repper für die technische Unterstützung, Christian Piochaz für Rat und Tat und Markus Reiner und Thomas Gigl für die DBAR Messungen.

Benjamin Löwe danke ich für die Überlassung seiner Software und Charakteristika der gepixelten Germanium Detektoren. Genauso danke ich Ulrich Ackermann für die Informationen über sein Projekt.

Bei allen Mitarbeitern von E21 möchte ich mich für die gute Zusammenarbeit bedanken. Ganz besonders bedanke ich mich bei Andreas Bauer für Kristalle und PPMS Messungen, bei Georg Benka fürs Cryomahlen, bei Marco Halder für die VSM Messungen, bei Wolfgang Kreuzpaintner für manche XRD Messung und bei Birgit Wiedemann für weitere XRD Messungen.

Ich danke Sebastian Widmann für die WDX Messung.

Vielen Dank Konstantin. Für Alles.